Investigating the Impact of Trees on Airflow within Street Canyons through the use of CFD and Field Measurements

Nina Glover

Department of Civil, Environmental and Geomatic Engineering

UCL

A thesis submitted for the degree of

Doctor of Philosophy

August 2015

I, Nina Glover confirm the work presented in this thesis is my own. Where information has been provided from other sources, I confirm that this has been indicated in the thesis.

I would like to dedicate this thesis to my loving parents Barbara and Roy for all their support over the years.

Acknowledgements

I would like to acknowledge and express my sincere appreciation to all those who have supported me throughout this PhD.

First and foremost to my supervisors Dr Liora Malki-Epshtein and Dr Ben Croxford for their invaluable expertise and guidance and continuing to find the time to support me after all these years. To Serge Guillas for introducing me to the world of Bayesian Calibration and for his enthusiasm, advice and guidance during our collaboration. To those who assisted in the field measurement campaign: Les Ansdell for his expert assistance in carrying out field measurements and providing much appreciated company and excellent sandwiches throughout the campaign. Gulmira Tulegenova and Ryan Schuster for their assistance in carrying out the measurements. To all those in the Building Physics group at Arup for providing expertise and resources in the application of CFD to the built environment. To the EPSRC for providing the stipend necessary to carry out this PhD.

On a personal note I would like to thank: my fellow post-graduate students at UCL, in particular Stella Karra, for providing much needed advice and moral support throughout this process, my parents for their support, encouragement and faith which gave me the confidence to undertake this PhD and finally my partner, Valentine, for his never ending patience and unfaltering support over the years without which none of this would have been possible.

Abstract

The local wind climate within the urban environment plays a key role in the removal of heat and pollutants from pedestrian occupied areas as well as having an impact on pedestrian comfort and safety. One component of the urban landscape which is often neglected in the consideration of airflow is tree planting which can constitute a major component of the built environment. The aim of this research was therefore to gain a greater understanding into the effect of tree planting on airflow within street canyons and investigate the use of CFD modelling in predicting such effects.

This aim was accomplished through the use of CFD modelling and field measurements of tree-lined and non tree-lined streets. Tree canopies were represented within the CFD model by porous sub-domains containing momentum and turbulence sinks. This simple representation was found to offer favourable comparison against field measurements and would therefore provide a simple and effective method for the inclusion of trees within CFD models of the urban environment.

Results of both the CFD models and field measurements found reduced wind speeds at pedestrian level as well as a significant reduction in vertical wind speeds at roof level within the tree-lined street. There was also seen to be a significant reduction in turbulence levels within the street containing trees. Based on these findings it can be concluded that trees are likely to be a useful aid in urban design helping to reduce high wind speeds and turbulence thus creating outdoor environments which are comfortable and safe for pedestrian use. However the results also indicate that the addition of trees to streets

can reduce the amount of air exchange at roof top level that occurs and thus may lead to a reduction in natural ventilation and potential build-up of pollutants within pedestrian occupied areas.

Contents

List of Figures

Nomenclature

A	Constant used in specification of turbulence profiles of atmospheric boundary layer (-)
B	Constant used in specification of turbulence profiles of atmospheric boundary layer (-)
C_d	Drag coefficient (-)
C_n	Form drag coefficient (m^-1)
C_μ	k-ε model constant (-)
$C_{\varepsilon 1}$	k-ε model constant (-)
$C_{\varepsilon 2}$	k-ε model constant (-)
$C_{\varepsilon 4}$	Closure constants in turbulence dissipation source term (-)
$C_{\varepsilon 5}$	Closure constants in turbulence dissipation source term (-)
D^M	Design of calibration parameters (-)
F	Drag Force (N)
H	Building Height (m)
h	normalised height (-)
k	Turbulence kinetic energy (m^2/s^2)
K_s	Sand-grain roughnes height (m)

K_{s+} Sand-grain roughness (-)

L_k Sink term describing the turbuent loss due to the short circuiting of the Kolmogorov scale (m^2/s^3)

n Number of CFD runs (-)

P_k Source term relating to the production of TKE by the wakes formed by plant elements (m^2/s^3)

S_k Term to be added to the turbulence kinetic energy equation due to influence of plant elements (m^2/s^3)

S_ε Source term to be added to the turbulence dissipation equation due to influence of plant elements

S_u Sink in momentum equation due to influence of plant elements ($kg/m^2\ s^2$)

U Wind Speed (m/s)

u Wind velocity vector in direction parallel street length (m/s)

$\overline{u_i' u_j'}$ Reynolds stresses (N/m)

u_t Tangential velocity at a distance Δy from the wall (m/s)

u^* Frictional velocity (m/s)

v Wind velocity vector in direction perpendicular street length (m/s)

v Kinematic viscosity (m^2/s)

W Street Width (m)

w Wind velocity vector in vertical direction (m/s)

y^F (h) Experimental data used in calibration process (m^2/s^2)

$y^M(x)$ Empirical output of the computer model used in the calibration process (m^2/s^2)

z	Height above ground level (m)
z_0	Roughness length (m)
β_d	Dimensionless coefficient to account for the short circuiting of the turbulence cascade (-)
β_p	Fraction of kinetic energy converted to tubulence kinetic energy due to drag(-)
Δy	Distance from wall boundary (m)
δ_{ij}	Kroneckar delta (-)
ε	Turbulent dissipation (m^2/s^3)
$\eta(x)$	Numerical intrinsic error (%)
θ	Calibration Parameters (-)
κ	Von Karman constant (-)
λ_η	Hyperparameters (-)
μ_t	Turbulence visocity (Pa s)
ρ	Density of fluid (kg/m^3)
σ_ε	k-ε model constant (-)
σ_k	k-ε model constant (-)
τ	Shear stress (Pa)
CFD	Computational fluid dynamics
LAD	Leaf Area Density (m^-1)
LDV	Laser-Doppler Velocimetry
LHS	Latin Hypercube Sampling

RANS Reynolds Average Navier Stokes Equations

TKE Turbulence Kinetic Energy (m^2/s^2)

UQ Uncertainty Quantification

Chapter 1

Introduction

There has been an increase in the urban population over the past decades with cities now housing over half the world's population. This has led to an increased initiative towards intelligent urban design which can address the common issues relating to the outdoor urban environment such as excessive pollution levels, problems relating to pedestrian safety and comfort and increased energy consumption.

In the quest for urban design which can provide outdoor spaces which are healthy, comfortable and safe for use by pedestrians the detailed understanding and accurate prediction of wind effects within these areas is key. For example the problems relating to excessive pollution levels within cities is often exacerbated by reduced wind speeds and stagnant airflow. There is therefore a desire to design urban areas which can provide natural ventilation (i.e. the removal of pollutants via air exchange with the atmosphere above roof top level) and thus protect occupants from unhealthy pollution levels. For example in Hong Kong where pollution has become an increasing problem over recent years, authorities require that an air ventilation assessment is carried out for any major development, in which the developer must prove that their development does not have a negative effect on air ventilation rates in order to obtain planning permission.

The introduction of buildings to the landscape does not always lead to reduced airflow, in some cases it can cause an increase in wind speeds which can result in problems with pedestrian safety and comfort. Where buildings protrude above neighbouring surrounds downdrafts can occur leading to accelerated winds at ground level. Funneling between narrow gaps between buildings can also lead

to increased wind speeds. In extreme cases such effects can have dangerous and potentially fatal consequences, although the more likely outcome of such effects is to result in environments which are uncomfortable and unsuitable for their intended use. The potential severe consequences of such wind effects has led to the introduction of government legislation and local planning policy within the UK regarding the wind climate impacts of any new major developments.

One component of the urban morphology which can suffer from problems both relating to wind comfort for pedestrians and high pollution levels is the street canyon. The airflow occurring within the street canyon has been the subject of extensive research in the past and it has been shown that the flow varies significantly with wind direction. A wind direction which is parallel to the street can lead to channeling and increased wind speeds whereas a wind direction which is perpendicular to the street can result in rotational vortices which trap pollutants within the street resulting in poor ventilation.

Opportunities exist to alleviate the problems described by manipulating the local wind microclimate through urban design. This may be done through: the adaption of building design such as chamfering of building corners to reduce excessive wind speeds or through the master plan layout by ensuring the spacing and orientation of buildings promotes natural ventilation and the removal of pollutants. One of the most commonly used tools in urban design is tree planting and soft landscaping as it offers shelter and shade to pedestrians, creating a more comfortable and aesthetically pleasing environment.

The attempt at manipulating the local micro-climate should be undertaken with care as the solution to one problem could potentially exacerbate another. For example the street canyon described may benefit from extensive tree planting which can provide shelter to pedestrians from adverse wind effects. However this may have a negative effect on the ventilation within the street and thus has the potential to lead to increased pollution levels.

Creating a safe, healthy and comfortable microclimate within either an existing or proposed development through the introduction of tree planting can therefore become a delicate balancing act between providing significant shelter from adverse wind effects but also the necessary ventilation to provide satisfactory air quality. In order to create such environments the following is required:

- The ability to accurately model and predict the airflow within the complex built environment
- A fundamental understanding of the effects of tree planting on the airflow within the built environment along with ability to accurately model such effects

The ability to accurately model the airflow within the built environment has been the subject of extensive research over the years with the most common modelling tools being wind tunnel testing and computational fluid dynamic (CFD) modelling. Wind tunnel tests are a well established and validated method for predicting wind environment within urban areas and allow for the accurate prediction of gust effects. The disadvantage of such methods is the high cost involved and point measurements are generally taken which can make it difficult to interpret results where complex flow patterns are present.

CFD modelling of airflow within the built environment has become more common place in recent years. The advantage that CFD has to offer over other physical methods is that it is comparatively low cost and can provide results with high spatial and temporal resolution. CFD can be used as a way of informing and interpreting field measurement data as it can provide a three dimensional picture of the flow which is not available from a limited number of point measurements taken in the field. CFD can also be used in isolation as a valuable tool in urban design for example it can be used to carry out a parametric study of various landscaping schemes to assess which provides the optimal wind environment.

The accuracy of CFD models is of crucial importance for its effective use as a tool in urban design. CFD models of the outdoor environment often rely on the specification of a large array of input parameters with often little information on the values some of these parameters should take. Therefore the assessment and reduction of parametric uncertainty is a crucial part of CFD development for these types of applications. In addition to this, comparison and validation of CFD methods against field measurements is necessary in order to improve the ability of such models to accurately predict airflow within the urban environment however such comparisons are currently hindered by the lack of available field data.

The second element in the aim to design comfortable, healthy and safe urban environments is the ability to accurately predict the effect that tree planting has on airflow. The effect that trees have on airflow within the urban environment is currently not well known mainly due to the many variables involved such as tree shape, foliage density, weather conditions and many others along with a lack of research in this area. There is a limited amount of research into how to include the effects of trees within a CFD model and in particular how such models would compare against field measurements.

In summary the accurate prediction of airflow within the built environment is vital for understanding issues relating to pedestrian comfort, pollution and contaminant dispersal, thermal comfort and energy use. Tree planting and vegetation constitute a large part of the urban landscape and have the potential to be useful measures in manipulating the local microclimate to create safe, comfortable and healthy environments. There is therefore a need to gain a greater understanding into the fundamental effects urban vegetation has on wind flow within the built environment and develop reliable and accurate methods for predicting such wind effects.

This forms the motivation for this research which has the following aims:

- To gain a greater understanding into the effect of tree planting on airflow within street canyons through the use of field measurements and CFD modelling
- To assess the capabilities of CFD modelling to predict airflow within tree lined streets through comparison with field measurements

This research focuses on the street canyon as this is one of the most well studied components of the built environment. Therefore in the quest for a greater understanding of the effect of tree planting on the built environment this would seem like the ideal place to start.

1.1 Structure of Thesis

The structure of this thesis is as follows:

Chapter 1 has provided the motivation behind this research as well as the aims and structure of the thesis.

Chapter 2 of this thesis gives the background into the subject of airflow within the urban environment. Starting out by discussing the boundary layer produced over urban areas, moving on to discuss the airflow patterns specific to street canyons and finally looking at airflow within tree lined streets.

Chapter 3 takes a more in depth look into the use of CFD in modelling airflow within the urban environment and the inclusion of trees or vegetation within CFD as well as a brief summary of the fundamental theory behind CFD modelling.

Chapter 4 summarises the method and results of a bench-mark test in which a CFD model of a simple street canyon was created and results compared with wind tunnel measurements. This allows for the validation of the use of CFD in the modelling of simple street canyon flow. It is important to determine the limitations of CFD for modelling this type of flow. These limitations will need to be taken into account when assessing the results of the full scale model. Performing this study also allowed for the investigation of statistical techniques which could be used in the assessment of uncertainties within the CFD model in particular those uncertainties relating to the turbulence model constants.

Chapter 5 summarises the method and results of the field measurement campaign which took measurements of wind velocities in two neighbouring streets in South London. The aim of the field measurements was to assess the airflow patterns, velocity and turbulence levels taken for a non-tree lined and tree lined street and use these results to improve our understanding on the effect tree planting can have on airflow within street canyons.

Chapter 6 discusses the method undertaken to carry out CFD modelling of both tree-lined and non tree-lined full scale street canyons. The results of these studies are then discussed in comparison with the field measurements to assess the ability of CFD to model flow both within a complex street canyon under variable wind conditions and airflow within a tree-lined street canyon. The results are also used to further our understanding of airflow within a street canyon containing tree planting.

Chapter 7 provides a discussion on the main findings of this research and how these relate to the original aims set out and the motivation of the research. In addition the limitations of the research are discussed.

Chapter 8 summarises the main conclusions of the work along with areas for future research

Chapter 2

Airflow within the Urban Environment - A Review

The environmental issues relating to pollution, pedestrian comfort and energy efficiency within cities have been discussed in the introduction to this thesis. Wind flow within the city plays a key role in regulating pollution levels, heat and energy use through the process of ventilation. Understanding airflow within the built environment has therefore become a popular area of research with the aim to help facilitate healthy urban design and offer solutions to existing problems such as high pollution levels, uncomfortable wind environmnets and excessive energy consumption.

As Oke [1988] explains in his summary on guidelines for effective street design, urban designers and city planners are faced with a range of problems which often have contradictory solutions. For example the aim to reduce pollution levels via maximising ventilation of outdoor spaces may result in increased wind speeds which are uncomfortable for pedestrian use or the excessive removal of heat from buildings which leads to increase energy usage. Oke [1988] goes on to provide some initial guidelines on street spacing and density which can offer a compromise between these conflicting aims. He concludes by noting that many modern city design such as those in North America do not conform to these guides and comprise of two extremes - the city which is densely packed and contains many high rise buildings and the suburbs which are scattered and sprawling. The

increased shelter within the city effects the pressure coefficients on the external facades of buildings resulting in a decreased opportunity for natural ventilation within the buildings and thus a potential increase in cooling loads and energy consumption. The other extreme is the suburbs in which very little shelter can lead to excessive removal of heat from homes and thus increase heating demands.

In an attempt to gauge a city or urban region's effectiveness at self-ventilation Hamlyn and Britter [2005] analysed the exchange velocity at canopy level above arrays of cubes with various packing density. The exchange velocity is defined as the average velocity for transfer of mass into or out of the urban canopy. They found that the greater the packing density the lower the exchange velocity implying that urban areas with high density have reduced effectiveness in the dispersal and removal of pollutants and heat from street level.

Panagiotou et al. [2013] extended the work carried out by Hamlyn and Britter [2005] through the investigation of the flow exchange processes within a real neighbourhood area of London. CFD modelling of this case study found higher exchange velocities than those found by Hamlyn and Britter [2005] and other researchers who had studied homogeneous building blocks. It was suggested that the inhomogeneous layout of the buildings along with the inclusion of tall buildings helped aid the exchange process of mass and momentum at canopy level and thus more breathable cities.

Although the tall buildings in Panagiotou et al. [2013] study were found to be an aid in pollution dispersion, the addition of tall buildings to cities are the most likely cause of accelerated winds which create problems regarding pedestrian comfort and safety. This was noted by Blocken et al. [2007] in their review of pedestrian wind environment around buildings in which they showed that past studies have indicated that for a single high rise building corner streams and frontal vortex are the most important causes for wind nuisance. Other problematic areas that were highlighted were passageways through or between buildings. They conclude by suggesting that solving wind environment problems after the design has been finalised is difficult, expensive and in-effective. Therefore wind environmental conditions should be taken into account during and even before design stage. They also stress that if CFD is to have a future in prediction of pedestrian wind environment validation is needed and highlight the lack of data

currently available to preform such tasks.

2.1 Street Canyon Flow

One important component of the built environment morphology is the street canyon. This is defined as a street which is continuously flanked by buildings on both sides. In order to understand the environmental issues within a street canyon such as pollution dispersion and pedestrian comfort we must have a detailed understanding of the airflow present within the street. For this reason the regular street canyon has become one of the most commonly studied components of the built environment.

This section of the literature review will take a more detailed look at how researchers have investigated street canyon flow in the past and the main findings. The typical flow features within a street canyon are mainly dependent on two factors, namely: the background wind direction and the street geometry. We will discuss each of these in turn.

2.1.1 Wind Direction

The wind direction relative to the street axis can be divided into three categories: perpendicular, parallel and oblique.

Street canyons subject to **perpendicular** wind conditions are the most commonly studied wind direction as this represents the worst case in terms of pollution removal from the canyon. Under such conditions some typical flow features we would expect to see for a symmetrical regular street canyon would be: flow separation and reattachment at the upwind roof, flow impingement in front of the upwind building with a stagnation point forming at approximately half the height of the building, a slow moving elongated vortex forming behind the downwind building and a rotational vortex or vortices formed within the street canyon [Oke, 1988]. The numbering and positioning of these vortices will be dependent on the street geometry which will be discussed in the following section.

It has been shown that the rotational vortex or vortices within the street are not present when the background wind speeds are low. Analysis of the velocity

measurements taken within a street canyon, DePaul and Sheih [1986] demonstrated the presence of a primary rotational vortex within the canyon. They found that this vortex was only present for wind speeds exceeding approximately 1.5 m/s - 2m/s.

In the presence of a rotational vortex we would expect to see negative vertical velocities on the downwind side of the street (downdrafts) and positive vertical velocities on the upwind side of the street (updrafts). This was demonstrated by DePaul and Sheih [1986] who showed a negative w velocity on the downwind side of the street with a peak velocity occurring at approximately 2/3 the height of the street and positive vertical velocity on the upwind side of the street with a peak velocity occurring at approximately half the height of the street. The vertical velocities were found to be larger on the downwind side of the street, this is common in street canyon flow under perpendicular wind conditions as momentum is lost as the flow moves across the street.

Under perpendicular wind conditions flow over an isolated street canyon results in a shear layer being shed from the corner of the upwind building. This results in a peak in turbulence kinetic energy above the upwind roof top which is advected downstream via turbulence transport. The shear layer spreads vertically with energy being advected from the core of the shear layer down into the street canyon. The turbulence kinetic energy (TKE) levels within the street canyon are highest on the down wind side of the street and reduce with height within the street.

There is less research available for flow within street canyons under **parallel** wind conditions compared with perpendicular conditions. It has generally been noted that for flow under parallel conditions the wind is channelled along the street leading to a strong horizontal flow [Louka et al., 2000]. Yamartino and Wiegand [1986] found that under parallel winds the along street wind component was directly proportional to the above-roof wind component parallel to the street with the constant of proportionality a function of the approach flow azimuth. They also provided a simple description of the along canyon velocity v in terms of a logarithmic profile with height.

Under an **oblique** wind direction the wind within the street canyon is known to form a helical or corkscrew like pattern. Field measurements carried out by

Eliasson et al. [2006] showed a persistent elliptical helix pattern which was rotated with respect to the ambient wind direction and noted that this type of flow pattern is typical when the wind direction is at least 30 degrees off parallel.

This type of flow pattern can be thought of as the linear superposition of a channelling of the wind described for parallel wind conditions and rotational vortex described for perpendicular wind conditions. Analysis of in street and above street wind components from the field measurements taken by Dobre et al. [2005] showed the the along street chanelling is linearly dependent on the component of the above-roof wind parallel to the street and the across-street rotational vortex depends linearly on the component of the above-roof wind perpendicular to the street.

2.1.2 Street Geometry

All investigations presented up until now have looked at street canyons which contain buildings with flat roofs. It is important to consider the effect different roof geometries have on airflow as the geometries in real city landscapes are highly inhomogeneous. Kastner-Klein et al. [2004] investigated the effect pitched roofs had on airflow patterns. They found that the addition of pitched roofs prevented the formation of the typical vortex you would find in street canyons with flat roofs. A recirculation zone forms from the downwind roof top across to the upwind rooftop above the street (see Figure 2.1). The flow within the street canyon becomes almost stagnant since there is little vertical mixing between the canyon and the flow above.

However in contrast to this, field measurements conducted by Louka et al. [1998] showed the influence roof shape could have on turbulence and mixing within the street. They found that comparison of the velocity spectra produced by a pitched shape roof with a flat roof showed that the pitched roof resulted in more energetic eddies and greater turbulence intensities and concluded that roof shape is an important factor in mixing the air within streets and pollution dispersion.

The aspect ratio of a street which is the building height divided by the street width (H/W) has been shown to have a dominant effect on flow patterns. Wind

flow patterns within idealised street canyons with airflow perpendicular to the street direction can be categorised into 3 regimes depending on their aspect ratio. If the street is wide i.e. H/W<0.3 then the flow fields surrounding the buildings on either side of the street do not interact this is known as an isolated roughness flow regime [Oke, 1988]. For larger aspect ratios (0.3<H/W<0.7) wake interference flow regimes occurs. The wake behind the leeward building interacts with the recirculation in front of the windward building [Li et al., 2006]. For narrow streets with tall buildings (H/W>0.7) a stable recirculation zone is formed inside the street canyon and there is little air exchange at roof top level leading to very poor ventilation within the canyon particularly towards the bottom of the street. This is known as a skimming flow regime [Oke, 1988]. This is shown graphically in Figure 2.2.

For particularly narrow streets (H/W>1.4) a secondary minor vortex can form in the canyon. This was demonstrated by Kovar-Panskus et al. [2002]. Numerical modelling and wind tunnel experiments were used to examine the effect varying the aspect ratio had on the flow patterns within the canyon. They found that for canyons with aspect ratios H/W>1.4 a secondary recirculation region forms near the ground next to the downstream wall. Chang and Meroney [2003] also found that for H/W = 1 and perpendicular wind direction there will be two circulation flows within the street with the upper one flowing clockwise and the lower one anti-clockwise.

Internal obstacles within the street canyon, such as trees, stationary cars and low walls can cause significant changes in airflow patterns and pollution dispersion.

McNabola et al. [2009] carried out a CFD simulation of street canyons containing low boundary walls and found that the addition of these walls reduced pollution concentration levels. The extent of these reductions depended on the location of the boundary walls within the canyon, the street geometry and wind direction. In the case of perpendicular wind direction the air flow pattern within the canyon was significantly altered by the addition of a central boundary wall with additional vortices being formed on the leeward side wall.

A wind tunnel experiment conducted by Gayev and Savory [1999] used vertical cylinders to model internal roughness within a street canyon. Results show the

addition of the obstacles increased turbulence and ventilation within the street canyon. The local intensity of velocity fluctuations were seen to increase by up to 200% when the obstacles were added to the street canyon.

2.2 Effect of Tree Planting on the Urban Environment

The benefits of the addition of trees to urban areas are known to be wide reaching. By changing the aesthetics of their surroundings they have been shown to have a social and psychological beneficial effect on a city and its residents. They also have a significant effect on their local microclimate, impacting the wind flow and mass and heat transport. The impact trees have on the urban environment has thus become a popular area of research over recent years.

In a study conducted by Dimoudi and Nikolopoulou [2003] into the thermal impact of tree planting on the urban environment it was shown that trees were able to reduce the urban heat island effect through the process of shading and evapotranspiration this in turn led to an improvement of outdoor thermal comfort and reduction in energy use of surrounding buildings.

The addition of trees to cities are also believed to have a beneficial effect on pedestrian wind comfort. Trees are one of the most extensively employed tools in urban design and landscaping to reduce high wind speeds and provide wind environments which are suitable for pedestrian use and thus satisfy planning requirements. Despite their prevalence in urban design the quantification of the effect of trees on wind and how this relates to pedestrian comfort has not been well studied. If trees are to be used as an effective tool in landscape design as a way to provide comfortable local wind microclimates then this is a topic which requires much more attention.

Unlike the effect of trees on pedestrian comfort the relationship between trees and urban pollution is a well-researched topic. Beckett et al. [1998] looked at the role of vegetation and urban woodland in reducing particulate pollution. They found that the large leaf area and the surface properties result in large reduction in particulate matter due to the depositions on the tree surface. They also found

that the local wind speed had an effect on the process of deposition with higher wind speeds resulting in much lower deposits on the tree surface due to the greater likelihood of particles to bounce off rather than remain attached to the surface.

Deposition is not the only process by which trees can remove pollutants from the air. Pollutants can also be removed through uptake via the leafs stomata. Novak estimated that US urban trees were responsible for the removal of approximately 711000 tons of pollution annually through this process.

In contrast to the beneficial effect of tree planting on pollution described in the previous two studies, a study carried out by Gromke et al. [2008] highlighted the negative effect tree planting within street canyons can have on ventilation. In a wind tunnel experiment of two streets one tree-lined and one non tree-lined concentration levels of a passive gas were measured. It was found that the concentration levels on the tree-lined street were higher due to presence of the trees reducing the ability for natural ventilation.

Based on the studies described above it is clear that if we are to maximise the beneficial effects of trees and minimise any potential negative effects we need a clear understanding of effects trees have on wind flow within the urban environment.

2.2.1 Aerodynamic Effects of Tree Canopies

The airflow pattern surrounding a tree can be characterised by a decrease of mean horizontal wind speed within and behind the canopy [Foudhil et al., 2005], [Endalew et al., 2009]. This decrease is caused by momentum from the flow being absorbed by form drag and skin friction as the air moves through the branches [Raupach and Shaw, 1982]. The wind speed increases above and to the sides of the canopy as well as around the trunk [Foudhil et al., 2005], [Gross, 1987], [Leenders et al., 2007]. A wake region develops downwind of the tree. The wind speed in this region is less and in most cases the wind direction reverses forming a recirculating eddy. The size and strength of this eddy depends on the density of the foliage and the geometry of the tree [Gross, 1987]. This can be seen graphically in Figure 2.3.

The geometry of the tree has an important impact on the airflow character-

istics. [Gross, 1987] found that varying the dimensions of a cone shaped tree affected the dimensions of the eddy formed on the leeward side of the tree. As the diameter of the tree was increased the width of the area containing negative airflow increased. Increasing the height caused an increase in the depth and length of the eddy. Changing the tree shape from a cone to a ball showed that the ball shaped was a more pronounced obstacle causing the wake region to be nearly twice the size of that produced by the cone shaped tree.

Trees can have a number of effects on turbulence levels. The moving branches within the tree canopy store mean kinetic energy as strain potential and release it as turbulence kinetic energy [Raupach and Shaw, 1982]. Wakes form in the lee of tree elements increasing turbulence levels. Large scale turbulence is broken down into smaller scale turbulence which rapidly dissipates, decreasing the overall TKE levels.

Within forests the turbulence intensity is greatest within the tree canopy and smallest around the trunk. The intensity levels are affected by the density of the canopy. For deciduous trees turbulence levels will increase during summer when the tree canopy is more dense and decrease in the winter months [Cionco, 1972] . This can be seen in the results from an experiment by [Tourin and Shen, 1966]. Measurements were made in a deciduous forest 17m in height. At a height of 10m turbulence intensities were found to be approximately 53 % during winter and 77% during summer. This 45% increase in turbulence intensity highlights the effect foliage can have on airflow.

Although turbulence levels have been noted to increase inside the tree canopies, the effect of trees on turbulence levels outside the canopy can be quite different. Studies into the effects of windbreaks on airflow have shown that a 'quiet zone' develops in the lee of the windbreak in which turbulent velocity fluctuations are found to reduce compared with the approach flow. [Heisler and Dewalle, 1988] found that this zone extended from a line beginning near the top of the windbreak to ground level at a distance 8H, where H i the height of the windbreak, in the lee of the windbreak. They also found that magnitude of the turbulent velocity fluctuations were inversely proportional to the porosity of the windbreak.

Loeffler et al. [1992] measured wind speeds behind nine windbreaks to investigate the effect optical porosity of the windbreaks had on wind speed reduction.

Results showed that a decrease in porosity led to a decrease in the minimum wind speed and suggested that optical porosity can be used to predict minimum wind speed behind windbreaks. Endalew et al. [2009] also found that porosity of the tree canopy had a significant effect on wind speed. Using CFD simulations he found there was a ten fold reduction in wind speed for trees with dense canopies compared with leafless canopies. The effect of varying canopy densities was explained by Grant and Nickling [1998] using the analogy of flow regimes. As the air passes through the canopy the flow around each element forms a wake. These wakes interact with each other and extract momentum from the flow. As the porosity increases the distance between each element increases and therefore the interaction between the wakes surrounding the elements becomes less reducing the amount of momentum lost.

2.2.2 Airflow within Tree-Lined Street Canyons

Gromke et al. [2008] performed wind tunnel experiments to investigate the effect of avenue-like tree planting on airflow within urban street canyons. Porous and non porous tree canopies were modelled using a rectangular Polyurethane foam block and a Styrofoam block respectively. They were located in the centre of the street and took up approximately 1/3 of the street canyon volume. Results showed a reduction in ventilation within the street canyon. There was still evidence of a vortex forming within the canyon but this was reduced towards the outer regions of the canyon leading to lower ventilation rates. A large reduction in velocity was found at the leeward wall and a small reduction on the windward wall. The vertically entering flow rate at the roof top was also reduced.

Czder et al. [2009] recreated the same wind tunnel experiment using a numerical model the set up was tested for an oblique wind direction of 45 degrees to the canyon axis. Detailed analysis of the wind flow patterns showed the addition of vegetation caused the canyon vortex to split up into two main parts. An eddy forms on the leeward wall and further downstream on the windward wall a slow clockwise rotating vortex forms. This results in a reduction in the natural ventilation of the street canyon leading to higher pollution concentration levels.

Amorim et al. [2013] investigated the impact of urban trees on the dispersion

of CO emmited by road traffic through the use of both CFD modelling and field measurements. Results of the CFD model predicted an increase in CO levels under a wind direction of 45 degrees due to reduced exchange of air at roof top level. However, they found a decrease in CO levels under a parallel wind direction although hot spots of increased pollution were identified due to trees causing a re-arrangement of vortical flow structures within the street. Field measurement montioring sites were found to be located within these hotspots and therefore gave a false impression of increased pollution level for the entire street. Amorim et al. [2013] highlighted the importance of using a combination of CFD techniques and field measurements to provide a full picture of the complex and spatially dependent air flow and pollution dispersion within tree-lined streets due to the combined effect of trees and complex street geometry.

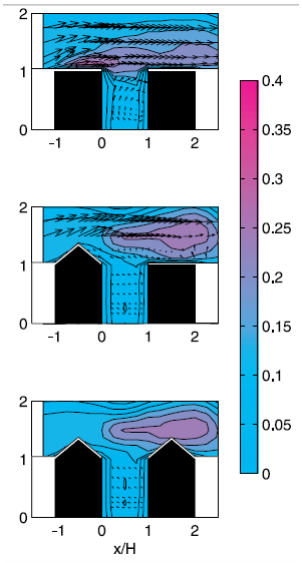

Figure 2.1: Velocity on central vertical plane of isolated street canyon with three different roof configurations. Mean velocity field is represented by vectors and colour shows normalised variance of the u-velocity component. [Kastner-Klein et al., 2004]

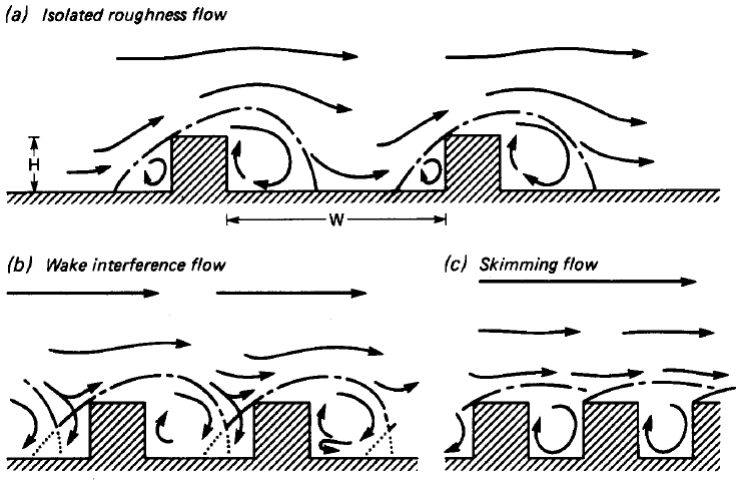

Figure 2.2: The flow regimes associated with airflow over buildings of increasing H/W. [Oke, 1988]

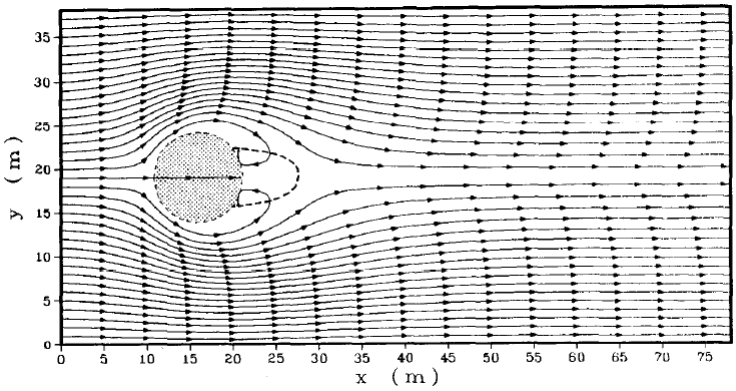

Figure 2.3: Streamlines of horizontal airflow 1m above ground. The contour of the tree is dotted, the dashed line indicates the region where the u velocity is less than zero. [Gross, 1987]

Chapter 3

CFD modelling of Airflow within the Urban Environment: Fundamentals and Background

Computational Fluid Dynamics or CFD is a computational tool used in the modelling and prediction of fluid flows. Since its inception in the 1970's it has been used to study a wide variety of flows across many disciplines and industries. In recent years it has become more popular in modelling outdoor airflow within the built environment and has the potential to be an extremely useful tool to aid in design of urban areas provided the numerical models used are well validated.

This chapter will expand on the background given in Chapter 2 with a focus on how CFD techniques have been used in the past to model the urban boundary layer, airflow within street canyons and flow through tree canopies and vegetation.

In order to commence this detailed discussion on the use of CFD modelling of airflow within the built environment it is first necessary to have an understanding of the basic theory and processes underlying CFD techniques. This chapter will therefore begin with a brief description of the basic principles regarding CFD modelling. This is to aid understanding and provide context to the later discussions on the use of CFD modelling for the built environment. There are many detailed works on CFD theory such as Tu [2008] [Versteeg, 2007], which may be referred to if a more in-depth explanation of the mathematical theory behind

CFD is required.

3.1 Introduction to CFD

3.1.1 Governing Equations

The process of CFD involves the discretization of a flow field both temporally and spatially. This is when the field properties such as pressure and velocity are approximated at a number of locations within the flow field. In order to do this the equations which represent the fluid flow must be discretized by algebraic approximations.

Different methods for discretization exist such as finite element, finite difference and finite volume. Here we will consider finite volume as this is the method used by the software Ansys CFX which will be used throughout this PhD. The advantage of this method over others is it allows for a wide range of geometry and fluid phenomena to be modelled [Aspley, 2014].

The flow field of a fluid can be described by equations based upon the physical conservation principles as follows:

- conservation of mass
- conservation of momentum
- conservation of energy

Conservation of Mass

Considering the change of mass within an arbitrary volume and employing the physical principle of mass conservation we arrive at the following:

$$\text{rate of change of mass within volume} + \text{net outward mass flux} = 0 \tag{3.1}$$

This expression can be written in differential form by considering an infinitesimally small Cartesian volume as follows:

$$\frac{\partial \rho}{\partial t} + \frac{\partial (\rho u_j)}{\partial x_j} = 0 \tag{3.2}$$

This is also known as the continuity equation [Aspley, 2014].

Conservation of Momentum

The total change of momentum for a fluid passing through a control volume can be thought of as the rate of change of momentum inside the volume plus the net outward momentum flux. Applying Newtons Second Law which states that the rate of change of momentum is equal to force we get the following expression:

Rate of change of momentum in a volume + net outward momentum flux = force (3.3)

This can be written as the following differential equation:

$$\frac{\partial(\rho u_i)}{\partial t} + \frac{\partial(\rho u_i u_j)}{\partial x_j} = -\frac{\partial p}{\partial x_i} + \frac{\partial \tau_{ij}}{\partial x_j} + f_i \tag{3.4}$$

This is the Navier-Stokes equation [Aspley, 2014].

Incompressible Flows

When simulating flow for the outdoor urban environment the flows can often be assumed to be incompressible. Equations 3.2 and 3.4 can therefore be simplified as follows:

$$\frac{\partial(\rho u_j)}{\partial x_j} = 0 \tag{3.5}$$

$$\frac{\partial(\rho u_i)}{\partial t} + \frac{\partial(\rho u_i u_j)}{\partial x_j} = -\frac{\partial p}{\partial x_i} + \mu \Delta^2 u_i + f_i \tag{3.6}$$

3.1.2 Grid Generation and Grid Independence

In order to analyse fluid flows using CFD a mesh must first be created. This process involves descritizing the computational domain into smaller volumes or "cells". The governing equations are then solved for each of these cells. The process of mesh generation can affect the accuracy of the CFD output as well as the rate of convergence and computational time required to obtain a solution. It is therefore recommended that a mesh sensitivity test be carried out before running any CFD simulation. This involves testing different size meshes until

little or no variation is found in the output of the CFD model.

3.1.3 Wall Treatment

In CFD a wall function is often used to model the flow in the region closest to the wall. Within this region the law of the wall is applied. This states that:

$$u^+ = \frac{1}{\kappa} ln(y^+) + C \tag{3.7}$$

Where u^+ and y^+ are dimensionless variables given by:

$$u^+ = \frac{u_t}{u^*} \tag{3.8}$$

$$y^+ = \frac{u^* \Delta y}{v} \tag{3.9}$$

Where u_t is the known tangential velocity at a distance Δy from the wall, u^* is the frictional velocity in the wall region and v kinematic viscosity.

When modelling flow over an urban region it may be necessary to specify a ground roughness without explicitly modelling the geometry of the underlying roughness. This can be incorporated into the wall function. Ground roughness can be incorporated into a model by either specifying a roughness length z_0 or a sand grain roughness height K_s. Most commercial CFD software use sand grain roughness to modify the wall boundary conditions. This assumes that the wall is covered in tightly packed spheres. The height of these spheres is called the sand-grain roughness height K_s. The sand-grain roughness (K_{s+}) is a dimensionless quantity which is found by dividing the sand grain roughness height by the characteristic length of the wall layer δ_v.

$$K_{s+} = \frac{K_s}{\delta_v} = \frac{K_s u^*}{v} \tag{3.10}$$

The difference between K_s and K_{s+} is that the first is a geometrical quantity and the later is a flow quantity as it is dependent on $u*$ and v.

This sand-grain roughness is used to adapt the wall function. The wall roughness causes turbulence in the shear layer and shifts the logarithmic profile down-

wards. The law of the wall is modified in the following way:

$$u^+ = \frac{1}{\kappa} ln(y^+) + B - \Delta B(K_{s+}) \tag{3.11}$$

Where B=5.2. For fully rough regimes such as flow over urban areas the downward shift ΔB can be expressed as:

$$\Delta B = \frac{1}{\kappa} ln(K_{s+}) - 3.3 \tag{3.12}$$

As shown by V. A. Ioselevich [1974].

Combing equation 3.11 and equation 3.12 we get the modified logarithmic law of the wall [Blocken et al., 2007]:

$$u^+ = \frac{1}{k} ln \frac{y^+}{K_{s+}} + 8.5 \tag{3.13}$$

Each CFD commercial software will have its own version of this wall function. For the case of Ansys CFX [Ansys, 2009] which is being used here the logarithmic law of the wall for fully rough surfaces is specified as:

$$u^+ = \frac{1}{k} ln \frac{y^+}{K_{s+}} + 5.2 \tag{3.14}$$

3.1.4 Turbulence Modelling

Turbulent flow is characterized by random fluctuations of velocity. It is possible to model turbulent flow within CFD without any adjustments to the Navier-Stokes equations. This type of simulation is known as direct numerical simulation (DNS) and is prohibitively computationally expensive. Turbulence models used within CFD simulations enable the capture of the main features of the flow without having to explicitly model all the details of the turbulence, thus saving on computer costs.

Large eddy simulations (LES) save computing time compared with DNS by explicitly resolving only the large and most important turbulent eddies in the flow and approximating the smaller scale turbulence. However this technique is either still out of reach for simulation of the outdoor environment, or when

computational power is available, is very difficult to tune, which may make it imprecise, see Blocken et al. [2011] and references therein.

We can reduce the amount of computing power needed by focusing on the mean properties of the flow. This results in the Reynolds-Averaged Navier Stokes (RANS) equations. These equations contain correlations of the fluctuating velocity components $\overline{u_i' u_j'}$ which are known as the Reynolds stresses. The turbulence model is a way of closing the RANS equations by approximating the Reynolds stress.

A popular choice of RANS model is the Standard k-ε turbulence model. The formulation of this model is as follows:

The Reynolds stresses $\overline{u_i' u_j'}$ are related to the shear stress of the flow, τ, by the following equation:

$$\tau = -\rho \overline{u_i' u_j'} \tag{3.15}$$

where ρ is the density of the fluid. We can find the value for τ, and hence $\overline{u_i' u_j'}$, by the following formula:

$$\tau = \mu_t \left(\frac{\partial \bar{u}_i}{\partial x_j} + \frac{\partial \bar{u}_j}{\partial x_i} \right) - \frac{2}{3} \rho k \delta_{ij} \tag{3.16}$$

where μ_t is the turbulence viscosity and δ_{ij} is the kroneckar delta. In the case of the standard k-ε turbulence model, turbulence viscosity is defined as

$$\mu_t = \rho C_\mu \frac{k^2}{\varepsilon} \tag{3.17}$$

where C_μ is a model constant [Jones and Launder, 1972].

By solving the following differential equations for the turbulence kinetic energy, k, and the turbulence dissipation, ε we can find a value for μ_t [Jones and Launder, 1972]:

$$\frac{D(\rho k)}{Dt} = \frac{\partial}{\partial x_j} \left(\left(\mu + \frac{\mu_t}{\sigma_k} \right) \frac{\partial k}{\partial x_j} \right) + \tau_{ij} \frac{\partial \bar{u}_i}{\partial x_j} - \rho \varepsilon \tag{3.18}$$

$$\frac{D(\rho \varepsilon)}{Dt} = \frac{\partial}{\partial x_j} \left(\left(\mu + \frac{\mu_t}{\sigma_\varepsilon} \right) \frac{\partial \varepsilon}{\partial x_j} \right) + C_{\varepsilon 1} \frac{\varepsilon}{k} \tau_{ij} \frac{\partial \bar{u}_i}{\partial x_j} - C_{\varepsilon 2} \rho \frac{\varepsilon^2}{k} \tag{3.19}$$

where σ_k, σ_ε, $C_{\varepsilon 1}$, $C_{\varepsilon 2}$ and C_μ are all empirical model constants. The default values for these constants in most commercial CFD softwares, including ANSYS CFX used here, are shown in Table 3.1. These values were found through data fitting for a wide range of flows [Launder and Spalding, 1974].

Table 3.1: standard values used for model constants

C_μ	$C_{\varepsilon 1}$	$C_{\varepsilon 2}$	σ_ε	σ_k
0.09	1.44	1.92	1.3	1.0

3.2 CFD Modelling of the Atmospheric Boundary Layer

The first section of this Chapter discussed the theoretical framework of CFD, in the second half of this Chapter we will take a look at how CFD has been applied in practice for use within the built environment.

In order to accurately model the airflow within the built environment using CFD it is first necessary to create the correct boundary layer flow conditions. Accurate simulation of the atmospheric boundary layer within CFD is a complex problem which brings with it many complications. This section will take an indepth look at some of the previous problems faced by researchers when trying to replicate both a full scale urban boundary layer and a boundary layer created within a wind tunnel experiment.

3.2.1 Problems Faced when Modelling the Urban Boundary Layer using CFD

Computational Fluid Dynamics is regularly used to model the atmospheric boundary layer. This can be used in urban areas to investigate processes such as pollution dispersion, pedestrian comfort and wind effects on buildings. To gain an accurate representation of a horizontally homogeneous atmospheric boundary layer within CFD, profiles must be specified for velocity and turbulence at the inlet of the computational domain.

The main problem encountered when trying to model a horizontally homogeneous atmospheric boundary layer is the flow profiles have a tendency to change rapidly as they move downstream. Figure 3.1 shows results taken from a study carried out by Blocken et al. [2007] who performed a CFD simulation of atmospheric boundary flow in an empty domain. It shows velocity, turbulence kinetic energy and turbulence dissipation profiles taken at the inlet along with profiles taken 100m, 1000m and 10000m downstream of the inlet. The profiles are shown up to a height of 50m. The results show a clear acceleration in velocity profiles close to the ground as well as decay in turbulence kinetic energy and dissipation profiles. By the time the flow reaches the area of interest the profiles have

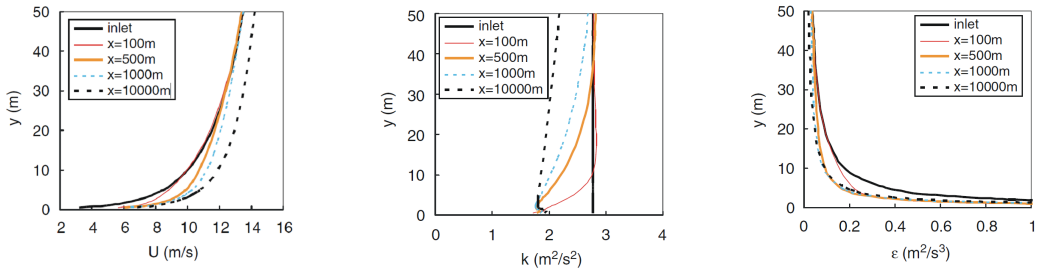

Figure 3.1: Results taken from Blocken et al. [2007] illustrating the stream-wise gradients present in vertical profiles for mean wind speed (left), turbulence kinetic energy (centre) and turbulence dissipation (right)

deviated from those specified at the inlet.

3.2.1.1 Suitable Inlet Boundary Conditions for Urban Boundary Layer Flow

The acceleration in the velocity at ground level and a decay in turbulence profiles as we move downstream occurs when the boundary conditions are not consistent with the turbulence model and its associated constants [Richards and Norris, 2011]. In the case of the standard k-ε turbulence model, which will be used here, the velocity, turbulence kinetic energy and turbulence dissipation profiles specified at the inlet must satisfy the transportation equations for TKE and turbulence dissipation (equations 3.18 and 3.19).

In order to overcome this problem Richards and Hoxey [1993] derived inlet boundary conditions which satisfied the k-ε turbulence model. To do this they simplified equations 3.18 and 3.19 by assuming that the atmospheric boundary layer could be modelled as a horizontal homogeneous turbulence surface layer and showed that the following inlet profiles were solutions to these simplified equations:

$$u(z) = \frac{u*}{\kappa} ln\left(\frac{z + z_0}{z_0}\right) \tag{3.20}$$

where u(z) is the velocity at height z, u* is the frictional velocity, z_0 is the surface

roughness length and κ is the von karman constant.

$$k = \frac{u*^2}{\sqrt{C_\mu}} \tag{3.21}$$

Where k is the turbulence kinetic energy, C_μ is one of the model constants contained in the k-ε turbulence model and usually takes the value 0.09

$$\varepsilon = \frac{u*^3}{\kappa(z + z_0)} \tag{3.22}$$

Where ε is the turbulence dissipation.

These equations satisfy the standard k-ε model if the following relationship between the model constants holds

$$\sigma_\varepsilon = \frac{\kappa^2}{(C_{\varepsilon 2} - C_{\varepsilon 1})\sqrt{C_\mu}} \tag{3.23}$$

The Richards and Hoxey [1993] profiles are commonly used when simulating flow over an urban region due to their ease of implementation and the fact that horizontal homogeneity can be achieved. However, research has shown that comparisons of these profiles with either real life atmospheric boundary layer data or wind tunnel data showed an under-prediction of TKE, and also found TKE to be non-uniform with height, which is not reflected in the profiles.

In an effort to find inlet conditions which both satisfied the standard k-ε model and gave a good match with available boundary layer data, Yang et al. [2009] derived a new set of inlet boundary conditions which were an approximate solution to the k-ε model transport equations. The equations take the following form:

$$u = \frac{u*}{\kappa} ln\left(\frac{z + z_0}{z_0}\right) \tag{3.24}$$

$$k = \sqrt{Aln\left(\frac{z + z_0}{z_0}\right) + B} \tag{3.25}$$

$$\varepsilon = \frac{\sqrt{C_\mu}u_*}{\kappa(z+z_0)}\sqrt{Aln(z+z_0)+B} \tag{3.26}$$

The constants A and B can be found through non-linear fitting of experimental data for boundary layer flow.

Gorl et al. [2009] noted that these equations only satisfy the TKE conservation equation and in order to satisfy the momentum and dissipation conservation equations the following relations for the k-ε model constants must hold

$$C_\mu = \frac{u_*^4}{Aln(z+z_0)+B} \tag{3.27}$$

$$\sigma_\varepsilon(z) = \frac{k^2(-A/2+k(z)^2)}{u_*^2(C_{\varepsilon 2}-C_{\varepsilon 1})k(z)} \tag{3.28}$$

This raises the problem that two of the k-ε model constants become a function of height and therefore are no longer constants. Such an adaption of the constants is not supported by all commercial softwares. Richards and Norris [2011] also comment on the fact that this non-standard version of the k-ε model has not been thoroughly tested for uses such as wind engineering applications.

Both sets of profiles require that the k-ε model constants must be altered in order to maintain a homogeneous boundary layer profile. There will be a more in depth discussion on the choice of k-ε model constants and how they effect the CFD output in the section 4.1.4.

We have discussed here the problems relating to the standard k-ε model and the fact that boundary conditions and turbulence model must be consistent however, this is not a problem that is just confined to the standard k-ε the same restriction apply to all turbulence models as discussed in the paper by Richards and Norris [2011] in which inlet profile equations are derived for RNG k-ε, Wilcox k-ω and LRR QI turbulence models.

3.2.1.2 Sand Grain Roughness and the Wall Function Model

Problems with stream-wise gradients in boundary layer profiles are not only caused by inconsistent boundary conditions but also incorrect modelling of the aerodynamic roughness.

Having carried out extensive research on the topic of appropriate sand grain roughness for the atmospheric boundary layer Blocken et al. [2007] found the following relationship between the sand grain roughness height and the roughness length, z_0.

$$Ks = 30z_0 \tag{3.29}$$

3.3 CFD Modelling of Street Canyon Flow

CFD modelling has been increasingly used as a tool in the prediction of street canyon flows within recent years due to its ability to provide a fully three dimensional picture of the airflow patterns. In order for CFD modelling to be reliably used to predict flow within the built environment it must be validated against field measurements and experimental testing. This section of the thesis will therefore discuss previous studies which have looked at the capabilities of CFD in accurately predicting street canyon flow.

The choice of turbulence model is important when modelling street canyon flow as correct prediction of turbulence quantities within the street canyon are essential for correctly modelling the dispersion of pollutants within these areas. The most commonly used turbulence model for street canyon flow is the Standard k-ε model. Since its inception four decades ago it has won favourability amongst the CFD community due to its simplicity, robustness and reasonable accuracy and become the industrial standard for modelling outdoor flow [Kim and Boysan, 1999]. It has the advantage over other more sophisticated turbulence model in that the only prior knowledge of the turbulence conditions is the initial conditions and it also requires relatively little computational time compared with other turbulence models [Lien et al., 2004].

With regards to its performance for street canyon flows it is shown to give a good qualitative comparison against experimental data and capture the main flow features. This was demonstrated in an investigation carried out by Lien et al. [2004], which simulated flow over 2-D rectangular building array comparing different variation of the k-ε model. These results were then compared with detailed data taken from a wind tunnel investigation. They showed that the Standard k-ε model was able to predict most of the qualitative features in the

flow field over and within the building array. The separation zone where the flow detaches from the windward roof top edge was correctly predicted along with the absence of this separation zone on the subsequent rooftops. It also gave a good prediction of the single recirculating vortex within the street canyon. They found the quantitative agreement of stream wise velocity profiles to be well predicted throughout most of the flow domain.

Although the Standard k-ε model is able to predict the location of the separation zone above the upwind roof Lien et al. [2004] and Speziale [1987] found that the model has a tendency to under-predict the reattachment length for separated flows. In this type of flow the Reynolds stresses are highly anisotropic and also highly influential on the velocity fields. The incorrect assumption within the formulation of the std. k-ε model that the Reynolds stresses are isotropic thus results in incorrect flow predictions.

The Standard k-ε model is also noted to have problems when dealing with flows containing impingement. It is common to see an over prediction of TKE at the stagnation point on the upwind face of a bluff body or building. This problem again arises from the Standard k-ε model inability to capture normal-stress anisotropy. This is commonly referred to as the stagnation point anomaly [Murakami, 1993].

Although many studies have shown this over-prediction of TKE when impingement occurs infront of a bluff body, there are many CFD studies on street canyon flow which show an under-prediction of TKE at street level and also above the roof top of the upwind building. Lien et al. [2004] gave two main reasons for this under-prediction. Firstly the Standard k-ε model inability to account for streamline effects on turbulence production in particular the strong concave streamlines which form upstream of the upwind building. This source of TKE is not captured by the Standard k-ε model and therefore leads to an under prediction of TKE at street level. Secondly the oscillation of the high shear layer above the buildings roof tops not being effectively captured by the Standard k-ε model, which is displayed as an under-prediction of the TKE peak just above roof top level.

Solazzo et al. [2009] identified a lower rate of vertical mixing in the shear layer as being a contributing factor to the under-prediction of TKE at street level and attempted to remedy this problem by modifying the diffusive model constants σ_ϵ

and σ_k which resulted in a larger spread of TKE in the shear layer and a reduction in the under prediction of TKE within the street canyon.

3.4 CFD Modelling of Vegetation and Trees

Airflow through a tree canopy is complex, 3-dimensional and highly inhomogeneous. This section of the thesis will look at how researchers have incorporated such complex systems into their CFD models in the past as well as how to determine the constants required in specification of tree models such as drag coefficient and leaf area density.

To directly model a tree using CFD would be extremely computationally expensive therefore it is common to take the spatial average of the properties of interest within the plant canopy. Raupach and Shaw [1982] demonstrate the spatial averaging technique on the governing equation of the flow. This results in additional source and sink terms within the momentum and turbulence equations. The physical meaning of such terms can be described as follows:

> A sink term, S_u, can be added to the equation for momentum due skin friction and form drag extracting momentum from the flow
>
> A source term, P_k, can be added to the TKE equation to account for the wakes forming behind the canopy which convert mean kinetic energy into turbulence kinetic energy thus adding to the overall TKE budget
>
> A sink term, L_k, can be added to the TKE equation as there is a short circuiting of Kolmogorav Scale in which large scale turbulence is broken down into smaller scale eddies which dissipate rapidly, this leads to a loss in the TKE budget

Raupach and Shaw [1982] derived a numerical form for these equations based on the drag coefficient and leaf area density of the tree to be modelled. These are as follows:

$$S_u = -\rho C_d LAD u^2 \tag{3.30}$$

where C_d is the drag coefficient and LAD is the leaf area density. This term only takes into account form drag as viscous drag is assumed to be negligible in comparison [Raupach and Shaw, 1982]. Equation 3.30 is often re-written using the form drag coefficient C_n which is equal to 2LADC_d.

$$S_u = -\frac{\rho}{2} C_n u^2 \tag{3.31}$$

The source term, P_k, relating to the production of TKE by the wakes formed by the plant elements can be modelled as follows

$$P_k \propto \frac{C_n}{2} U^3 \tag{3.32}$$

The sink term, L_k describing the turbulence loss due to the short circuiting of the Kolmogorov scale can be represented as

$$L_k \propto \frac{C_n}{2} Uk \tag{3.33}$$

This can be combined into one term, S_k, to be added to the turbulence kinetic energy equation:

$$S_k = \frac{C_n}{2} (\beta_p U^3 - \beta_d Uk) \tag{3.34}$$

β_p is the fraction of kinetic energy converted to turbulence kinetic energy by drag, β_d is the dimensionless coefficient to account for the short-circuiting of the turbulence cascade.

Since the turbulence kinetic energy and the rate of dissipation are linked we can not alter one without changing the other. The source term to be added to the dissipation rate equation is perhaps the least well understood of the three source terms [Katul et al., 2004]. Green et al. [1995] derived such a term from the length scale formulation.

$$S_\varepsilon = C_{\varepsilon 4} \frac{\varepsilon}{k} S_k \tag{3.35}$$

This was then adapted by Liu et al. [1996] to improve experimental predictions

against windtunnel data, to the following form

$$S_\varepsilon = \frac{C_n}{2}(C_{\varepsilon 4}\beta_p \frac{\varepsilon}{k} U^3 - C_{\varepsilon 5}\beta_d U \varepsilon) \tag{3.36}$$

where $C_{\varepsilon 4}$ and $C_{\varepsilon 5}$ are closure constants

Sanz [2003] derived the following equations for β_d and $C_{\varepsilon 4}$

$$\beta_d = \sqrt{C_\mu}\left(\frac{2}{\alpha}\right)^{\frac{2}{3}} \beta_p + \frac{3}{\sigma_k} \tag{3.37}$$

$$C_{\varepsilon 4} = \sigma_k \left(\frac{2}{\sigma_k} - \frac{\sqrt{C_\mu}}{6}\left(\frac{2}{\alpha'}\right)^{2/3}(C_{\varepsilon 2} - C_{\varepsilon 1})\right) = C_{\varepsilon 5} \tag{3.38}$$

where $\alpha' = 0.05$ is a constant related to the mixing length model. Using these relation the only values that need to be obtained are for β_p and the form drag, C_n.

There have been many different variations of the canopy model prescribed above. Mochida et al. [2008] categorised the different modelling approaches researchers had taken in the past. They then went on to test two of these canopy models in more detail, looking specifically at how alterations to some of the model coefficients affected the output of the CFD model. One of the canopy models tested, referred to as model C, had the same form as the canopy model specified by Liu et al. [1996] above, the other canopy model, model B, had a similar form to this model but did not include the sink term L_k in either the term S_k or S_ε. Various values were tested for constants $C_{\varepsilon 4}$ and $C_{\varepsilon 5}$ and the output of the CFD results compared against field data of measurements of velocity and turbulence profiles taken in the wake zone of a pine tree. It was found that the optimal values for model constants were $C_{\varepsilon 4} = 1.8$ and $C_{\varepsilon 5} = 1.5$. A comparison between model B and model C showed that model C gave better predictions of the turbulence profiles where as model B was found to show slightly improved prediction of the velocity profiles.

Amorim et al. [2013] also implemented the canopy model suggested by Liu et al. [1996] in their CFD model of an urban area containing tree planting. Unlike Mochida they chose values of $C_{\varepsilon 4} = 1.5$ and $C_{\varepsilon 5} = 1.5$ for the model closure terms along with values of $\beta_p = 1$ and $\beta_d = 4$. Results of CO levels taken from

the CFD model were then compared against CO levels from field data. It was found that the addition of tree to the CFD model improved model accuracy when compared with field data, with uncertainty of the CFD model decreasing from 60% to 19% and the value of the normalised mean square error reducing by 71%. The authors thus highlighted the importance of inclusion of tree canopies and vegetation within CFD models of urban areas for accurate prediction of wind environment and pollution dispersion.

In order to quantify the effect of the tree canopies within the numerical model there are certain co-efficients which must be determined. These are: the drag coefficient, the leaf area density, the volume porosity and coefficients relating to the turbulence source / sinks. We will now discuss how other authors have defined values for both the leaf area density and drag coefficient in the past.

3.4.0.3 Leaf Area Density of Trees

The leaf area density (LAD) is defined as the total one sided leaf area per unit canopy volume (m^{-1}). This is a particularly difficult value to determine due to the difficulty in obtaining 3-dimensional measurements on the structure of tree canopies.

Several researchers have developed methods for estimating leaf area density based on certain characteristics of the tree such as trunk diamter (dbh), crown height, crown width etc.

In their study Paula J. Peper [2001] took measurements of tree height, crown width, crown height, dbh and leaf area of 12 common street tree species, including the London Plane. Based on there findings they were able to provide a relationship between dbh of the various tree species and the leaf area, this is as follows:

$$LA = e^{A} * e^{(bDBH)-1} * e^{MSE/2} \tag{3.39}$$

where LA is the leaf area (m^2), A, b and MSE are all empirical constants which can be found in Paula J. Peper [2001].

Nowak [1996] developed logarithmic regression equations based on detailed field measurement studies which allowed the prediction of both leaf area and leaf

biomass based on either crown parameters or stem diameter of urban trees.

Nowak [1996] collated data from 88 urban trees regarding crown dimensions, stem diameter and leaf area. This data was used to find the following regression equations for predicting leaf area:

$$lnY* = b_0 + b_1X + b_2S \tag{3.40}$$

when based on dbh and of the form:

$$lnY = b_0 + b_1H + b_2D + b_3S + b_4C \tag{3.41}$$

when based on crown parameters, where Y is leaf area (m^2), X is stem diameter (cm), H is crown height (m), D is average crown diameter (m), S is the average shading factor and C is the outer surface area of the tree crown (m^2) which can be calculated using the following formula $\pi D * (H + D)/2$. The values for the empirical constants b_0, b_1, b_2, b_3 and b_4 are provided by Nowak [1996] and are found though regression analysis. The shading factor is a measure of the percentage of light intensity intercepted by foliated tree crowns. An extensive list of values for shading factor for various tree species is provided by McPherson [1984].

The findings of Nowak [1996] and Paula J. Peper [2001] offer a simple way of calculating leaf area providing the tree canopy or trunk dimensions are known. Once the leaf area has been calculated it is possible to calculate the leaf area density by dividing the leaf area by the volume of the tree canopy.

3.4.0.4 Drag Coefficient of Trees and Vegetation

In order to understand how momentum is extracted from airflow through a tree it is essential to determine the drag force that is acting on the tree components. It is known that the drag force acting on a body is directly proportional to the density of air, ρ, the area of the body, A, and the square of the air speed, u. This is commonly written as:

$$F = \rho u^2 A C_d \tag{3.42}$$

Where C_d is the drag coefficient. In the case of drag force for a tree the value of A is commonly taken to be the leaf area density, which tells us the leaf area per unit volume.

Typical values for drag coefficients of trees and vegetation often cited in literature range from 0.1 to 1 [Da Silva et al., 2006], [Gross, 1987], [Koizumi et al., 2010] and will vary depending on the size, species, wind speed and location of the tree in question. Various methods have been employed to determine these values.

Da Silva et al. [2006] conducted wind tunnel experiments to determine the wind profiles upstream and downstream from an artificial canopy. These measurements were used along with the assumption that the velocity decrease through the canopy was exponential to determine a drag coefficient of 0.3.

Gross [1987] employed a numerical model to investigate the airflow and turbulence surrounding a single tree. He used trial and error to determine the combination of leaf area density and drag coefficient which provided the best match with experimental data. He found a leaf area density of 1 m^2/m^3 and drag coefficient of 1 offered the best solution.

These investigation found a single drag coefficient based on a single wind speed, however it has been shown that the drag coefficient can vary with wind speed due to the variation in tree shape with the changing winds.

Both Koizumi et al. [2010] and Roodbaraky [1994] noted lack of data on drag coefficients for broadleaf trees as previous studies had focused on the wind effects on coniferous trees. Broadleaf trees tend to make up a large proportion of urban trees and therefore understanding the drag on these types of trees is important in determining the wind effects in urban areas containing tree planting.

In an aim to understand the drag coefficient of broad leaf trees Koizumi et al. [2010] took field measurements of wind velocity and stem deflection of Black Poplar trees in the field. Drag coefficients were found to decrease with increasing wind speeds. For wind speeds over 10m/s drag coefficients were within the range of 0.1 - 0.25 and there was little variability in the measurements. For wind speeds below 10m/s average drag coefficients were within the range 1.2 - 0.25 with large variability in the results.

Roodbaraky [1994] carried out full scale measurements on London Plane trees to determine values for typical drag coefficients. The drag coefficients were calcu-

lated based on data collected for a mean wind speed of 5.8 m/s. The data showed a typical drag coefficient of 0.8 this agreed well with the findings of Koizumi et al. [2010].

In their research into the drag coefficients of broadleaf trees Koizumi et al. [2010] and Roodbaraky [1994] also noted the effects of defoliation can have on C_d. They both found that the drag coefficient decreased when the tree was without leaves. Koizumi et al. [2010] found that the drag coefficient without leaves decreased to 0.133 at a wind speed of 10m/s compared to 0.25 with leaves. Roodbaraky [1994] found that the drag coefficient of the London Plane tree without leaves was 0.2 compared to 0.8 with leaves at an average wind speed of 5.8m/s.

Chapter 4

Benchmark Study: CFD modelling of the Urban Boundary Layer and Street Canyon Flow

This chapter summarises the findings of a benchmark study carried out to investigate the use of CFD in the prediction of boundary layer flows and airflow within a simple street canyon. Firstly the flow within an atmospheric boundary layer wind tunnel is recreated using CFD to explore the issues related to recreating a homogeneous boundary layer flow. Secondly statistical methods will be employed to calibrate the k-ε model constants and determine if appropriate choice of these constants can help in the accurate prediction of boundary layer flow. Finally flow within a simple street canyon will be modelled to assess the capabilities and limitations of CFD and the Standard k-ε model in accurately predicting airflow within a street canyon.

4.1 CFD Modelling of the Atmospheric Boundary Layer Produced in a Wind Tunnel

In order to gain a better understanding of the problems faced when modelling the urban boundary layer in CFD, a CFD model will be constructed which aims to replicate the conditions created in boundary layer wind tunnel experiments. Results will then be compared against experimental data allowing an assessment of the level of streamwise gradients in the boundary layer profiles and how this may be reduced.

4.1.1 Wind Tunnel Set Up

The wind tunnel data used in the validation of the CFD results was taken from a study carried out by Kastner-Klein et al. [2001] this is shown in Figure 4.1. Kastner-Klein has carried extensive wind tunnel tests for flow within various types of street canyons which is summarised in the following papers Kastner-Klein et al. [2001], Kastner-Klein, Kastner-Klein et al. [2004] and Kastner-Klein and Plate [1999]. In order to perform these tests they first had to ensure the correct boundary layer conditions were created within the wind tunnel. This was done through the placement of roughness blocks on the floor of the test section of the wind tunnel and vortex generators, spires and fence posts to create turbulence flow at the entrance to the test section.

All tests were carried out at the atmospheric boundary layer wind tunnel at the university of Karlsruhe which has test section dimensions of 2m wide by 1m high. Measurements were taken using the Laser-Doppler velocimetry technique (LDV) as well as a single hotwire. The LDV measurements provided mean and turbulence velocities of all three directional components. For more details of the wind tunnel set up please refer to Kastner-Klein et al. [2001].

4.1.2 CFD Settings

Full details relating to CFD geometry, mesh and model settings can be found in Appendix .2.1.

There has been some debate in the past over the optimal way to specify the inlet conditions for a CFD model of the atmospheric boundary layer. This has been discussed in section 3.2.1.1. Based on this discussion 3 different methods of specifying the inlet boundary were tested. All three models had the same geometry and mesh described in Appendix .2.1. The only difference between the models was the way in which the inlet boundary conditions for velocity, TKE and turbulence dissipation were specified. Three inlet conditions were tested as follows:

Scenario 1: For the first model the experimental data obtained from the wind tunnel data was input directly into the CFD model. The data consisted of velocity and turbulence measurements taken at several heights. This was used to form the velocity and TKE profiles at the inlet, Ansys CFX uses an interpolation function in between the measurement location to form the full profile. The profile is homogeneous across the width of the inlet.

Scenario 2: The second model implements the inlet profiles first suggested by Richards and Hoxey [1993] and commonly used for atmospheric boundary layer applications. These are

$$u(z) = \frac{u*}{\kappa} ln\left(\frac{z + z_0}{z_0}\right) \tag{4.1}$$

u(z) is the inlet velocity at height z, the values of the frictional velocity u* = 0.56 , the roughness height $z_0 = 0.0008$m were taken from the wind tunnel data.

$$k = \frac{{u*}^2}{\sqrt{C_\mu}} \tag{4.2}$$

k is the turbulence kinetic energy at the inlet and C_μ is the k-ε model constant of value 0.09.

$$\varepsilon = \frac{{u*}^3}{\kappa(z + z_0)} \tag{4.3}$$

ε is the turbulence dissipation at the inlet, κ is the von karmen constant of value of 0.4.

Scenario 3: The final model used the inlet boundary conditions suggested

by Yang et al. [2009]:

$$u(z) = \frac{u*}{k} ln\left(\frac{z+z_0}{z_0}\right) \tag{4.4}$$

$$k(z) = \frac{u*^2}{\sqrt{C_\mu}} \sqrt{Aln\left(\frac{z+z_0}{z_0}\right) + B} \tag{4.5}$$

$$\varepsilon(z) = \frac{u*^3}{\kappa(z+z_0)} \sqrt{Aln\left(\frac{z+z_0}{z_0}\right) + B} \tag{4.6}$$

The values of A and B where 0.6 and 0.83 respectively. These values were found by fitting a curve to the TKE data, this was done using the Matlab function lsqcurvefit which solves non-linear curve fitting problems in the least-squares sense.

The k-ε model parameter were left to their default value except for σ_ε whos value was set according to equation 4.8. CFX does not allow for C_μ to be a function it can only take a constant value, therefore its default value of 0.09 was used rather than the relation stated in equation 3.27.

4.1.3 Results of CFD Model of the Atmospheric Boundary Layer produced in a Wind Tunnel

Figure 4.2 - 4.3 show results of velocity and TKE profiles from all three scenarios compared against data taken from the wind tunnel experiment. Profiles at both the inlet and outlet of the CFD domain are given to assess the level of change in the profiles as we move downstream.

The profiles taken at the inlet of the CFD domain for Scenario 1 are found to provide the best match with experimental data however Scenario 2 and 3 provide a good match at heights below $z/H = 0.2$. There is seen to be little change in the profiles as we move downstream. The greatest change is seen for Scenario 1 which shows some decay in the velocity profile at greater heights, however the domain tested here is relatively small for larger domains a greater change in the velocity profile may be witnessed [Blocken et al., 2007].

The TKE profiles are shown in Figure 4.3. Both Scenarios 1 and 3 show a

good match with experimental data for the inlet profile. Scenario 2 shows a poor match due to the fact TKE is constant with height which is not reflected in the experimental data. The profiles taken at the outlet show streamwise gradients for all scenarios tested. In the case of Scenario 1 and 3 there is a decay in TKE at lower levels although the profile remains constant at greater heights for Scenario 3. Scenario 2 shows an increase in TKE at lower levels.

All three scenarios tested have reinforced the findings of previous literature and highlighted the difficulty in obtaining a homogeneous boundary layer profile. Recommendations from previous literature on how to obtain a homogeneous boundary layer have included ensuring the correct sand grain roughness is used, specifying the shear stress at the top boundary of the domain and ensuring the profiles used to specify the inlet conditions are consistent with the turbulence model being used. Both Scenario 2 and Scenario 3 satisfies all three of these requirements however streamwise gradients are still found in the boundary layer profiles produced in the CFD domain.

One possible cause of such gradients could be inconsistencies in the way the Standard k-ε model constants are specified. In the next section of this chapter we will look at a method which allows us to asses the uncertainty relating to the value these parameters should take as well as the TKE output itself and how adapting these constants can lead to a more stable boundary layer profile.

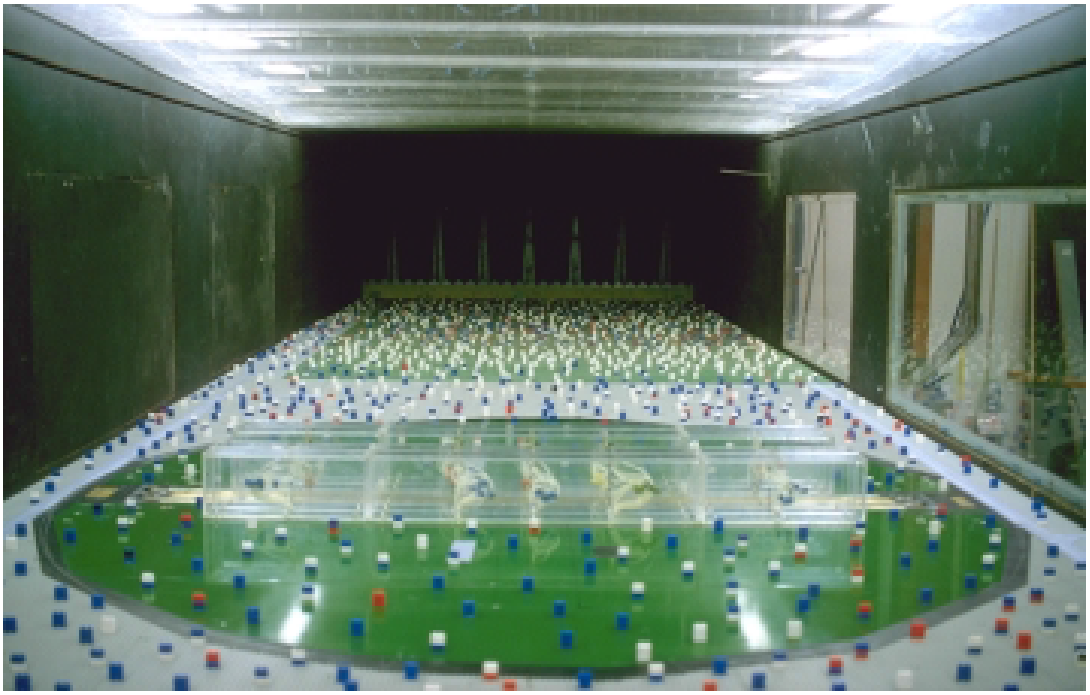

Figure 4.1: Atmospheric boundary-layer wind tunnel at the University of Karlsruhe, taken from Kastner-Klein

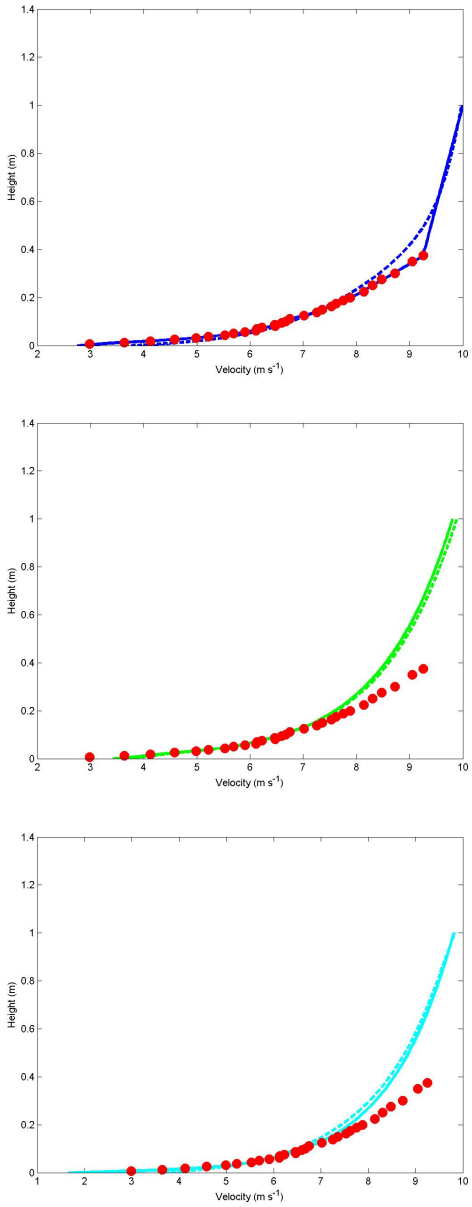

Figure 4.2: Comparison between velocity profile taken from wind tunnel data (red) and CFD model scenario 1 (top), scenario 2 (middle) and scenario 3 (bottom). CFD data is given at the inlet (solid line) and outlet (dashed line)

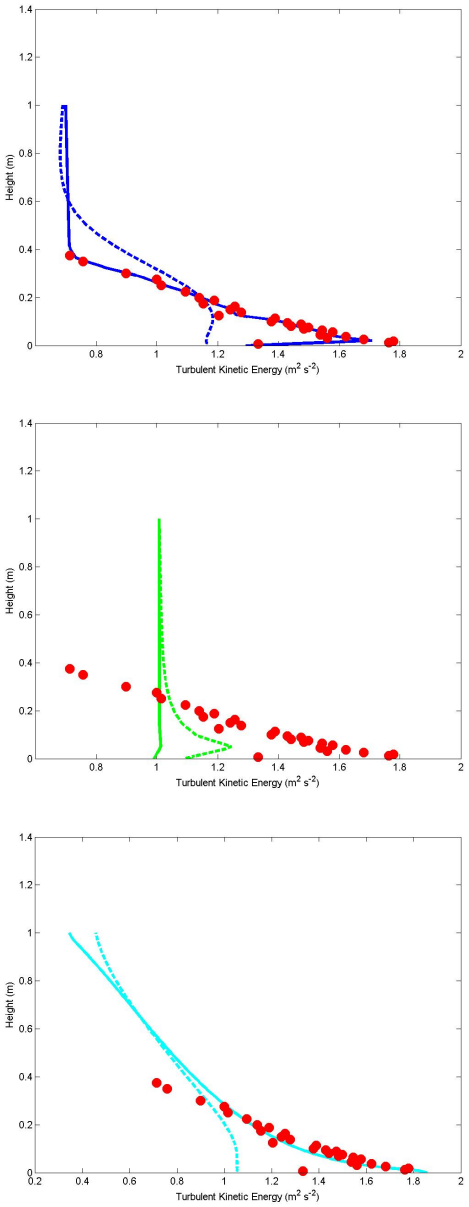

Figure 4.3: Comparison between TKE profile taken from wind tunnel data (red) and CFD model scenario 1 (top), scenario 2 (middle) and scenario 3 (bottom). CFD data is given at the inlet (solid line) and outlet (dashed line)

4.1.4 Bayesian Calibration of the k-ε Model Constants for use in Atmospheric Boundary Layer Flows

The initial results of this chapter have shown the difficulty in obtaining a homogeneous boundary layer flow within CFD. The choice of appropriate inlet boundary conditions along with correct modelling of the wall roughness along the floor of the domain has been highlighted as important factors in obtaining boundary layer flow without streamwise gradients. In addition to this the choice of k-ε model constants also plays a part in obtaining a homogeneous boundary layer flow however there is still some uncertainty relating to the values these parameters should take under boundary layer flow conditions.

This section of the chapter will therefore address the common problem of parameter uncertainty within CFD modelling and investigate statistical methods which enable the quantification and reduction of such uncertainties. We will start by discussing the importance uncertainty quantification within CFD modelling and examples of how this has been addressed in the past followed by a more detailed look at the k-ε model constants and how the value for these constants have been obtained in the past. The technique of Bayesian calibration will then be used to calibrate four of the five k-ε model constants for use in modelling the urban boundary layer. This will provide posterior probability distributions for each of the k-ε model constants. We will then discuss the best way to use such information to improve CFD model predictions and obtain information on uncertainty within the CFD output.

4.1.4.1 Uncertainty Quantification in CFD modeling

There are several sources of uncertainty present within CFD models. These can come from the model inputs, the form of the model, the assumptions made in the mathematical model, and numerical approximation errors which are due to the differential equations being approximated rather than solved explicitly (an example of this would be discretization error). It is therefore important that we are able to characterise such uncertainties, propagate them through to the model output and ultimately try and reduce them. This is the aim of uncertainty quantification or UQ.

Different techniques can be applied to tackle each type of uncertainty. Model verification deals with the uncertainties relating to numerical approximation. It is a way of providing evidence that the computer model accurately represents the conceptual model of the system. Whereas model validation is used to ensure the computer model is an accurate representation of the physical system of interest and deals with the uncertainty related to model form. This involves comparing the CFD output against experimental data. A full description of these types of uncertainties and statistical methods for quantifying them can be found in Roy and Oberkampf [2011].

Uncertainty quantification in CFD and in numerical models in general can be carried out using a variety of statistical methods. One such method, Polynomial Chaos, is discussed in detail and examples of applications of this technique to different types of flows such as incompressible and reacting flows are discussed in a review by Najm [2009]. Le Maitre et al. [2001] applied this technique to incompressible flow in a micro channel with low Reynolds Number.

Although uncertainty quantification is an important topic within CFD particularly within the field of turbulence models, it is not routinely addressed in CFD studies. However there are a number of studies that have demonstrated different statistical techniques to address the issue of uncertainty within RANS turbulence models. One such study conducted by Dunn et al. [2011] looked at the uncertainty contained within the model coefficients of the k-ε model. They used the Latin Hypercube Sampling method to investigate these uncertainties in the case of flow over a backward step and found that model coefficients had a significant effect on stream wise mean velocity, turbulence intensity, reattachment point location, pressure and wall shear stress.

An example of Bayesian Calibration of RANS turbulence models is given by Oliver and Moser [2011]. The Bayesian approach was used to analyse both model and parameter uncertainty within several types of turbulence models and applied to the case of incompressible channel flow. They were able to make a comparison between different uncertainty quantification models as well as different turbulence models and found both to impact the quantity of interest (QoI's). They found that after calibration the Chien k-ε model gave a prediction of the QoI's with an uncertainty of approximately $\pm$ 4%. Another example of a study which used

Bayesian Calibration to assess uncertainty within RANS models is Cheung et al. [2011]. The Spalart-Allmaras turbulence model was used to model the case of an incompressible boundary layer flow. Seven constants within the SA model were calibrated against experimental data, and predictions of the quantities of interest were produced. In their work they looked at the plausibility of competing models for uncertainty evaluation. Cheung et al. [2011], having made the first step in their calibration of a CFD model, highlighted for future research the areas of a comparison uncertainty analysis of RANS turbulence models, as well as the use of statistical emulators to save computing time on computationally expensive CFD models.

4.1.4.2 The Standard k-ε Model Constants

The formulation of the k-ε model given in section 3.1.4 requires the specification of five closure constants, C_μ, $C_{\varepsilon 1}$, $C_{\varepsilon 2}$, σ_ε and σ_k in order for the model to be complete. Launder and Spalding [1972] noted that, in the vicinity of a wall, production and dissipation terms are equal, reducing the energy equation to:

$$\frac{\tau}{\rho k} = \sqrt{C_\mu} \tag{4.7}$$

Where τ is wall shear stress and k is the turbulence kinetic energy. Using experimental data for flow near walls Launder and Spalding [1972] makes an initial suggestion of a value of 0.08 for C_μ. A value of $C_{\varepsilon 1}$ is similarly found by considering near wall turbulence and an initial suggestion of 1.5 is made based on the values of the other parameters. The value of $C_{\varepsilon 2} = 2$ was initially suggested by Hanjalic and Launder [1972]. This value was based on theory of decay of turbulence behind a grid. These initial values have been adapted over the years based on computer optimisation and a greater data set, to give the default values commonly used today (see Table 4.1). The values for σ_ε and σ_k were similarly found through computer optimisation.

Table 4.1: standard values used for model constants

C_μ	$C_{\varepsilon 1}$	$C_{\varepsilon 2}$	σ_ε	σ_k
0.09	1.44	1.92	1.3	1.0

Although these are the most commonly used values for the k-ε model constants and are generally left unaltered there have been a few occasions when researchers have suggested that alternative values should be used either due to dependencies placed on the constants due to the boundary conditions being used or in order to improve model performance.

In their study into the use of the Standard k-ε model for self similar free shear flows and equilibrium boundary layers Poroseva and Iaccarino [2001] found that by tuning the model constants they could successfully reproduce mean-velocity and shear stress profiles. They found that the relation between σ_k and σ_ε to be more important than their absolute value and recommended that the values $\sigma_\varepsilon/\sigma_k = 1.5$ be used for such flow types. They also state that the value of $C_{\varepsilon 1}$ has a significant impact on results and that its value should be based on the flow type and the Reynolds number.

Beljaars et al. [1987] discuss the choice of k-ε model constants relevant to atmospheric boundary layer flow. They suggest that, since C_μ is related to the ratio of shear stress to turbulence kinetic energy, a value of 0.09 is not deemed appropriate for the atmospheric boundary layer and using the experimental data of Panofsky and Dutton [1984] they suggest a more appropriate value is 0.032. Based on this new value of C_μ and the fact that the following relation must hold between the k-ε model constants if a logarithmic velocity profile is used for the inlet boundary conditions:

$$\sigma_\varepsilon = \frac{k^2}{(C_{\varepsilon 2} - C_{\varepsilon 1})\sqrt{C_\mu}} \tag{4.8}$$

A new value of $\sigma_\varepsilon = 1.85$ is chosen. All other model constants are left to their default value. However Beljaars et al. [1987] do stress the importance of the value of $C_{\varepsilon 1}$ on the CFD output and make the suggestion for future work to tune the value of $C_{\varepsilon 1}$ against detailed turbulence data particularly in the case of in-homogeneous surface layer flow.

The work of Richards and Hoxey [1993] on providing inlet boundary conditions for use in atmospheric boundary conditions has been discussed in Section 3.2.1.1. When demonstrating the use of these profiles against experimental data they found the default value of C_μ to be inadequate at reproducing the levels of

turbulence found in the atmospheric boundary layer. Based on their experimental data they tuned C_μ to give a value of 0.013. Similarly to Beljaars et al. [1987] the accordingly adapted the value of σ_ε to 3.22 as per equation 4.8.

The updated inlet profiles specified by Yang et al. [2009], which were shown to give a better match against experimental data for TKE profiles, produced new dependencies between the k-ε model constants as derived by Gorl et al. [2009].

$$C_\mu(z) = \frac{u_*^4}{Aln(z + z_0) + B} \tag{4.9}$$

$$\sigma_\varepsilon(z) = \frac{k^2(-A/2 + k(z)^2)}{u_*^2(C_{\varepsilon 2} - C_{\varepsilon 1})k(z)} \tag{4.10}$$

The term k-ε model constants is no longer technically correct as these parameters are a function of height. As mentioned in the previous section most commercial softwares do not allow C_μ to be a function. Yang et al. [2009] chose a value of $C_\mu = 0.028$, while Gorl et al. [2009] chose a value of $C_\mu = 0.017$ based on equation 3.27 and the height taken to be that of half the cell height next to the wall. In addition to changing the value of C_μ, Yang et al. [2009] also changed the value of σ_k and σ_ε based on the recommendation provided by Poroseva and Iaccarino [2001] of a ratio of $\sigma_\varepsilon/\sigma_k = 1.5$, although the absolute values they give to the constants differ to those given by Poroseva and Iaccarino [2001], with Yang et al. [2009] choosing values of $\sigma_k = 1.67$ and $\sigma_\varepsilon = 2.51$. They choose a value of $C_{\varepsilon 1} = 1.5$ based on recommendation given by Durbin [1995].

The main purpose of this research is to demonstrate the technique of Bayesian calibration as a method of uncertainty quantification for CFD modelling. In light of the above discussion it would seem there is still some uncertainty surrounding the preferable values for the k-ε closure constants and the effect changes to these parameters have on the CFD output. It would therefore seem that the k-ε closure constants would make a good choice of calibration parameters as there is a need to better understand the uncertainties relating to these constants and find a way of reducing the range of possible values they could take.

The calibration will be carried out on the CFD model of the atmospheric boundary layer which uses the inlet profiles suggested by Yang et al. [2009]. The calibration process consists of running several CFD models (150 in total) with

varying values of the k-ε model constants. The TKE profile will be extracted at the outlet from each of the 150 models. Since we would like to find the parameter values which show the least decay in the TKE profiles over the length of the domain we will be comparing the outlet TKE profiles against the TKE profile specified at the inlet. Through this process we are able to obtain probability distributions for each of the parameters. These probability distributions show, over a given range of values, the likelihood of those values producing a good match with the inlet data (i.e. which parameters can offer the least decay in the TKE profiles).

4.1.4.3 Bayesian Calibration Method

The calibration process consists of putting distributional assumptions (prior distributions or simply priors) on the calibration (also called tuning) parameters $C_{\varepsilon 1}, C_{\varepsilon 2}$, σ_k and C_μ before comparing with observations (in our case data taken from the inlet of the CFD domain), and letting the information contained in the data update this a priori assumption to get as a result a posterior distribution of the calibration parameters. The advantage of such a Bayesian analysis [Kennedy and O'Hagan, 2001] over standard estimation of parameters (e.g. by minimizing the differences between observations and simulator outputs) lies mainly in the ability to retrieve a full description of the uncertainties about the parameters and consequently about the simulator outputs. Moreover, the possibility for the modelers to express their -uncertain- scientific beliefs in terms of priors on the parameters enables a natural integration of scientific knowledge and evidence given by measurements.

It was decided to calibrate four out of the five k-ε model constants and not σ_ε due to its strong interdependence on the other model constants. The following formula was used to set the value of σ_ϵ:

$$\sigma_\varepsilon(z) = \frac{k^2(-A/2 + k(z)^2)}{u_*^2(C_{\varepsilon 2} - C_{\varepsilon 1})k(z)} \tag{4.11}$$

For simplicity we now denote $C_{\varepsilon 1}$ and $C_{\varepsilon 2}$ as C_1 and C_2. The intervals chosen to be tested for the calibration constants were as follows C_1 : 0.5 - 1.5, C_2: 0.6 - 2.5, C_μ: 0.01 - 0.15 and σ_k:0.5 - 2.5. These were chosen based on the standard

values suggested for the model constants and how these had been changed in the past. We put uniform priors on these parameters, allowing for equal initial probability of being at any location in these intervals. In addition the value of C_1 was restricted so it did not exceed C_2.

The complete set of inputs $x = (h, \theta)$ consists of parameters divided into two categories: the known parameters (normalized height h in $[0, 2]$) and the unknown calibration parameters $\theta = (C_1, C_2, C_\mu, \sigma_k)$. We denote by $y^M(x)$ the empirical output of the computer model as a function of $x = (h, \theta)$ and $\eta(x)$ the expected output of the computer model as a function of $x = (h, \theta)$. The difference between $y^M(x)$ and $\eta(x)$ is the numerical intrinsic error. The computer code output $\eta(x)$ is an approximation of the reality $y^R(h)$. To learn about the values of the calibration parameters, the CFD model is run at inputs x in a design (i.e. choice of values) D^M. Observations (i.e. TKE data taken from the inlet profile) $y^F(h)$ are collected at a number of input heights h.

For our design of experiments D^M corresponding to the calibration parameters, we use a maximin Latin Hypercube (LHS) design. With this design we try to cover as much space as possible in the five-dimensional space of the calibration parameters with only $n = 150$ runs. For the spatial coordinates of the computer design D^M, we choose the same locations as the experimental design. Figure 4.4 shows the CFD computed TKE values at these heights. This is the first step in our study.

The following equations constitute an extension of Kennedy and O'Hagan [2001] as they specify the intrinsic CFD model numerical error. They describe the relationships between the CFD model and the observations at the design points, using bias $\delta(h)$, intrinsic CFD model numerical error ν_η and observation error ν (both assumed constant across heights h):

$$y^M(h, \theta) = \eta(h, \theta) + \nu_\eta \tag{4.12}$$

$$y^R(h) = \eta(h, \theta^*) + \delta(h) \tag{4.13}$$

$$y^F(h) = y^R(h) + \nu \tag{4.14}$$

Here, θ^* is used to represent the true (unknown) values of the calibration parameters. These equations suggest that even if the CFD model were run at the true

values of the calibration parameters, it would still be a biased representation of reality. Thus the model can never perfectly match observations without some additional process of adjusting for model errors. It is crucial that such a discrepancy (or bias) term be introduced in order to avoid overfitting the data with an unrealistic choice of parameters. Furthermore, the bias must vary according to height, as the CFD model shortcomings are strongly dependent on height. This is unnecessary for the numerical error in the CFD model as this may vary only very slightly according to height and are much smaller than the model bias.

Because the simulator output $\eta(\cdot)$ is unknown except at the design points D^M, we assume that the unknown function follows a Gaussian stochastic process (GP) distribution. That is, we model the N observed simulator responses $\eta(x), x \in R^p$ (here $p = 5$ since D^M is over a range of C_1, C_2, C_μ, σ_k and h, values), as coming from a multivariate normal distribution with mean μ and $N \times N$ variance-covariance function Σ. Since we initially standardize the entire set of responses (CFD model and observed) by the mean and standard deviation of the CFD responses, $\mu = 0$ above and the variability in the simulator $(1/\lambda_\eta)$ below is approximately 1. Thus, we approximate the CFD model by specifying a distribution of functions that interpolate the response $\eta(x)$ in between the design points x in D^M. The random function is certain at the design points, and uncertain at untried points.

To specify Σ according to the calibration parameters we use a product Gaussian variance-covariance. Thus, the $(i,j)^{th}$ element of Σ, $cov(\eta(x_i), \eta(x_j))$, is (conveniently using the notation θ_4 for h):

$$\frac{1}{\lambda_\eta} exp(-\sum_{k=1}^{4} \beta_k |\theta_{ik} - \theta_{jk}|^2).$$

The notation θ_{ik} denotes the i^{th} design point in D^M for θ_k. The hyperparameters λ_η (the precision of the GP model), β_k (which we call "correlation hyperparameters") are to be estimated from the model output and the observations as described below. The unknown bias function $\delta(h)$ is also modeled as a GASP random function with mean 0 and correlation matrix with precision λ_δ and correlation parameter β_5. Finally, the random error and intrinsic error com-

ponents are modeled as independent $\nu \sim N(0, 1/\lambda_\nu)$ and $\nu_\eta \sim N(0, 1/\lambda_{\nu_\eta})$. Only the θ's are deemed to be calibration parameters, or quantities to be tuned for the CFD model to perform better. All the other quantities, such as observation and numerical errors, as well as the hyperparameters, are only auxiliary quantities for the analysis (but are of interest nevertheless).

The likelihood can be written, for a joint vector of given observations y^F and CFD model outputs y^M,

$$\begin{bmatrix} y^F \\ y^M \end{bmatrix} \sim MVN(0, \Sigma_y) \tag{4.15}$$

where

$$\Sigma_y = \Sigma_\eta + \begin{bmatrix} \Sigma_b & 0 \\ 0 & 0 \end{bmatrix} + \begin{bmatrix} \Sigma_\nu & 0 \\ 0 & \Sigma_{\nu_\eta} \end{bmatrix} \tag{4.16}$$

For the estimation of the calibration parameters, and all the other quantities, we employ the Markov Chain Monte Carlo (MCMC) algorithm. The chains are dependent random samples that ought to be distributed in the long run as the so-called posterior distributions of the parameters of interest, which are combinations of prior information about the values of these parameters and the information about the parameters provided by the data. We then retrieve the posterior distributions of the various calibration parameters, which allows us to make inferences and quantify our uncertainty about the true values of these unknown quantities.

All the unknowns in the model (i.e. the calibration parameters and the hyperparameters such as variances -here actually precisions-, correlation parameters β's) require specified prior distributions which represent uncertainty about the values of these parameters before any data is collected. The following choices are made for the priors:

- To represent vague prior information about the true calibration parameter values, we specify a uniform prior distribution over the interval on which they were sampled for simulator runs.

- To model the correlation hyperparameters in Σ, we conservatively place most of its prior mass on values for the corresponding correlations near

1 (indicating an insignificant effect). Similarly, conservative priors were used for the hyperparameters associated with the correlations in the bias function.

- Gamma prior distributions were used for each of the precision (i.e. inverse of the variance) hyperparameters λ_η, λ_δ and λ_ν. Specifically, we use priors $\lambda_\eta \sim GAM(10, 10)$ (with expectation 1 due to standardization of the responses), $\lambda_\delta \sim GAM(10, .3)$ (with expectation around 3% of standard deviation of the standardized responses), and $\lambda_\nu \sim GAM(10, .03)$ 0.3% and $\lambda_{\nu_\eta} \sim GAM(10, .001)$ 0.01%. These prior assumptions are based on our original scientific understanding of the problem: we want the CFD model to capture most of the variations in order to tune our calibration parameters, and the bias ought to be small as a result.

Because our choice of priors make the full conditional distributions of the unknowns difficult to sample, we implement a Metropolis-Hastings algorithm to explore the multidimensional space of parameters. The algorithm makes use of a proposal distribution to draw a future value conditional on the current state. Then this move is either accepted or rejected according to a random toss with a probability of acceptance that depends upon the target distribution. This eventually yields draws from the target distribution (here the posterior). We used multiple chains to confirm the convergence towards a stationary posterior distribution (after an initial burn-in period), saving wall-clock time by running the chains in parallel.

4.1.4.4 Results of Bayesian Calibration

Figure 4.4 shows the TKE profiles for all 150 CFD runs against the inlet profile. This allows us to see clearly how the choice of k-ε model parameters can affect the amount of decay in TKE boundary layer profiles. The variation in these constants is shown to have a large effect on the TKE levels particularly at those heights closest to ground level. It also shows us that none of the combinations of parameters chosen can stop the decay of TKE happening at the very lowest height (z/h = 0.0125)

The calibration process produces a posterior probability distribution for each of the calibration constants. These are plotted in the form of a histogram. The probability distribution will tell us how likely each of the values within the chosen intervals is to give a good match against the inlet profile. Those with high probability will give a closer match than those with low probability. Therefore by looking at where the peak of the histogram occurs we can determine the most likely value for each parameter to give the best match against the inlet profile. We can also determine from the spread of the histogram the uncertainty attached to each parameter, those histograms with a narrow distribution and high peak have less uncertainty associated to them than those with a wide spread and not such a distinct peak.

The histogram for C_μ, shown in Figure 4.5, shows values at the lower end of the interval are given higher probability of providing a better match with the inlet profile. In particular we can see that the default value of 0.09 is not deemed a suitable value in this context. This supports the findings of previous research in which the values of C_μ have been decreased when simulating the atmospheric boundary layer to provide a better prediction against experimental data and reduce the decay of the TKE profiles [Beljaars et al., 1987], [Richards and Hoxey, 1993].

The histogram for C_1 shows that slightly lower value of 1.2 compared with the default 1.44 is likely to provide a better match against the inlet profile.

The histograms for C_2 and σ_k do not show such a clear peak as those for C_μ and C_1. There is a greater amount of uncertainty attached to these values compared to C_μ and C_1. This may be due to the fact that there is more than one value that will provide a good match with the inlet or these parameters do not have as much impact on the decay of TKE making it less clear what values they should take. For C_2 we notice that the default value of 1.92 is not deemed to be appropriate in this case and more likely values lie in the range 1 - 1.5. In the case of σ_k the histogram shows most likely values will lie within the mid range of our chosen interval around the value of 1.5.

4.1.4.5 Discussion on Results of Bayesian Calibration

We have seen the information that can be obtained through the process of Bayesian calibration the question now becomes how to utilise such information to improve our CFD model output. One option would be to use the information contained within the histograms to select updated values for the k-ε model parameters. To do this we can select the value which occurs at the peak of each histogram to give the new post calibration k-ε model parameters. These values are given in Table 4.2.

The CFD model is then run again with these updated values for the k-ε model constants. This new model will be referred to as the post-calibration model and the CFD model with the default k-ε model constants will be referred to as the pre-calibration model.

The results from the post-calibration CFD model are shown in Figure 4.9 along with the results for the CFD model with the default k-ε model constants. The effect of altering the k-ε model constants is to reduce the amount of decay occurring in the TKE profile as we move downstream of the inlet. Above a height of 0.2m the inlet and outlet profile of the post-calibrated model remain fairly consistent. Below a height of 0.2m there are still some problems with decay in the TKE levels particularly at ground level although this is improved compared to the pre-calibration model.

Due to restraints on computer resources it was only possible to calibrate a single 1-D profile with a single quantity of interest (QoI) but, with ever increasing computing capabilities, calibrations which use experimental data taken from two and even three-dimensional space and calibrate against multiple QoI's are not far out of reach. However the calibration process is likely to be most useful for applications where experimental data is sparse.

The question of whether we are able to apply the calibration results to other quantities of interest which we did not calibrate against and even different flow scenarios is still open ended. Although we cannot answer these questions in full we can begin to investigate such queries by running some initial tests of our post-calibrated model. First we will compare the velocity profiles for the models with the default closure parameters and the updated "calibrated parameters" to see if

the alteration of these parameters has had a significant effect on the velocity. The inlet velocity profile was plotted against the outlet velocity profile for both the pre and post calibrated model. The results shown in Figure 4.10 show that there is no discernible difference between the three velocity profiles and therefore changing the k-ε model parameters has not had a detrimental effect on the velocity profile.

Another important question is whether the k-ε model parameters found from the results of the calibration are only relevant to our CFD model or if they can be used for other CFD models. This question will be explored in the next section of this chapter.

Here we have seen one use of the Bayesian calibration results which is to find more appropriate values for the calibration constants by using the posterior distribution. Although this has been proven to be a simple and effective way of improving CFD output the disadvantage of such a method is that it does not make full use of all the information obtained from the calibration. The advantage of the Bayesian calibration process over other forms of best fit calibration is that it can provide information on the uncertainty relating to the calibration parameters.

The calibration process also takes into account the complex dependencies between the calibration parameters which by simply choosing the best value from the histogram we are neglecting. How do we then make use of this information and propagate these uncertainties through to the CFD output? One solution may be to use ensemble modelling. This requires that rather than one model being run with a single set of input parameters a number of CFD models are run with a range of input parameters. By selecting parameter combinations from the chains produced during the calibration process we can run a range of CFD models where the probability distribution for the k-ε model constants would resemble those produced by calibration process. Thus the CFD output would no longer consist of single point values but each point would have a range of values for each output. The disadvantage of such a method would be the large computational cost of running many CFD models and the difficulty in both processing and displaying the CFD results.

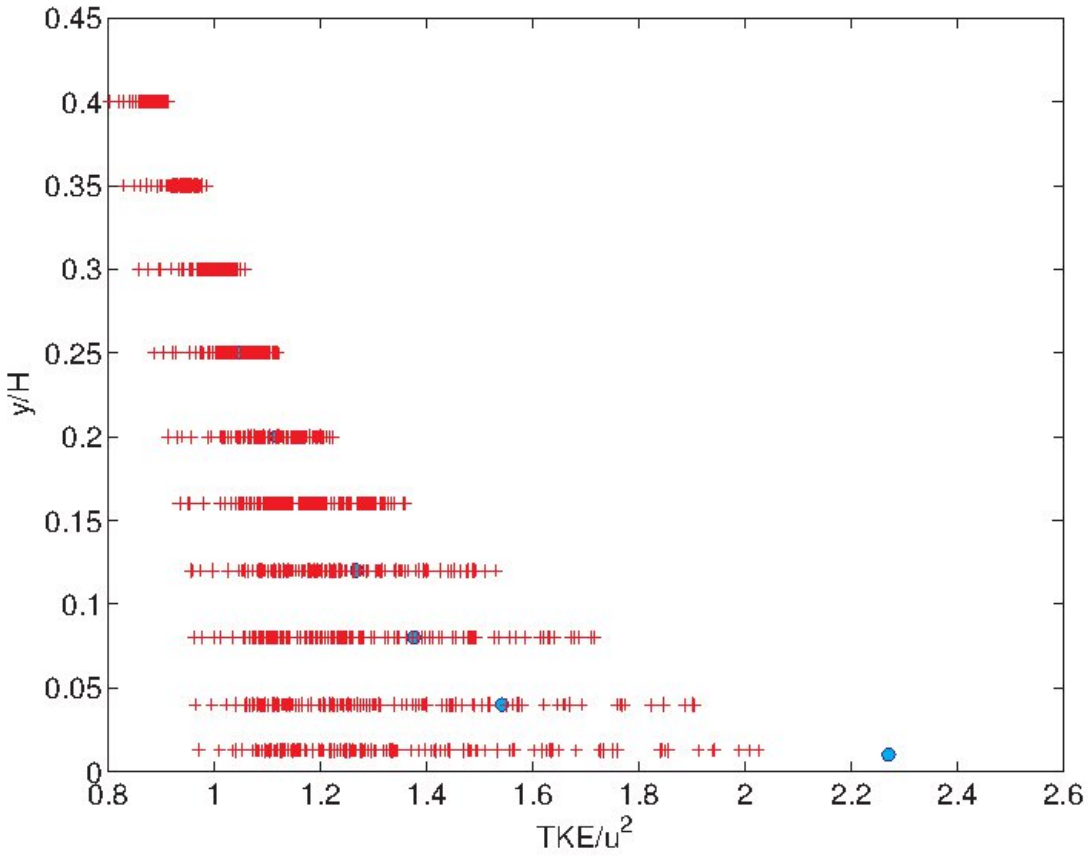

Figure 4.4: Results of TKE profiles taken from all 150 CFD runs (red crosses) shown against the inlet profile (blue circles).

Table 4.2: updated values used for model constants

C_μ	$C_{\varepsilon 1}$	$C_{\varepsilon 2}$	σ_k
0.025	1.2	1.25	1.5

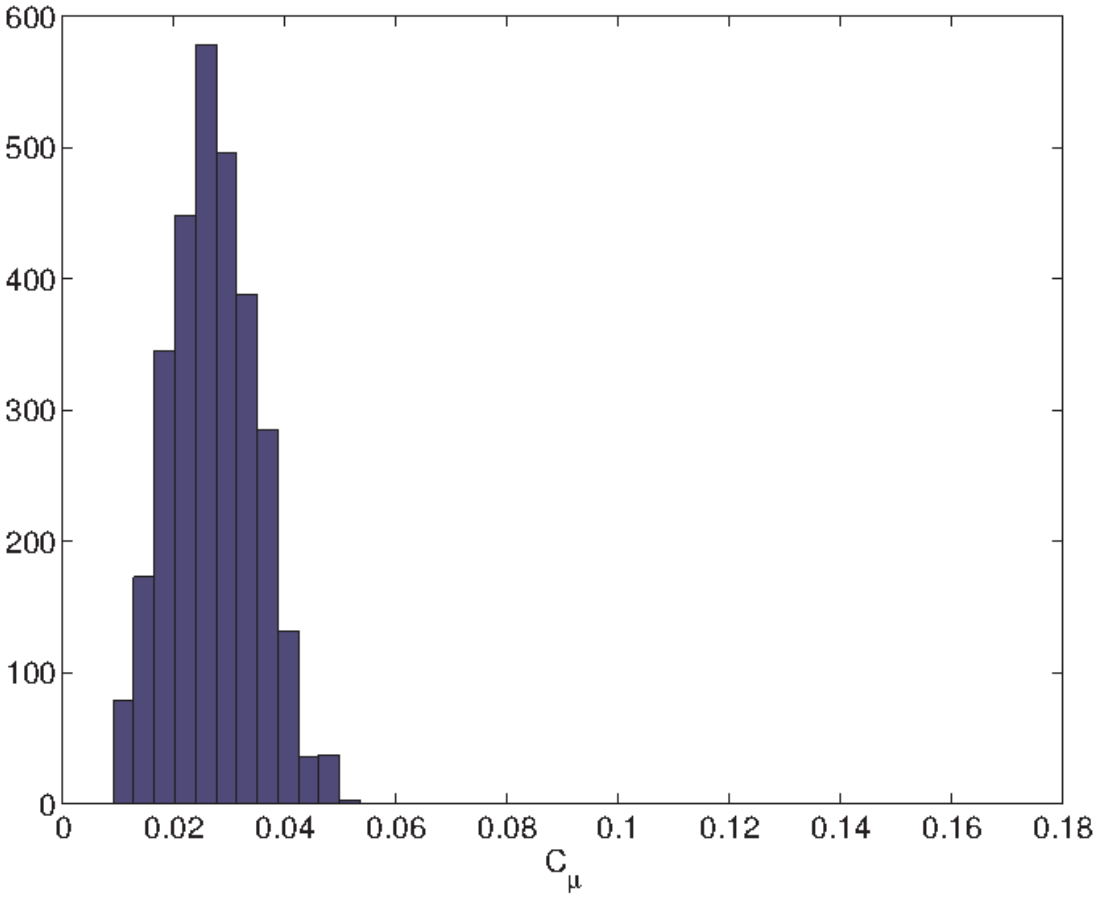

Figure 4.5: Histogram showing the posterior probability distrubution of C_μ.

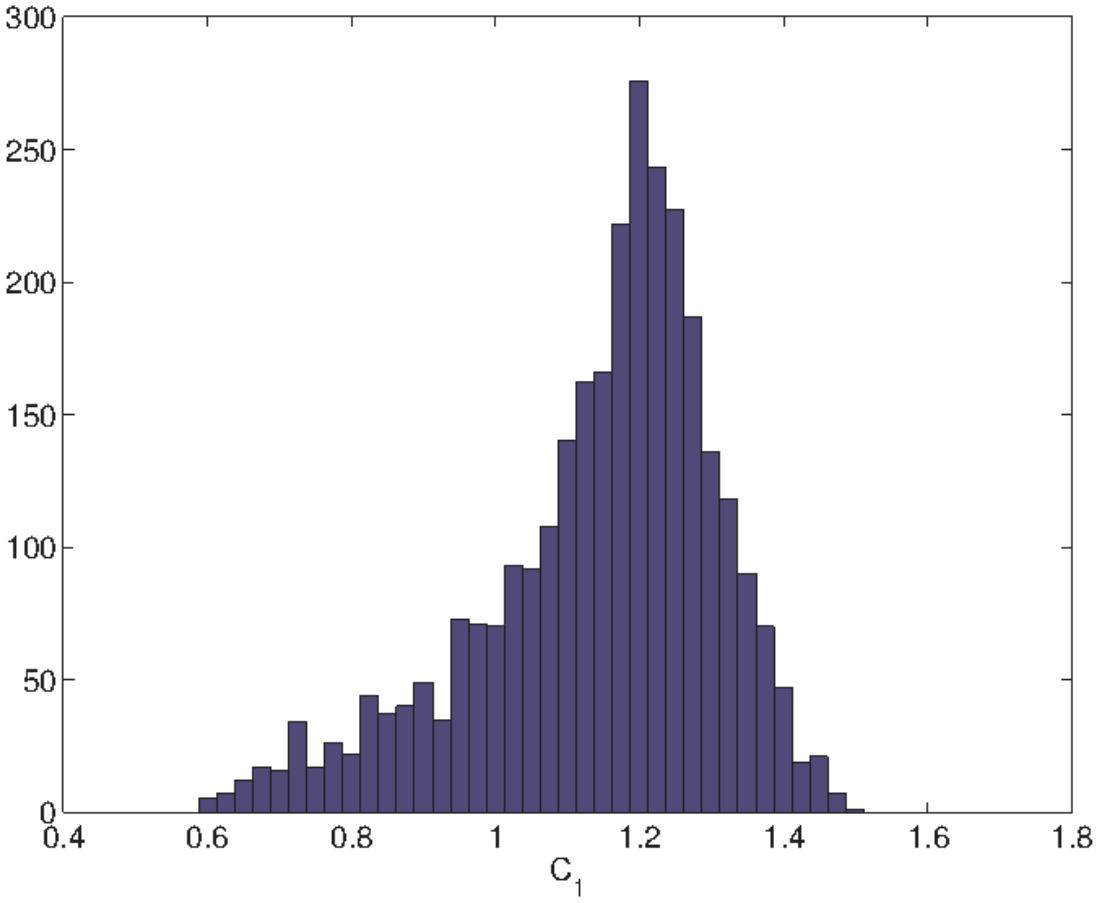

Figure 4.6: Histogram showing the posterior probability distrubution of C_1.

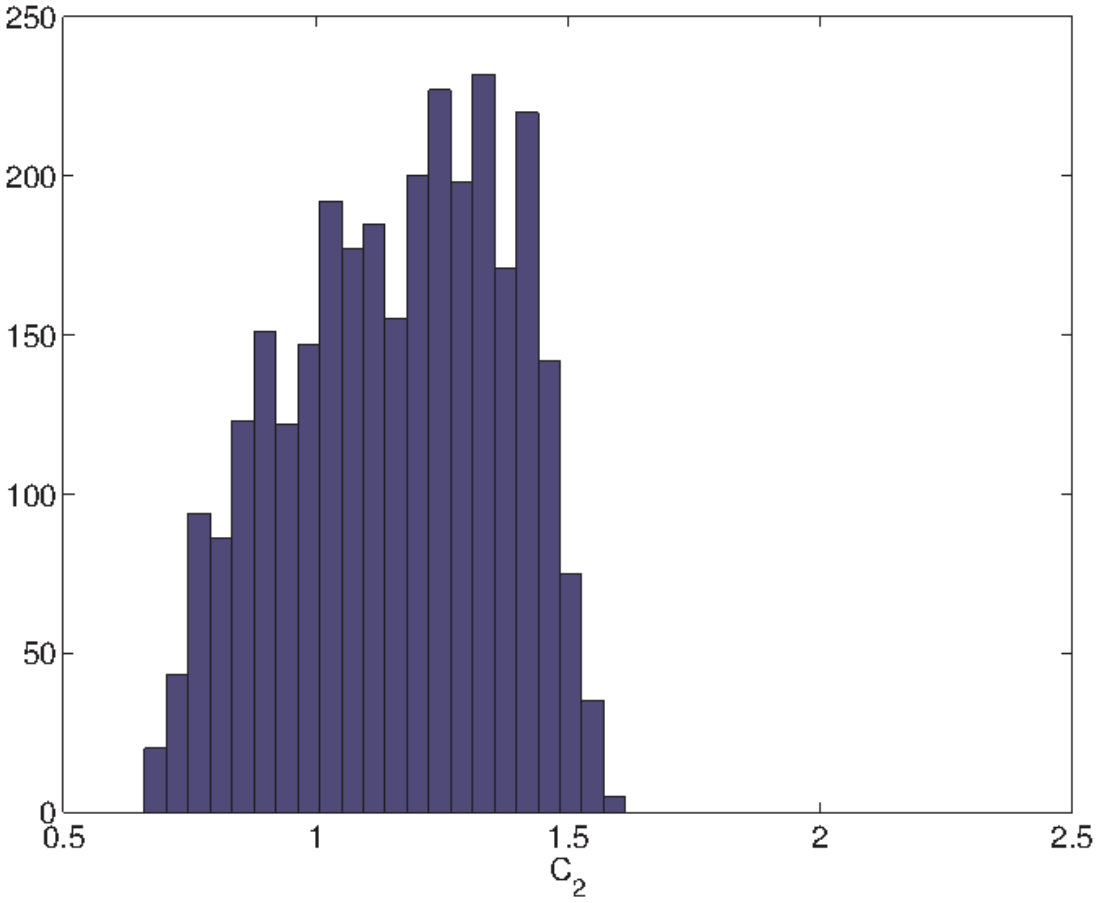

Figure 4.7: Histogram showing the posterior probability distrubution of C_2.

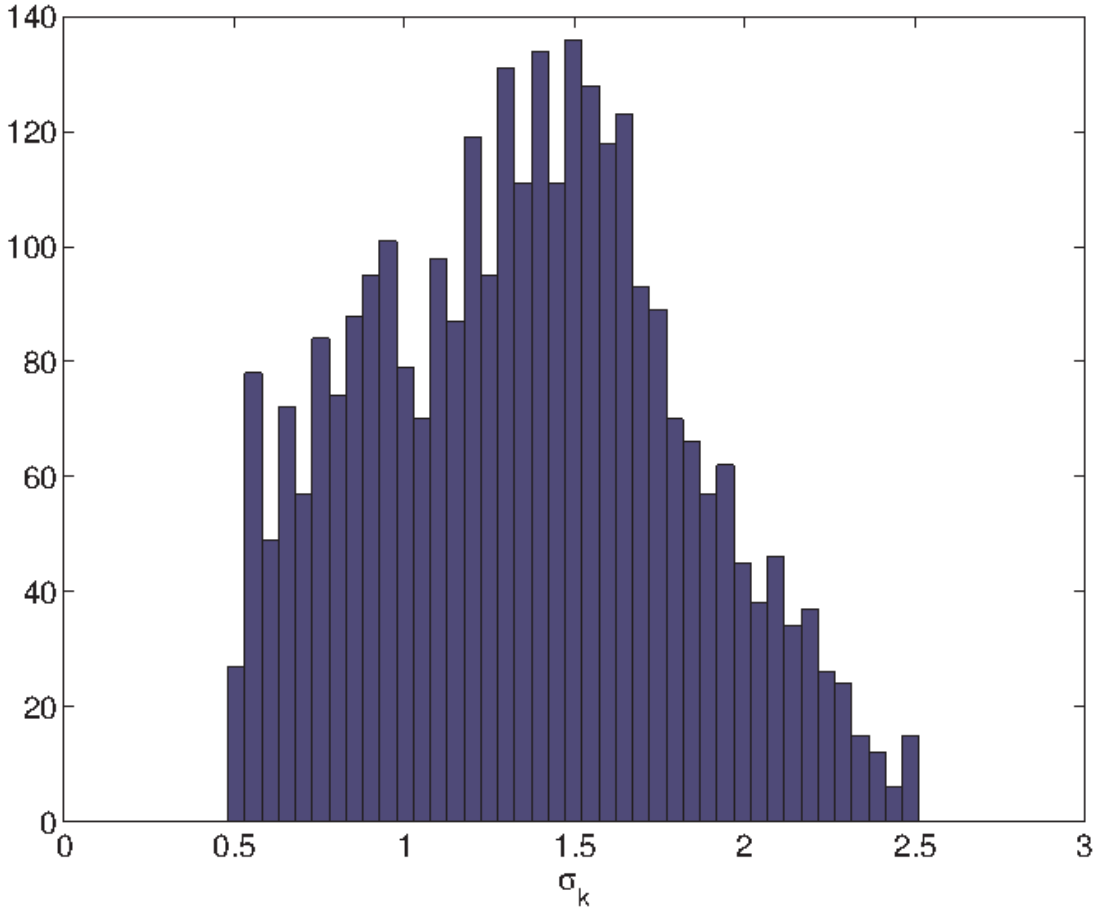

Figure 4.8: Histogram showing the posterior probability distribution of σ_k.

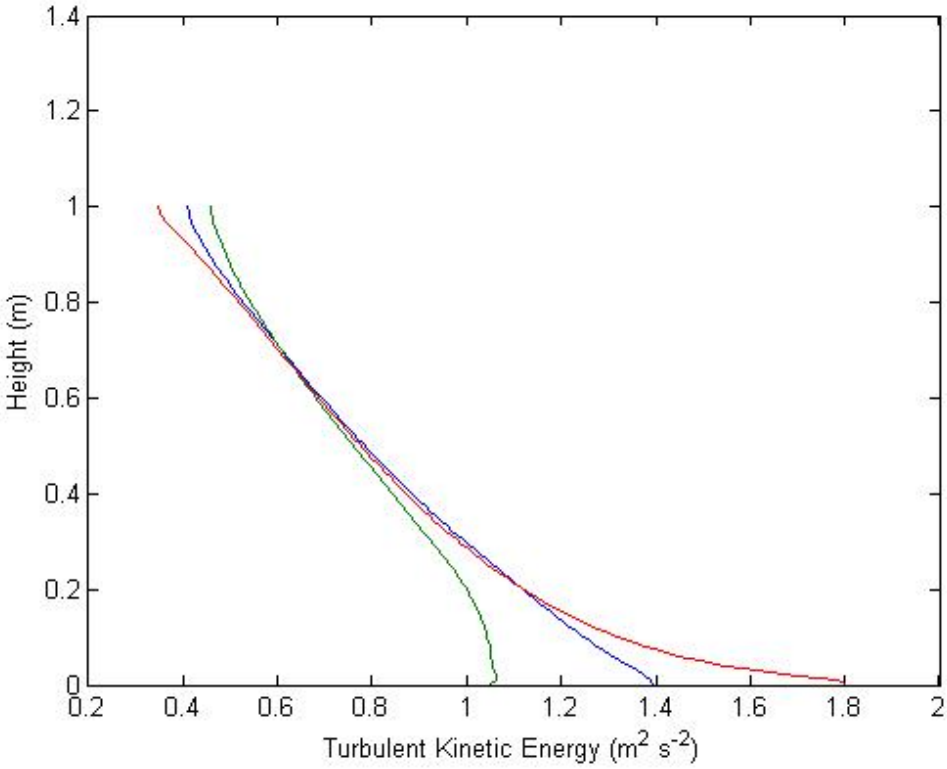

Figure 4.9: TKE profile at the inlet (red), outlet of the post-calibration model (blue) and outlet of pre-calibration model (green).

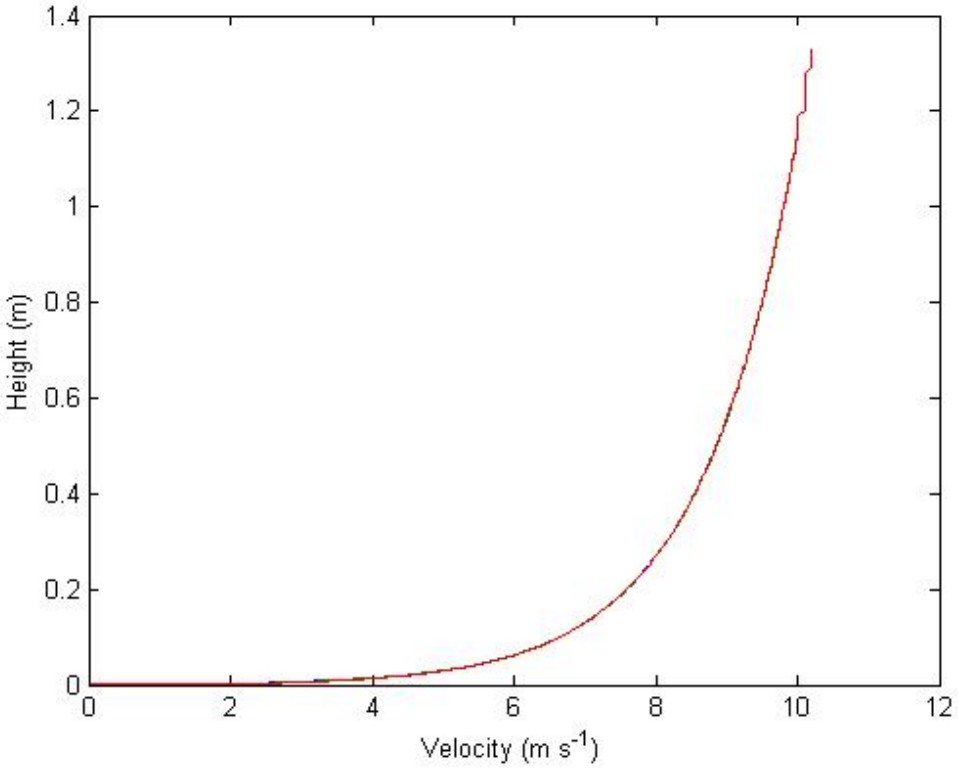

Figure 4.10: Velocity profile at inlet (red), outlet of the post-calibration model (blue) and outlet of pre-calibration model (green).

4.2 CFD Modelling of Street Canyon Flow Produced in a Wind Tunnel

In this section of the chapter we will expand on the work done in the previous section on how to model the urban boundary layer by including the geometry of a simple street canyon in our computational domain. This will allow us to assess the capabilities and limitations of CFD in predicting flow within a simplified street canyon through comparison with wind tunnel data. Finally we will look at the effect of altering the k-ε model constants to the updated values found in section 4.1.4.5.

4.2.1 Wind Tunnel Set Up

Data was taken from a windtunnel experiment carried out by Kastner-Klein et al. [2001]. Full details of the wind tunnel set up can be found in the previous section. The street canyon was represented by two rectangular blocks. The dimensions of these blocks were 0.12m high by 1.2 m long with a 0.12 m spacing between the two blocks, giving the street an aspect ratio of one (see Figure 4.1). The wind direction was perpendicular to the street length. Figure 4.11 shows the measurement location scheme for the measurements taken at the centre of the street canyon.

4.2.2 CFD Settings

For full details of the CFD geometry, mesh and model settings please refer to Appendix .2.2.

Based on the results found in Section 4.1 the profiles used to specify the velocity, TKE and dissipation at the inlet are given by equations 4.4, 4.5 and 4.6. The k-ε model constants were kept at the default values.

4.2.3 Results of CFD Model of Airflow within Homogeneous Street Canyon

4.2.3.1 Airflow Patterns

A qualitative comparison between the flow fields produced by the CFD model against those of the windtunnel show a good match (see Figure 4.12). The main features of the flow are captured by the CFD model. These include the separation and reattachment of the flow above the roof of the upstream building, the lack of separation on the downwind building roof and the single vortex formed within the street canyon.

The location of the centre of this vortex is also reasonably well captured. For multiple street canyons we would expect to see the centre of the vortex at the centre of the street canyon however, since this is an isolated street canyon the vortex centre is slightly to the right and above the central point of the street canyon. This is shown in both the windtunnel and CFD results however the prediction of this point for the CFD results is found to be slightly higher than in the windtunnel. A speed up of the flow as it travels up and over the leading edge of the building is also well captured by the CFD results.

4.2.3.2 Velocity Profiles

Figure 4.13 show the vertical profile of the mean streamwise velocity, u, at seven locations across the width of the street canyon (see Figure 4.11 for measurement locations). From these plots we can again see that the main features of the flow are well captured. There is clear speed up above roof top level. The negative u velocities in the lower portion of the street canyon are of the same magnitude as the positive u velocities in the upper portion of the canyon. The shear layer, above roof top level is well captured, as indicated by the inflection point in the velocity profile at a height z = H. The velocity profiles within the street canyon are symmetrical about the centre as shown by both the wind tunnel and CFD results. Velocities decrease with increasing proximity to the wall.

There are some minor discrepancies between the CFD results and windtunnel. There is a tendency of the CFD model to overpredict the velocity above a height

of 1.5H and under-predict the velocity between 0.4H and 1.2H. The wind shear above roof top level is slightly overpredicted as shown by the velocity gradient du/dz

4.2.3.3 Turbulence Profiles

Figure 4.14 shows contour plots of TKE levels for both the CFD and wind tunnel results. The CFD results show two distinct peaks. The first is at the leading edge of the first building located slightly upstream of the building. This peak is not present in the wind tunnel results which leads to an overprediction of TKE levels in the region directly upstream of the first building. This overprediction of TKE is a common problem when using the Standard k-ε model to simulate impinging flows. It occurs due to the way in which the turbulent production component is modelled. The turbulence production term, P_k, can be divided into two parts, the normal component, P_{kn} and the shear, P_{ks}. The true form of these terms is as follows:

$$P_{kn} = -(< u_1'' > - < u_3'' >)\frac{\partial < u_1 >}{\partial x_1} \tag{4.17}$$

$$P_{ks} = - < u_1 - u_3 > \left(\frac{\partial < u_1 >}{\partial x_3} + \frac{\partial < u_3 >}{\partial x_1}\right) \tag{4.18}$$

The Standard k-ε model uses an Eddy Viscosity model to approximate these terms:

$$P_{kn} = 4\nu \left(\frac{\partial < u_1 >}{\partial x_1}\right)^2 \tag{4.19}$$

$$P_{ks} = \nu \left(\frac{\partial < u_1 >}{\partial x_3} + \frac{\partial < u_3 >}{\partial x_1}\right)^2 \tag{4.20}$$

From equations 4.18 we can see that in reality P_{kn} and P_{ks} have the potential to be negative which can occur in areas of high $\frac{\partial < u_i >}{\partial < x_j >}$, however the approximations given by equations 4.20 will never be negative. This leads to the overprediction of TKE on the upwind corner of our building for which in reality we would see negative turbulent production terms these are predicted as being positive by the

Standard k-ε model [Murakami, 1993].

The second peak is above the roof top of the first building, this peak is present in the wind tunnel data however the CFD model under-predicts the magnitude of this peak. Since the TKE is exported downstream by advection and turbulent transport an under-prediction of the TKE levels here will lead to an under-prediction further downstream. This is clearly visible within the street canyon in which we can see the TKE levels are much lower. In their study Louka et al. [2000] describe how the peak in TKE is produced by the shear layer shed from the upwind roof. This layer is unstable through the Kelvin-Helmholtz instability and contains unsteady fluctuation. These unsteady processes are unlikely to be accurately captured by a steady state RANS model thus leading to an under-prediction of the overall TKE budget.

Aside from the underprediction of TKE the overall shape of the profiles are well predicted. The model is able to correctly predict the higher levels of TKE on the downwind side of the street against the upwind side. This is due to the vertical spreading of the shear layer. Turbulence energy is exported vertically from the shear layer core by pressure or turbulent transport. This size of the spread increases as we move downstream. Therefore as we reach profile number 6 and 7 we see a greater amount of TKE being advected down into the street canyon.

In summary by comparing windtunnel data against CFD predictions of flow within a simple street canyon we were able to asses the performance of the Standard k-ε model. It was shown that the model gave a good prediction of the qualitative features of the flow. The velocity profiles on the whole were well predicted. The model performed less well at predicting turbulence levels. With an overall under-prediction of TKE levels within and just above the street canyon. This is due to the under-prediction of the peak in TKE which occurs directly above the upstream roof top. Despite these short comings the Standard k-ε turbulence model is still in regular use for the modelling of flow within street canyons and the built environment.

4.2.4 Updating the k-ε Model Constants

In section 4.1.4 we saw how updating the values used for k-ε model constants improved predictions of homogeneous urban boundary layer by reducing the amount of decay in the turbulence profiles as we moved downstream. In this section we investigate whether these updated constants can offer improved prediction of street canyon flow.

The CFD model described in section 4.2 was updated using the k-ε model constants given in Table 4.2 in addition the function given in equation 4.11 was used to define σ_ε. It was found that with these constants a reasonable level of convergence of the residuals was not achieved. Monitoring points were placed at several locations across the domain. It was found that velocity and turbulence levels fluctuated at these locations at did not reach a stable solution. Therefore it can be concluded that with the street canyon present within the domain updating the k-ε model constants results in instabilities within the numerical model and convergence cannot be achieved. This would suggest that the Bayesian Calibration is case specific i.e. the results only apply to the case being calibrated and can not easily be transfered to other scenarios.

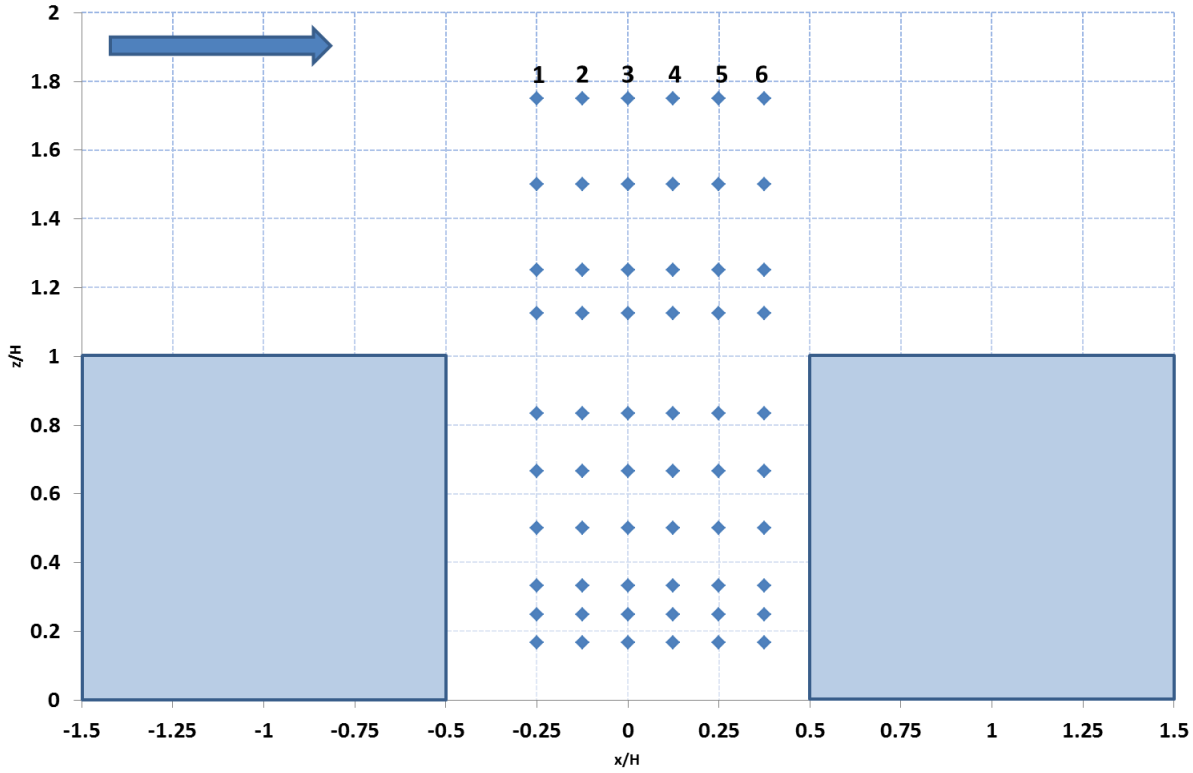

Figure 4.11: Measurement location for measurements taken across a vertical cross section at the centre of the street length

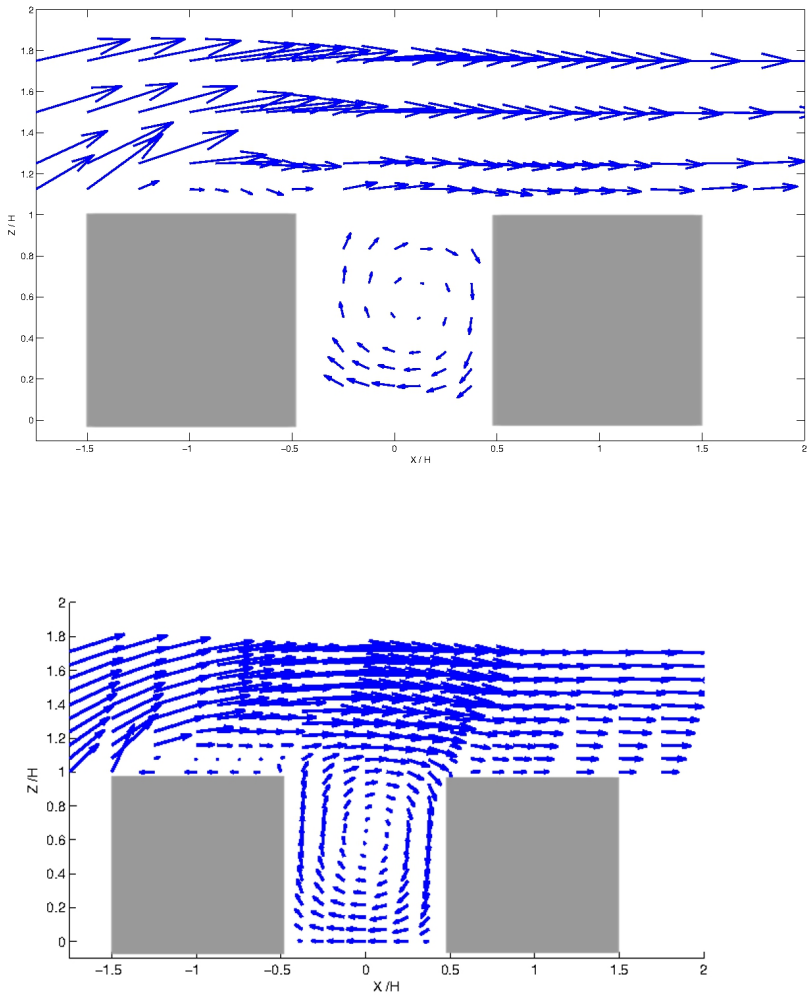

Figure 4.12: Vector plot of wind flow above and within the street canyon, for the windtunnel results (top) and CFD results (bottom)

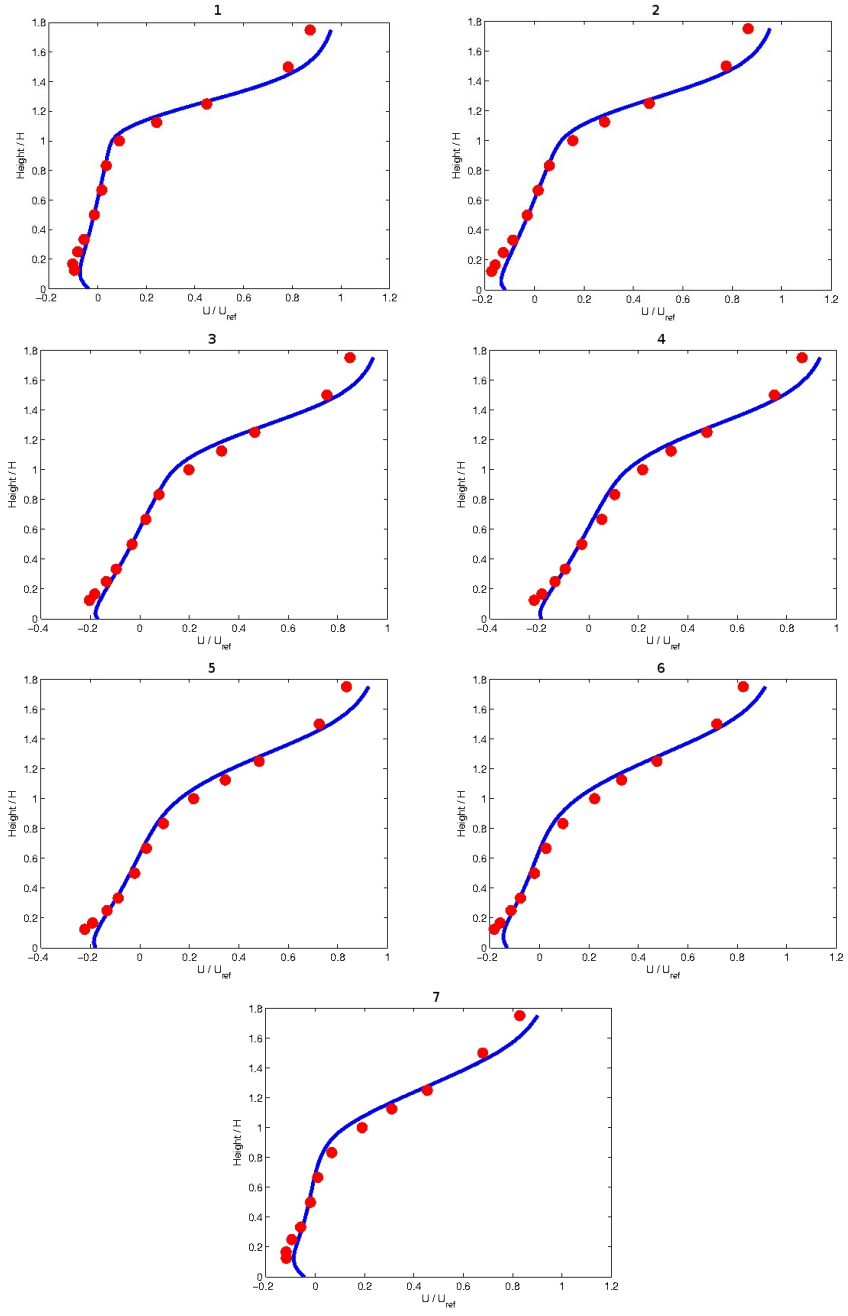

Figure 4.13: Vertical profiles of streamwise velocity component, u, taken at the locations shown in Figure 4.11. CFD results shown in blue, experimental data shown in red

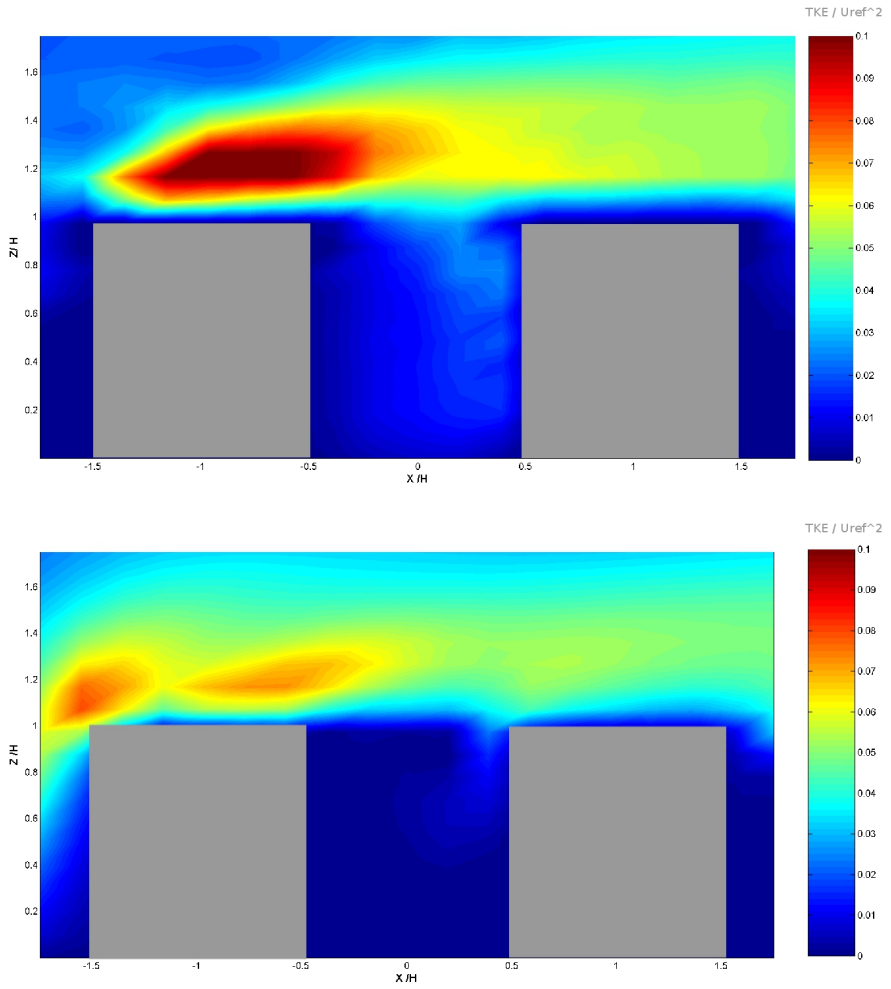

Figure 4.14: Contour plot of TKE above and within the street canyon, for the windtunnel results (top) and CFD results (bottom)

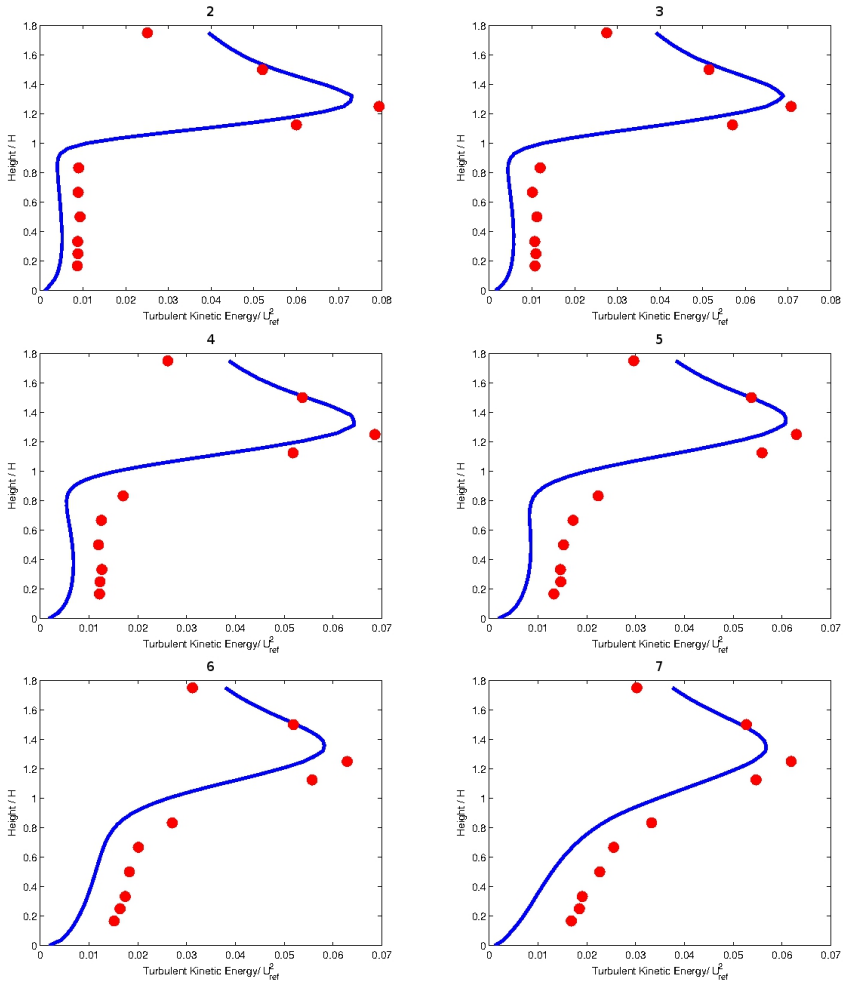

Figure 4.15: Vertical profiles of TKE, taken at the locations shown in figure 4.11

4.3 Summary of Main Findings

This chapter summarised the work carried out in a benchmark study undertaken in order to understand the capabilities and limitations of the Standard k-ε model and CFD in accurately modelling urban boundary layer flow and flow within a simplified street canyon.

It was shown that there are problems recreating urban boundary layer due to the decay in turbulence profiles as we move downstream of the inlet. It was found that this can be improved by:

- Selecting inlet profiles which are in agreement with the turbulence model
- Adjusting the k-ε model constants

Updated values for k-ε model constants were found through the statistical method of Bayesian Calibration. Bayesian Calibration was shown to be a promising method for investigating and reducing the amount of uncertainty contained within CFD model parameters. The updated k-ε model parameters helped to reduce the amount of decay in the turbulence profiles for the urban boundary layer flow.

Through the modelling of flow within a simplified street canyon and comparison with wind tunnel data it was found that:

- CFD and the k-ε model are able to provide a good qualitative prediction of the flow features within a regular street canyon
- Velocities within and above the street are well predicted
- Qualitative prediction of turbulence within and above the street were generally well predicted. With the main features of peak in TKE above the upwind roof, spread in TKE within the shear layer and higher TKE values on the downwind side of street all recreated within the CFD model
- Quantitative comparison of TKE values showed that the TKE levels were generally underpredicted within and above the street canyon due to the underprediction of TKE above the upwind roof

The updated k-ε model constants found for the urban boundary layer through Bayesian calibration were also implemented for street canyon flow. It was found that these values had a negative effect on the level of convergence obtained for the CFD simulation and did not offer improvements of TKE prediction within or above the street canyon. Therefore although Bayesian calibration can be a useful tool in assessing and reducing the amount of parametric uncertainty within a CFD model, the selection of model parameters for calibration should be done with care as complex dependencies between the parameters could result in instabilities within the model.

To improve turbulence predictions it would generally be recommended to test different turbulence models. This is out of the scope of the current research but is currently an active area of research and recommended as a way of expanding on the work carried out in this thesis.

Chapter 5

Field Measurements of Airflow within Street Canyons, both with and without Tree Planting

This chapter summarises the findings of a field measurement campaign of wind velocity measurements carried out in two streets in South London, one tree-lined and one non tree-lined. The aim of the field measurement campaign was to make an assessment as to the effect of tree planting on airflow patterns, wind speed and wind turbulence within street canyons.

The chapter starts with an overview of the methodology used to carry out the field measurement campaign, followed by a summary of the results of the field measurements taken in the non tree-lined street and how these compare with the results found in Chapter 4 as well as previous research. There will then be a discussion on the results taken from the tree-lined street and finally a comparison between the two sets of data.

5.1 Field Measurements Methodology

5.1.1 Choice of Field Measurement Site

The aim in selecting a site suitable for the field measurement campaign was to find two streets which would be subject to similar background wind conditions with the main influence on the local wind microclimate being the difference in tree planting. To accomplish this aim the following selection criteria was used:

- Two streets containing significantly different tree planting. One street containing large mature tree planting and one street with little to no tree planting.
- Neigbouring streets or two streets within close proximity to one another. The building morphology surrounding the measurement site will have a significant impact on the local wind environment. To ensure this is kept constant during all measurements, two streets within close proximity should be chosen. Neighbouring streets also allows for quick transfer of monitoring equipment between the two streets thus allowing measurements to be taken under similar wind conditions.
- Similar building geometry on both streets. The geometry of the buildings flanking the street canyon can have a significant impact on the local wind environment within the street. In particular the roof geometry and aspect ratio of the street have been shown to have a significant influence on the local wind climate and therefore these factors should be kept constant.
- Low traffic flow. Movement of vehicles within the street can create turbulence at low levels within the street canyon and influence the local wind microclimate therefore it is important to choose two streets in which traffic flow will not be high enough to have a significant influence on field measurement results.

Based on this selection criteria two streets in South-West London were chosen for use in the field measurement campaign. Drakefield Road contained only a few ornamental trees whereas Streathbourne Road contained large mature tree

planting with very little spacing between the tree canopies. These will be referred to as our tree-lined and non tree-lined streets respectively.

5.1.2 Description of Site

The immediate area surrounding the measurement site comprises mainly of low rise residential housing with some shops, schools and office buildings. To the South-East of the streets is Tooting Bec Common which is a large parkland area. Although the tree planting within the park does provide some shelter the park is relatively open leaving the streets of interest exposed to any South-Easterly winds. The topology of the land is fairly flat with some slightly hilly terrain. A satellite view of the field measurement site is given in Figure 5.1.

The field measurements were taken within two streets, Streathbourne Road and Drakefield Road, as well as a reference measurement taken above roof top level.

The streets are lined either side by continuous uniform houses with pitched roofs. Drakefield Road contains terraced housing while Streathbourne Road has small gaps (approximately 1m) every 4th building. The streets are approximately 500m long and have pavements and parking bays along both sides of the road. Choosing streets of this length allows the focus of the study to be on the flow effects occurring at the centre of the length street canyon without considering the flow at the end of the streets which is known to be complex [Dobre et al., 2005].

An important consideration when considering flow pattern formation in street canyons is the aspect ratio which is street width divided by the building height (H/W). The typical height of buildings on Streathbourne Road is 10.5m and the street width is 22.5m giving an aspect ratio of 0.47. The typical height of buildings on Drakefield Road is 9.5m and the width is 19.1m giving and aspect ratio of 0.5. The roof geometry of both streets is a pitched roof with large dormer windows. All houses have a small front garden approximately 3m in depth, usually bounded by a low wall or hedge. Photo's of each street can be found in Figure 5.2.

These two particular streets were chosen due to the difference in tree planting. Streathbourne Road contains large mature trees which dominated the street canyon space, while Drakefield road only has a few small ornamental trees which

could be considered to be on the same scale as the street furniture such as lamp-posts and signposts. This allows for the assessment of how wind conditions vary due to the difference in tree planting. The tree species planted in Streathbourne Road is the London Plain tree which is a deciduous tree species. This species is extremely common in London and many other big cities. The trees are planted along the pavement edge along both sides of the street with spacing between the tree trunks varying between 2.8m and 10.7m. Generally there is very little spacing between the tree canopies with the trees almost touching in most cases. The largest gap between canopies is 10m. Figure 5.3 shows a 3-D representation of the canopy size and position.

5.1.3 Meteorological Conditions

The dominant wind direction for London is West to South-Westerly. Since the orientation of the street axis is North-West to South-East we would expect to see a wind direction which is perpendicular to the street axis in most cases. This is known to be the worst case scenario for pollution dispersion and is therefore the most commonly studied case. Details of temperature humidity and a brief description of the weather was recorded for each of the measurement days.

5.1.4 Choice of Equipment

The equipment used to measure wind conditions within the street were Gill windsonic 2 axis ultra-sonic anemometer and 3 axis ultra-sonic anemometer. The sonic anemometer measures the time it takes an ultrasonic pulse of sound to travel from transducer A to transducer B. This is then compared against the time it takes a similar pulse to travel from B to A (see Figure 5.4). The magnitude and direction of the wind can be determined from the difference in the two times . The number and positioning of these transducers determines how many directional components of the wind can be captured. For example the 2 axis anemometer could capture the North-South and East-West directional wind components whereas the 3 axis anemometer could capture the North-South, East-West and vertical components of the wind.

Ultrasonic anemometers were chosen over other anemometers such as propeller or cup anemometers due to the fact that these anemometers do not require a start up speed and can therefore measure the low wind speeds commonly experienced in street canyons, they can give the directional components which some anemometers such as the cup anemometers can not and they can take measurements at a relatively high sampling frequency which is important when calculating turbulence statistics.

Wind velocities were measured along 3 axis, these were the direction aligned with the street length (u velocity), across the street (v velocity) and vertical direction (w velocity). The orientation of these axes is defined in Figure 5.3.

5.1.5 Weather Station

A weather station was set up on the roof of a nearby church to take reference measurements during the field measurement campaign. The church is located 1 mile South-West of the measurement site. The height of the church roof is 16m and the anemometer was placed on top of a 3m tripod (see Figure 5.5). Instantaneous wind speed, direction, temperature and humidity measurements were taken every minute. The anemometer used was a 2-D Gill sonic anemometer. The temperature and humidity were taken using a Hydroclip2. The weather station stayed on the roof for a period of 12 months and logged data continuously for the entire time. It was powered by a 12volt battery and solar panel. Measurements were sent remotely using a GPRS logger to a website which displayed the live data and also logged all data.

It is important to have a background reference measurement as the field measurements within the streets will be carried out over a number of different days and the varying wind conditions will need to be accounted for. The measurements from the weather station will be used to normalise the field data to allow for comparison of data taken on different days as well as comparison with results from CFD models.

5.1.6 Street Measurements Description of Method

Street measurements of wind velocities, temperature and humidity were carried out on a total of 24 days. Two types of measurements were taken: vertical profiles which consisted of measurements taken at several heights on either side of the street and horizontal profiles which consisted of measurements taken at the same height at various points along the length of the street.

5.1.6.1 Vertical Profiles

The locations of the vertical profile measurements are shown on the satellite map in Figure 5.1. To obtain measurements at different heights within the street a 6m mast was used. The amount of equipment available varied throughout the measurement campaign and therefore the number of heights at which measurements were taken and number of simultaneous measurements were varied accordingly. Table 1 in the appendix gives full details on heights at which measurements were taken for each day as well as which measurements were taken simultaneously. The table also specifies the number of masts used, in the case where two masts were used these were placed either side of the road in order to obtain simultaneous measurements for both sides of the street (see Figure 5.6).

The anemometers were attached to the mast using a metal rod and clamp. The distance between the mast and the anemometers was 30cm (see Figure 5.7). An extension was added to the top of the mast to obtain the top height of 7 m. The sampling frequency for all wind velocity measurements was 1Hz. Temperature and humidity readings were taken once per minute. These measurements were carried out on both sides of Streathbourne and Drakefield Road.

5.1.6.2 Horizontal Profiles

Four 2-d sonic anemometers were used to take measurements along the length of the street. Two anemometers were placed on each side of the street and arranged at right angles to one another as described above. The height of the tri-pods on which the anemometers were placed was 1.5m (see Figure 5.8 for details). Measurements were taken for a duration of 10 minutes at each location after which the two tri-pods were moved a set distance along the road to the next

location. The location of the measurements in relation to the tree canopies is given in Figure 5.9. The sampling frequency for all measurements was 1Hz.

5.1.7 Data Processing

5.1.7.1 Sampling Period

Due to the high cost of field equipment it is likely that in some cases more measurement locations are required than instrumentation available therefore staggered measurements will have to be carried out. In such cases we would ideally look to minimise the time between each set of measurements to avoid changing wind conditions. However a compromise must be reached between minimizing the time difference between each set of measurements and leaving the equipment in place long enough to acquire meaningful results.

In order to inform the decision on the sampling period to be used for the current set of measurements the cumulative mean was calculated for each measurement location over a number of different days and wind conditions. Analysis of the data showed that after a period 5 minutes, sampling at a rate of 1 Hz the mean wind speed becomes stable this can be seen in Figure 5.10.

In their research into flow at a complex intersection, Dobre et al. [2005], performed a time series analysis of their field data taken from a London street canyon. They found that the most energetic scales lay in the region 1-300s or 3.3 x 10^{-3} to 1 x 10^{-1} Hz. They concluded that an averaging period of 10 minutes would give a reasonable picture of the dynamics of the largest scales of the flow. They also found that 10 minute period corresponds to the time scales associated with the cross street recirculation vortices.

For these reasons, along with the fact that the 10 minutes averaging period has commonly been used in these types of studies in the past and therefore makes for easy comparison with other research, an averaging period of 10 minutes was chosen for each measurement location.

5.1.7.2 Averaging Technique

Measurements from the 2-D anemometer were output as a wind speed and direction. Output from the 3-D anemometer was given in the form of 3 separate wind

components. Since we are interested in the vector components the output from the 2-D anemometer was split into its 2 components using simple trigonometric techniques. Given a wind speed S and direction θ for N data samples the along street, u, and the across street component, v these were calculated as:

$$\bar{u} = \frac{1}{N}\Sigma S_i cos\theta_i \tag{5.1}$$

and

$$\bar{v} = \frac{1}{N}\Sigma S_i sin\theta_i \tag{5.2}$$

In the case where the 2-D anemomters were measuring the across street, v, and the vertical component these were found by:

$$\bar{v} = \frac{1}{N}\Sigma S_i sin\theta_i \tag{5.3}$$

and

$$\bar{w} = \frac{1}{N}\Sigma S_i cos\theta_i \tag{5.4}$$

The same process was used to calculate the average wind components for the reference wind velocity. In the case where and average wind speed or direction is needed rather than just the vector this was calculated as:

$$\bar{S} = \sqrt{\bar{u}^2 + \bar{v}^2 + \bar{w}^2} \tag{5.5}$$

$$\bar{\theta} = arctan\left(\frac{\bar{u}}{\bar{v}}\right) \tag{5.6}$$

This vector averaging process is used instead of simply taking the scalar average of S and θ as it has been reported that under light wind conditions (< 2 m/s) there can be noticeable differences between scalar averaged and vector average wind speed and direction Thuillier [1995]. Therfore a vector average was used throughout.

5.1.7.3 Calculating Turbulence Characteristics

The turbulence was characterised by the calculation of turbulence intensity and turbulence kinetic energy. The presence of turbulent eddies within a flow creates fluctuations within the velocity. This can be seen if we plot the velocity taken at a single point over a period time. It will be seen that the velocity fluctuates about mean. The velocity can be decomposed into its mean and fluctuating part

$$u(t) = \bar{u} + u'(t) \tag{5.7}$$

This is commonly referred to as the Reynolds Decomposition. To characterise the strength of the velocity fluctuations we can calculate the root mean square, or standard deviation, of the velocity.

$$u_{rms} = \sqrt{\frac{1}{N}\Sigma_{i=1}^{N}(u_i')^2} \tag{5.8}$$

The turbulence intensity is then commonly given as:

$$u_{TI} = u_{rms}/\bar{u} \tag{5.9}$$

The turbulence kinetic energy can be derived based on the values of the u_{rms}

$$TKE = \frac{1}{2}(u_{rms}^2 + v_{rms}^2 + w_{rms}^2) \tag{5.10}$$

Figure 5.1: Satelite view of the two streets in which field measurements were taken. Drakefield Road left, Streathbourne Road right. Red indicates location at which vertical profiles were taken.

Figure 5.2: Photos showing Drakefield Road (left) and Streathbourne Road (right)

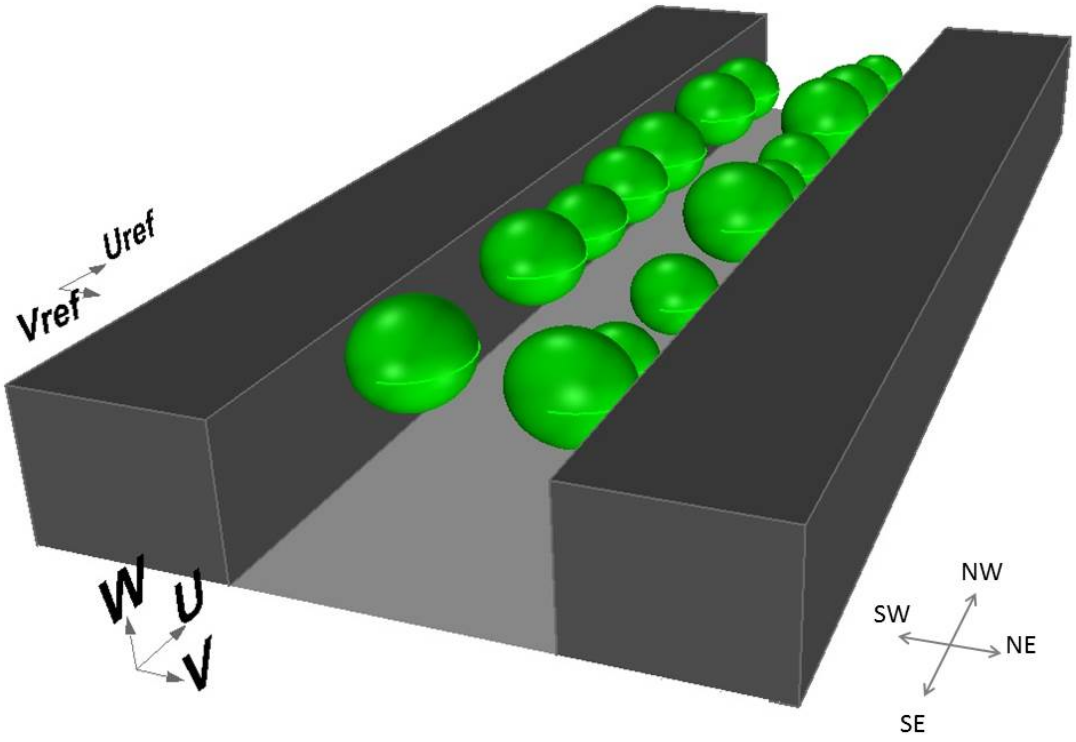

Figure 5.3: Three-Dimensional view of tree canopy locations within the street and measurement axis definition

Figure 5.4: Sonic 3-D anemometer used to carry out field measurements

Figure 5.5: Weather Station set up to obtain reference wind speed measurements

Figure 5.6: Masts and anemometers used to take vertical measurement profiles

Figure 5.7: 2-D anemometers attached in pairs

Figure 5.8: Anemometers used to take horizontal field measurements

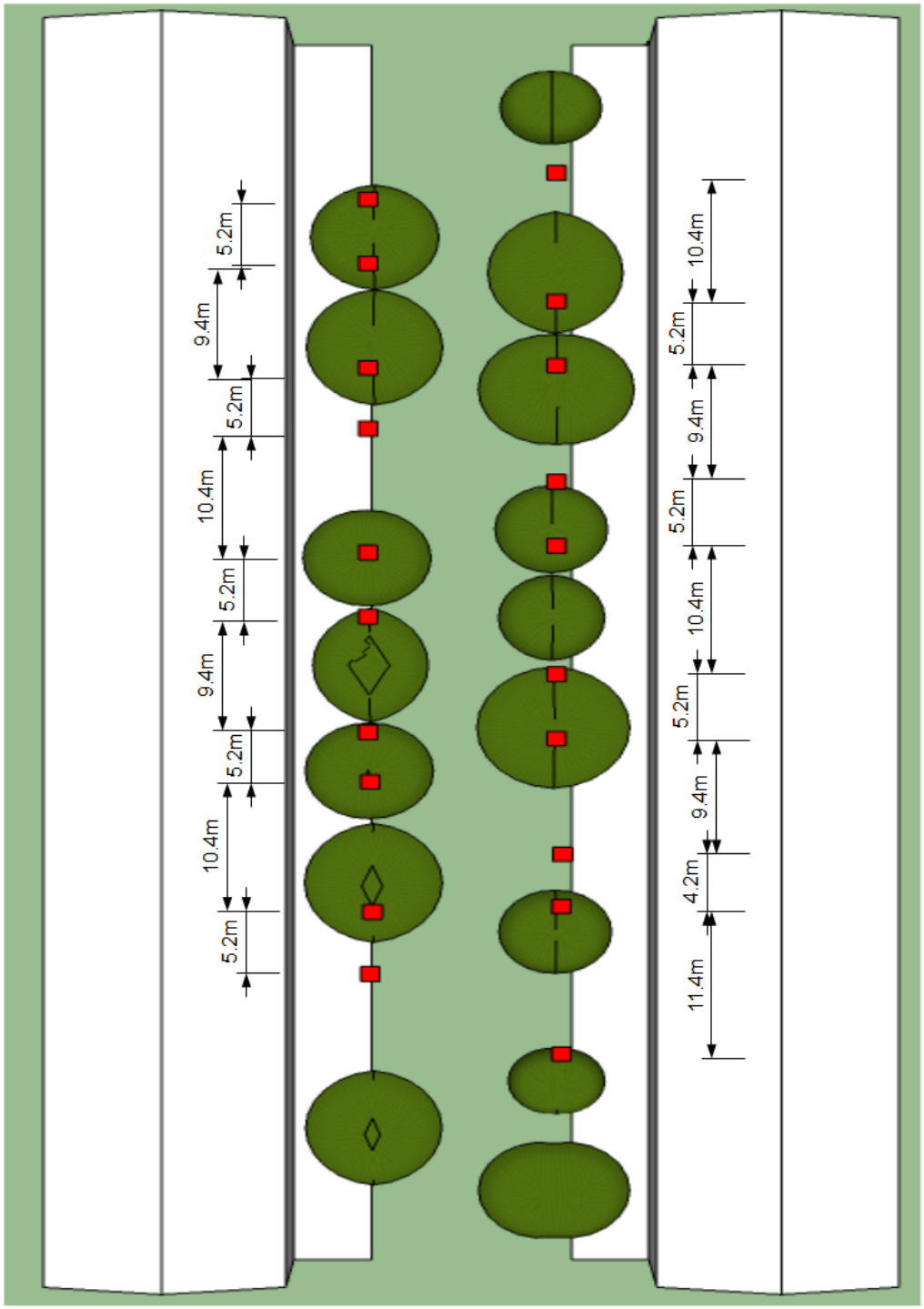

Figure 5.9: Locations along the street length at which measurements were taken

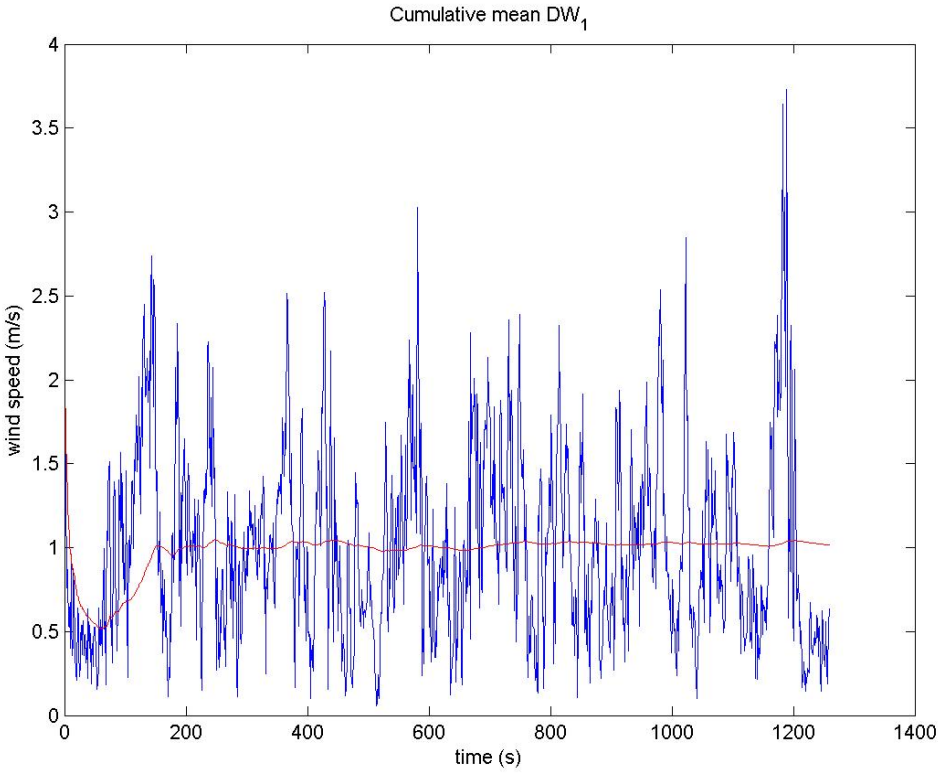

Figure 5.10: Cumulative mean of the wind velocity shown in red

5.2 Field Measurements of Air Flow within a Non Tree-Lined Street Canyon

Experimental and computational studies of street canyon flow often focus on very simplified versions of street canyons. In reality street canyons are far more complex, with detailed building geometry, street furniture and subject to highly variable wind conditions. It is therefore highly important to have field measurements which can give an indication as to whether the simple street canyons often studied in literature provide an accurate representation of reality. This section of the chapter will analyse the set of field measurements taken from what we will term non tree-lined street i.e. the street canyon which does not include mature tree planting. The aim of this analysis is to determine if the classical flow features presented in Chapter 4 and previous research are evident from the results of the field measurements.

5.2.1 Airflow Patterns

In order to gain an understanding of the flow patterns within the streets vector plots of the u, v and w velocity components of the wind data were analysed (see Figure 5.3 for orientation of u,v and w). Two types of vector plots are given, one which shows a vertical cross section of the street and one which shows a horizontal cross section. Figure 5.6 and Figure 5.9 gives an indication of the measurements locations within the street.

Two such vector plots are shown in Figures 5.11 and 5.12. The data for these plots was taken on the 6th September and 5th April respectively. The wind roses relating to the background wind conditions on both of these days can be seen in Figure 5.13. It can be seen that on the days when this data was collected the background wind direction was oblique to the street axis. The average wind speed for the 6th September was 6m/s and 4m/s for the 5th April.

Figure 5.11 shows the vector plot of a vertical cross-section of the street, produced for the data taken on the 6th September, the arrow at the top of the vector plot indicates the direction of the background wind. From the vector plot we can see that there is a negative w velocity, or downdraft, on the downwind

side of the street and a positive w velocity, updraft, on the upwind side of the street. Such features are indicative to the kind of recirculating vortex we saw in the wind tunnel street canyon in Chapter 4 and is common in literature.

Analysis of the across street velocity, v, shows a shift in direction at the uppermost heights on the downwind side of the street. It switches from being positive (in-line with the background wind direction) to negative (opposite to the background direction) and remains in this direction for all lower heights. This is again in support of the presence of a recirculating vortex within the street. The location of the switch in direction of the v velocity is an important feature as it gives an indication of where the centre of the vortex may occur. This always happens between the top two heights, which are 6 m and 7 m or z/H = 0.63 and z/H = 0.74.

In order to understand the 3-dimensional nature of the flow within the street a vector plot showing flow along a horizontal cross section taken at a height of 1.5 m is shown in Figure 5.12. Due to the fact that not all measurements are taken simultaneously the vector plots show both the in street velocity and the reference velocity taken for the same 10 minute period. The v velocity consistently shows the opposite direction to the reference v velocity which is in support of the findings from the vertical profiles. The u velocity within the street is in the same direction as the reference u velocity for the majority of cases.

Under oblique wind direction the vector plots produced would indicate that the flow within the street can be thought of as a composition of an across street recirculating vortex and an along street wind component. This can be thought of as a helical or cork-screw like flow pattern often discussed in literature.

5.2.1.1 Effect of Background Wind Direction on Flow Patterns

Based on previous findings within literature we know that the background wind direction has a dominant effect on the flow patterns within the street. We will therefore investigate how the flow patterns discussed above change with wind direction.

Figure 5.14 shows two vector plots taken on a vertical cross-section of the street. The top figure shows data taken on the 6th September and the bottom

figure shows data taken on the 29th July. The main difference between the two plots is the direction of the background wind direction. On the 6th September the wind direction is West South-Westerly on the 29th July the wind direction is East North-Easterly. This has the effect of changing the direction of the vortex from clockwise to anti-clockwise.

In order to understand how the along street velocity component, u, varies with wind direction, vector plots showing flow along a horizontal cross section are shown in Figure 5.15 for data taken on the 5th April, 2nd April and 30th June respectively. By plotting the data for these 3 different days we are able to see how the above street wind direction impacts the in-street wind direction. The v velocity consistently shows the opposite direction to the reference v velocity which is in support of the findings from the vertical cross-sections. The u velocity within the street is in the same direction as the reference u velocity for the majority of cases.

Measurements taken on the 5th April show a background wind direction that is almost perpendicular to the street length this is reflected in the in-street wind direction for which the majority of the measurement locations show a perpendicular direction. As we move on to measurements taken on the 2nd April and 30th June the u component of the background wind direction becomes more dominant and the wind direction becomes oblique to the street axis. It can be seen that this variation in wind direction above the street is reflected for the wind direction within the street. This suggests there is a strong relationship between the above roof top and in-street wind direction.

5.2.1.2 Effect of Stability of Background Wind Direction on Flow Patterns

The variability in wind direction throughout the day can have an impact on the flow patterns within the street. To assess this impact the 15 days worth of vertical measurements were split into two groups. Those days on which the wind conditions can be considered fairly stable and there is little variation in wind direction and days on which there are large variations in wind direction. In order to assess the extent of wind direction variability two methods were used

the first was to use the wind rose diagrams which were produced for each day of measurements (see Appendix .1). This allows us to see the percentage of time the wind is coming from a certain direction. The second is to calculate the standard deviation in wind direction. The greater the standard deviation the less stable the wind direction.

Table 5.1 shows typical wind statistics for each of the 15 days of measurements. The average wind direction is shown, this is taken to be the mode, or most common wind direction, rather than the mean as taking the mean can sometimes give a distorted view of the wind direction. Group 1 shows the days on which the background wind direction can be considered to be stable with little variation, this is categorised as a standard deviation of less than 100 or if at least 80% of the wind direction lies within a 90 degree quadrant. Group 2 can be thought of as the days on which there was high variability in the background wind direction, this is categorised as a standard deviation of grater than 100 or if less than 80% of the wind direction recordings lies within a 90 degree quadrant. These groups are shown in Table 5.1.

The vector plot shown in Figure 5.17 is taken from group 2 in which the background wind conditions are considered to be unstable. The vector plot produced in this case is very similar to Figure 5.16. Although the wind direction does vary throughout the day it does remain within the 90 degree sector of Southerly to Westerly wind direction. The wind direction is always either oblique or perpendicular to the street axis. It would seem that under such wind conditions it is still possible to see the formation of a stable vortex within the street.

Figure 5.18 shows the vector plot produced on a day in which the background wind direction was switching between South South-Easterly and North-Easterly. This represents a situation in which the flow is switching between an oblique and parallel direction to the street. It can be seen that the vector plot produced for such conditions is very different to the previous plots. The flow is highly chaotic and no clear pattern is present.

It is not always the case that highly variable wind direction inhibits the formation of a vortex within the street. Figure 5.19 shows data taken on a day in which the background wind direction is split between two quadrants similar to wind conditions on the 25th July (Figure 5.18) however it is still possible to

see the same features present in previous plots with positive w velocities on the upwind side of the street and negative on the downwind side of the street. It is possible that a vortex is still able to form within the street if the wind direction is stable only for a short period of time.

All 15 days of measurement can be seen in Apppendix .1 along with their respective wind roses. The majority of vector plots are very similar to those shown in Figures 5.11 to 5.17 with downdrafts on the downwind wall and updrafts on the upwind wall and across street flow direction opposite to that above the street. The exceptions are data taken on the 6th June and 25th and 26th of July which show highly chaotic flow patterns due to the variability in background wind direction.

5.2.2 Velocity Profiles

5.2.2.1 Vertical Profiles

Taking vertical profiles allows for the assessment of variation in velocity values with height within the street. Profiles are given for v and w velocities. The velocities have been normalised by the background v_{ref} velocity which is the velocity measurement taken at the weather station of wind component which is perpendicular to the street axis.

Analysis of the airflow patterns showed the impact of varying background wind direction could have on the results. In this section we will plot the vertical profiles for the groups shown in Table 5.1 to assess the effect varying wind conditions has on the velocity profiles within the street.

First we will assess profiles of the across street, v, velocity and vertical, w, velocity of data taken from group 1 (stable wind conditions). These profiles are shown in Figures 5.20 and 5.21. The figures show the mean value at each height along with box and whisker diagrams. The central line of the box indictes the median of the collected data, the ends of the box indicates the first and third quartiles while the ends of the whiskers show the maximum and minium data values collected. Plotting the data in this way allows for a clearer presentation of the results and for easy comparison with other data sets.

Vertical profiles of the v velocity within the street taken when wind conditions

were stable (see Figure 5.20) show a linear trend with height within the street. V velocities decrease with increasing height up to the point where they cross the zero mark after which they increase with increasing height. The point where they cross zero velocity is around z/H = 0.62 on the downwind side of the street and 0.67 on the upwind side of the street. Below a height of z/H = 0.3 on the upwind side of the street the linear relationship breaks down and there is a decrease in velocities within this region. This is likely due to the presence of street furniture which is interfering with flow at this level which will be discussed further in later sections. The presence of the street furniture is also likely to account for the greater variability in the the wind speed measurements at lower heights which can be seen by the larger whiskers at these heights.

Vertical w velocity profiles are shown in Figure 5.21 for days when the wind conditions are stable. Under these wind conditions we find positive values on the upwind side of the street and negative values on the downwind side of the street as would be expected if there is a rotational vortex within the street. The shape of the profile is curved with velocities increasing with increasing height up to a height of between z/h = 0.4 - 0.5 after which the velocities begin to decrease. On the whole velocities tend to be larger on the upwind side of the street particularly at the point where the peak w velocity occurs.

The velocity profiles taken on days when the wind conditions were not stable are shown in Figures 5.22 and 5.23. Only the individual profiles are plotted in this case due to the variability of data across the different days a mean profile would not be useful.

The v velocity profiles taken on the days on which wind conditions were variable are shown in Figure 5.22. It can be seen that the profiles are significantly different to those obtained when the wind direction was stable and show great variability with height.

The w velocity profiles taken on days when the wind conditions were unstable are shown in Figure 5.23. Again the profiles are significantly different to those taken on days when the wind conditions were stable. The profiles show a linear profile with height unlike the measurements take on stable days which show a curved profile with height. However they do show clear updrafts on the upwind wall and downdrafts on the downwind wall.

Overall the profiles shown for stable conditions support the presence of a rotational vortex within the street canyon. There is seen to be a linear relationship between the v velocities and height within the street as well as downdrafts on the downwind wall and updrafts on the upwind wall. The measurements taken on days on which the wind conditions are unstable were significantly different to those taken on stable days and generally do not show evidence of a rotational vortex being present.

5.2.2.2 Horizontal Measurements

As well as taking measurements at various heights within the street, measurements were also taken along the length of the street. These measurements will be used to analyse how background wind conditions effect the velocities within the street canyon.

The vector plots presented in the previous section suggest that the flow within the street canyon can be thought of the superposition of an across street rotational vortex and an along street channeling of the wind. The strength and direction of the rotational vortex appears to be controlled by v_{ref}, this is the velocity component of the background wind which is perpendicular to the street length and the magnitude of the along street velocity component would appear to be controlled by u_{ref} this is the velocity component of the background wind which is parallel to the street axis. To further test this hypothesis all three wind components u, v and w from measurements taken at head height were plotted against both the parallel, u_{ref} and perpendicular v_{ref} wind velocities taken from the weather station for the corresponding time period.

Figure 5.24 shows all 3 in street wind components plotted against u_{ref}. The u velocity within the street shows a linear correlation ($r = 0.7$) with u_{ref}. There is no clear correlation between u_{ref} and the vertical, w, component and the across street, v, component.

Plotting the data against v_{ref} (see Figure 5.25) we see no correlation with the in street u velocity. There is a linear correlation with the v and w components ($r = 0.56$ and 0.47 respectively) although not as strong as u_{ref} vs. u correlation.

Overall the data supports the hypothesis that the flow within the street can

be decomposed into the wind flow channeled along the length of the street, which is driven by the background wind which is parallel to the length of the street and an across street rotational vortex rotational vortex driven by the perpendicular background wind component. This allows us to compare data taken on different days under different wind directions by splitting the wind within the street into its directional components of u, v and w and normalising by the relevant background wind component.

5.2.3 Turbulence Statistics

The turbulence intensity is a measure of the velocity fluctuation calculated for each directional component. This is given as the standard deviation of the velocity fluctuations normalised by the mean wind speed. Different methods for normalising of the standard deviation have been used in the past for street canyon studies. Some prefer to normalise by the local mean wind speed taken at the anemometer for which the standard deviation is being calculated others use a reference mean wind speed taken above roof top level. Here I will be normalising by the wind velocity taken above roof top level, as this is seen to be the more appropriate method when comparing data taken at different locations within the street and different data sets such as CFD or experimental.

Figures 5.26 and 5.27 show profiles for the turbulence intensities within the street. The profiles show highest values are given at the greatest heights on the downwind side of the canyon these values decrease as we move down inside the canyon. The turbulence intensities are smaller on the upwind side of the street compared with the downwind. This is likely to be due to the loss in momentum as turbulence is advected down from the shear layer above the roofs and across the street.

To test the level of isotropy or anisotropy of the turbulence within the street the contribution each turbulence component makes to the overall TKE budget is calculated. Since $TKE = 1/2(\sigma_u^2 + \sigma_v^2 + \sigma_w^2)$ we calculate $\sigma_i^2/2 * TKE$ for i = u, v and w. If the turbulence is isotropic then we would expect this value to equal 1/3 for all σ_u, σ_v and σ_w. These calculations were made for both vertical and horizontal measurements and can be seen in Figures 5.28. Results show that generally turbulence within the street is anisotropic with σ_u making up the largest part of the TKE budget.

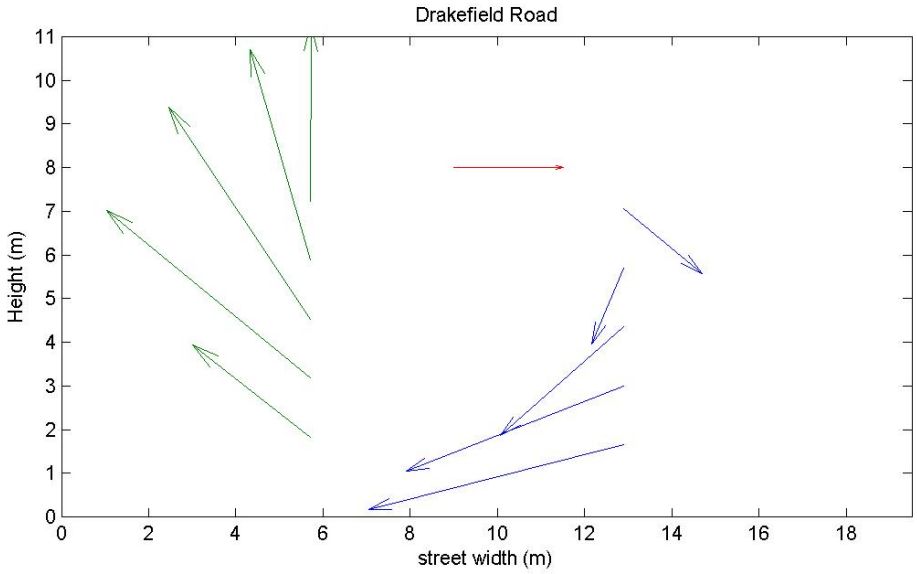

Figure 5.11: Vector plot for 6th September for non tree-lined street. Red arrow gives the background wind direction and velocity of 1m/s for scale

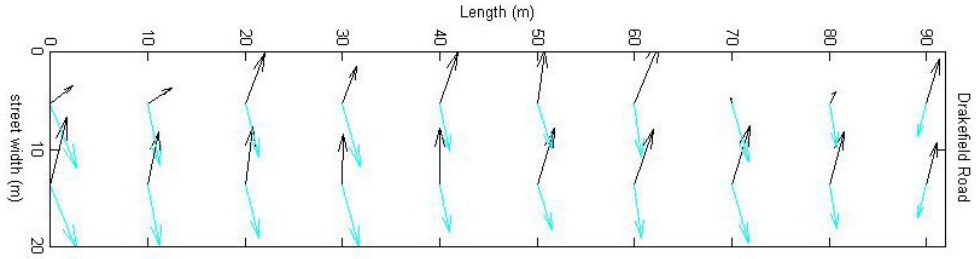

Figure 5.12: Horizontal vector plot for 5th April for non tree-lined street. Black arrows show in-street velocities, blue arrows show background wind velocities

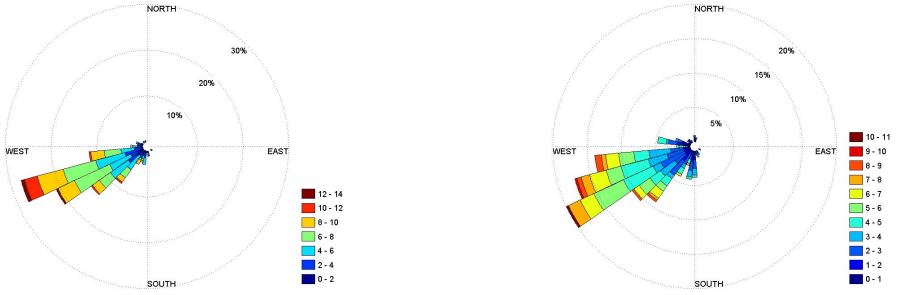

Figure 5.13: Windrose showing background wind conditions for 6th September (left) and 5th April (right)

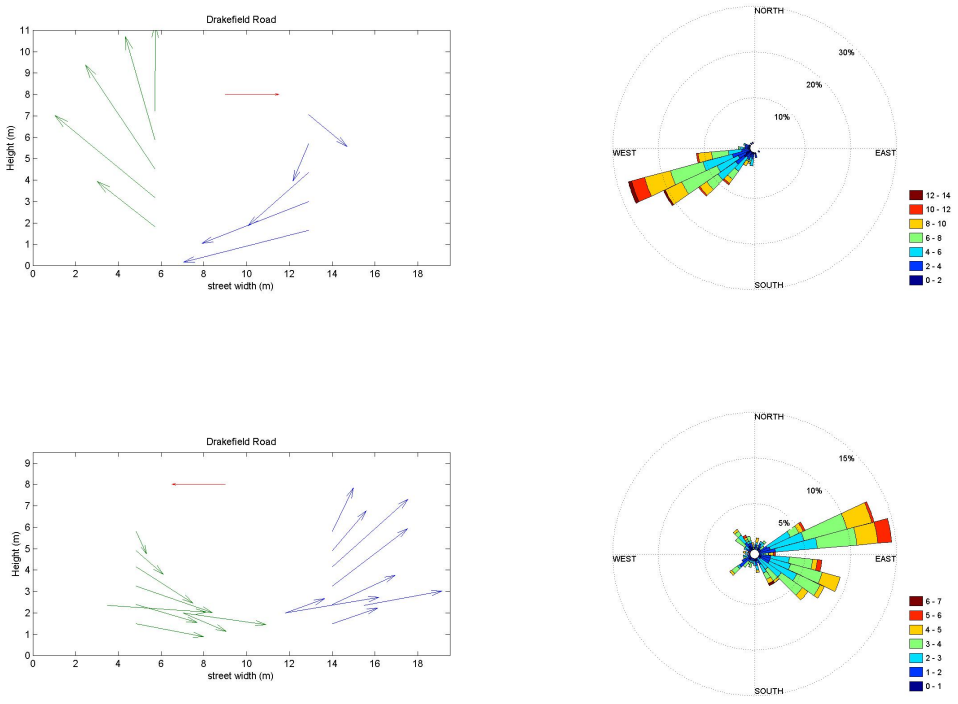

Figure 5.14: Vector plot and windrose showing background wind conditions for 6th September and 29th July for the non tree-lined street

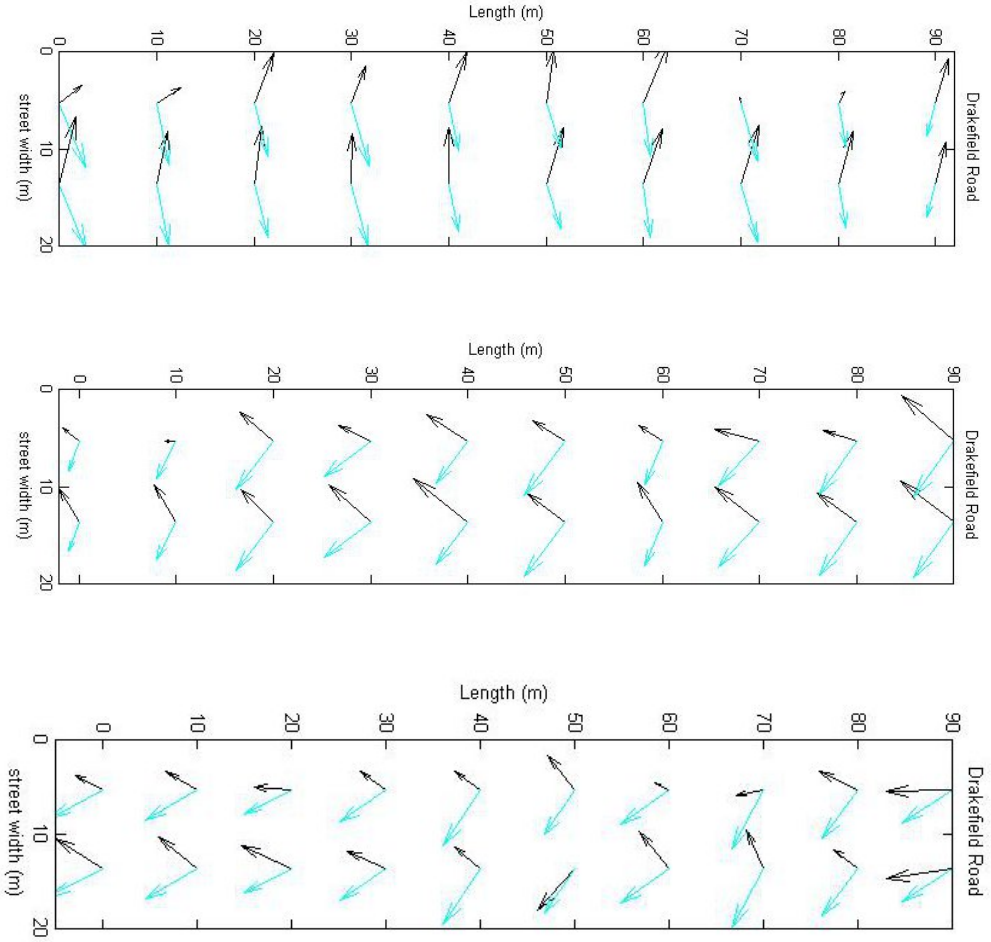

Figure 5.15: Horizontal vector plot for 5th April (top), 2nd April (middle) and 30th June (bottom) for non tree-lined street. Black arrows show in-street velocities, blue arrows show background wind velocities

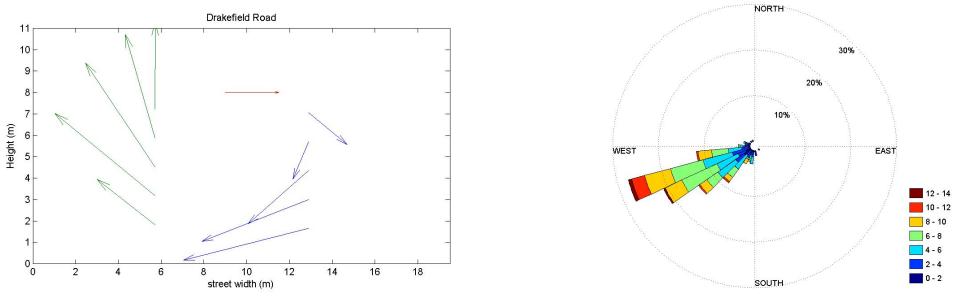

Figure 5.16: Vector plot and windrose showing background wind conditions for 6th September for the non tree-lined street

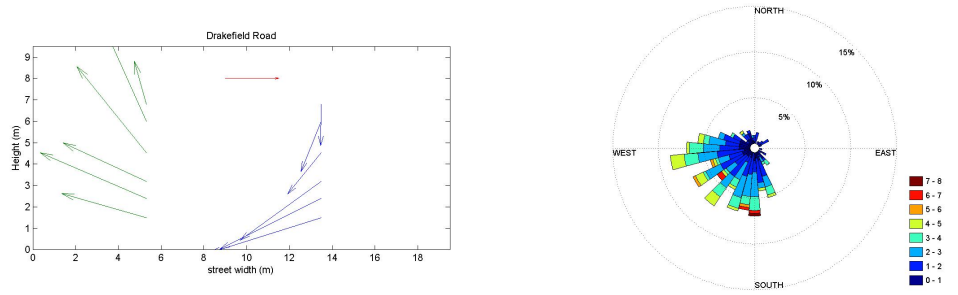

Figure 5.17: Vector plot and windrose showing background wind conditions for 10th June for the non tree-lined street

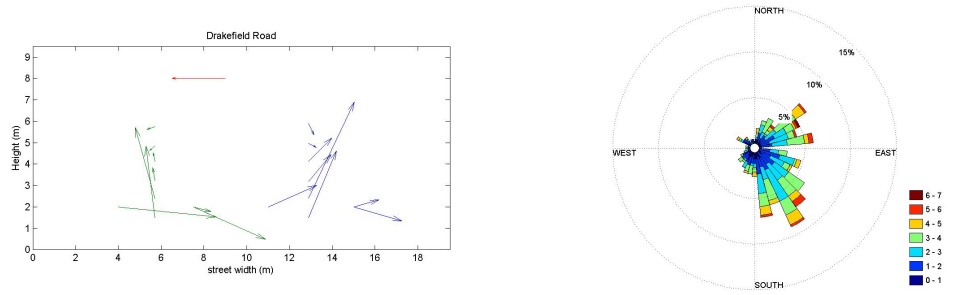

Figure 5.18: Vector plot and windrose showing background wind conditions for 25th July for the non tree-lined street

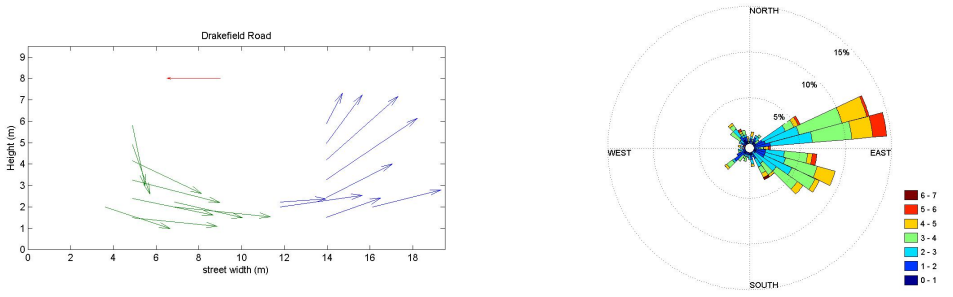

Figure 5.19: Vector plot and windrose showing background wind conditions for 27th July for the non tree-lined street

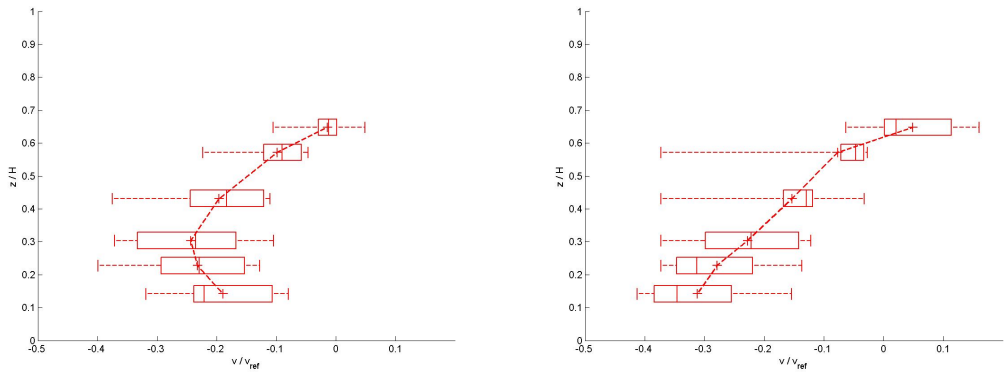

Figure 5.20: Vertical profiles of v velocity component for upwind (left) and downwind (right) side of the non tree-lined street with box and whisker plots showing first and third quartiles and maximum and minimum data points

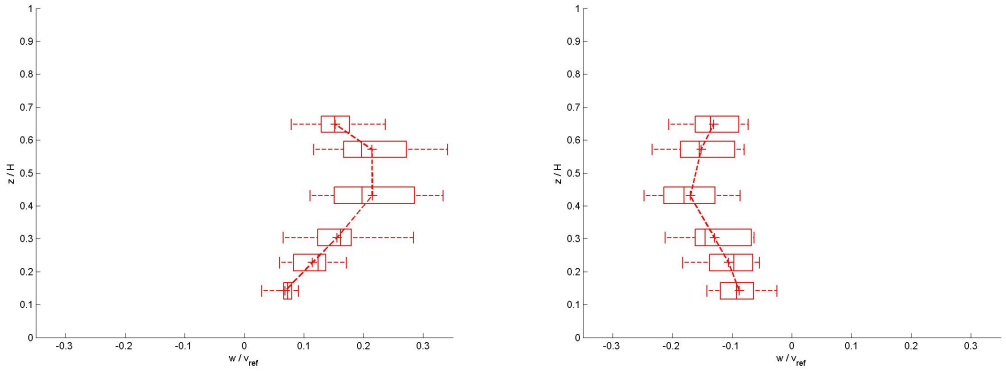

Figure 5.21: Vertical profiles of w velocity component for upwind (left) and downwind (right) side of the non tree-lined street with box and whisker plots showing first and third quartiles and maximum and minimum data points

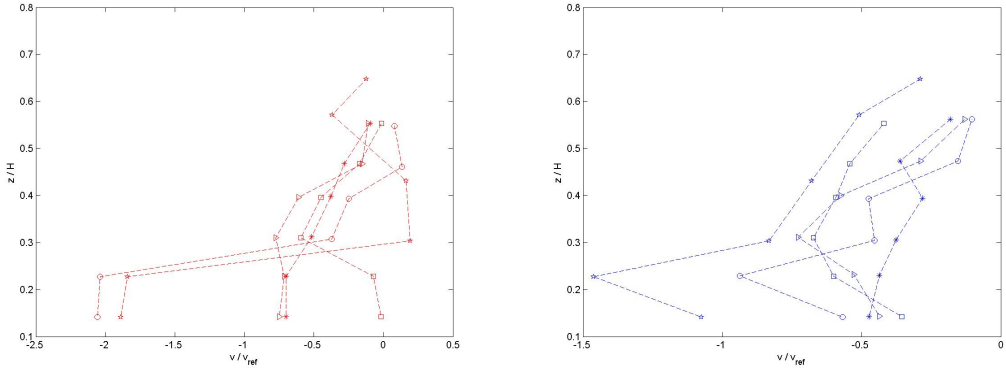

Figure 5.22: Vertical profiles of v velocity component for upwind (left) and downwind (right) side of the non tree-lined street with box and whisker plots showing first and third quartiles and maximum and minimum data points

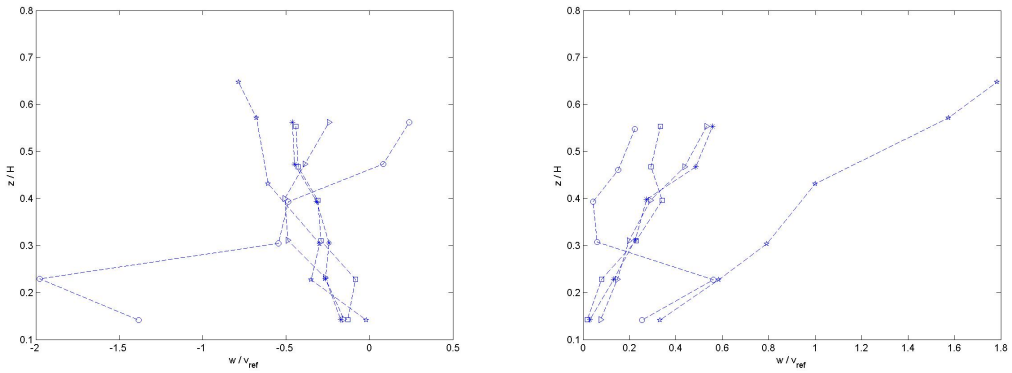

Figure 5.23: Vertical profiles of w velocity component for upwind (left) and downwind (right) side of the non tree-lined street with box and whisker plots showing first and third quartiles and maximum and minimum data points

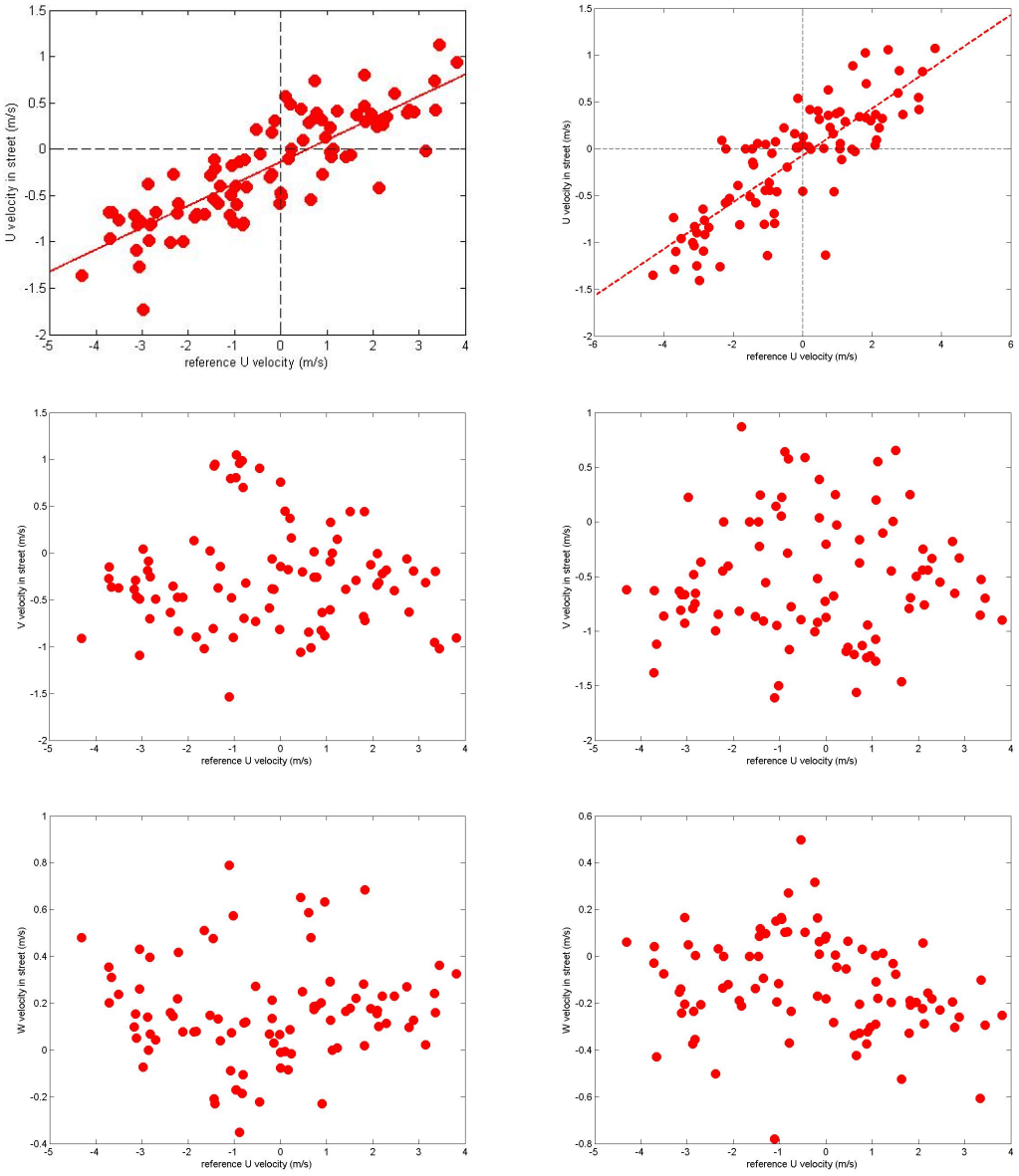

Figure 5.24: Comparison between reference u velocity and in-street u, v and w velocities, for Upwind (left) and Downwind (right) side of the non tree-lined street

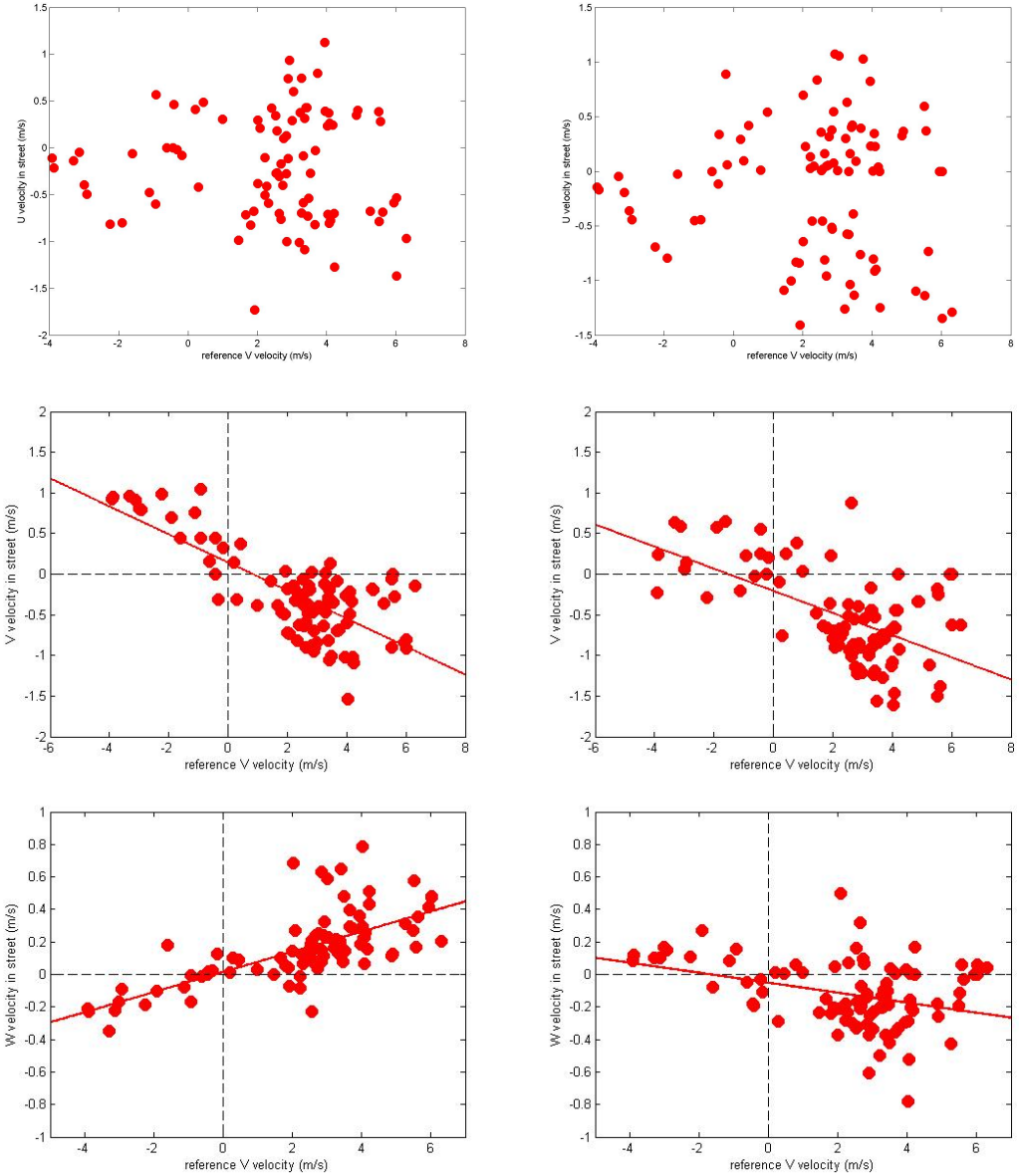

Figure 5.25: Comparison between reference v velocity and in-street u, v and w velocities, for Upwind (left) and Downwind (right) side of non tree-lined street

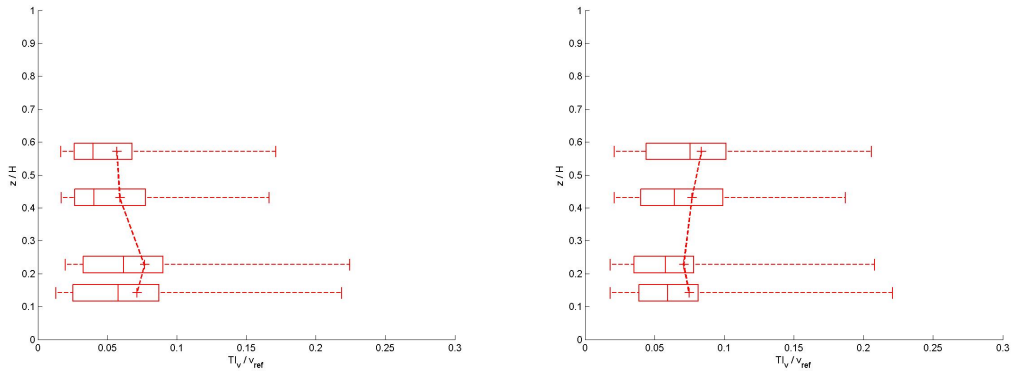

Figure 5.26: Mean normalised v component turbulence intensity profile for non tree-lined street with box and whisker plots showing first and third quartiles and maximum and minimum data points. Left figure shows profiles for upwind side of the street, right figure shows profiles for downwind side.

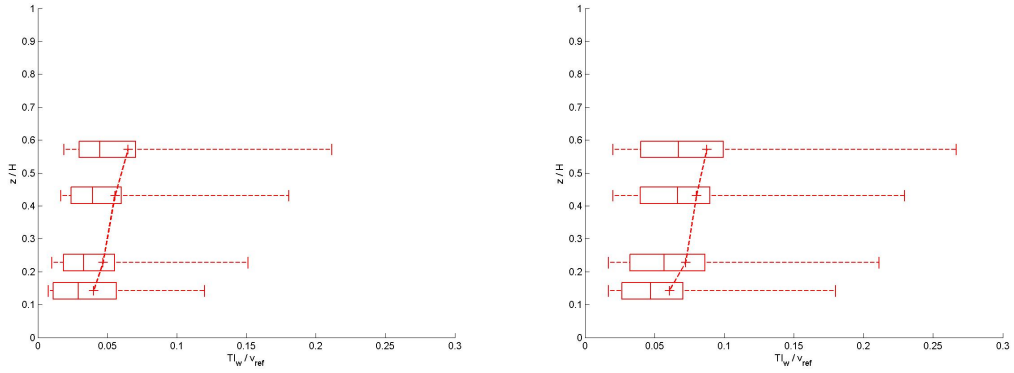

Figure 5.27: Mean normalised w component turbulence intensity profile for non tree-lined street with box and whisker plots showing first and third quartiles and maximum and minimum data points. Left figure shows profiles for upwind side of the street, right figure shows profiles for downwind side.

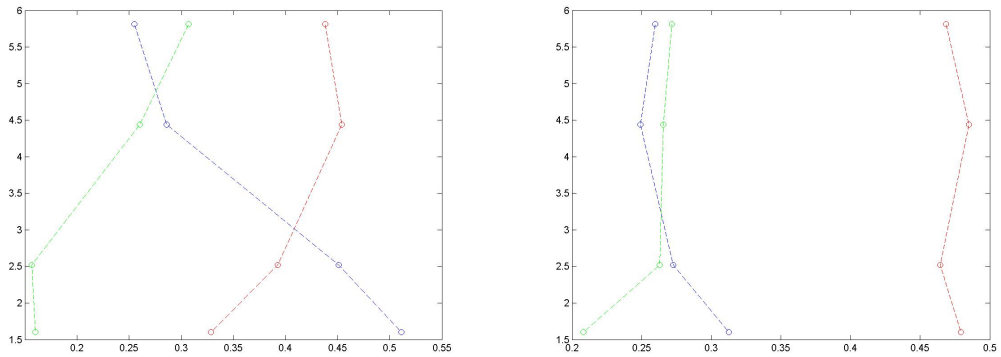

Figure 5.28: Fraction that each turbulence intensity contributes to overall TKE value. u TI - Red, v TI - Blue and w TI - Green. Left hand figure shows upwind side of street, right hand figure shows downwind

Date	**Average Wind Speed**	**Average Wind Direction**	**Standard Deviation Wind Direction**	**Group** [1]
07/06/2011	4.3	195	33	Group1
08/06/2011	5.0	194	28	Group 1
09/06/2011	3.4	263	31	Group 1
10/06/2011	2.1	218	60	Group 1
02/09/2011	2.5	196	39	Group 1
05/09/2011	5.1	226	31	Group 1
06/09/2011	5.9	201	23	Group 1
07/09/2011	4.7	242	25	Group 1
08/09/2011	2.9	237	30	Group 1
29/07/2011	2.5	31	92	Group 1
06/06/2011	1.7	25	130	Group 2
25/07/2011	2.5	40	123	Group 2
26/07/2011	2.3	16	136	Group 2
27/07/2011	2.9	9	139	Group 2
28/07/2011	2.2	23	135	Group 2

Table 5.1: Wind statistics for vertical measurement days

[1]Criteria for Group 1: standard deviation of less than 100 or at least 80% of the wind direction lies within a 90 degree quadrant. Criteria for Group 2: standard deviation of more than 100 or less than 80% of the wind direction lies within a 90 degree quadrant

5.2.4 Comparison with Wind Tunnel Results

The wind tunnel results shown in Chapter 4 are typical of the flow features found in an idealised street canyon often studied in literature. We are not able to make a direct quantitative comparison between the wind tunnel results and field measurement results as the geometry of the two streets is different and the height at which the reference wind velocity used to normalise the data is also different. However it is still useful to compare the two sets of results to see if any of the classic flow features often discussed in literature can be detected in the field measurements.

Figure 5.29 shows a comparison of the vector plot produced by wind tunnel data and field measurements. In both cases on the downwind side of the street the flow is directed downwards into the street and then across the street canyon floor to the upwind side of the street. On the upwind side of the street the flow is directed upwards towards roof level. In both cases the magnitude of the vectors is greatest at lower levels within the street and decreases towards the centre height of the canyon.

The main difference between the two sets of data is the magnitude of the vectors. The magnitude of the field measurement is larger than that of the wind tunnel. This will largely be due to the fact the wind tunnel data was normalised by the wind speed at boundary layer height whereas the field measurement data was normalised by the wind speed taken at a height of 19m which is well below boundary layer height and therefore a much lower velocity.

Comparison of the across street velocity, v, profiles is shown in Figure 5.30. By comparing the field data with the data taken from the wind tunnel experiment we can see that on the upwind side there is no change in the velocity profile at lower heights as measurements were taken in an empty street canyon. Comparing the field measurement profiles with the wind tunnel data taken on the downwind side of the street we can see a similar linear profile. The gradient of this profile is slightly steeper for the wind tunnel data. One possible explanation for this is the differences in aspect ratio of wind tunnel and field measurement streets.

The point at which the two profiles cross the zero mark is relatively similar in both field measurements and wind tunnel. In both cases this point is above the

height of z/h = 0.5. In the case of the wind tunnel this is due to the fact that an isolated street canyon was tested, multiple street canyons leads to a stabilized flow and the centre of the vortex lies at the centre of the street canyon. In the case of the field measurements there are multiple streets present however there are large spacing between the streets due to the large garden sizes. The aspect ratio of the street will also effect where the centre of the vortex lies.

Figure 5.31 shows the profile for the vertical velocity, w for both wind tunnel and field measurement data. Comparison of the data shows some similarities in the shape of the profile although the field measurement profiles are much more curved than those produced by the wind tunnel. The wind tunnel data shows increasing w velocities with increasing height whereas the field measurements show increasing velocities up to a height of between z/H = 0.4 - 0.5 at which point the velocities decrease with height. Both sets of data show a decrease in velocities on the downwind compared with the upwind side of the street.

The TKE values for the wind tunnel data taken on the downwind side of the street show a linear profile in which the TKE levels increase with height. A similar profile is shown for the field measurement data. This increase in turbulence at greater heights within the street on the downwind side can be explained by the results shown in Chapter 4. Figure 4.14 shows the TKE contour produced by both the CFD and wind tunnel results. TKE is produced in the shear layer above the building roof tops this is then advected downwards into the canyon by downdrafts on the downwind wall and across to the upwind side of the street by the recirculating flow. As the TKE is advected into the canyon momentum is lost and therefore TKE levels decrease we move down inside the street. This results in highest TKE levels at the greatest heights on the downwind side of the street. These levels decrease as we move lower into the canyon. On the upwind side of the street TKE values remain fairly low and are shown to be uniform with height. This process explains the TKE profiles obtained from the field measurement data, this also supports the idea of a recirculating vortex being present within the field measurement streets.

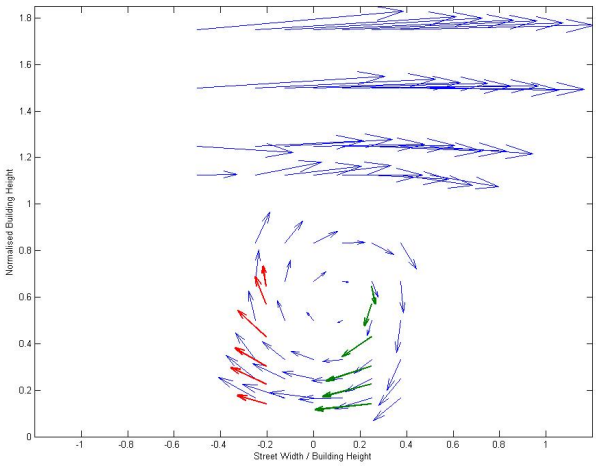

Figure 5.29: Comparison between vector plot for wind tunnel data and field measurements taken on 6th September. Field measurement shown in red and green and wind tunnel results shown in blue

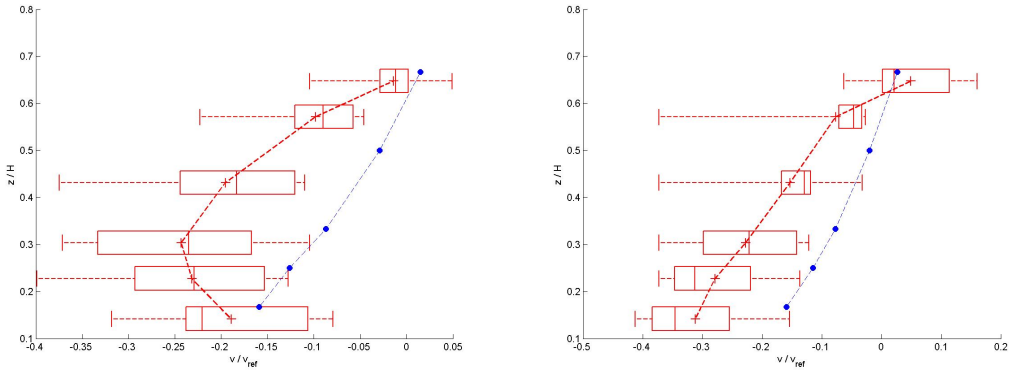

Figure 5.30: Comparison between v velocity profiles for wind tunnel and averaged field data taken on upwind (left) and downwind (right) side of the tree-lined street. Field measurements shown in red and wind tunnel results shown in blue

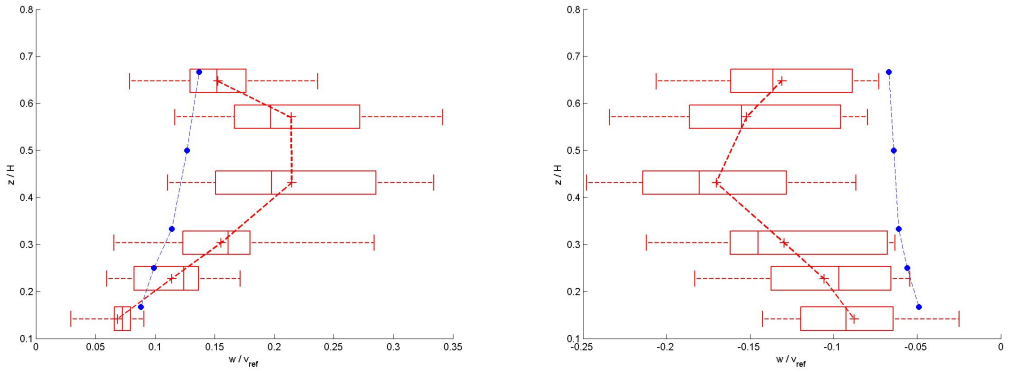

Figure 5.31: Comparison between w velocity profiles for wind tunnel and averaged field data taken on upwind (left) and downwind (right) side of the tree-lined street

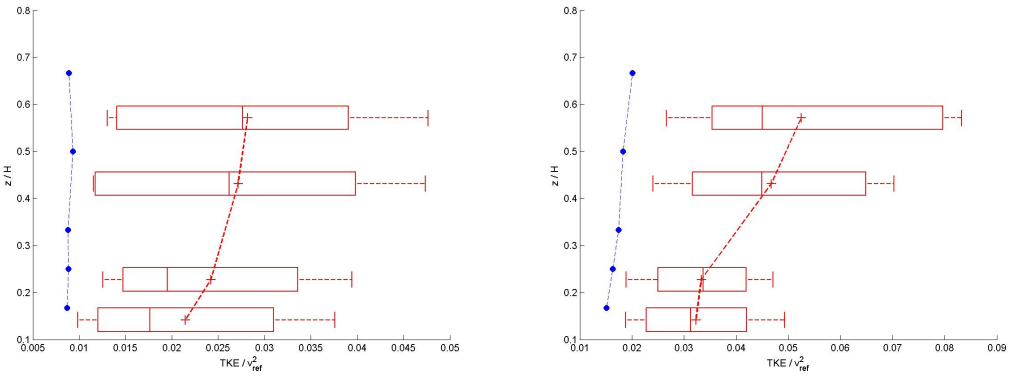

Figure 5.32: Comparison between TKE profiles for wind tunnel and field data taken on upwind (left) and downwind (right) side of the tree-lined street

5.3 Field Measurements of Airflow in a Tree-Lined Street

In the previous section of this chapter we have discussed field measurement results taken from a non tree-lined street and how these compare with results for simple idealised street canyons. In this section of the chapter we will discuss the results of the field measurements taken from the tree-lined street.

5.3.1 Airflow Patterns

In order to gain an understanding of the type of flow patterns occurring within the street, field data is plotted in the form of vector plots. Two types of vector plots are presented: those taken from measurements at different heights within the street, these are referred to as vertical cross sections and those taken at the same height but different locations along the length of the street, these are referred to as horizontal cross sections.

Figure 5.33 shows the vector plot of field data taken on the 6th September. Key flow features identified in our non tree-lined street are also present in the tree-lined street. The across street wind component, v, acts in the opposite direction to the background v wind component, v_{ref}, with the exception of the upper most height on the downwind side of the street. On the upwind side of the street there is found to be a consistent updraft at all heights, i.e. a positive w velocity.

There are also some differences between the two sets of data. In the presence of a rotational vortex we would generally expect to see downdrafts on the downwind side of the street (negative w velocities) however the results taken for the tree-lined street show a variation of positive and negative w velocities with typical vertical velocities remaining low.

Therefore although the flow patterns share many similarities of those of a rotational vortex, it is not clear how intermittent the formation of any such vortices would be and the level of disruption caused to typical street canyon flow patterns by the introduction of the tree canopies. To truly understand the flow conditions within the street a much greater number of measurements would be required over a longer time period.

A vector plot of a horizontal cross section of the street taken at a height of 1.5m is shown in Figure 5.34 along with the background wind direction given in blue. At this height all across street, v, velocities are in the opposite direction to the background v velocity with the exception of one location on the upwind side of the street. The direction of the along street, u, component generally matches the background u velocity. The flow pattern remains fairly uniform across the length of the street with the exception of two locations on the upwind side of the street.

5.3.1.1 Effect of Background Wind Direction on Airflow Patterns

Figure 5.35 shows the vector plot for a vertical cross section of the street for data taken on the 29th July. The background wind direction on this day was North-Easterly. Comparing with the vector plots taken on the 6th September, for which the wind direction was South-Westerly, we can clearly see the impact the changing wind direction has had on the in street flow patterns. The v velocities on the upwind side of the street are in the opposite direction to the reference v velocity. The v velocities on the downwind side of the street do not show any clear relation with the background wind direction as the v direction varies with height. The wind flow on this side is dominated by the w velocity component.

Figures 5.36 show vector plots for horizontal cross sections of the street taken for days on which the wind direction was at three different oblique angles to the street length. Unlike the previous vector plots on a vertical cross section, these vector plots show a clear relation between the background wind direction and in street wind velocity. The direction of the in street u velocity is the same as the reference u velocity. The direction of the in street v velocity is opposite to the reference v velocity in most cases. The wind direction within the street follows the reference wind direction, as the wind direction above the street becomes more parallel to the street so does the wind direction within the street.

5.3.1.2 Effect of Stability of Background Wind Direction

The impact stability of wind direction can have on flow patterns within streets was shown in section 5.2. To investigate the effect wind direction stability has

on flow within the tree lined street data is plotted for two days on which the wind direction was unstable. These are shown in Figures 5.37 and 5.38 It can be seen that the flow patterns on these days are highly chaotic with no clear relation with the reference wind direction and there is no evidence of the formation of a rotational vortex within the street.

5.3.2 Velocity Profiles

5.3.2.1 Vertical Profiles

Taking vertical profile measurements allows for the assessment of velocity variation with height within the street. Profiles are given for the normalised across street wind velocity (v velocity) and the vertical wind velocity (w velocity). The v and w velocities are normalised by the component of the background wind which is perpendicular to the street length (v_{ref}). The data presented in this section is taken on days when the background wind conditions are stable and foliage is present on the trees (spring and summer months). The days used for analysis are shown in Table 5.1 labeled group 1. Data is presented as the mean value of all the measurement days along with box and whisker plots showing the maximum and minimum normalised velocity recorded at each height.

Figure 5.39 shows the v velocity profile on the downwind and upwind side of the tree-lined street. On the downwind side of the street the highest velocities are experienced at the lowest heights and then decrease with increasing height towards the point where they reach zero velocity. This type of profile is typical for a street canyon subject to perpendicular or oblique wind conditions containing a rotational vortex. On the upwind side of the street the velocities remain fairly similar at the lowest three heights, the velocity increases slightly at the fourth height and then decreases to zero above this height. The velocities are lower on the upwind side compared with the downwind side, due to the loss in momentum as the flow crosses the street. Overall the velocities remain fairly similar and close to zero. The spread in velocity data is larger at the lower heights and becomes narrower at greater heights.

Figure 5.40 shows the normalised w velocity profiles for the upwind and downwind side of the street. For the w velocity profile taken on the downwind side of

the street the maximum velocities occur at z/H = 0.3 and z/H = 0.65 but overall the velocities are all of similar order of magnitude and tend to stay close to zero. The average values are either negative or zero, however the spread in the data shows that positive values are recorded on certain days. This is contrary to what we would expect if there is a rotational vortex within the street, for which we would expect to see downdrafts on the downwind wall.

On the upwind side of the street the maximum velocities between z/H = 0.4 and z/H = 0.6, although again all velocities remain fairly similar, staying close to zero. All mean values are positive and the spread in data does not cross over into the negative values at any point, therefore updrafts are always experienced on the upwind side of the wall.

5.3.2.2 Horizontal Measurements

In the previous section 5.2 we discussed the effect of background wind direction on flow patterns within non tree-lined streets. Under oblique wind direction it is believed that a helical or corkscrew type flow patterns develop within the canyon. This can be thought of as the superposition of along street channeling and across street rotational vortex.

Field measurements taken from the non tree-lined street supported the hypothesis that the along street channeling is controlled by the background wind component which is parallel to the street and the across street rotational vortex is controlled by the background wind component which is perpendicular to the street. To test whether this relation still holds for tree-lined streets, measurements taken along the length of the street at head height are plotted against the background wind velocity. Figure 5.41 shows the u velocity component within the street plotted against the background u component (u_{ref}), Figure 5.42 shows the v velocity component against background v component (v_{ref}) and Figure 5.43 shows the w velocity component against v_{ref}, the line of best fit is included in all figures.

Results show a clear linear relationship between the along street component u against the background u_{ref} wind component. Similarly there is a linear relationship between in street v and w components and the background v_{ref} wind

component. This supports the hypothesis that flow within the street canyon can be decomposed into two parts; along street channeling which is driven by the background wind parallel to the street and across canyon rotational vortex which is driven by the background wind component which is perpendicular to the street.

5.3.3 Turbulence Statistics

Figures 5.44 and 5.45 show profiles for the turbulence intensities within the street. We can see that there is little variation in turbulence with height within the street. Turbulence levels are lower on the upwind side of the street compared with the downwind side. This was discussed in section 5.2 and is likely to be due to the loss in momentum as turbulence is advected down from the shear layer above the roofs and across the street.

To test the level of isotropy or anisotropy of the turbulence within the street the contribution each turbulence component makes to the overall TKE budget is calculated. Since $TKE = 1/2(\sigma_u^2 + \sigma_v^2 + \sigma_w^2)$ we calculate $\sigma_i^2/2 * TKE$ for i = u, v and w. If the turbulence is isotropic then we would expect this value to equal 1/3 for all σ_u, σ_v and σ_w. These calculations were made for both vertical and horizontal measurements and can be seen in Figures 5.46. Results show that generally turbulence within the street is anisotropic with σ_u making up the largest part of the TKE budget.

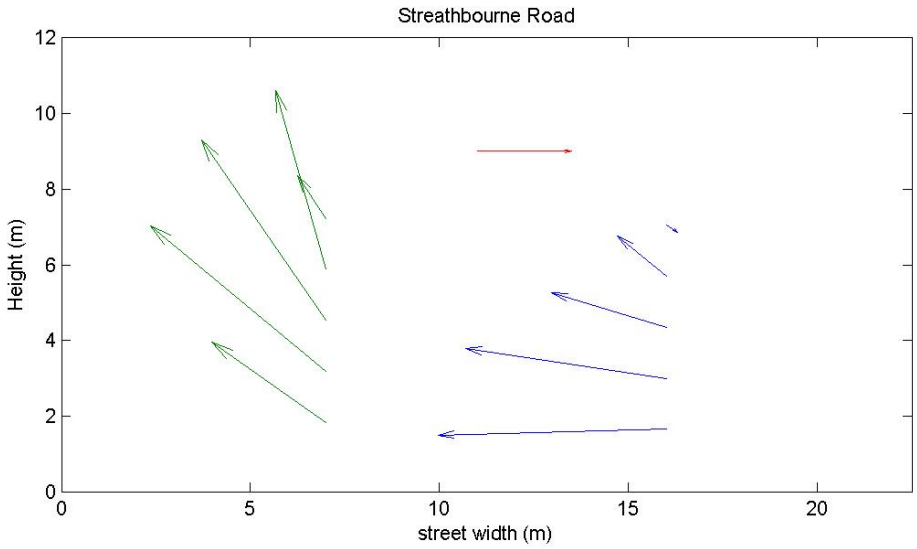

Figure 5.33: Vector plot for 6th September for the tree-lined street

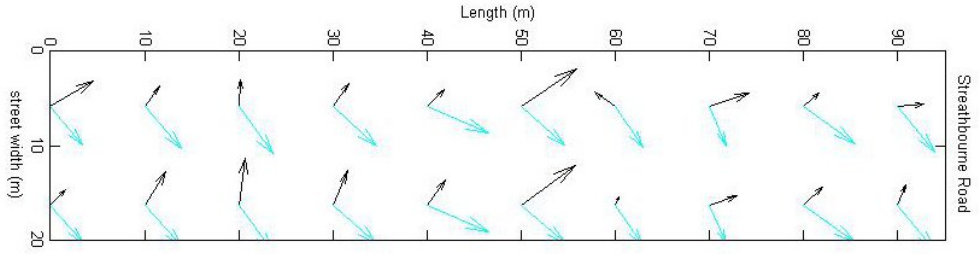

Figure 5.34: Vector plot for 5th July for the tree-lined street. In street velocity vectors shown in black and background wind vectors shown in blue

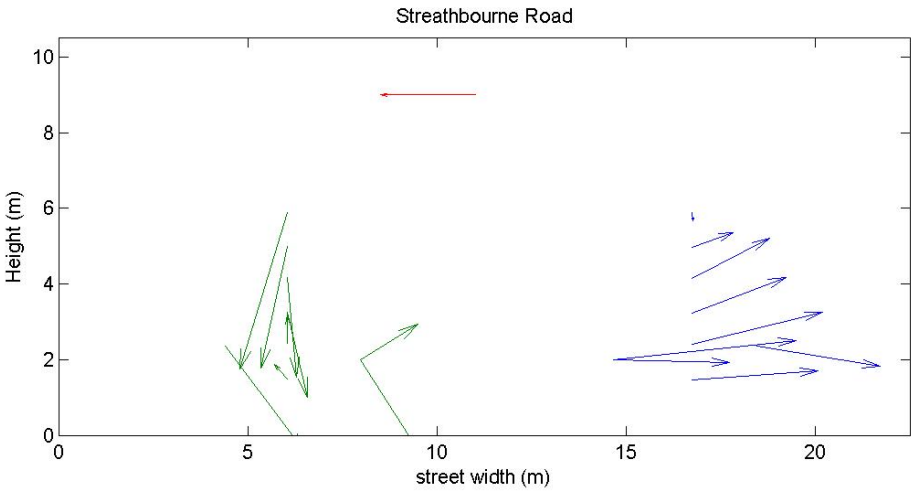

Figure 5.35: Vector plot for 29th July for the tree-lined street

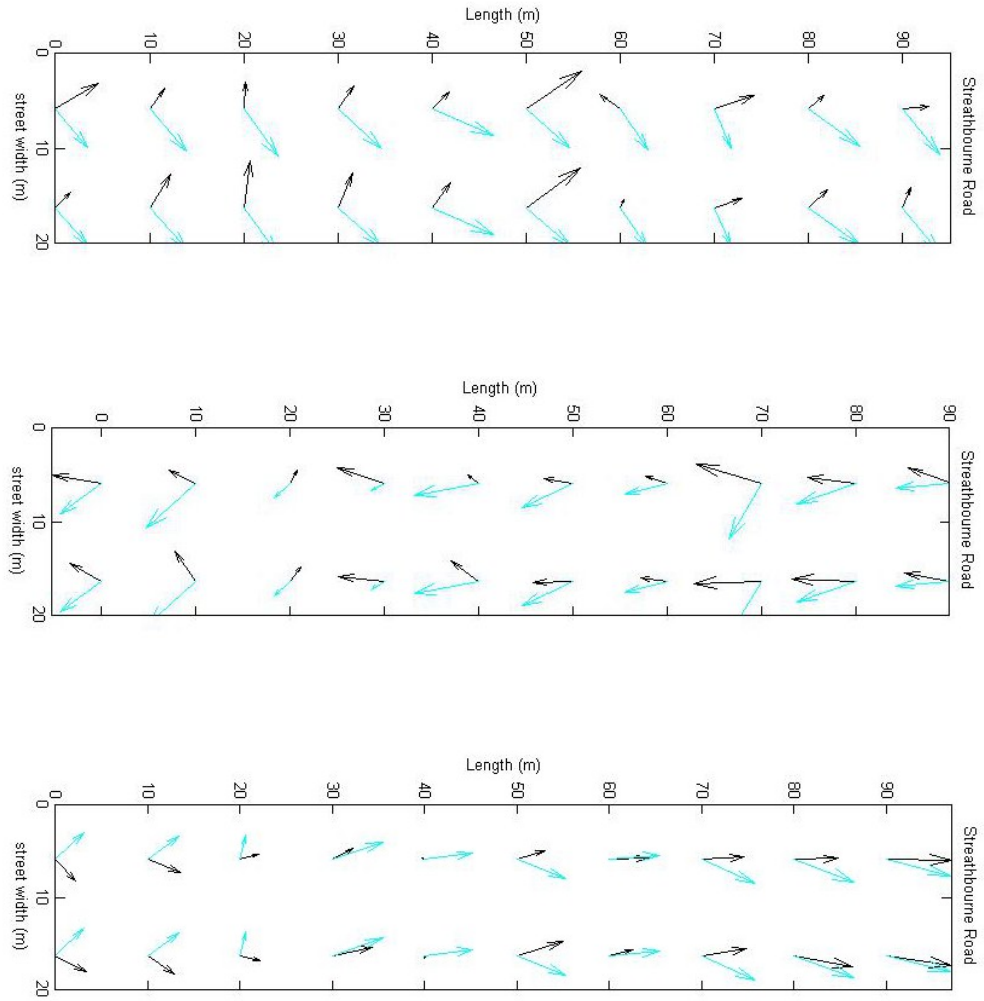

Figure 5.36: Vector plot for 5th July (top), 30th June (middle) and 2nd July (bottom) taken on the tree-lined street. In street velocity vectors shown in black and background wind vectors shown in blue

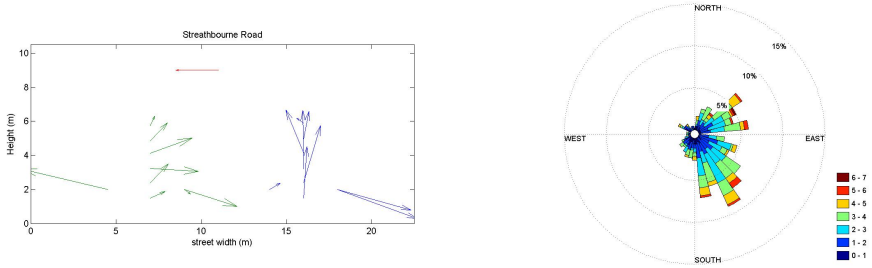

Figure 5.37: Vector plot for 25th July for the tree-lined street (left) and background wind conditions (right)

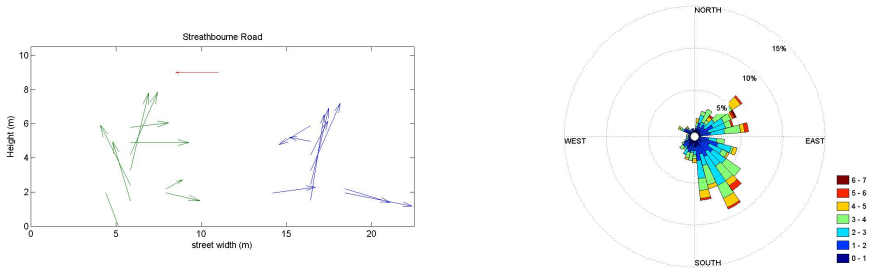

Figure 5.38: Vector plot for 26th July for the tree-lined street (left) and background wind conditions (right)

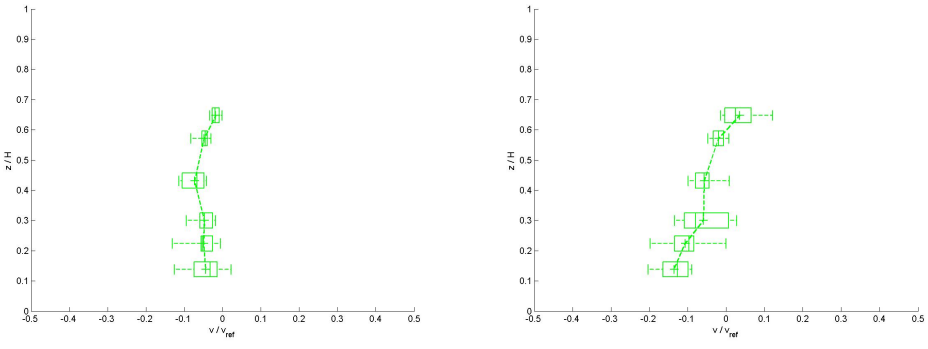

Figure 5.39: Mean normalised v velocity profile for tree-lined street with box and whisker plots showing first and third quartiles and maximum and minimum data points. Left figure shows profiles for upwind side of the street, right figure shows profiles for downwind side.

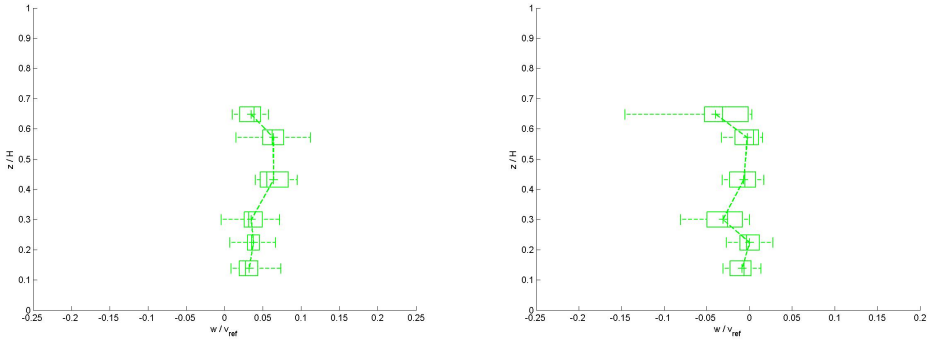

Figure 5.40: Mean normalised w velocity profile for tree-lined street with box and whisker plots showing first and third quartiles and maximum and minimum data points. Left figure shows profiles for upwind side of the street, right figure shows profiles for downwind side.

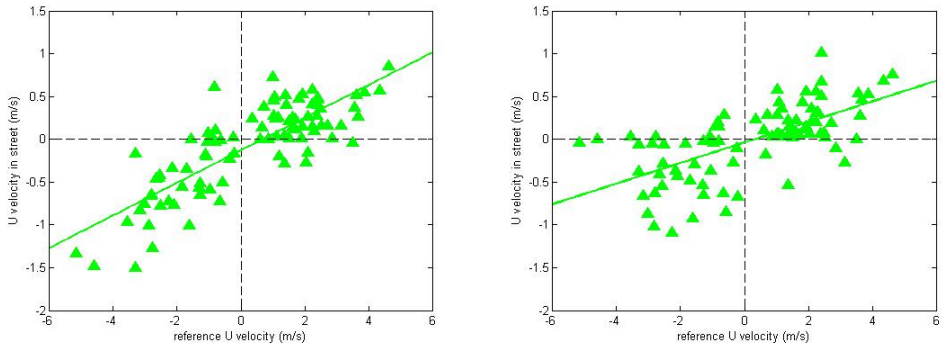

Figure 5.41: Reference u velocity against in street u velocity for tree-lined street. Left figure shows data for upwind side of the street, right figure shows profiles for downwind side.

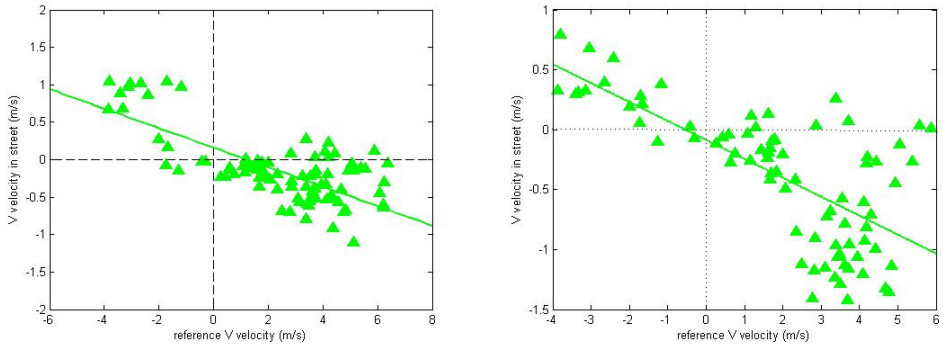

Figure 5.42: Reference v velocity against in street v velocity for tree-lined street. Left figure shows data for upwind side of the street, right figure shows profiles for downwind side.

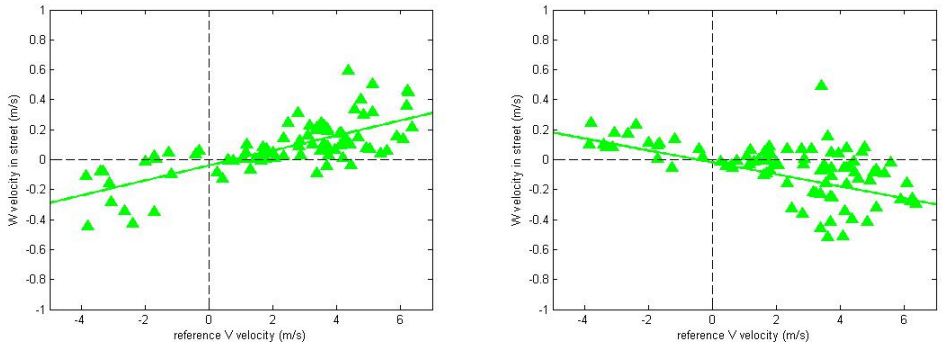

Figure 5.43: Reference v velocity against in street w velocity for tree-lined street. Left figure shows data for upwind side of the street, right figure shows profiles for downwind side.

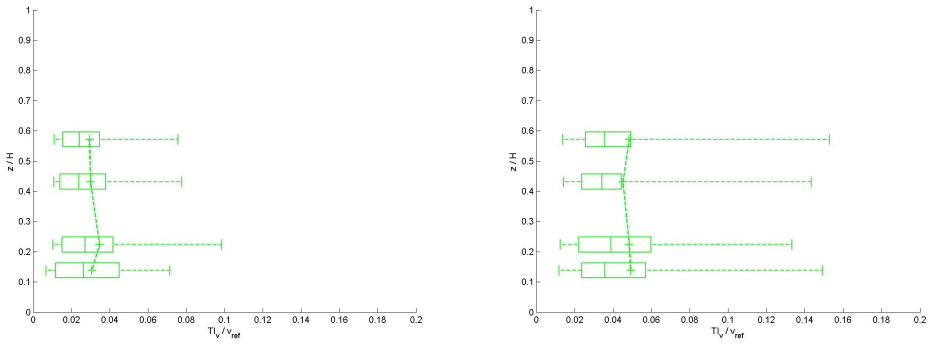

Figure 5.44: Mean normalised v component turbulence intensity profile for tree-lined street with box and whisker plots showing first and third quartiles and maximum and minimum data points. Left figure shows profiles for upwind side of the street, right figure shows profiles for downwind side.

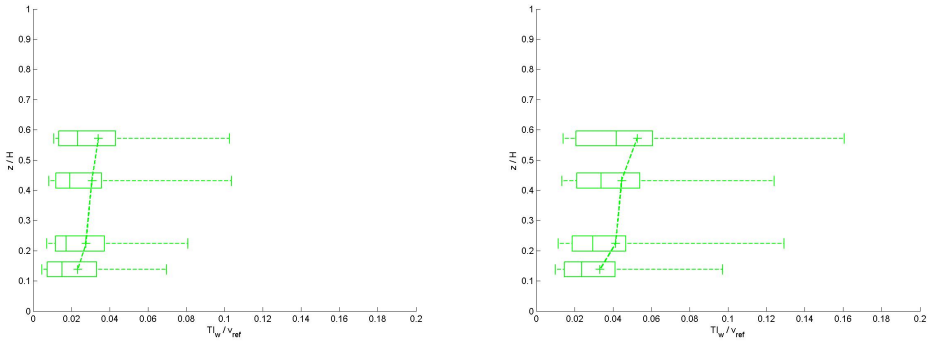

Figure 5.45: Mean normalised w component turbulence intensity profile for tree-lined street with box and whisker plots showing first and third quartiles and maximum and minimum data points. Left figure shows profiles for upwind side of the street, right figure shows profiles for downwind side.

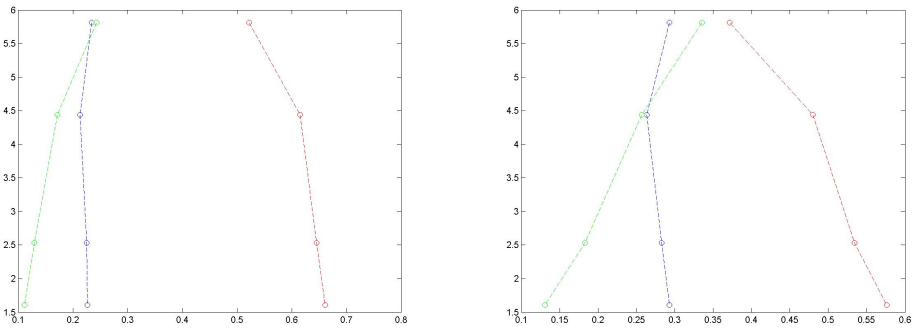

Figure 5.46: Fraction that each turbulence intensity contributes to overall TKE value. u TI - Red, v TI - Blue and w TI - Green. Left hand figure shows upwind side of street, right hand figure shows downwind

5.4 A Comparison Between Tree-Lined and Non Tree-Lined Streets

5.4.1 Airflow Patterns

A vector plot of a vertical cross section of the two streets taken on the 6th September is shown in Figure 5.47. Results taken for the non tree-lined street show strong evidence of the formation of a rotational vortex, with downdrafts on the downwind side of the street and updrafts on the upwind side of the street as well as across street velocities in the opposite direction to the background wind direction. Evidence of a rotational vortex is less clear for the data taken on the tree-lined street. Although across street velocities are acting in the opposite direction to the background wind direction and there is a consistent updraft on the upwind side of the street, vertical velocities on the downwind side of the street remain largely positive which is not what we would expect in the presence of a rotational vortex.

Vector plots for all measurement days are given in Appendix .1. Vector plots across all measurement days for the non tree-lined street show a consistent flow pattern occurring within the street with the exception of those days on which the background wind is unstable in which no clear flow pattern is produced. In the case of tree-lined street however the vector plots show a greater day to day variability most notably on the downwind side of the street where the w velocities vary between positive and negative values. It is likely that the presence of the tree canopies leads to a reduction in the wind velocities entering the street from above roof top level inhibiting the formation of a rotational vortex, however more detailed measurements would be needed to prove this is the case.

A vector plot of a horizontal cross section of both streets taken on the 4th April are shown in Figure 5.48. It can be seen that results taken on the two streets remain fairly similar with u velocities generally acting in the same direction as the background u velocity and v velocities in the opposite direction to the background v velocity. All measurements were taken at a height of 1.5m, the similarity in flow patterns between the two streets would suggest that at this height the trees have less of an effect on the flow patterns within the street. Again further investigation

is needed to test this hypothesis.

5.4.2 Velocity Profiles

Figure 5.49 shows the v velocity profile on the downwind and upwind side of the street for both tree-lined and non tree-lined streets.

Profiles taken on the downwind side of the street show a similar trend with the highest velocities experienced at the lowest heights and a decrease in velocity with increasing height towards the point where they reach zero velocity. The point at which the two profiles cross zero is at a height of approximately z/H = 0.65 for both streets. The spread in data, as indicated by the whisker plots, is very similar for the two streets with a greater spread in the data collected at the lower heights compared with greater heights within the street. There is a clear reduction in velocities for the tree-lined street compared with the non tree-lined street. The reduction in velocity is greatest at the lowest heights within the street and decreases as the height within the street increases. The two profiles reaching the point $v/v_{ref} = 0$ at around the same normalised height of z/H = 0.7.

On the upwind side of the street the velocity profiles differ slightly. The values taken on the tree-lined street remain close to zero and there is little difference with height. Data collected on the non tree-lined street shows a much greater variation in velocity with height, with peak velocities occurring at a height of approximately z/H = 0.3 and velocities decreasing with height above this point. Similaraly to the downwind side of the street we see that the most significant difference between the two sets of data is the reduction in mean velocities for the tree-lined street with the greatest reduction at the lowest heights and the two profiles reaching the point of $v/v_{ref} = 0$ at approximately the same height. This is in support of the hypothesis that trees extract momentum from the flow and thus reduce wind velocities within the street.

Figure 5.50 shows the normalised w velocity profiles for the upwind and downwind side of both streets. The w velocity profile on the downwind side of the tree-lined street varies to that taken on the non tree-lined street. Data collected on the non tree-lined street shows consistent downdraft with a peak in velocities at a height of z/H = 0.45. However on the tree-lined street there is no clear peak

in velocities and velocity values vary between positive and negative values. This is contrary to what we would expect if there is a rotational vortex within the street, for which we would expect to see downdrafts on the downwind wall.

The w velocity profile on the upwind side of the tree-lined street shows a greater similarity with that taken on the non tree-lined street. The maximum velocities occur for values of z/H between 0.4 and 0.6. All mean values are positive and the spread in data does not cross over into the negative values at any point, therefore updrafts are always experienced on the upwind side of the street. Comparison of the profiles taken for the two streets show that there is a significant reduction in w velocities on the tree-lined street, most notably at heights of z/H = 0.4 and z/H = 0.6 This is a clear indication of the effect that trees can have on airflow within streets, suppressing the amount of vertical flow that can occur within the street.

In the previous section 5.2 it was shown that any channeling of the wind along the street is driven by the magnitude of the background wind component which is parallel to the street and rotational vortices within the street are driven by the perpendicular component of the background wind. The scatter plots showing this relationship are given in Figures 5.51, 5.52 and 5.53. The line of best fit for both sets of data are included in all plots and clearly shows the reduction in velocities for the tree-lined street. The percentage reduction in each velocity component between the two streets is given in Table 5.3.

To calculate the level of correlation between the in street wind component and the background wind, the r values are calculated for each plot and given in Table 5.2. The r values show a linear relation between u and u_{ref} with a weaker relation on the downwind side of the street compared with the upwind. v_{ref} shows a linear relation with the v and w components within the street, again this is stronger on the upwind side of the street and weaker on the downwind side of the street. Comparisons with r values show that overall the connection between in street wind and reference wind is strongest on the non tree-lined street except for the vertical velocity component, w, which is stronger on tree-lined street.

5.4.3 Turbulence Statistics

Comparisons of turbulence intensities between the two streets given in Figures 5.54 and 5.55 show a clear decrease in turbulence within the tree-lined street compared with the non tree-lined. Typical reductions in turbulence intensities range between 34% - 62% (see Table 5.3). The addition of tree canopies to the street canyon results in large scale turbulence being broken down into small scale turbulence which is quick to dissipate. This short circuiting of the turbulence cascade results in overall lower turbulence levels in the street containing tree planting. We have also seen in previous chapters how turbulence is advected down into the street from the shear layer above roof top level this process is likely to be disrupted by the presence of the tree canopies.

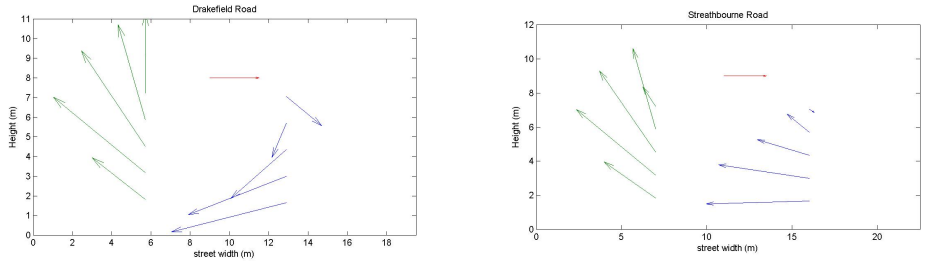

Figure 5.47: Vector plot for 6th September for non tree-lined street (left) and tree-lined street (right)

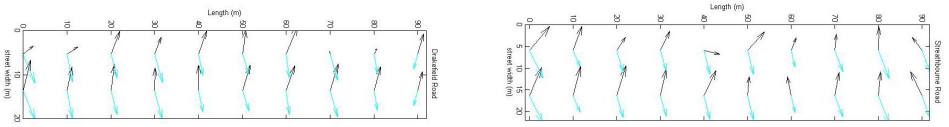

Figure 5.48: Vector plot for 5th April for non tree-lined street (left) and tree-lined street (right)

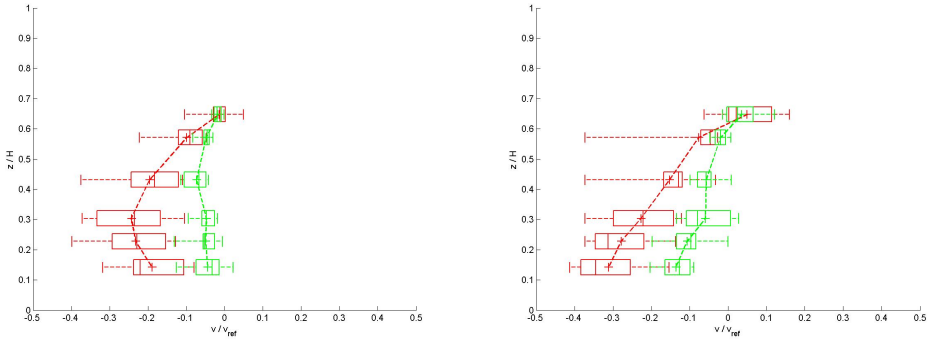

Figure 5.49: Mean normalised v velocity profile for tree-lined street (green) and non tree-lined street (red) with with box and whisker plots showing first and third quartiles and maximum and minimum data points. Left figure shows profiles for upwind side of the street, right figure shows profiles for downwind side.

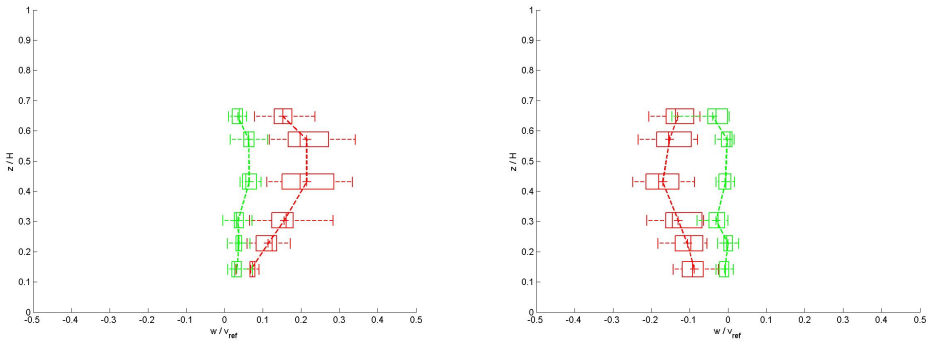

Figure 5.50: Mean normalised w velocity profile for tree-lined street (green) and non tree-lined street (red) with with box and whisker plots showing first and third quartiles and maximum and minimum data points. Left figure shows profiles for upwind side of the street, right figure shows profiles for downwind side.

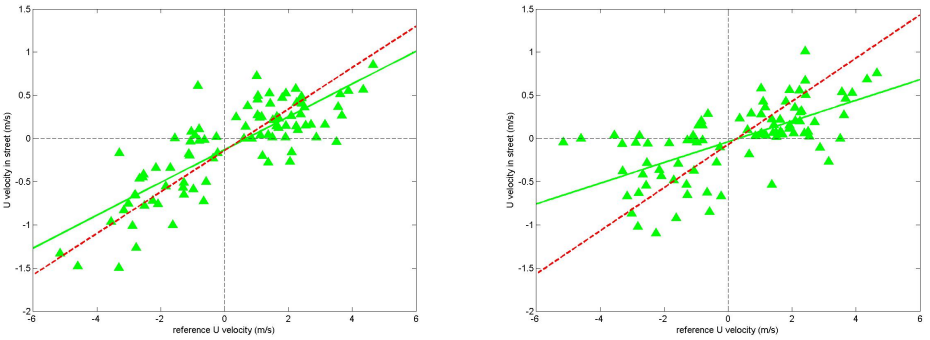

Figure 5.51: Reference u velocity against in street u velocity for tree-lined street (green). Dashed red line shows line of best fit for data taken from non tree-lined street. Left figure shows data for upwind side of the street, right figure shows profiles for downwind side.

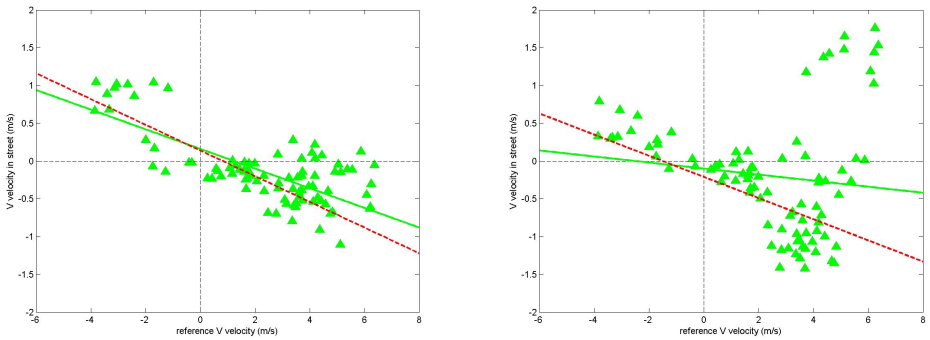

Figure 5.52: Reference v velocity against in street v velocity for tree-lined street. Dashed red line shows line of best fit for data taken from non tree-lined street. Left figure shows data for upwind side of the street, right figure shows profiles for downwind side.

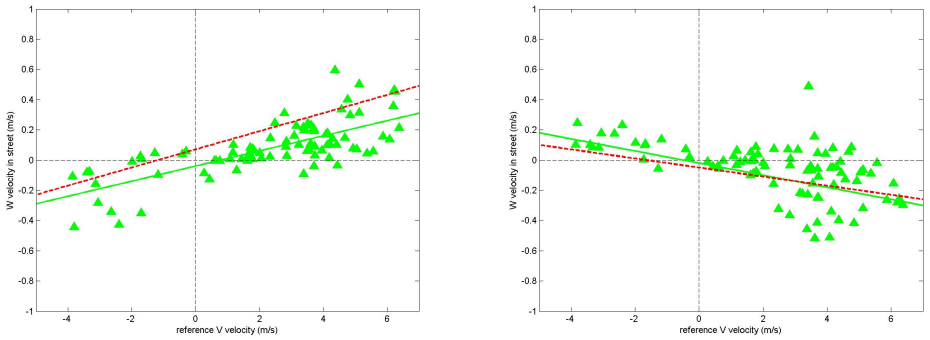

Figure 5.53: Reference v velocity against in street w velocity for tree-lined street. Dashed red line shows line of best fit for data taken from non tree-lined street. Left figure shows data for upwind side of the street, right figure shows profiles for downwind side.

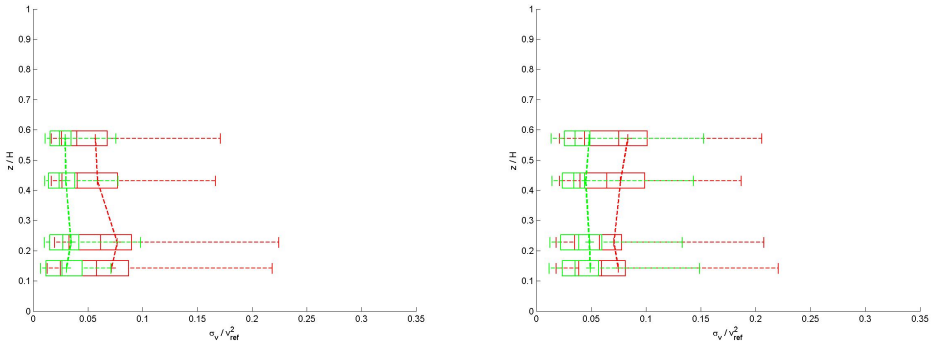

Figure 5.54: Mean normalised v component turbulence intensity profile for tree-lined street (green) and non tree-lined street (red) with box and whisker plots showing first and third quartiles and maximum and minimum data points. Left figure shows profiles for upwind side of the street, right figure shows profiles for downwind side.

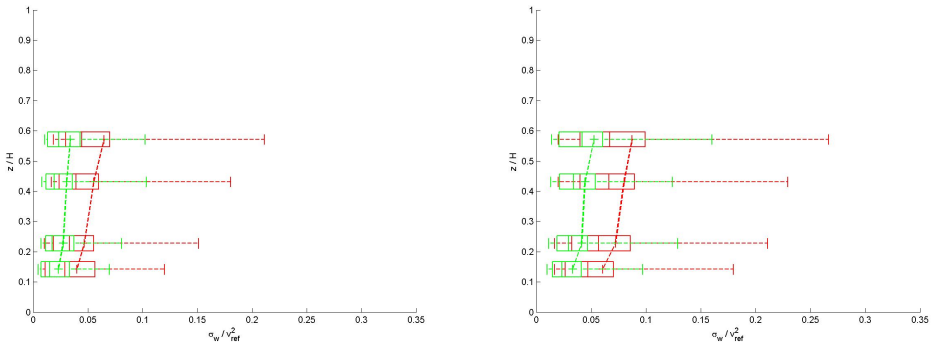

Figure 5.55: Mean normalised w component turbulence intensity profile for tree-lined street (green) and non tree-lined street (red) with box and whisker plots showing first and third quartiles and maximum and minimum data points. Left figure shows profiles for upwind side of the street, right figure shows profiles for downwind side.

Side of Street	Reference velocity	in-street velocity	r value tree-lined	r value non tree-lined
Upwind	U	U	0.82	0.84
Downwind	U	U	0.65	0.83
Upwind	V	V	-0.72	-0.75
Downwind	V	V	-0.12	-0.58
Upwind	V	W	0.74	0.69
Downwind	V	W	-0.55	-0.35

Table 5.2: Correlation co-efficients (r values) for reference velocity versus in-street velocity

Location	u/u_{ref}	v/v_{ref}	w/w_{ref}	TI_u/u_{ref}	TI_v/v_{ref}	TI_w/v_{ref}
Upwind	51	46	39	34	47	50
Downwind	78	34	4	58	62	59

Table 5.3: % reduction in normalised velocities and turbulence intensities

5.5 Summary of Main Findings

This chapter has summarised the findings of a field measurement campaign carried out in two neighbouring streets in South London. The main findings of these results were as follows:

Results taken from the non tree-lined street showed evidence of helical type flow structure under oblique wind directions. This flow structure comprises of the superposition of an along street channeling of the wind and an across street rotational vortex. The along street channeling of the wind is dependent on the component of the background wind which is parallel to the street length and the across street rotational vortex is driven by the wind component which is perpendicular to the street length.

The results of the non tree-lined street showed many similarities to the results taken from the idealised street canyon studied in Chapter 4. Vertical cross sections of the flow patterns within the street showed many similarities in terms of magnitude and direction of velocity vectors. Similarities were also found when plotting the vertical profiles of wind velocities and turbulence. These findings would indicate that the idealised street canyon often studied in literature is a viable method for studying the airflow within real streets with complex geometry subject to variable conditions.

Comparison of results between tree-lined and non tree-lined street found that the consistent flow patterns presented for the non tree-lined street were no longer present indicating that the presence of the trees leads to a disruption of the rotational vortex within the street.

Reduction in 10 min mean wind velocities were found for the tree-lined street for both vertical profiles (measurements taken at various heights within the street) and horizontal profiles (measurements taken at a height of 1.5m at various points along the length of the street. These reductions were found for all diretional velocity components and are believed to be due to presence of trees extracting momentum from the flow. Reductions were also found in turbulence levels within the tree-lined street for both the horizontal and vertical profiles. The percentage reduction in turbulence intensity levels varies between 34% and 62%. This reduction is believed to be due to the presence of the trees disrupting the turbulence

cascade by breaking down large scale turbulence into smaller scale turbulence which is quick to dissipate. The implications of these findings will be discussed in Chapter 7.

Chapter 6

CFD Modelling of Airflow within Tree-Lined and Non Tree-Lined Street Canyons: A Comparison with Field Measurements

In previous chapters of this thesis we have assessed the capabilities of CFD in predicting the airflow within a simplfied idealised street canyon and analysed the results of field measurements taken in both tree-lined and non tree-lined street canyons. We will now take what we have learnt from these chapters to construct simplfied CFD models of street canyons in which field measurements were taken. The results from these CFD models will then be compared against field measurements to assess the capabilities of simple CFD models in predicting complex airflow within real life street canyons, in particular those containing tree planting.

The chapter will start with a discussion of the results from a simplified CFD model of the non tree-lined street canyon. This will involve the investigation into how different simplified street geometries compare with our field measurements as well as investigating different techniques for including the effects of street furniture. The limitation of the CFD model will be discussed as any limitations at this stage will be carried through to the tree-lined street model.

Taking what we have learnt from the first section we will then construct a simplified CFD model of the tree-lined street canyon. The results of which will be compared against field measurements to assess the capabilities of CFD modelling in accurately predicting airflow within tree lined streets.

Finally we will compare the two sets of CFD simulations to further our understanding on the impact of trees on airflow within streets.

6.1 Choice of Field Measurement Data for Comparison with CFD Results

In Chapter 5 we saw the impact that the stability of the wind direction could have on flow within the street canyon. The CFD simulation was run with a single wind direction therefore field measurements taken on days with high wind direction variability were left out from the comparison. These are the days labeled group 2 in Table 5.1.

As seen in Chapter 5 the flow within the street canyon can be thought of as the superposition of a recirculating vortex controlled by the reference v wind component and an along street wind component controlled by the reference u wind component. Since we are comparing the field data with results from a CFD model subject to perpendicular wind conditions we will only be comparing the v and w components of the field data.

To allow for comparison between the field measurement data and CFD results all CFD data will be normalised by v_{ref}, which is the background wind velocity perpendicular to the street length taken at a height of 19m. For a definition of u, v, w, u_{ref} and v_{ref} see Figure 6.1.

6.2 Full Scale CFD Model of a Non Tree-Lined Street Canyon

Chapter 4 discussed the ability of CFD to capture the flow within a regular street canyon under the controlled conditions of a wind tunnel experiment. In this section we will extend this discussion to look at the ability of CFD and the k-ε model to predict the flow within a complex street canyon under variable conditions and make the comparison with the field measurement data described in Chapter 5. The section will start with an investigation into the simplification of building geometry. Two simplified roof geometries will be tested to determine which provides the closest match with experimental data. Secondly we will investigate the impact street furniture has on flow wihin the street and assess two simple methods for inclusion of street furniture within the CFD model.

The settings used for the CFD models were informed by the findings of the benchmark study in Chapter 4. Full details relating to the geometry and settings of all CFD models can be found in Appendix .2.3.

6.2.1 Roof Shape

A topic which has received some attention in recent years is the impact roof shape has on airflow within a street canyon. It has been shown that the roof geometry can have a dominant effect on the airflow patterns, velocity and turbulence levels within the street canyon, with Kastner-Klein et al. [2004] stating the roof geometry has just as much impact on the flow patterns as does the aspect ratio of the street.

The roof geometry within the field measurement streets is homogeneous, the roofs are the same height along the length of the street. Each house has the same roof type. However the geometry of the roof is more complex than the simple shapes often seen in literature. It consists of a pitched roof with the addition of dorma windows. These dorma windows also have sloping roofs.

Rather than explicitly modelling the geometry of the roof two simple shapes were tested to see if they could provide a reasonable prediction of the flow patterns within the street. These were a pitched roof and flat roof (see Figure 6.2) for

details.

Choosing these simple roof shapes allows for easier comparison with previous research as well as reducing the amount of computational power required due to a smaller mesh size. The pitched roof offers a good approximation to the true roof geometry, however where the dorma windows are located the flat vertical facade of the building extends to the full height of the building. Therefore wind within the street canyon at roof level will be subject to both the sloped section of the roof and the vertical wall of the dorma window which will have an impact on the flow.

6.2.1.1 Airflow Patterns

Figure 6.3 shows the vector plots of the v and w velocities taken from the two CFD models overlayed by field measurement data. In the case of the flat roof a rotational vortex forms within the canyon. This vortex is contained within the street and spans the entire height of the canyon. In the case of the pitched roofs a rotational vortex also forms, however this does not span the entire height of the buildings and therefore the centre of the vortex is slightly lower than in the flat roof case. We also see separation occurring on the upwind roof and an additional vortex forming here.

Comparison of the flat roof model and the field measurements show that the flow direction and velocity magnitudes are generally well predicted by the CFD model. The point at which the v velocity switches direction would appear to be at a greater height for the field measurements implying the centre of the vortex is higher within the field measurement street than the CFD model. The flow patterns is less well predicted by the pitched roof model as the centre of the vortex is shifted downwards within the street canyon, thus providing a poor match with field data for the upper most heights.

6.2.1.2 Velocity Profiles

Velocity profiles with height within the street are shown in Figures 6.4 and 6.5 for both CFD models along with the field measurement results.

V velocity profiles taken on the downwind side of the street show an excellent

match between the flat roof CFD model and the field measurements with mean velocities well predicted by the CFD model as well as the location at which the v velocity equals zero. The pitched roof model performs less well when compared against the field measurements with a general under-prediction of velocities.

On the upwind side of the street the v velocities are generally under-predicted by both CFD models with the exception of the flat roof model at the lowest height at which point velocities are over-predicted. The flat roof model generally provides a better prediction against field measurements compared with the pitched roof model with the velocity profile staying within the range of field data collected for most heights.

W velocity profiles are provided in Figure 6.5. The shape of the profiles is well captured by the CFD results although there is less of a peak in velocities at values of z/H between 0.4 and 0.6. Both sets of data under-predict velocities compared with the field measurements. The flat roof model again offers a better prediction of w velocities compared with the pitched roof model with the profiles generally lying within the range of field data at most heights.

6.2.1.3 Turbulence Statistics

The effect of the different roof geometries on turbulence intensities within the street can be seen in Figures 6.6 and 6.7. Both sets of results lie below the mean turbulence intensities found in the field measurements however both results lie with the range of field data collected (i.e. within the error bars). The pitched roof is found to offer slightly higher turbulence intensities and therefore offers better agreement against field data.

The issue of simplifying building architecture particularly roof geometry is a complex problem and clearly one that requires further investigation. From these brief tests its clear that the roof shape impacts flow patterns and turbulence values within the street. Ideally a CFD test would be carried out that explicitly modelled the roof geometry this would allow us to see if it is possible to simplify the roof geometry to the shapes shown here without compromising the results. However given the scope of this study is to assess the effect of trees on the flow

within the street and the flat roof geometry gave a reasonable agreement with the flow patterns and velocities obtained from the field measurements, this roof shape was chosen for use throughout the rest of the study.

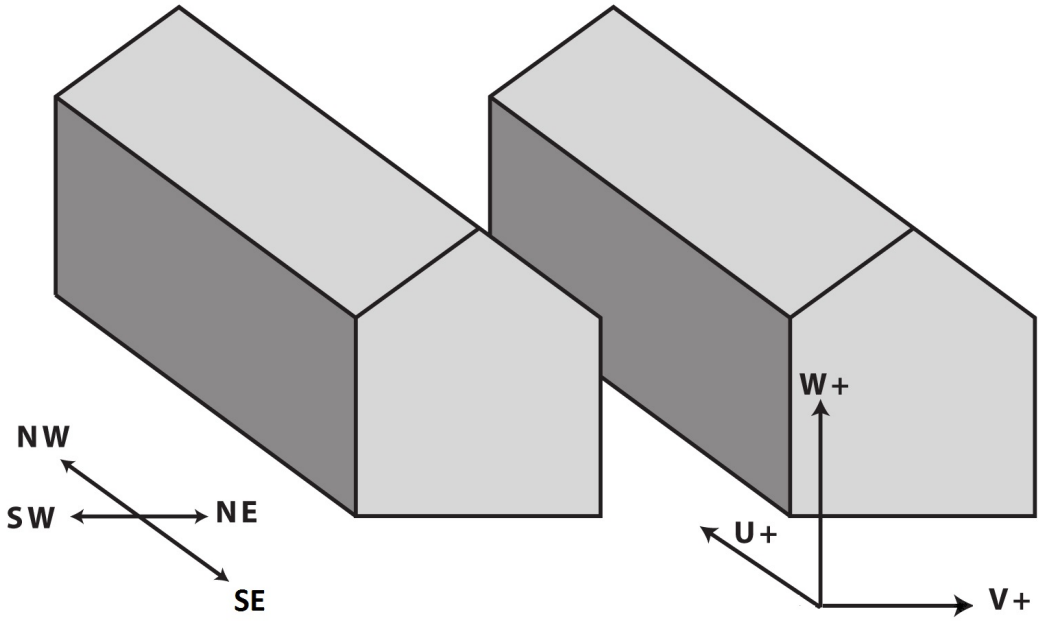

Figure 6.1: Geometry and axis reference of CFD model

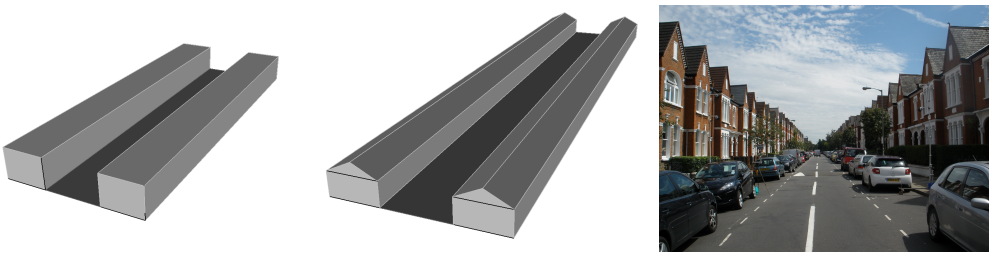

Figure 6.2: Flat roof geometry (left), pitched roof geometry (centre) and actual roof geometry (right)

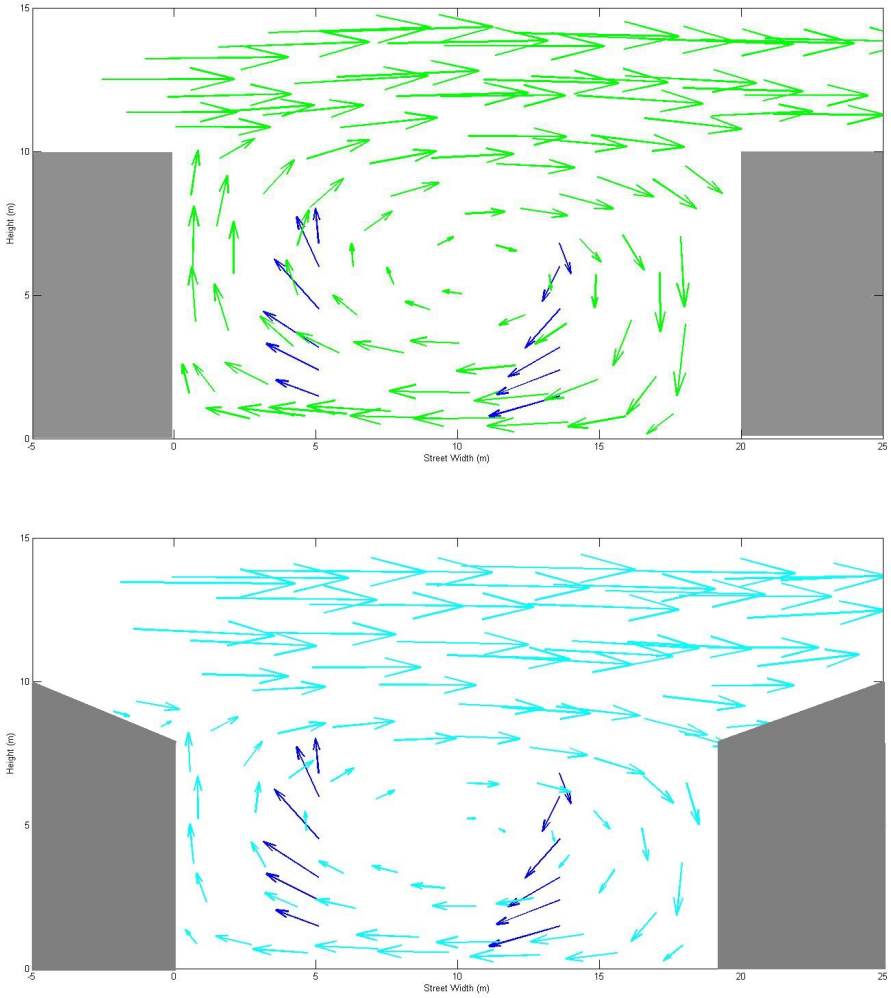

Figure 6.3: Vector plots showing the flow patterns for CFD simulation with flat roof (top) and CFD simulation with pitched roof (bottom). Field Measurement data shown in blue.

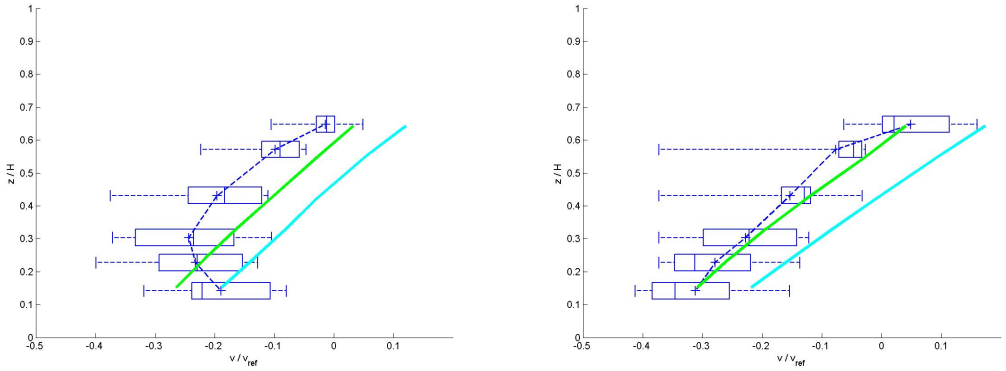

Figure 6.4: V Velocity profile taken from flat roof model (green) and pitched roof model (light blue) and field measurements (dark blue). Profile taken on upwind side of the street (left) and downwind side of the street (right)

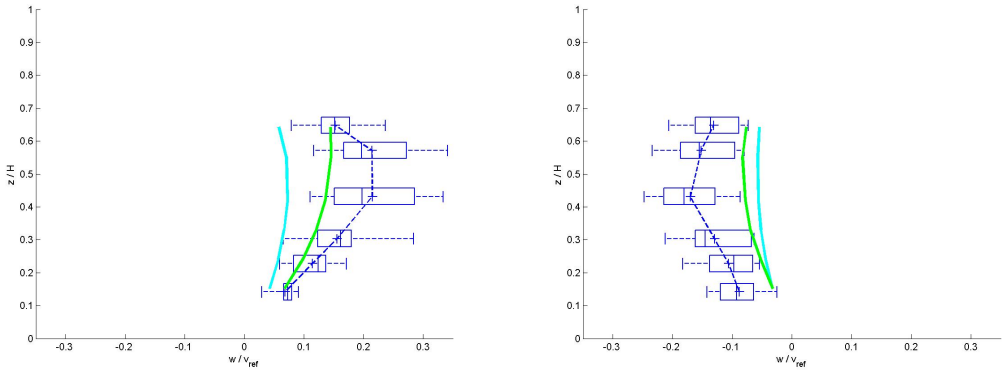

Figure 6.5: W Velocity profile taken from flat roof model (green) and pitched roof model (light blue) and field measurements (dark blue). Profile taken on upwind side of the street (left) and downwind side of the street (right)

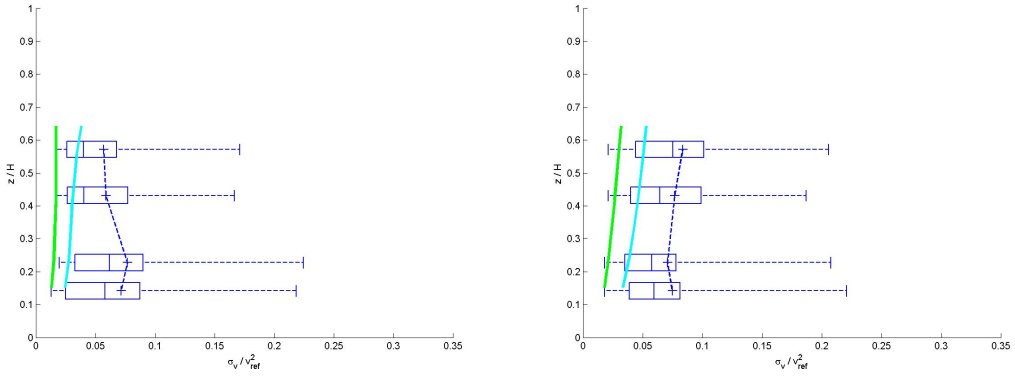

Figure 6.6: V Turbuence Intensity profile taken from flat roof model (green) and pitched roof model (light blue) and field measurements (dark blue). Profile taken on upwind side of the street (left) and downwind side of the street (right)

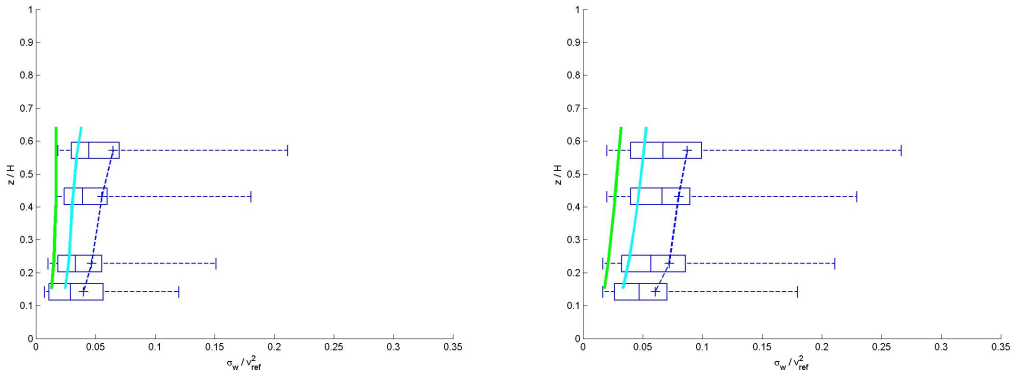

Figure 6.7: W Turbuence Intensity profile taken from flat roof model (green) and pitched roof model (light blue) and field measurements (dark blue). Profile taken on upwind side of the street (left) and downwind side of the street (right)

6.2.2 Street Furniture

Results of field measurements showed evidence of a decrease in wind velocities at lower heights for the upwind side of the street as well as a greater spread in data at these heights i.e. a greater variability in the day to day measurements. Parked cars, hedges, boundary walls and other street furniture will have a localised effect on the wind flow and may be responsible for such phenomena. In order to gain a greater understanding in to the effect of street furniture and how this may be incorporated into CFD models the results of three simulations are discussed. These are:

- An empty street canyon
- A sand grain roughness applied to the floor of the street
- Street furniture included as rectangular blocks along the length of the street

The geometry of the street furniture model is shown in Figure 6.8.

6.2.2.1 Airflow Patterns

Vector plots of results from the three CFD models are given in Figure 6.9. The field measurement data is overlaid the CFD data in order to see how the two compare.

The flow patterns produced for the empty street canyon and the street canyon with sand grain roughness show little to no difference. A single rotational vortex is produced within the streets, this is in line with our findings from Chapter 4 and the simple wind tunnel street canyon. The centre of the vortex is shifted above and downwind of the centre of the street canyon. Comparison with the field measurements shows a very good correlation in terms of flow direction and velocity magnitude at most heights. The point at which the v velocity changes direction for the field measurements is slightly higher than for the CFD results suggesting the centre of the vortex within the field measurements street is higher than within the CFD model. The reduction in velocity magnitude at the lowest height on the upwind side of the street is also not well captured by the CFD models.

The flow pattern produced by the street canyon with the addition of street furniture also shows the formation of a large rotational vortex. This forms between the roof top and the top of the street furniture. Smaller rotational vortices are formed in the wake of the street furniture. The presence of the obstacles within the street results in the centre of the vortex being shifted further towards the downwind side of the street.

Comparison with field measurement data shows reasonable correlation on the upwind side of the street with flow direction generally being well predicted although the velocity magnitudes are generally lower for the CFD results. On the downwind side of the street flow direction is not well predicted due to the fact that the centre of the vortex within the CFD results has been shifted downwind thus providing a poor match with field data.

6.2.2.2 Velocity Profiles

Figure 6.10 shows the v velocity profiles against height for the three CFD models and the the field measurement results. On the upwind side of the street the empty street CFD model generally under-predicts the mean v velocities apart from below a height of 2m at which point the CFD model begins to over-predict the velocities. The shape of the velocity profile is not well predicted by the empty street CFD model. The field measurement show a decrease in velocity below a height of 3m this is not reflected in the CFD results which are linear with height. The results for the CFD model with sand grain roughness show an under-prediction of v velocities on the upwind side of the street at all heights except at the lowest height of 1.5m at which point the velocity is well predicted. The results of the CFD model with the addition of street furniture show a good match with the field measurement data in terms of profile shape on the upwind side of the street. The wake produced by the street furniture objects results in a reduction in velocities below a height of 2m. The magnitude of the v velocities produced by this CFD model are however under predicted when compared with the field measurements.

On the downwind side of the street the presence of street furniture has less of an effect. The field measurement v velocity profile is almost linear with height.

On this side of the street the empty street CFD model provides an excellent prediction of the field measurement data, with a good match of the data at almost all heights. The results of the CFD models with sand grain roughness and with street furniture show an under-prediction of the velocities but are still generally within the range of field measurement data.

Figure 6.11 shows the w velocity profiles with height for the three CFD models and the field measurement data. On the downwind side of the street the profile given by the empty street CFD model and the CFD model with the addition of roughness are very similar. Both models under predict the mean velocities of the field measurements although they still lie within the range of field measurement data collected. The shape of the profile is well predicted although the peak in the w velocities at a height of 4.5m in the field measurement results is not present in the CFD results. The results of the CFD model with street furniture shows a significant under prediction in the w velocities on the downwind side of the street and even predicts positive w velocities at the lowest height which is not reflected in the field measurements.

On the upwind side of the street the results from the empty street canyon show excellent correlation with the field measurement data at the lowest and upper most heights. The peak in w velocities at heights of 4.5m and 6m. is not well predicted by the CFD model however the profile still lies within the range of field measurement data collected. The profile produced by the CFD model with added roughness is slightly lower than the empty street model but the profile still lies within the range of field measurement data collected. The profile produced by the CFD model with street furniture again significantly under predicts the w velocities.

In addition to taking field measurements at different heights within the street, measurements were also taken at several locations along the length of the street at pedestrian head height (1.5m). The average of the 10 locations for normalised v, w and the resultant of v and w ($(v^2 + w^2)^{1/2}$) is given in Tables 6.1 and 6.2 along with the results of the three CFD models. These results agree with the results discussed for the vertical profile with the empty street over predicting the velocities, the addition of street furniture providing an under-prediction and the addition of roughness providing an excellent match with experimental data. For

this height the addition of sand grain roughness would offer the best solution in terms of predicting the velocity magnitudes within the street however at greater heights within the street the empty canyon CFD model performs best.

6.2.2.3 Turbulence Statistics

Figures 6.12 and 6.13 show the v and w turbulence intensities for all three CFD models and field measurements. All results show a higher level of turbulence on the downwind side of the street. This is in-line with the findings in Chapter 4 which turbulence generated in the shear layer is advected down into the street canyon at the downwind side of the street.

The differences between the results of the three models is small with the street furniture model showing a slight increase in turbulence with height within the street where as the other two models show little variation with height. All three models tend to under-predict the level of turbulence within the street although still lie within the range of data collected. This under-prediction is to be expected as we saw in the previous chapter the k-ε model has difficulties correctly predicting the level of turbulence within street canyons due to the under-prediction of turbulence above the roof of the upwind building. Overall the street furniture model provides the best match with the field measurement data, however the difference between the three models is small.

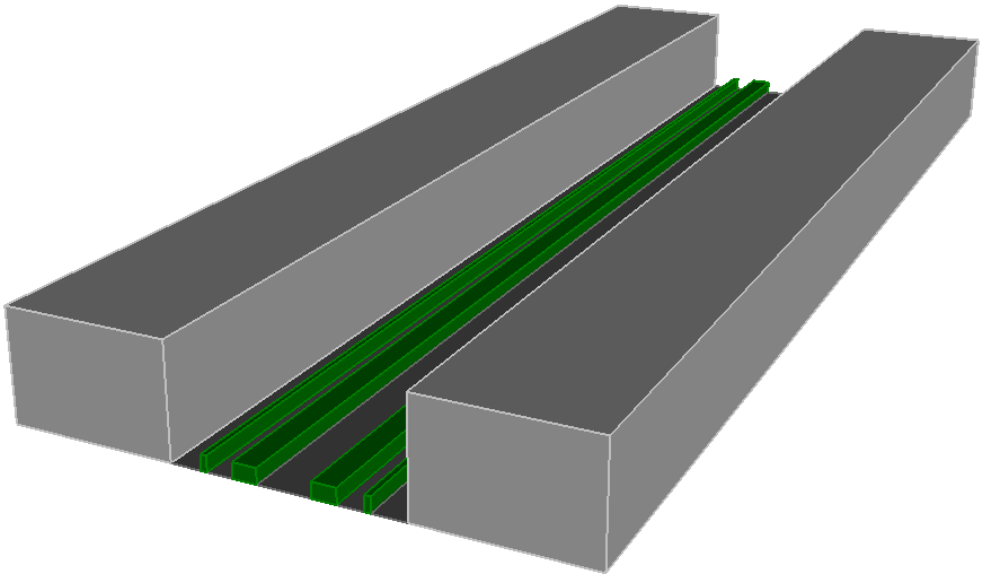

Figure 6.8: Geometry of street furniture model

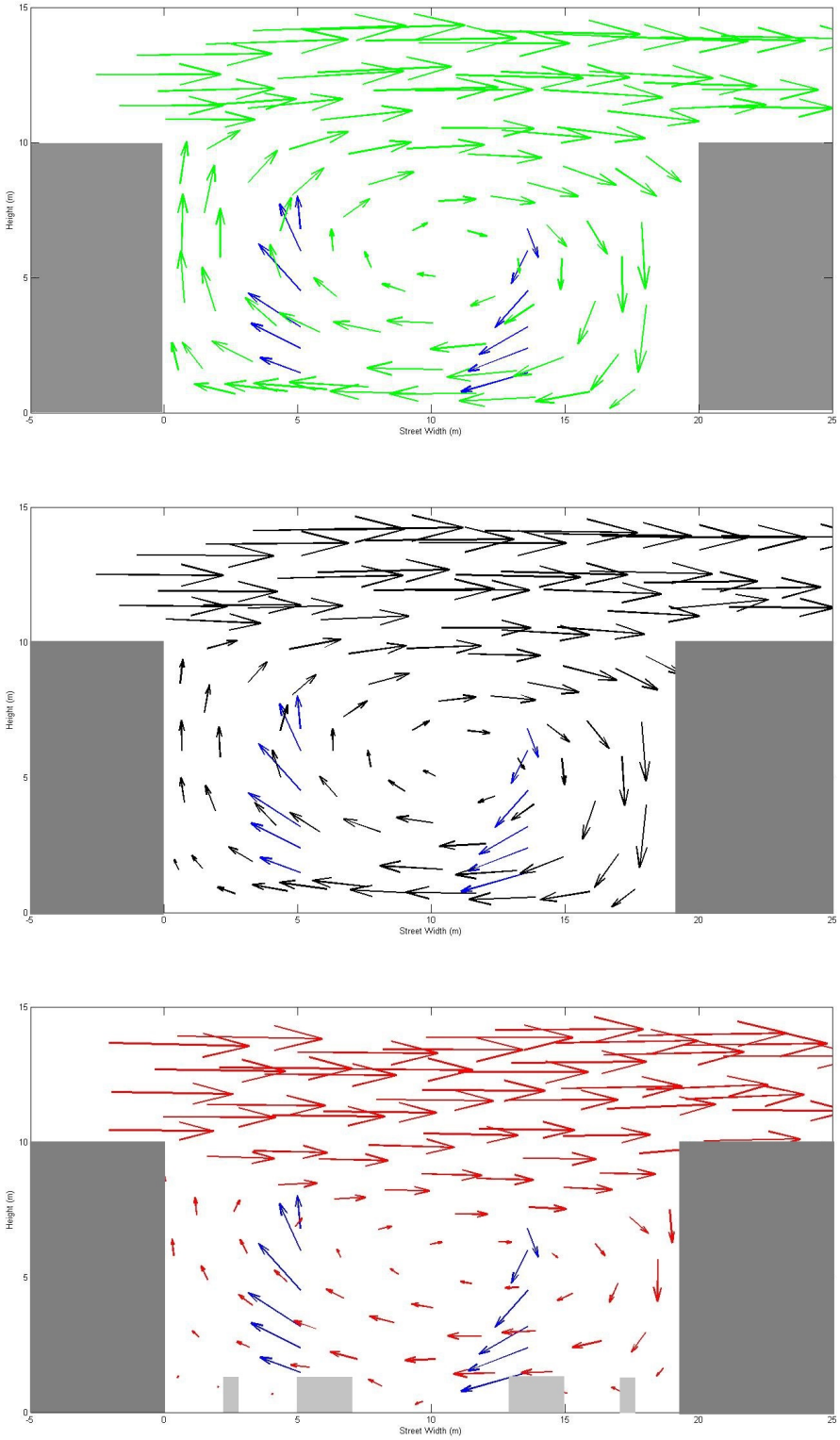

Figure 6.9: Vector plots showing CFD flow patterns at vertical cross section for no street furniture (top), floor roughness (middle) and street furniture (bottom). Field measurements shown in blue

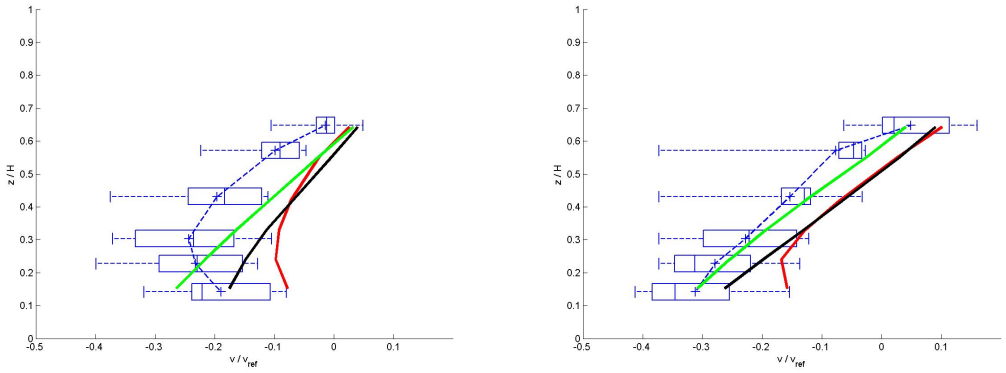

Figure 6.10: V velocity profile taken on the upwind (left) and downwind (right) side of the street. No street furniture model shown in black, floor roughness model shown in green and street furniture model shown in red. Field measurements shown in blue

.

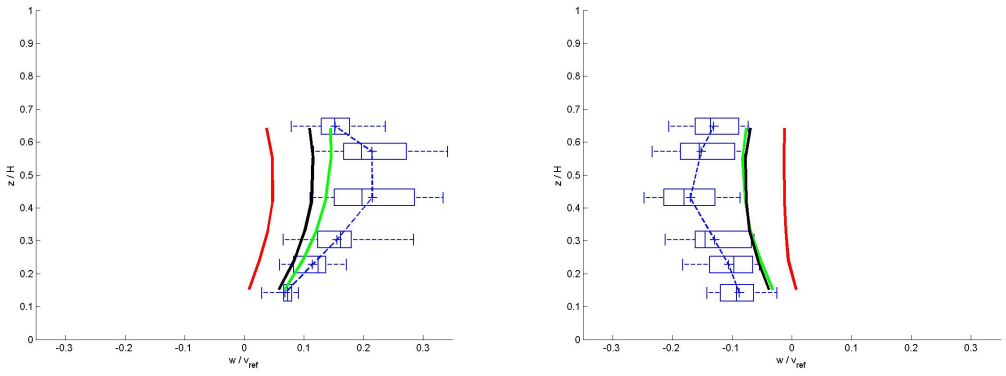

Figure 6.11: W velocity profile taken on the upwind (left) and downwind (right) side of the street. No street furniture model shown in black, floor roughness model shown in green and street furniture model shown in red. Field measurements shown in blue

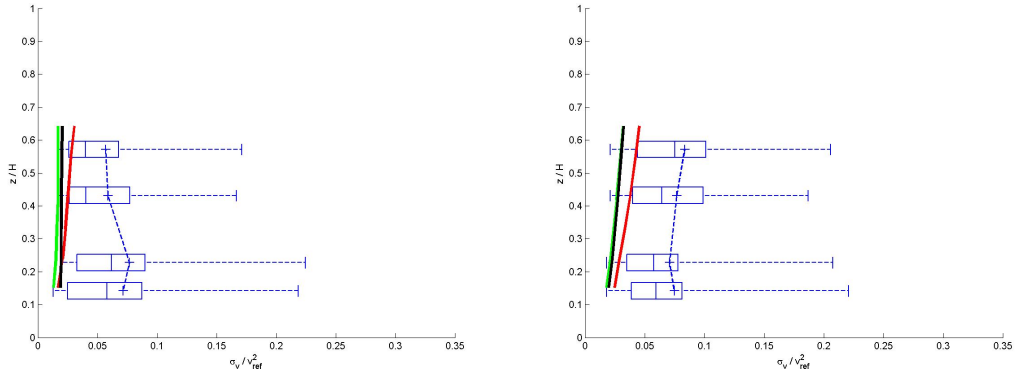

Figure 6.12: V turbulence intensity profile taken on the upwind (left) and downwind (right) side of the street. No street furniture model shown in black, floor roughness model shown in green and street furniture model shown in red. Field measurements shown in blue

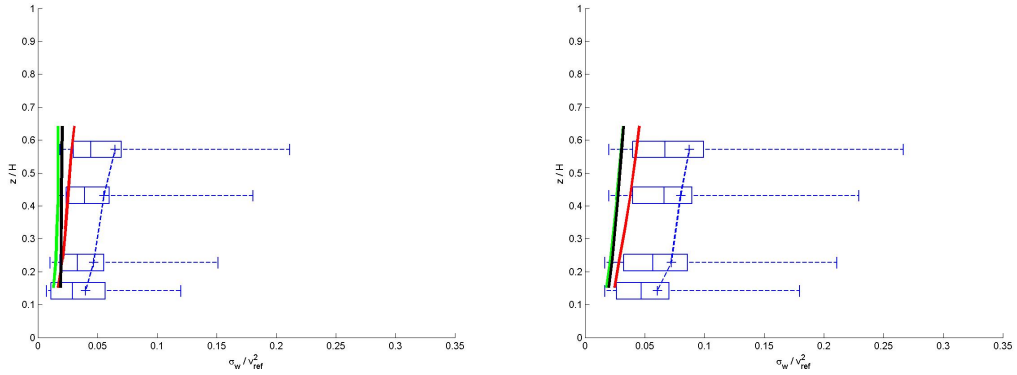

Figure 6.13: W turbulence intensity profile taken on the upwind (left) and downwind (right) side of the street. No street furniture model shown in black, floor roughness model shown in green and street furniture model shown in red. Field measurements shown in blue

Table 6.1: Comparison of normalised velocity components for upwind side of the street

Results	v/v_{ref}	w/v_{ref}	$\sqrt{v^2+w^2}/v_{ref}$
CFD empty street	-0.28	-0.05	0.28
CFD with roughness	-0.17	0.05	0.18
CFD with street furniture	-0.07	0.01	0.07
Field Measurements	-0.17	0.04	0.18

Table 6.2: Comparison of normalised velocity components for downwind side of the street

Results	v/v_{ref}	w/v_{ref}	$\sqrt{v^2+w^2}/v_{ref}$
CFD empty street	-0.30	-0.05	0. 30
CFD with roughness	–0.27	-0.03	0.27
CFD with street furniture	-0.15	0.01	0.15
Field Measurements	-0.27	-0.05	0.28

6.3 Full Scale CFD Model of Airflow within a Tree-Lined Street

This section of the thesis presents the results obtained from CFD simulations which aim to recreate the wind conditions found in Streathbourne Road, the tree-lined street in which field measurements were taken. The CFD model is full scale therefore the dimensions of the building height, street width, tree crown size and spacing is taken directly from Streathbourne Road. Based on the findings of the previous section the buildings are modelled as simplified rectangular blocks with flat roofs and no street furniture is included in the model. The geometry of the tree canopies is included as ellipsoids with dimensions and tree spacing taken from the field measurements. The tree trunks are not included in the model. Two methods for incorporating the effects of the tree canopies within the CFD model were tested. These were:

- Tree crowns included as solid objects
- Tree crowns included as porous domains with momentum and turbulence sinks

The porous tree canopy model is based on the work of Raupach and Shaw [1982] which is discussed in detail in Chapter 3. This model accounts for the aerodynamic effects of the tree canopies through the addition of sink and source terms to the CFD model. The extraction of momentum by the tree canopy is accounted for by the addition of a momentum sink term, the addition of turbulence via vortex shedding is incorporated as a turbulence source term and the reduction of turbulence due to the short circuiting of the turbulence cascade is accounted for by a turbulence sink term. These source and sink terms are dependent on the leaf area density and drag coefficient of the trees. For full details relating to both the porous and solid tree models as well as details of the CFD geometry and setting please refer to Appendix .2.3.

6.3.1 Airflow Patterns

The normalised velocity vectors for the CFD models with both solid tree crown and porous tree crown are given in Figure 6.15 along with field measurement data. The location at which these vector plots were taken is given in Figure 6.14.

Results presented for the CFD model with solid tree canopy show that the presence of the tree canopy is clearly causing significant disruption to the flow patterns within the street as the rotational vortex centered at the middle of the street canyon is no longer present instead a vortex is formed at the bottom downwind corner of the street beneath the tree canopy. Comparison with field measurement data shows velocities are reasonably well predicted on the upwind side of the street with the general flow direction and magnitude of vectors being similar. However on the downwind side of the street the vectors produced by the CFD model show no resemblance to those given by the field measurement data. This is due to the distortion of flow patterns produced by the solid tree crown. Although both results show a negative v velocity the CFD results clearly show a positive w velocity which is not reflected in the field measurements.

Results presented for the CFD model with porous tree crown show the familiar pattern of single rotational vortex which has been seen in both previous research and the results presented in earlier chapters. The centre of the vortex is shifted towards the downwind side of the street and slightly above $z/H = 0.5$ due to the presence of the tree canopies. The magnitude of the normalised velocity vectors within the street ranges from 0 to 0.3. Comparison with field measurement results on the whole show good qualitative comparison with the exception of heights 4 and 5 on the downwind side of the street for which the direction of flow varies from that given in the field measurements.

Figures 6.17 and 6.18 show the normalised velocity vectors for both CFD models at various locations along the street length, the position of which are given in 6.16. This allows for the assessment of how the flow patterns vary throughout the length of the street due to varying tree spacing. Field measurements data taken at a height of 1.5m are also given in the form of vector plots.

Results presented for the solid tree canopy show the formation of rotational vortex below the tree canopies, the shape and positioning of which varies de-

pending on the location within the street. Field measurements show that the v velocity component is consistently in the opposite direction to the reference wind direction and vertical velocity, w, is positive on the upwind side of the street and negative on the downwind side. The flow direction is captured by the CFD results on the upwind side of the street however on the downwind side of the street the flow is not well re-produced due to the shifting position of the rotational vortex within the street leading to some positive w velocities on the downwind side of the street.

Results presented for the porous CFD model show similar flow patterns throughout the length of the street. There is some variability in the position of the centre of the rotational vortex although this is consistently found on the downwind side of the street. The flow direction produced by the CFD model matches the field data well with the v velocity consistently in the opposite direction to the direction of flow above the roof top level and positive vertical velocities on the upwind side of the street and negative on the downwind side of the street. Overall the magnitudes of the velocity vectors are similar to those found for the field measurements.

6.3.2 Velocity Profiles

Figure 6.19 shows the normalised v velocity profile against normalised height within the street for results of both CFD models and field measurement. The error bars show the spread in the measurements taken. There is little variation in the v velocities between the solid and porous tree crown models on the downwind side of the street. However on the upwind side of the street there is a clear difference between the two models with the porous tree crown predicting negative v velocities and the solid tree crown predicting positive v velocities.

Comparison with field measurement data shows that both models provide an excellent prediction against field data on the downwind side of the street. On the upwind side of the street the porous model shows an excellent prediction of velocities at the upper 3 heights however at lower heights the results of the CFD model are higher than the mean values of the field data. A likely explanation for this is the fact that street furniture was not included in the CFD models in

particular the tree trunks were not included in the CFD model. The presence of the tree trunks may extract momentum from the flow resulting in lower velocities particularly on the upwind side of the street. Further investigation is needed to determine the effects of the trees trunks on the flow and whether they should be included in CFD models. The results of the solid tree crown do not provide a good prediction against field data on the upwind side of the street.

Figure 6.20 shows the normalised w velocities against normalised height within the street for both CFD and field measurements. The two sets of CFD results show distinctly different velocity profiles. Results from the porous tree crown show positive velocities on the upwind side of the street with velocities staying close to zero. The results of the solid tree crown show velocities varying between positive and negative. On the downwind side of the street the porous model gives largely negative values whereas vertical velocities of the solid crown model are generally positive.

Comparisons of the two sets of results with the field measurement data shows the porous model gives a reasonable prediction although velocities are slightly under predicted on the upwind side of the street. Results from the solid crown model bear little similarity to the field measurement data.

Figure 6.22 shows contour plots of v velocities taken at a height of 1.5m for both solid and porous tree crown models. Field measurements are also displayed for comparison within the black boxes, this was taken at the locations shown in Figure 6.21. It can be seen that the v velocities generally remain negative (i.e. in the opposite direction to the background wind) for the porous tree model this is in line with the field measurement data which generally shows a good match with CFD predictions. Results for the solid tree model show large areas in which positive v velocities are experienced (see red areas) this is not reflected by the field measurement data which always remains negative.

Figure 6.23 shows contour plots w velocities taken at a height of 1.5 m for both solid and porous tree crowns. Results for the porous tree crown generally show positive velocities on the upwind side of the street and negative on the downwind side of the street with the exception of a few isolated locations. Results of the solid tree crown show a variation of positive and negative vertical velocities on both sides of the street. Comparison with field measurements show the porous model

generally provides a good prediction of the field measurements particularly on the downwind side of the street. The solid model does not provide a good prediction against field measurement data due to the high variability between positive and negative velocities.

6.3.3 Turbulence Statistics

Figures 6.24 and 6.25 show the turbulence intensities profiles against height for both the CFD models and field data. All results show higher turbulence levels on the downwind compared with the upwind side of the street. Results taken from the CFD model with solid tree crown show little variation in turbulence with height.

The results of the porous tree crown show little variation with height on the upwind side of the street but show an increase of turbulence with height on the downwind side of the street. As we have seen in Chapter 5 and in previous research on the subject TKE is advected down into the street canyon from the shear layer above. This occurs at the downwind side of the street canyon hence the higher values in this region.

Comparison with field measurement shows an under-prediction when compared with the mean turbulence intensities taken from the field data. This is in line with the findings of Chapter 4 in which we saw that the k-ε model under-predicts the turbulence levels within homogeneous street canyon and also the findings of the first section of this chapter in which turbulence levels were under-predicted for our non tree-lined model. The level of under-prediction is greater for the solid model compared with the porous model. The porous model lies just below the range of data obtained from the field measurements. The field measurements show that the v component of turbulence intensity is fairly uniform with height whereas the w component increases with height. This is not reflected by either set of results as the k-ε model is isotropic meaning any variation between the directional components of turbulence will not be captured by this turbulence model.

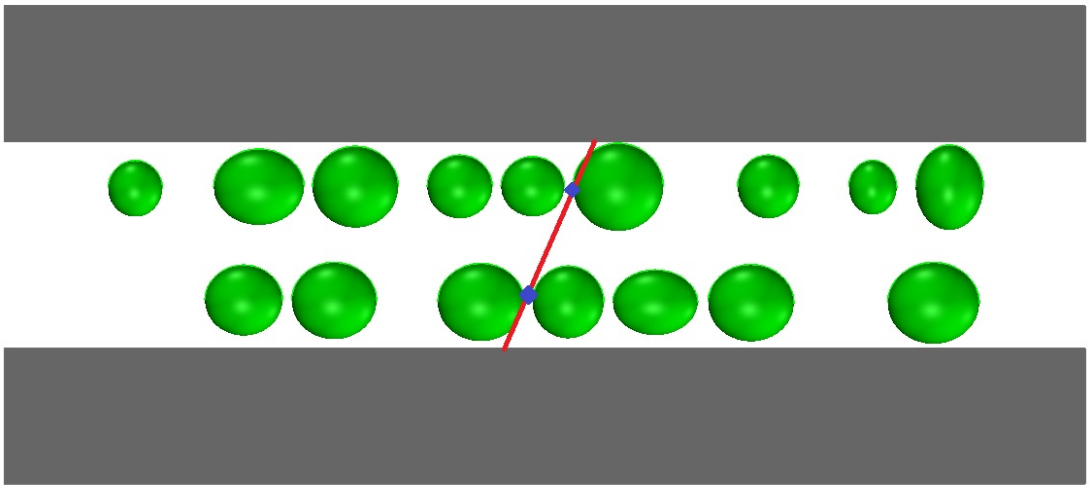

Figure 6.14: Location of CFD vector plots (red line) and field measurement location of field measurement (blue circles)

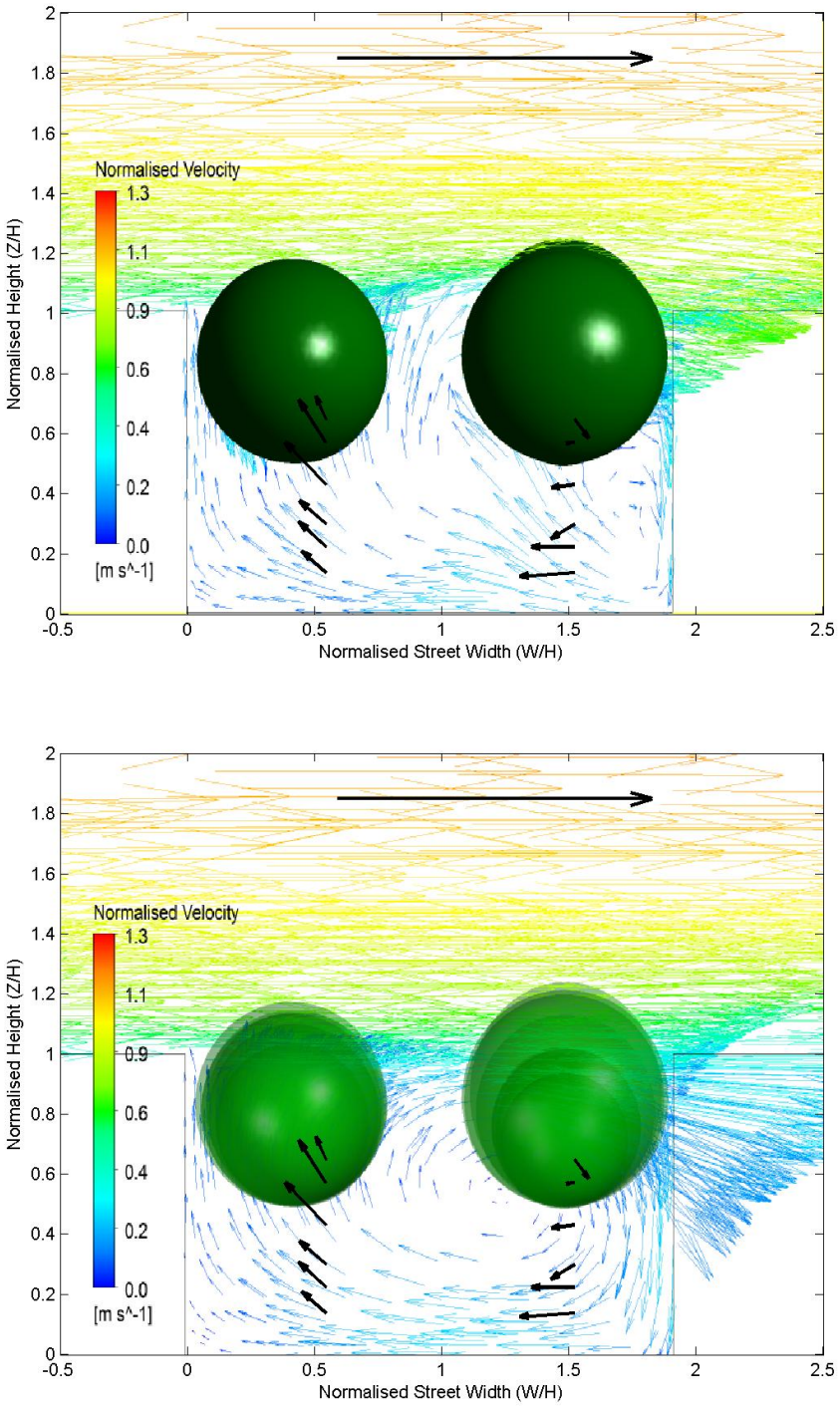

Figure 6.15: Normalised vector plots for CFD results with solid tree crown (top) and porous tree crown (bottom). Field measurements shown in black

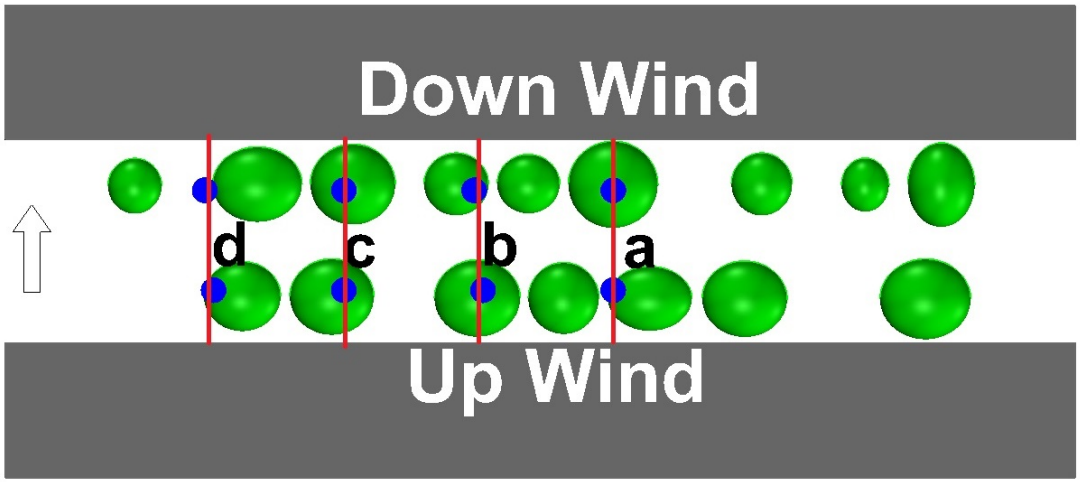

Figure 6.16: Location of CFD vector plots (red line) and field measurement location of field measurement (blue circles)

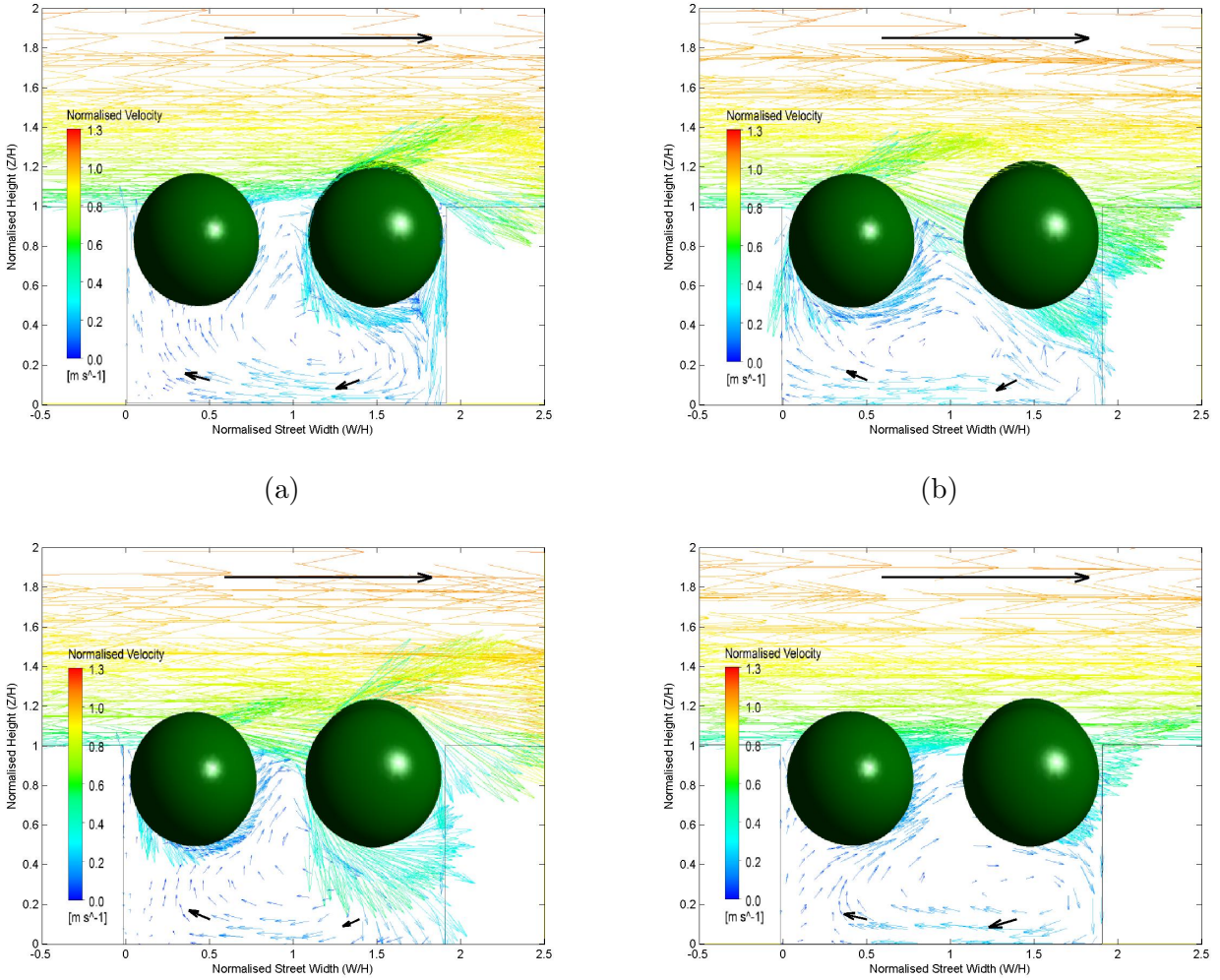

Figure 6.17: Normalised vector plots for CFD results with solid tree crown at various locations along the length of the street. Field Measurements shown in black.

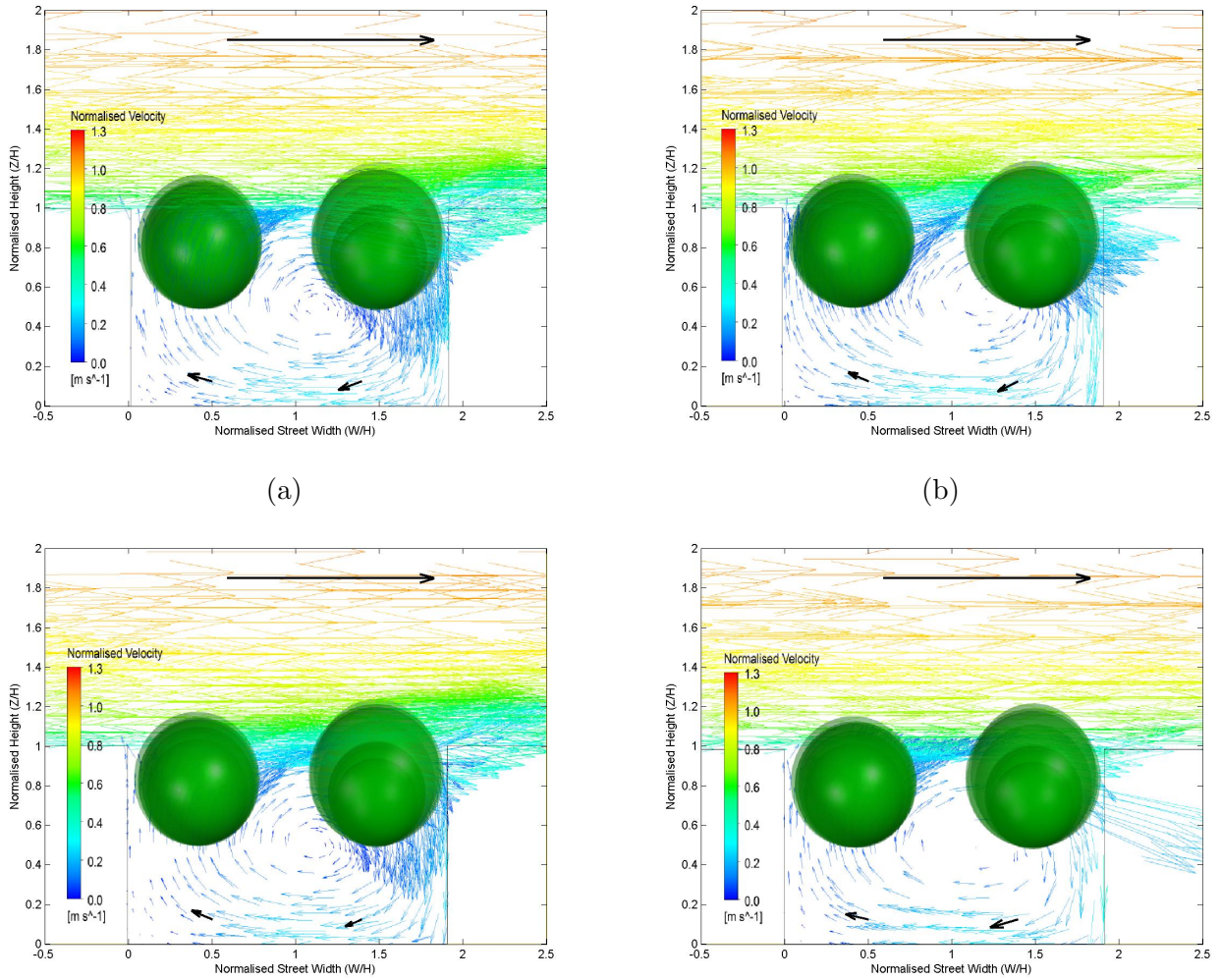

Figure 6.18: Normalised vector plots for CFD results with porous tree crown at various locations along the length of the street. Field Measurements shown in black.

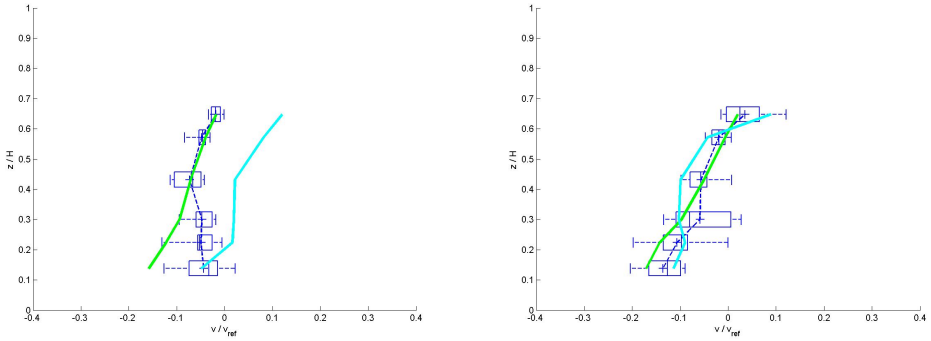

Figure 6.19: Vertical profile. Normalised v velocities for the upwind (left) and downwind (right) side of the street. Solid tree crown (light blue), porous tree crown (green) and field measurements (dark blue)

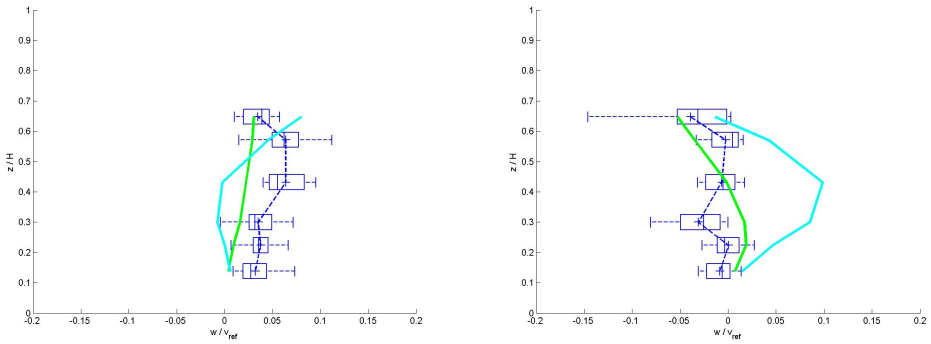

Figure 6.20: Vertical profile. Normalised w velocities for the upwind (left) and downwind (right) side of the street. Solid tree crown (light blue), porous tree crown (green) and field measurements (dark blue)

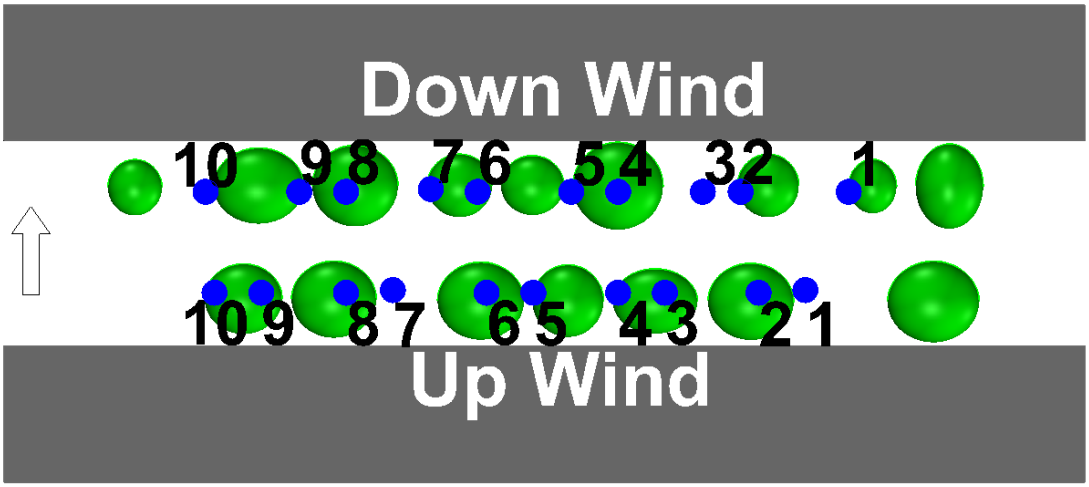

Figure 6.21: CFD and field measurement locations for horizontal profiles taken at a height of 1.5m

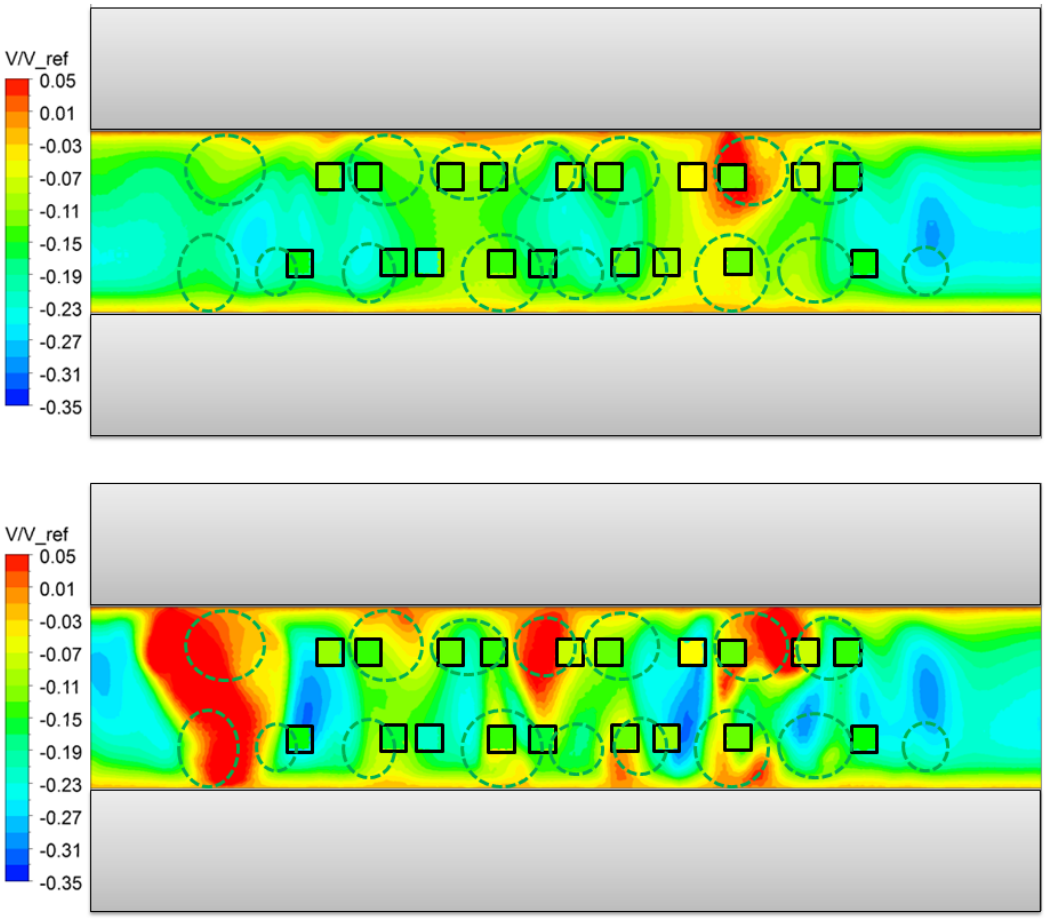

Figure 6.22: Contour plots showing normalised v velocity for porous (top) and solid (bottom) tree crown models. Field measurement data is outlined by black boxes

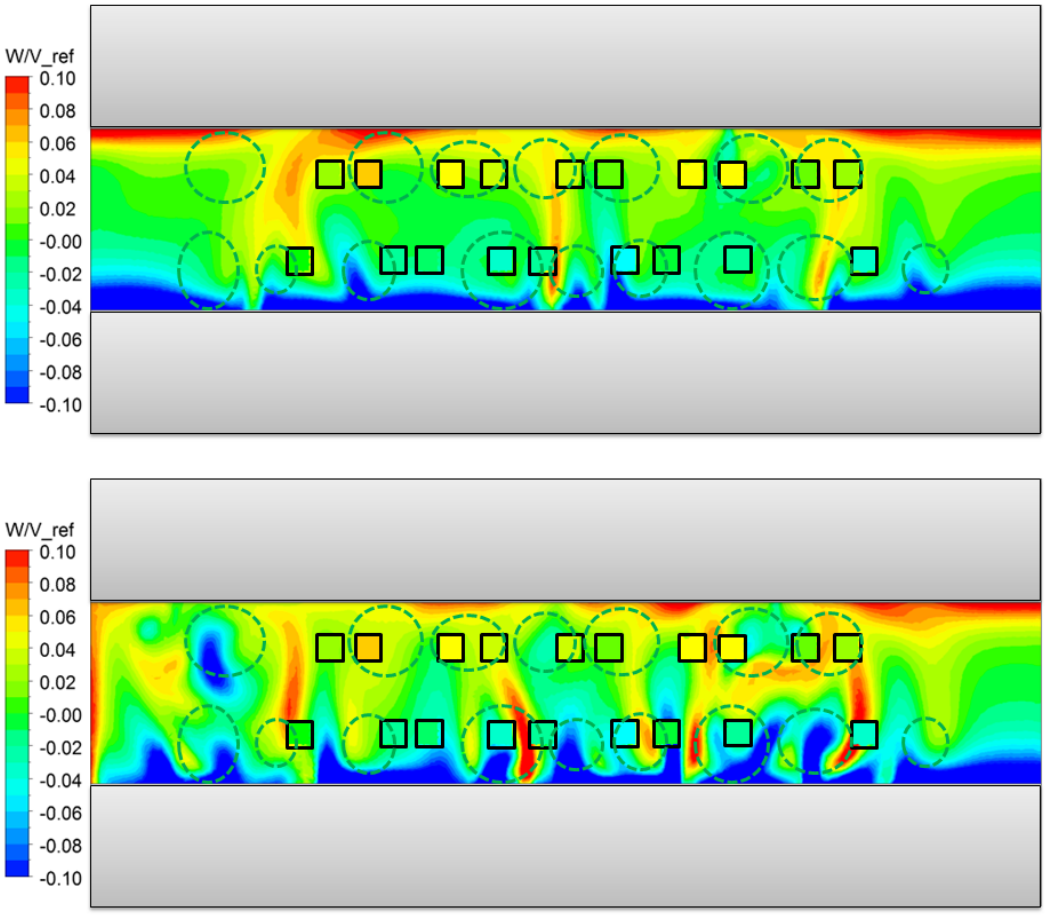

Figure 6.23: Contour plots showind normalised w velocity for porous (top) and solid (bottom) tree crown models. Field measurement data is outlined by black boxes

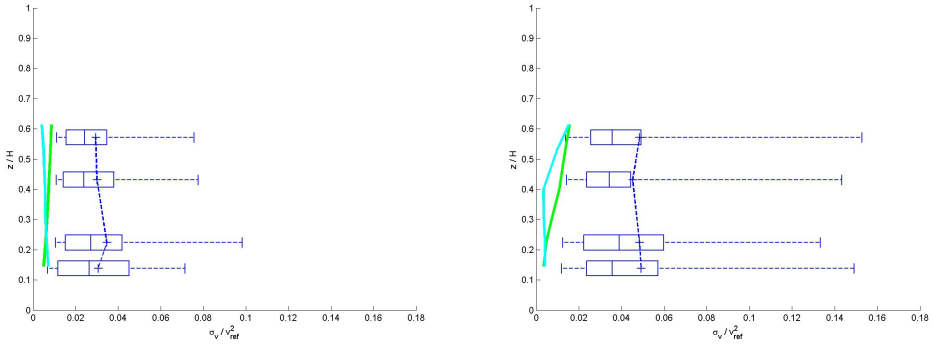

Figure 6.24: Normalised v turbulence intensities for the upwind (left) and downwind (right) side of the street. Solid tree crown (light blue), porous tree crown (green) and field measurements (dark blue)

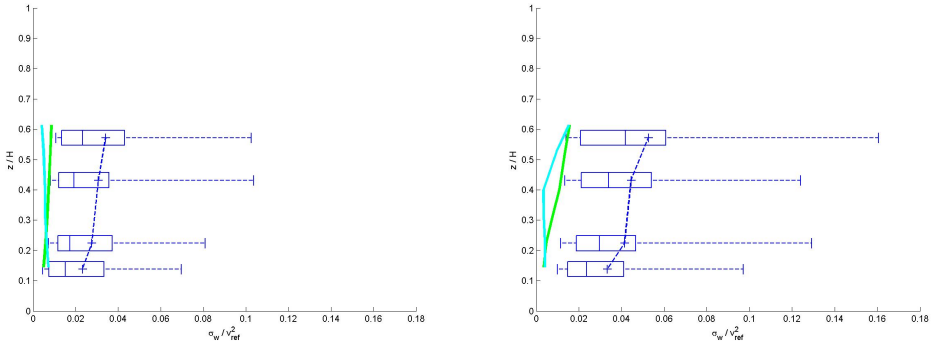

Figure 6.25: Normalised w turbulence intensities for the upwind (left) and downwind (right) side of the street. Solid tree crown (light blue), porous tree crown (green) and field measurements (dark blue)

6.4 Comparison between Tree-Lined and Non Tree-Lined Street

This section provides a comparison between the results of the non tree-lined street and tree-lined street. The CFD model containing trees represented as porous domains is used in this discussion as this was shown to provide the most accurate prediction of the wind field within the field measurement street.

6.4.1 Airflow Patterns

Vector plots taken from the CFD model of the non tree-lined street canyon showed a recirculating vortex forming within the street with the centre of this vortex slightly above the centre of the street canyon (see Figure 6.9). Results taken from the tree-lined street also demonstrated the presence of a vortex, however the size and location of this vortex varied throughout the length of the street (see Figure 6.18).

In order to investigate the three dimensional nature of the flow in greater detail streamlines were produced of the flow within each street canyon as shown in Figure 6.26. Based on this we can see the flow within the non tree-lined street is homogeneous along the length of the street and remains two-dimensional in nature, with a rotational vortex present along the length of the street. In contrast the rotational vortex in the tree-lined street is disrupted by the presence of the tree canopies resulting in a highly inhomogeneous, three dimensional flow. Such a complex flow would be difficult to interpret through point measurements alone. This highlights the importance of the use of CFD and physical measurements being used in tandem to gain a more complete picture of the complex flow which occurs within the built environment.

Although the CFD model represents a simplified version of the real-life street canyons in which field measurements were taken, the data obtained from the field measurements is in support of the CFD findings. The vector plots produced for the non tree-lined street show a consistent pattern across all days with a stable background wind direction unlike the data obtained for the tree-lined street which show a greater day to day variability in the flow patterns, this can be seen in

Appendix 8.0.3.

6.4.2 Wind Speed and Velocities

Comparisons of wind speed between the two streets showed a reduction in wind speeds within the tree-lined street. This was due to the trees being included as momentum sinks. This can be seen in Figure 6.27 which shows the normalised wind speeds at horizontal cross sections of heights of 1.5m and 6.8m. These heights were chosen to represent pedestrian level and canopy level height respectively.

At a height of 1.5m there is a clear reduction in wind speed within the tree-lined street with evidence of stagnation zones forming in which the velocity is zero or close to zero. The variation in flow pattern is evident as the non tree-lined street shows a typically uniform wind speed along the length of the street where as the tree-lined street shows variability in wind speeds along the length of the street, this will be effected by the positioning of the trees within the street.

In order to quantify this reduction in wind speed the measurement planes were split in half along the centre line of the street. The area average of the wind speed was calculated for each side of the street these values are compared and the reduction in wind speeds between the two streets is calculated. These values are reported in Table 6.3. A 43% reduction in the average wind speed is found on the upwind side of the street and 36% on the downwind side of the street at a height of 1.5 m. We can compare these values against the reduction in wind velocities taken from the field measurements. Field measurements showed a reduction of 46% on the upwind side of the street and 34% on the downwind side of the street in v velocities. The across street v velocity has been chosen as this will be the wind component that accounts for the majority of the wind speed under perpendicular flow and at a height of 1.5 m.

Wind speeds at a height of 6.8m are found to give similar findings to those at a height of 1.5m with a far more irregular flow pattern given in the tree-lined street. The total reduction in the average wind speed at this height was found to be 51% reduction on the downwind side of the street and a 44% on the upwind side. This increase reduction compared with a height of 1.5m is to be expected

as the tree canopies will have a greater influence on the flow field at this height.

It is important to not only consider wind speed but also vertical velocity as this parameter will effect the ventilation and pollution dispersion process within the street. Particularly for long streets under perpendicular wind conditions for which the main air exchange process within the street will be transfer of air at roof top level.

Contour plots were produced of the normalised vertical velocity at roof level, these are provided in Figure 6.28. The contour plot produced for the non tree-lined street shows vertical velocities to be typically negative on the downwind side of the street for which air is being brought into the street and positive on the upwind side of the street for which air is being removed from the street. In the case of the tree-lined street no such pattern exists and the location of positive and negative vertical velocities is highly variable. Calculation of the average magnitude of vertical velocities at roof level found a 51% decrease for the tree-lined street. This would equate to approximate 51% reduction in mass flow rate of air into and out of the street.

6.4.3 Turbulence Statistics

In Chapter 4 we saw how TKE is created in the shear layer above the roof tops and transported down into the street canyon level due to strong vertical velocities at roof top level. This process can be seen in Figure 6.29 which shows contour plot of TKE at vertical cross section taken from the non tree-lined street. TKE levels are found to be highest above roof top level and at greater heights on the upwind side of the street. Comparing this with the contour plot taken on the tree lined street we can see that the presence of the tree canopy disrupts this process and leads to a reduction in TKE levels within the street. In the case of the CFD model this is due to the presence of a turbulence sink, in reality this would be due to presence of trees causing large scale turbulence to be broken down into smaller scale eddies which quickly dissipate.

Figure 6.29 also shows contour plots of TKE taken in the area between tree canopies we can see that in this location the transport of TKE is less disrupted by the presence of the tree canopies however the TKE levels are still lower than

those found in the non-tree lined street.

Figure 6.30 shows the variation in TKE throughout the length of the street. We can clearly see the higher turbulence levels on the downwind side of the non tree lined street. Similarly on the tree lined street, higher turbulence levels are found on the downwind side of the street however this is interspersed with areas of low turbulence due to the presence of the turbulence sinks thus resulting in an overall reduced turbulence levels.

Table 6.4 gives the percentage reduction in turbulence intensity values between the two streets. Overall the turbulence levels are found to decrease by 66% on the downwind side of the street at both a height of 1.5m and 6.8m. On the upwind side of the street turbulence levels decrease by 76% at a height of 1.5m and 78% at a height of 6.8m. This is slightly larger than the percentage reduction calculated from the field measurements which found 34% - 50% reduction on the upwind side of the street and 58% - 62% reduction on the downwind side of the street.

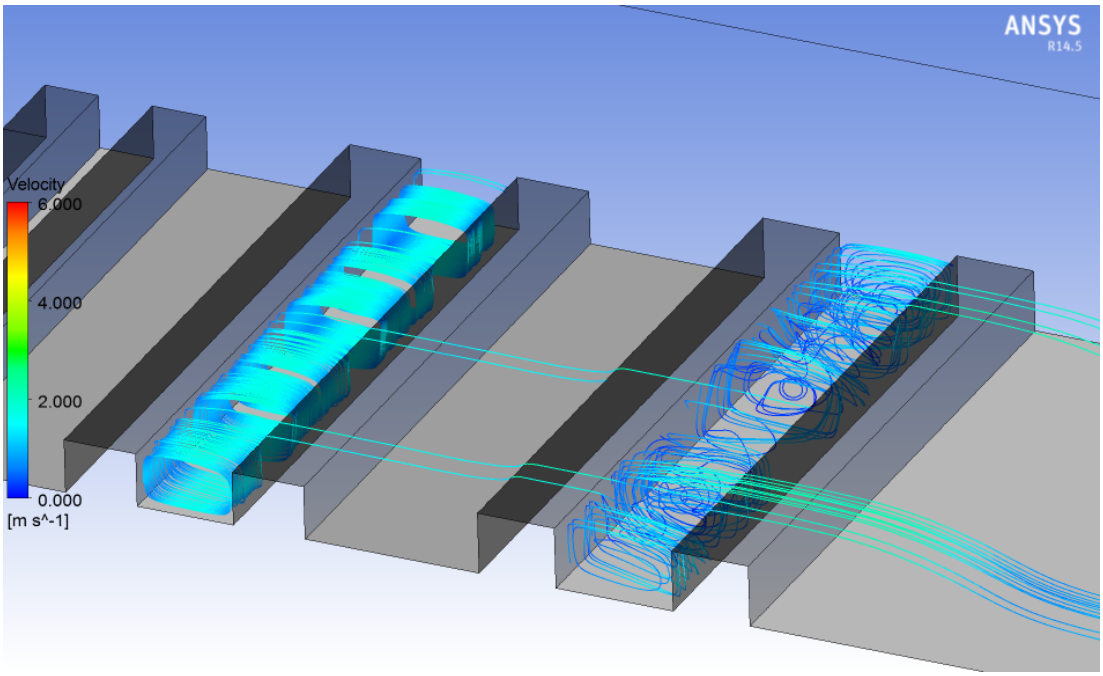

Figure 6.26: Streamlines illustrating flow patterns within empty street (left) and tree-lined street (right)

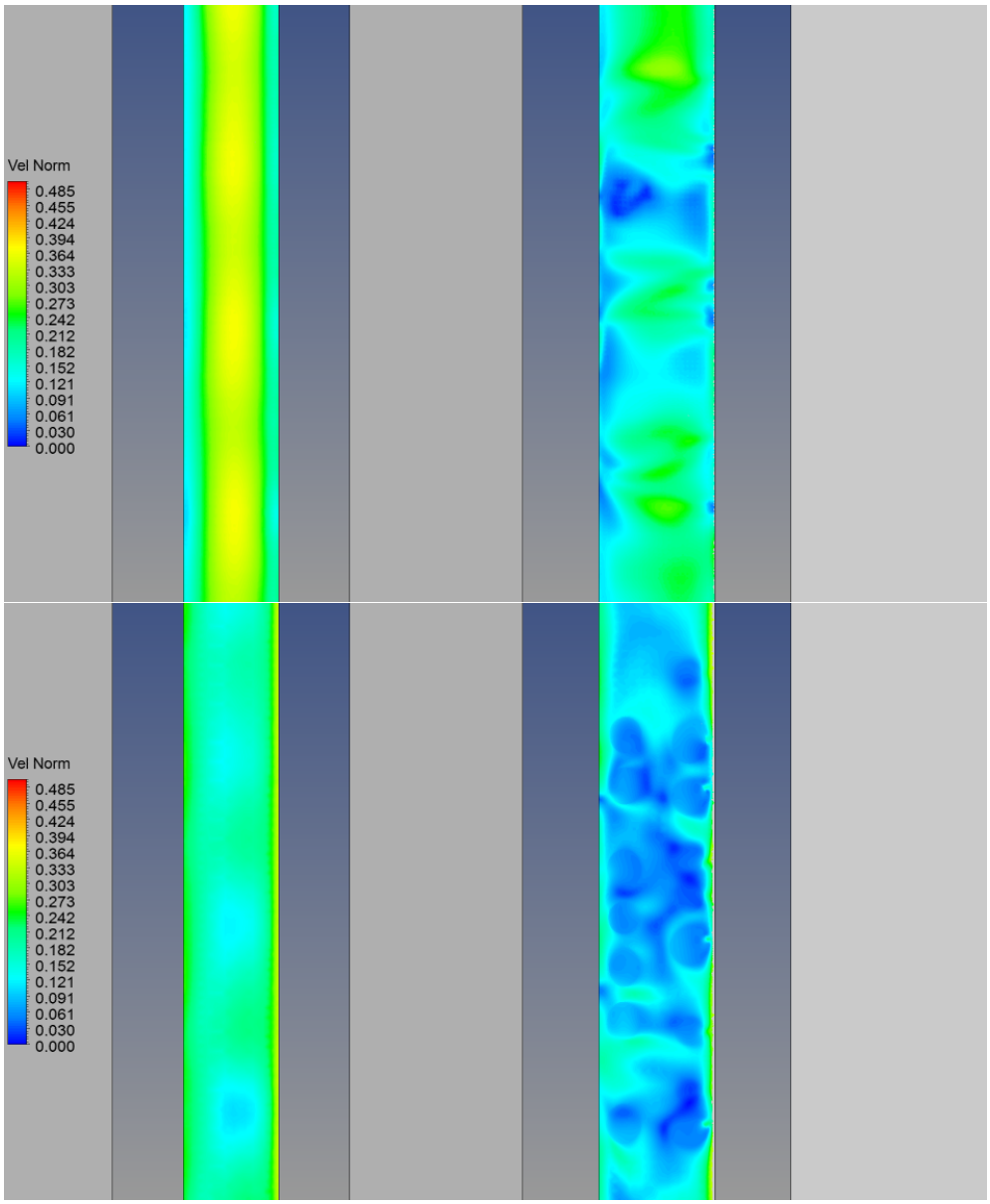

Figure 6.27: Contour plots showing horizontal cross-section of normalised wind speed for empty street (left) and tree-lined street (right) at heights of 1.5m (top) and 6.8m (bottom)

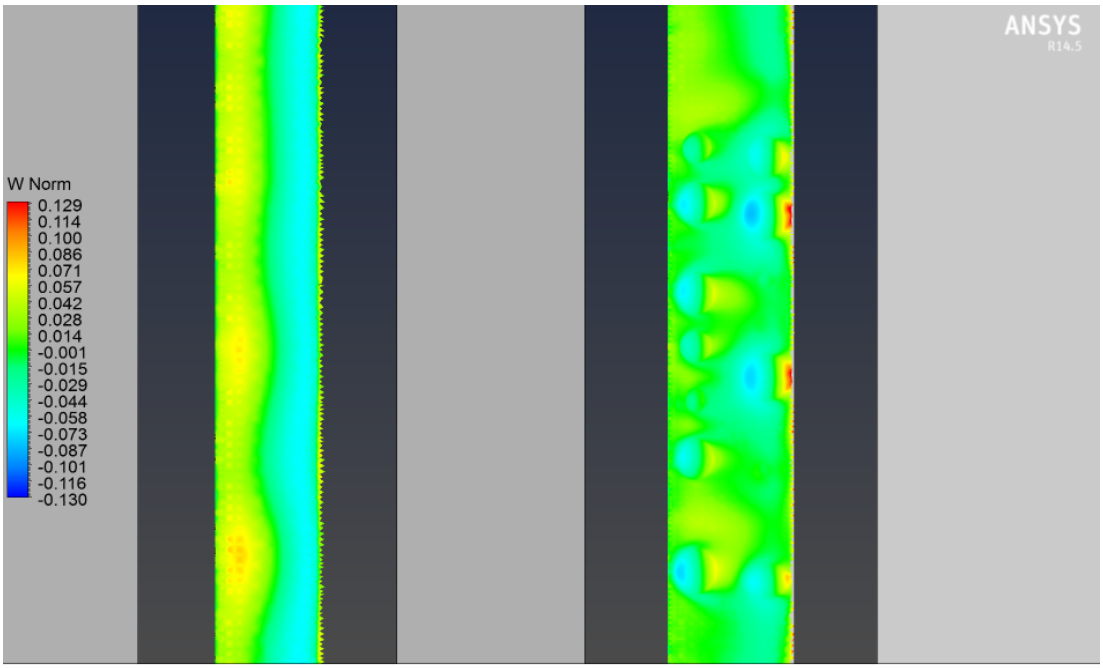

Figure 6.28: Contour plots showing horizontal cross-section of normalised vertical velocity for empty street (left) and tree-lined street (right) at roof height

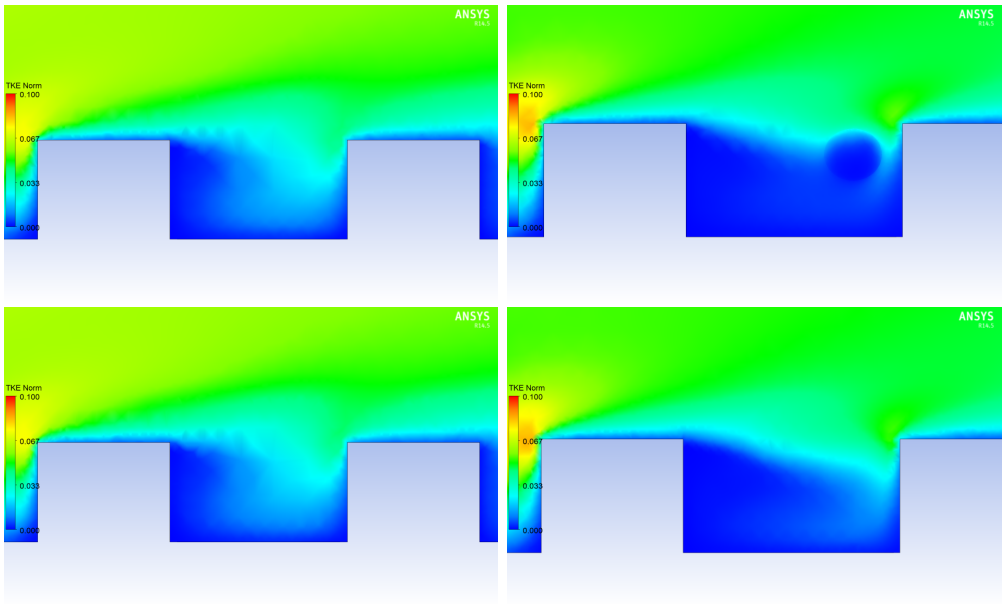

Figure 6.29: Contour plots showing normalised TKE for empty street (left) and tree-lined street (right) taken at two vertical cross sections within the street

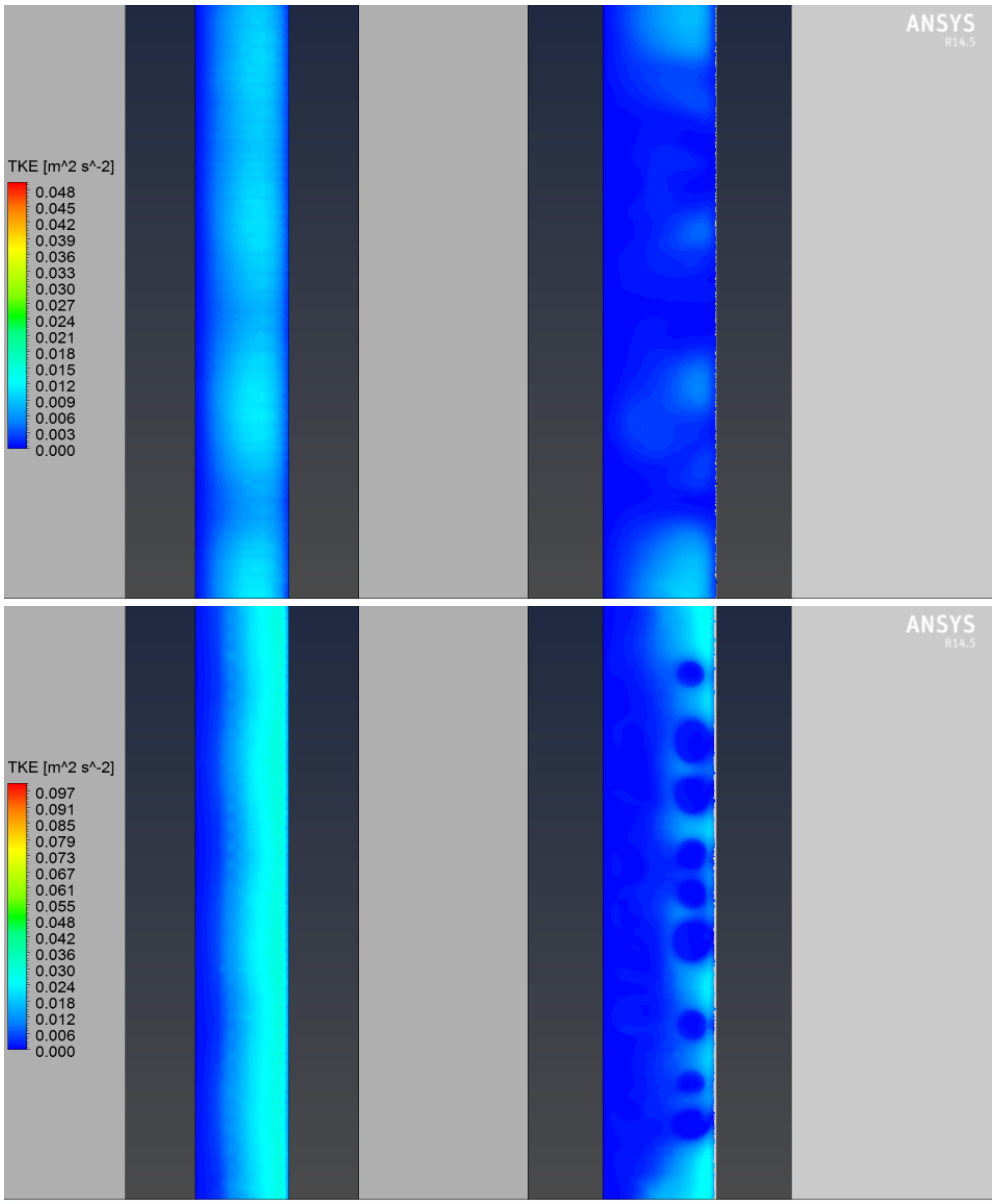

Figure 6.30: Contour plots showing horizontal cross-section of normalised TKE for empty street (left) and tree-lined street (right) at heights of 1.5m (top) and 6.8m (bottom)

Height [m]	Upwind % reduction	Downwind % reduction
1.5	43	36
6.8	43	51

Table 6.3: Percentage reduction in wind speeds at pedestrian height (1.5m) and canopy height (6.8m) between tree-lined and non tree-lined street

Height [m]	Upwind % reduction	Downwind %reduction
1.5	76	67
6.8	78	67

Table 6.4: Percentage reduction in turbulence intensities at pedestrian height (1.5m) and canopy height (6.8m) between tree-lined and non tree-lined street

6.5 Summary of Main Findings

6.5.1 Non Tree-Lined Street

In this section of the chapter we have assessed the ability of CFD to model the flow within a full scale street canyon through the comparison with field measurement data. We have explored the effect of both roof shape and street furniture on the flow within the street.

Two roof shapes were tested, a flat roof and pitched roof. It was found that the pitched roof shifted the centre of the vortex lower within the street canyon, thus providing a poor match with experimental data. The flat roof was therefore chosen to be used throughout the testing.

Two ways of including street furniture were tested: The addition of sand grain roughness to the floor of the domain and the addition of four rectangular blocks along the length of the street to represent the hedges, boundary walls and parked cars within the street. Both methods showed some promising results:

- The addition of roughness to the floor of the street gave excellent correlation with the field data taken at pedestrian level (1.5m) however above this height the velocities tended to be slightly under-predicted although still lay within the range of field data collected

- The addition of street furniture to the CFD model provided a good match with experimental data in terms of the shape of the velocity profile produced on the upwind side of the street however all velocities were under-predicted in particular the w velocities were significantly under-predicted when compared with the other two models. The flow pattern produced by this model did not provide a good match with experimental data

Although the addition of street furniture to the CFD model can provide improved prediction at certain locations it can also have a negative effect on the results in other areas. Therefore the addition of street furniture should be done with care and it is recommended that more work be carried out in this area.

6.5.2 Tree-Lined Street

The geometry of each individual tree canopy was included within the CFD model as an ellipsoid with dimensions taken directly from the field measurements. Through the analysis of the results from the CFD models for a tree lined street and comparison with experimental data the following conclusions have been found:

- A solid tree canopy model was shown to provide a poor prediction of flow patterns within a tree lined street when compared with field measurements.
- The porous tree canopy offers promising results when compared with field measurements. Flow patterns, velocity and turbulence profiles were generally well predicted by the porous model.

In conclusion it has been shown that the porous tree crown model with momentum and turbulence sink based on the leaf area density and drag coefficient can offer a good match with field measurement data and therefore offers a viable way of including trees and vegetation within CFD models of the built environment. However in order for this to be implemented in practical applications it will be necessary to generate guidelines on typical leaf area densities (including the effect of branches) and drag coefficients for various tree species. Drag coefficients will need to be provided as both a function of local wind speed and tree spacing / planting densities.

6.5.3 Comparison of Tree-Lined and Non Tree-Lined Street

Analysis of streamlines within the non tree-lined street showed a two dimensional flow pattern, with no variation in flow patterns along the length of the street. The tree-lined street however showed a highly complex three dimensional flow pattern with the centre of the rotational vortex shifting location along the length of the street.

The inclusion of trees to the street canyon were shown to significantly reduce wind speeds. This was quantified as a 42% reduction on the upwind side of the street and 36% at a height of 1.5m and a 44% on the upwind side and 51% at a height of 6.8m. There was also shown to be a 51% reduction in vertical velocities

at roof height this would dramatically reduce the amount of air exchange at roof height.

The presence of the trees also lead to a reduction in turbulence values. The percentage decrease was found to be 66% on the downwind side of the street at heights of both 1.5m and 6.8m and a reduction of 75% on the upwind side at a height of 1.5m and 78% at a height of 6.8m.

Chapter 7

Discussion

Throughout this thesis we have examined the capabilities of CFD modelling to provide accurate predictions of airflow within tree-lined streets. This involved the testing of several types of street canyon model within CFD; from the idealised street canyon used for wind tunnel modelling to the more complex full scale street canyon containing trees in which field measurements were taken. The information gained from carrying out this rigorous testing can provide guidelines to fellow CFD modellers on the lessons learned and limitations for CFD modelling of street canyon flow and flow around trees as well as developers of CFD software. This will form the first section of this Discussion chapter.

In addition to gaining a greater understanding into the capabilities of CFD modelling, this research has also provided insight into the effect of tree planting on airflow within street canyons. Through the use of field measurements and CFD modelling it was possible to assess the differences in the airflow patterns, velocity and turbulence levels between tree-lined and non tree-lined streets. These findings will be of interest to urban planners and designers who wish to use trees as a mitigation tool against issues relating to high wind speeds and pollution levels. The final section of this chapter will therefore aim to put the results of the previous chapters in a context which is relevant to the issues of pollution dispersion and pedestrian comfort.

7.1 Best Practice Guidelines on CFD Modelling of Street Canyons and Trees

The use of Computational Fluid Dynamics modelling in the built environment is widespread for indoor applications; however the successful and systematic application of CFD for the outdoor environment is still hindered by lack of understanding on turbulent characteristics and boundary conditions necessary for the accurate modelling of a variety of urban atmospheric flow [Guillas et al., 2014]. Through summarising the lessons learned in this research we hope to guide CFD users through important aspects of this type of modelling and any possible limitations or areas for future development.

Benchmarking and Validation

The importance of performing benchmark testing and validation was highlighted in this research. Carrying out a benchmark test allowed for the understanding of the strengths and weaknesses of the CFD model of a simple street canyon before moving on to modelling more complex cases. Once the weaknesses have been identified the modeller can determine the extent to which these weaknesses will impact the outcome of the study, determine the most appropriate choice of input parameters and numerical models, such as turbulence models, and how the specification of the geometry and mesh impact the results of the CFD model.

Performing a benchmark study at the early stages of this research allowed for an understanding of the limitations of the Standard k-ε model in the prediction of street canyon flows with the main limitation identified as being an underprediction of TKE within and above the street canyon. It important to identify the extent of this limitation at an early stage as this would have an influence on any results from further CFD models to be carried out later in the research process.

A mesh sensitivity at this stage allowed for a more detailed understanding of how the mesh construction can influence the results within the street canyon. In particular it was found that the often quoted mesh size to be used within a street canyon of H/10 with H being the height of the street canyon did not

provide the resolution needed to offer good prediction of TKE values above and within the street. In fact a mesh size of H/30 was needed to provide accurate predictions of TKE values. This was an important finding not just for the later models constructed as part of this research but in general for CFD research into street canyon flow.

Atmospheric Boundary Layer Flow

In order to accurately model airflow within the built environment it is first necessary to simulate the correct atmospheric boundary layer flow. Problems in producing such flow in CFD have been identified in the past, as boundary layer profiles have a tendency to change as they move downstream. This was highlighted in the benchmark study carried out for this research, in which turbulence levels varied downstream of the inlet.

In order to try and reduce this decay as much as possible three different ways of specifying the inlet boundary conditions were tested. From this it was determined that the profiles suggested by Yang et al. [2009] offered the best prediction of TKE downstream of the inlet when compared against experimental data. The disadvantage of this method is that the profile used to specify TKE levels contained two empirical constants which should be found through fitting the profile to experimental data. This is a problem if no experimental data is available, as was the case in modelling the full scale streets for this research, and is often the case when modelling the atmospheric boundary layer. To overcome this problem a prediction of the atmospheric boundary layer TKE profile was obtained using the ESDU method [Engineering Sciences Data Unit, 1984]. Based on the predicted velocity and turbulence profiles obtained using this method it was possible to find the two empirical constants required for the implementation of the profiles specified by Yang et al. [2009].

In addition to specifying the correct inlet boundary conditions it is also important to apply the correct roughness to the floor of the domain. This can be done by applying the sand grain roughness to the floor boundary rather than explicitly modelling roughness blocks. The suggested value to be used for the sand grain roughness height is 30*Zo [Blocken et al., 2007]. However there is also a fundamental restriction on the maximum height the sand grain roughness can

take as it should not be greater than half the height of cell next to the wall. It is therefore difficult to satisfy both criteria without using an extremely coarse mesh which can lead to inaccuracies in the simulated boundary layer. Therefore a compromise must be met between mesh size and sand grain roughness. By carrying out a mesh sensitivity test it is possible to find the optimal compromise between mesh size and sand grain roughness height. In addition since it is only necessary to specify sand grain roughness at the outer terrain and not within the area of interest it may be possible to use a coarser mesh within this region and finer mesh within the area of interest thus allowing for a larger sand grain roughness.

Altering the values of the k-ε model constants was found to offer a reduction in the amount of decay occurring in the TKE profiles as we move downstream of the inlet. In particular it was found that the default value of 0.09 for C_μ should be lowered to a value of 0.025 this is in support on previous recommendations on values of C_μ to be used when modelling the atmospheric boundary layer by authors such as Beljaars et al. [1987] and Richards and Hoxey [1993] who have also suggested that the default value of 0.09 is too high and should be lowered for such simulations. This is an important finding for anyone interested in modelling the atmospheric boundary layer using the k-ε model and CFD.

Parameter Selection and Calibration

CFD models of the built environment generally require the specification of a large array of input parameters with little information on the value these parameters should take. Therefore it is important to assess and, if possible, reduce the amount of parametric uncertainty within the CFD model. This was the aim of the Bayesian Calibration process, outlined in Section 4.1.4, which investigated the uncertainty in the empirical constants contained within the k-ε turbulence model for use in modelling atmospheric boundary layer flows. Through this calibration process we were able to update the values of the k-ε model parameters from the default values. As mentioned above these updated values were found to reduce the amount of decay present in the boundary layer TKE profiles and thus provide a more homogeneous boundary layer model. However it should be noted that although the Calibration process provided improved prediction of boundary

layer flow within an empty domain, when the updated constants were applied to a domain containing a street canyon improved predictions were not achieved. This would be considered a limitation of the current work as the results of the calibration process seem to be only relevant to the case study which has been calibrated and can not be easily applied to other scenarios.

Although the Calibration process may be case study specific it is still a useful tool as it allows for a greater understanding of the input parameters and any uncertainty relating to these values and provides a means for propagating this uncertainty through to the model output. This could be particularly useful in cases such as containment dispersal in which a clear understanding of the contaminant levels and how this varies with uncertain model input is crucial as this could mean the difference between safe and unsafe limits of exposure.

Geometry

The built environment comprises buildings of highly complex and intricate design as well as a large number of street level obstacles which can disrupt the flow. To model such detail within CFD would require a large amount of information often not available. The construction of the geometry and mesh would be extremely time consuming and the running of the CFD model would require a great amount of computational power. Often such accurate and detailed flow simulations are not needed. It is therefore necessary to simplify the geometry used for the CFD model.

The geometry used in the modelling of the full scale street canyons was greatly simplified. Two types of building geometry were tested; a flat roof and a pitched roof model. It was found that the flat roof model offered the most favourable predictions of airflow within the street when compared with field measurements. The simple street canyon geometry implemented here has been used by many researchers in the past when investigating flow field within streets. The results of this study would suggest that such simple models can be valid in the research into street canyon flow as they are capable of capturing the main flow features in real life streets with complex geometry and providing reasonable quantitative predictions of velocities. This is therefore a positive finding for this area of research.

It is however noted that the pitched roof model which offers a closer representation of the full scale street geometry did not provide the best match with experimental data. This raises the question as to whether the most accurate representation of the real life geometry always provides the best predictions of the flow. For example the Ahmed car [Ahmed et al., 1984] is a model car specifically designed for wind tunnel and water flume testing. Its shape has been altered from that of a traditional car in order to provide more accurate flow prediction. Clearly the question of best method for simplification of building geometry is still an open ended question and an interesting area for future research.

In addition to the building geometry, the street furniture also had to be simplified. Three cases were tested: one which contained no street furniture, a second in which sand grain roughness was applied to the floor of the domain and a third in which two rectangular blocks running the length of the street were included to represent the street furniture. The model containing no street furniture provided good predictions of wind velocities compared with field measurements with the exceptions of the velocities at the lowest height on the upwind side of the street. The model with sand grain roughness showed good predictions for the velocities at lowest height within the street (e.g. pedestrian level) but an underprediction of velocities above this height. The third model predicted the shape of the velocity profile within the street well but velocities were under predicted at all heights. Therefore the street canyon without street furniture was chosen to be used throughout this work. However in situations where wind speeds at pedestrian level are of most interest, the sand grain roughness method may be the most appropriate. Clearly this is an important area of research for flow within the built environment and one which requires further work.

Turbulence Model Selection

One important consideration in CFD modelling is turbulence model selection as this can impact not only the prediction of turbulence quantities but also flow patterns. The model selected for use in this study was the k-ε turbulence model due to its prolific use in previous street canyon studies thus allowing us to build on the work of previous researchers.

This research found that adaption of the Standard k-ε model in the form of

altering the model constants can provide improved predictions for atmospheric boundary layer flow. This may present an opportunity to developers in the field of CFD who are interested in providing new and updated turbulence models. However any alterations to the k-ε model constants should be done with care as improvement of the model for certain flow scenarios may be detrimental to other scenarios. For example if the k-ε model is to be adapted for use in atmospheric boundary layer flow it is likely that its use would be limited to these types of flows only, as has been demonstrated in this research.

Running a simple CFD model of a street canyon and comparing it with wind tunnel data found the Standard k-ε model was able to provide excellent prediction of both flow patterns and velocity values within the street. Comparisons of TKE data showed the Standard k-ε model was not able to accurately capture the peak in turbulent kinetic energy which occurs above the roof of the upwind building. Another limitation of the Standard k-ε model was found through analysis of field measurements which found the turbulence within the street canyon to be unisotropic; the k-ε model is an isotropic turbulence model and therefore will not fully be able to capture the turbulent field within the street.

Given these strengths and weaknesses the Standard k-ε model can be a viable option in those cases in which turbulence is not deemed to be a significant factor. However for those cases in which turbulence plays an important role, such as pollution dispersion studies, it is recommended that other turbulence models are investigated.

Tree Model

There have been a limited number of studies into how to include trees and vegetation within CFD models carried out in the past. The most popular method for inclusion of trees for those authors who have attempted these studies is to include the tree as a separate domain or sub-domain within the model with momentum sink and turbulence source or sink. There has however been no comparisons of such models against field measurements in order to validate their use.

The trees within this research were incorporated into the CFD model as porous domains with momentum and turbulence sinks. Comparisons of the CFD results against field measurements found good agreement of flow patterns within the

street. Excellent prediction of wind velocities were given at greater heights within the street. The CFD model was found to slightly over predict the velocities at pedestrian height. This is partly due to the lack of street furniture within the CFD model as well as the tree trunks being left out of the model. The tree trunks were not included in order to simplify the geometry of the model. It is recommended that further work be carried out into the significance of the effects of the tree trunks.

The formulation of the both the momentum and turbulence sinks requires the specification of the drag co-efficient and leaf area density. Thus a whole range of tree types could be modelled provided these two coefficients are known. Therefore a recommended useful extension to this work would be to determine a set of guidelines for approximate values of drag coefficient and leaf area density for example different tree species, sizes, seasons etc.

This method for inclusion of trees in CFD shows great promise due to its ease of implementation and the fact that it does not require a large mesh, the specification of a large number of unknown parameters or a great amount of computational power making it a practical choice for those in industry. The discussion presented here has highlighted some areas in which the model could be improved or further work which would make the implementation of such a model even more accessible.

In addition to providing guidance for fellow CFD modellers, the research carried out for this PhD may also be of interest for software developers within the field of CFD. Based on the methodology outlined in this research developers could potentially add a utility to their CFD software which allows users to include the effects of vegetation by simply specifying the region within the model which is effected by vegetation and, if the information is available, the type of tree species and time of year. This would offer a much more user friendly option to those within industry to include the effects of vegetation when modelling large scale urban areas.

7.2 The Effect of Tree Planting on Airflow within Street Canyons

In sections 5.4 and 6.4 of this thesis comparisons were made between airflow within a non tree-lined street and tree-lined street. It was found that trees cause significant disruption to the typical flow patterns we would expect to see in a regular street canyon. They also lead to a reduction in wind speed and turbulence within the street. The purpose of this section of the thesis will be to understand the implications of these findings on issues relating to the built environment, specifically pollution dispersion and pedestrian wind comfort.

7.2.1 Pollution Dispersion

The assessment of pollution levels in areas containing tree and vegetation planting is a complex problem. Trees can extract pollutants from the air through biological interactions with the pollutants and deposition on the surface of the tree. Trees can also impact the airflow and ventilation within a street. These airflow processes play a crucial role in removing pollutants away from pedestrian level and therefore a full understanding of the effect trees have on such processes is vital.

Results of the research presented in this thesis found there to be the formation of stagnation zones within the tree lined street. This was due to the presence of the trees disrupting the rotational vortex within the street and causing the centre of this vortex to shift position. This is illustrated in Figure 7.1 in which the dark blue areas indicate locations of little or no airflow it can be seen that these areas lie within pedestrian zones. A quantitative comparison of wind speeds taken in tree-lined and non tree-lined streets showed a significant reduction at pedestrian level within the tree-lined street. Table 7.1 shows the average reduction in wind speeds for the tree-lined compared with the non tree-lined street taken at pedestrian height (1.5m) and tree canopy height (6.8m) given by the CFD results. These findings would suggest that the presence of trees can reduce the level of ventilation which occurs at pedestrian level and thus have the potential to result in higher pollution levels as pollutants remain trapped in regions of stagnant airflow.

Velocities at roof level are key in the assessment of pollutant removal and ventilation of street canyons. The main method for pollutant removal for long street canyons under perpendicular wind directions, such as the one investigated here, would be via air exchange with the atmosphere above the street canyon. Therefore the rate at which this occurs is vital in determining the ventilation and air quality within the street. Results of the full scale CFD model carried out for this research found that vertical velocities were reduced at roof level by approximately half (see Table 7.2) for the tree-lined street. Therefore the tree-lined street is 50% less effective at transferring pollutants from the street canyon to the upper atmosphere thus leading to the potential for pollutant build up within the street.

In addition to affecting wind speeds within the street, trees also have an impact on turbulence levels. Comparisons of tree lined and non tree-lined streets found a significant reduction in turbulence levels within the tree-lined street. This is shown both graphically in Figure 7.2 and in quantitative form in Table 7.3. This is thought to be due to presence of the trees breaking down large scale turbulence into smaller scale turbulence which is quickly dissipated. This leads to an overall loss in the TKE budget.

Turbulence is an important mechanism in the removal and dispersal of pollutants from a street. Therefore such a reduction in turbulence levels is likely to have a negative impact on pollution levels. It should be noted that the sampling rate of the anemometer was 1 Hz and therefore any small scale turbulence would not be detected. This highlights a limitation of the field measurements, however the results still indicate a clear reduction in larger scale turbulence which is known to have the greatest effect on pollution transport.

7.2.2 Pedestrian Wind Comfort

Downdrafts and corner accelerations can lead to high wind speeds around buildings in pedestrian areas. Although such effects are not generally associated with street canyon of the type studied here it is still worth putting the findings of this investigation in the context of pedestrian comfort as the inclusion of trees is one of the most commonly used mitigation tools against high wind speeds.

Wind which can cause discomfort to pedestrians is generally defined as wind effects which are noticeable to the pedestrian to the point of annoyance and will lead to avoidance of certain areas. Wind safety refers to wind conditions which have the ability to destabilise or cause pedestrians to fall thus causing distress or danger to the pedestrian [Blocken and Carmeliet, 2004].

The criteria used to assess such wind effects in the built environment will often involve a minimum wind speed threshold for discomfort and a frequency of occurrence associated with the threshold. For example for an area to be comfortable for use as thoroughfare (e.g. passage from A to B) the associated wind threshold may be 6m/s and the probability of exceedance 5%. This means wind speeds of greater than 6m/s can not be exceeded for more than 5% of the year if this area is to be suitable for comfortable walking.

The wind speed often used in the specification of these criteria is the gust wind speed. This is a combination of both mean wind speed and turbulence levels as follows:

$$U_g = U + k.\sigma_u \tag{7.1}$$

Where U_g is the gust wind speed, U is the mean wind speed, k is a constant and σ_u is the turbulence intensity. The factor k varies within literature between the values of 1 - 6.

Turbulence and wind gusts are particularly important in the assessment of wind comfort and safety as people tend to be more susceptible to sudden changes in wind speed. For example Murakami and Deguchi [1981] reported the mean wind speed needed to destabilise a pedestrian in a steady flow was 25 -33 m/s where as Hunt et al. [1976] found that wind gusts (e.g. sudden change in wind speed over the period of a few seconds) of 15 - 23 m/s was enough to cause to destabilise or result in a safety issue.

This research undertaken for this PhD has shown the significant reduction in wind speeds and turbulence that can be caused by the presence of trees within the built environment. Since pedestrian comfort and safety is solely dependent on both mean wind speed and turbulence, if implemented correctly trees can provide a great aid in improving pedestrian wind comfort.

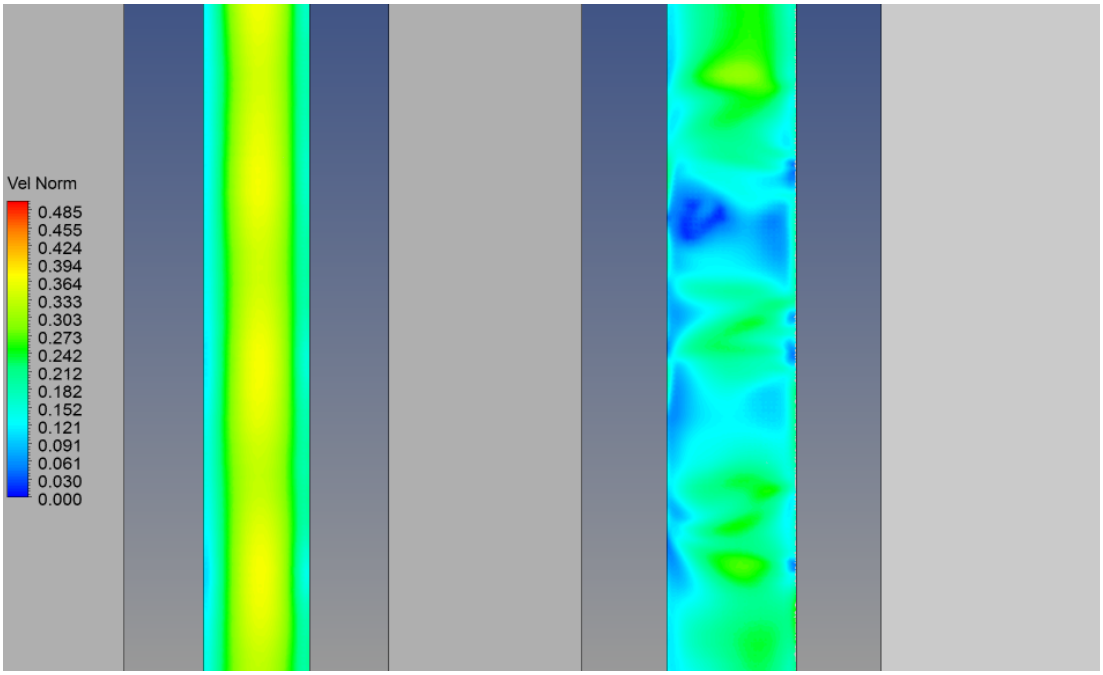

Figure 7.1: Contour plots showing horizontal cross-section of normalised wind speed for non tree-lined street (left) and tree-lined street (right) at height of 1.5m

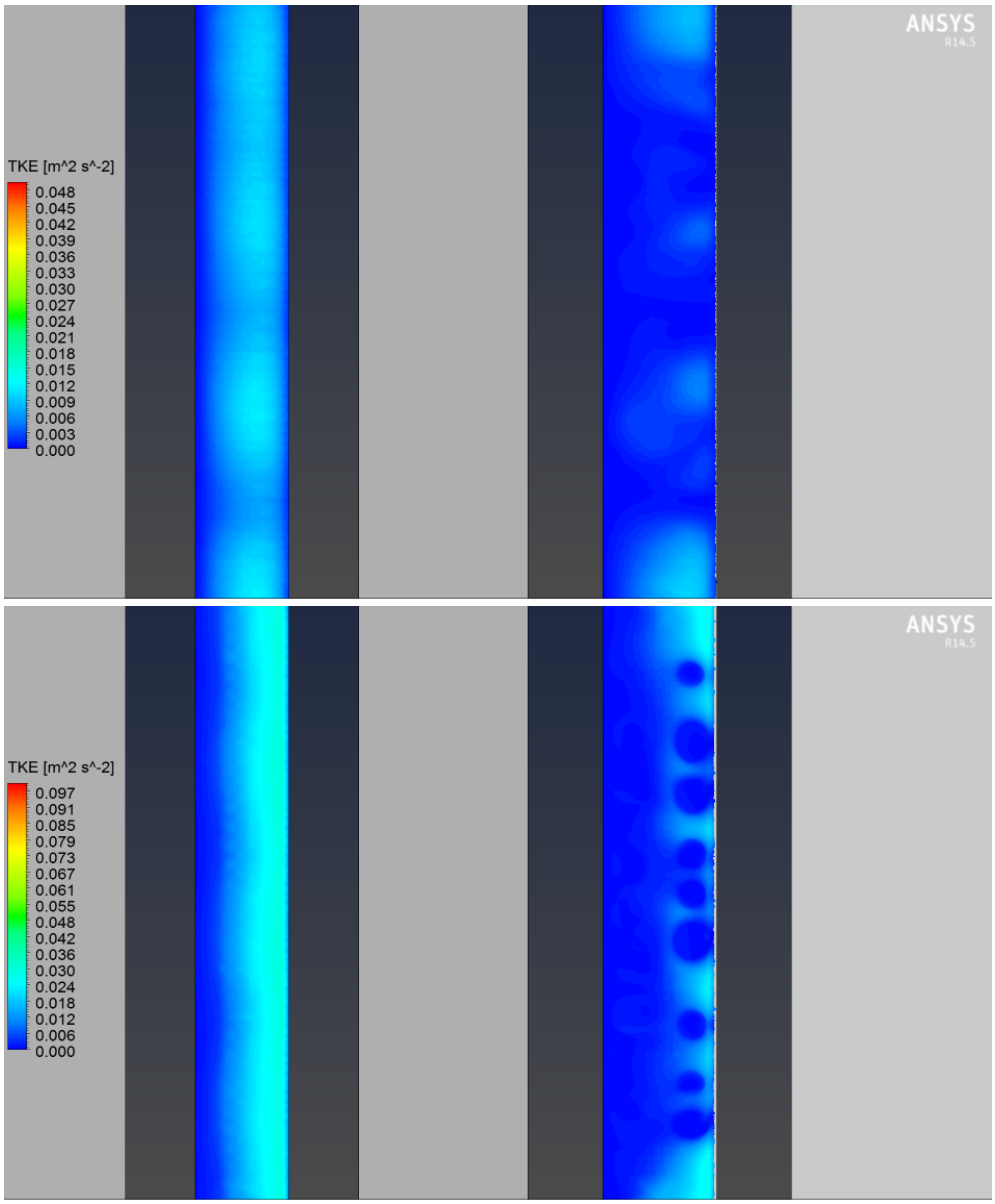

Figure 7.2: Contour plots showing horizontal cross-section of normalised TKE for non tree-lined (left) and tree-lined street (right) at heights of 1.5m (top) and 6.8m (bottom)

Height	Upwind % reduction	Downwind % reduction
1.5m	43	36
6.8m	43	51

Table 7.1: Percentage reduction in wind speeds at pedestrian height (1.5m) and canopy height (6.8 m) for tree-lined street as compared with non tree-lined street

Height	Upwind % reduction	Downwind % reduction
Roof Height	54	48

Table 7.2: Percentage reduction in vertical velocity at roof height for tree-lined street as compared with non tree-lined street

Method	Upwind % reduction	Downwind % reduction
CFD	76	67
Field Measurements	60	44

Table 7.3: Percentage reduction in average turbulence intensities at pedestrian height (1.5m) for tree-lined street as compared with non tree-lined street given by field measurements and CFD results

Chapter 8

Conclusions

The research undertaken for this PhD set out to investigate the influence of trees on airflow within street canyons and the capabilities of CFD in accurately predicting such flow. This involved the successful modelling of airflow within a tree-lined street using CFD techniques which showed favourable comparisons with field measurements. The information gained from this process can offer guidance to the CFD community on how to model the outdoor environment containing tree planting.

In particular, difficulties in replicating a homogeneous urban boundary layer were highlighted with strong interdependencies between the inlet boundary settings, turbulence model and turbulence constants found.

Geometry specification within the CFD model was also found to be an important consideration. Simplification of building geometry is often necessary in the CFD modelling of an outdoor urban area. The idealised street canyon consisting of two rectangular blocks was found to offer favourable prediction against field measurement results which is in support of many previous studies which have used this type of geometry.

Bayesian Calibration was found to be a useful method in quantifying and reducing the amount of uncertainty associated with input parameters of CFD models. One limitation of this process was found to be the fact that the calibration was case specific and the results did not readily apply to other scenarios.

The trees within the CFD model were represented as porous sub-domains with momentum and turbulence sinks the values of which were dependent on the

drag coefficient and leaf area density. This method was found to be successful in providing favourable predictions against field measurement data and offers a simple and effective way of including the effects of trees within CFD models.

The successful modelling of a tree-lined street within CFD along with the analysis of field measurements allowed for a greater understanding of the effect of trees on airflow within a street canyon. Under perpendicular and oblique wind directions the presence of trees disrupts the rotational vortex within the street resulting in complex inhomogeneous flow along the length of the street. Despite this disruption, the presence of the trees do not prevent the vortex from forming. It was found that the positioning and size of this vortex varied with location along the length of the street with the centre of the vortex generally shifted towards the downwind wall.

Wind speeds were found to be significantly reduced within the tree lined street. Results of the CFD analysis found that wind speeds were reduced by 43% on the upwind side of the street and 36% on the downwind side of the street at a height of 1.5m. These values gave excellent agreement with field measurement data which showed a typical reduction in v velocities of 46% on the upwind side and 34% on the downwind side of the street.

The average magnitude of vertical velocities was found to reduce significantly, with results from CFD analysis predicting an approximate 50% reduction at roof level. Thus significantly inhibiting the mechanism of ventilation and air exchange within the street.

Turbulence levels were also found to significantly decrease with the addition of trees to the street, this is believed to be due to the presence of the trees resulting in a short circuiting of the turbulent energy cascade by breaking large scale eddies into small scale turbulence which quickly dissipates. Results of the CFD model found reductions of between 67% and 78% in turbulence intensities and field measurements showing a reduction of between 44% and 60 %.

Based on these findings it can be concluded that trees are likely to be a useful aid in urban design reducing high wind speeds and turbulence thus helping to create outdoor environments which are comfortable and safe for pedestrian use. However the results also indicate that the addition of trees to streets can

reduce the natural ventilation that occurs within street canyons and therefore may lead to a build up of pollutants. This highlights the importance of obtaining an accurate method for modelling and predicting the aerodynamic effects of trees in order to ensure we optimise the beneficial effects of tree planting and minimise any potential negative impacts. This research has provided the first step towards this goal.

8.0.3 Opportunities for Further Work

The parameters of drag coefficient and leaf area density make up part of the formulation of the mathematical model of the tree canopy. If this model is to be used for more general applications it would be useful to have a set of guidelines these values should take under different conditions. For example it may be that the drag coefficient should vary with wind speed and the leaf area density will be different depending on the species and age of a tree. Guidelines on these parameters would therefore allow for the easy implementation of trees and vegetation within CFD models for the urban area. The formulation of these guidelines for leaf area density would most likely be based around a large scale field measurement campaign which may include measurement techniques such as laser scanning or leaf sampling in order to obtain total leaf area and the volume of the canopy. Guidance on the values drag coefficient for various tree types can also be obtained through field measurements. However such measurements tend to be challenging to obtain and therefore may need to be complemented by smaller scale testing such as wind tunnel tests.

Due to the limited field measurement data set available, only spring / summer data was analysed. The flow effects induced by deciduous trees in winter are expected to be considerably different to those in summer. Therefore it is recommended that further work is carried out to understand the effect of seasonality on airflow within tree lined streets as this is expected to have a significant effect on both pedestrian comfort and pollution dispersion. An example of such work would be to extend the current field measurement campaign carried out for this research by collecting field data during winter months. This data could then be analysed and compared against the current data set to gain an understanding

into the effect that seasonality and leaf cover has on airflow within the street.

Only tree canopies were included in the CFD model, tree trunks were neglected due to limitation on computational resources and meshing capabilities. An extension to the current work would therefore be to include the tree trunks within the CFD model in order to provide information on the effects the tree trunks would have on the airflow. The inclusion of all tree trunks when modelling a large urban area would likely be prohibitively time consuming due to the time needed to create the geometry and mesh as well as running the model. Therefore if the effects of the tree trunks are found to be significant enough to warrant the inclusion within the CFD model ideally a simplified way of including the effect of the tree trunks without explicitly modelling them would be found.

There is a limited amount of research available on the effect of street furniture on flow within street canyons. Results of the field measurements carried out showed that the velocity profile taken on the upwind side of the street did not match the typical linear profile we would expect to find in an empty street canyon. If we are to use CFD to provide accurate predictions of pedestrian level wind then more research is needed into the effects of street furniture and how this may be incorporated into the CFD model. One possibility in extending the current work would be to carry out wind tunnel tests of the non-tree lined street in which field measurements were taken and look at the effects of including street furniture such as parked cars, hedge planting etc. and comparing the results with the field measurement findings.

One limitation that was highlighted by the current works was the ability of the k-ε model to accurately capture the turbulence levels within a street canyon, both with and without tree planting. Currently there is a large amount of research being carried out on which turbulence model offers the best prediction of turbulence values in the built environment. Therefore an useful extension to this work would be to investigate the impact of running the current CFD model with different turbulence models and comparing against field measurements to see if this could provide improved predictions of turbulence values.

Trees are complex biological organisms which interact with their environment. One such interaction is evapotranspiration which accounts for the movement of water within the plant as well as transfer with its surrounding environment. This

process may have an effect on the trees macro wind climate and would therefore be an interesting field of research to complement the work carried out in this thesis. It may be possible to input the results of the CFD model conducted in this research into a much smaller scale model that investigates flow around a single tree or leaf in order to gain a greater understanding into the evapotranspiration process.

In conclusion this research has shown that the addition of trees to streets can reduce wind speeds and turbulence levels within the street. The potential impacts of such wind effects would be beneficial from a pedestrian wind comfort and safety point of view but may have a detrimental effect on pollution dispersion. Therefore the results of this research has highlighted the importance of being able to accurately predict and model the effect of trees on their local wind climate within the built environment in order to optimise any beneficial effects and minimise any negative effects tree planting may have. The research has provided a positive step forward in achieving this goal through the inclusion of trees canopies within the CFD model as simple porous sub-domains with momentum and turbulence sinks. With the addition of the further work discussed in this section this method could provide a useful tool within industry to aid in the design of urban environments which are safe, healthy and comfortable for their inhabitants.

Appendix 1

.1 Field Measurement Data

.1.1 Horizontal Measurements

10th March

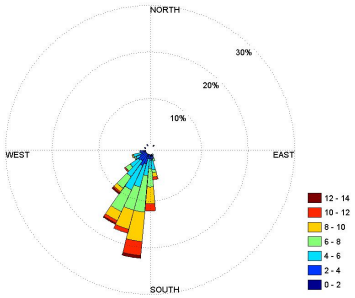

Figure 1: Wind Rose of Weather Station Data Taken on 10th March

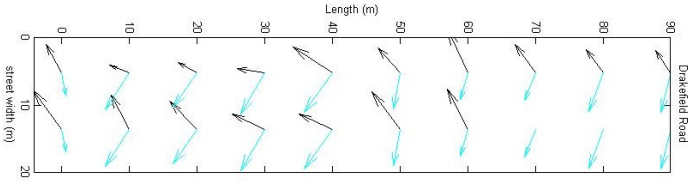

(a) Vector Plot Taken on Drakefield Road on 10th March

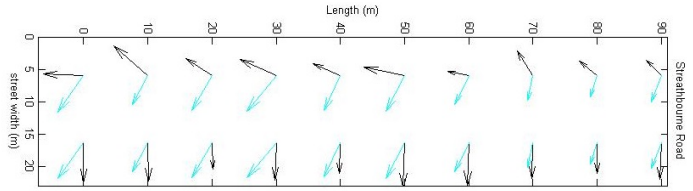

(b) Vector Plot Taken on Streathbourne Road on 10th March

11th March

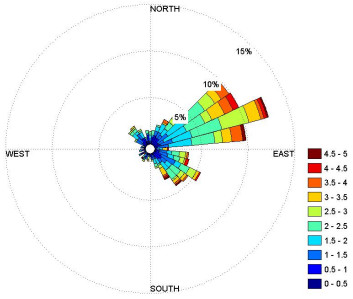

Figure 2: Wind Rose of Weather Station Data Taken on 11th March

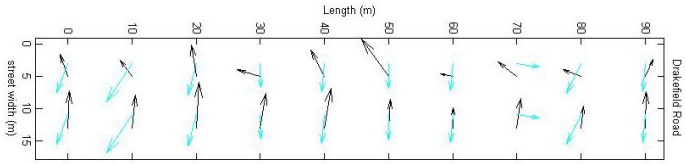

(a) Vector Plot Taken on Drakefield Road on 11th March

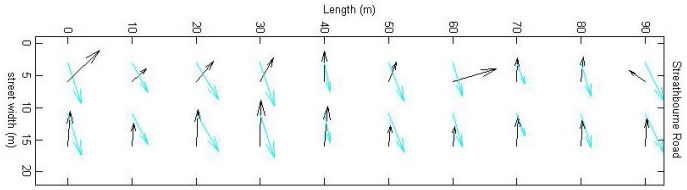

(b) Vector Plot Taken on Streathbourne Road on 11th March

16th March

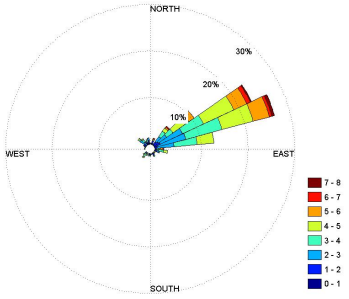

Figure 3: Wind Rose of Weather Station Data Taken on 16th March

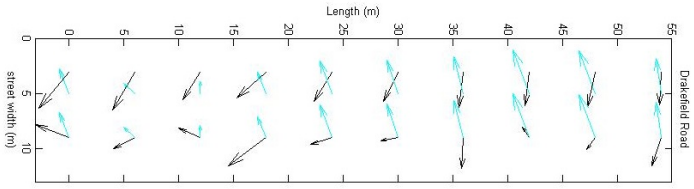

(a) Vector Plot Taken on Drakefield Road on 16th March

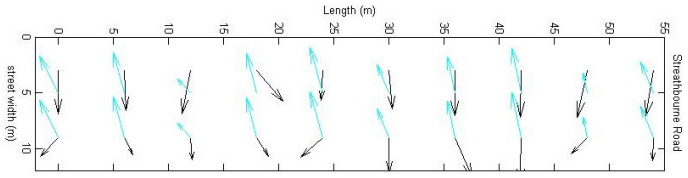

(b) Vector Plot Taken on Streathbourne Road on 16th March

2nd April

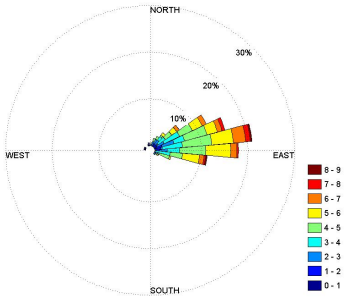

Figure 4: Wind Rose of Weather Station Data Taken on 2nd April

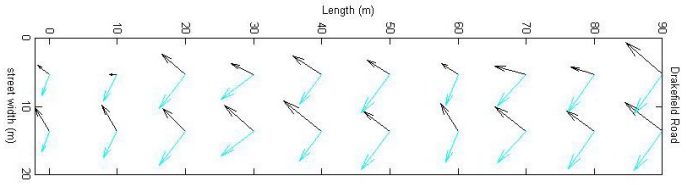

(a) Vector Plot Taken on Drakefield Road on 2nd April

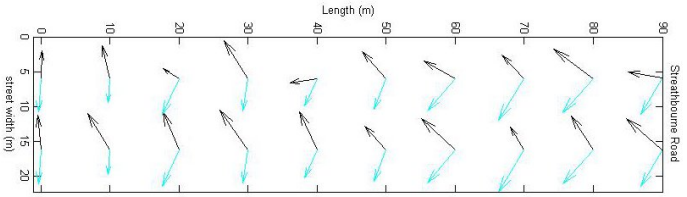

(b) Vector Plot Taken on Streathbourne Road on 2nd April

5th April

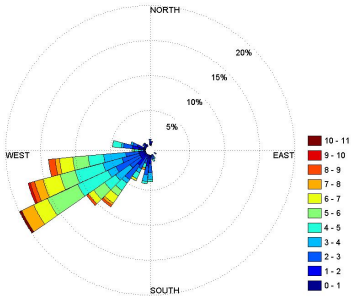

Figure 5: Wind Rose of Weather Station Data Taken on 5th April

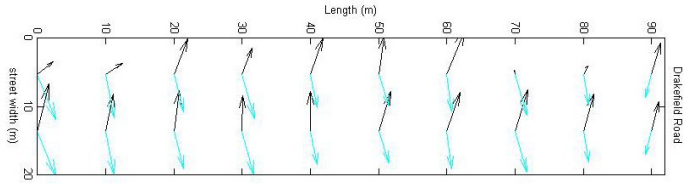

(a) Vector Plot Taken on Drakefield Road on 5th April

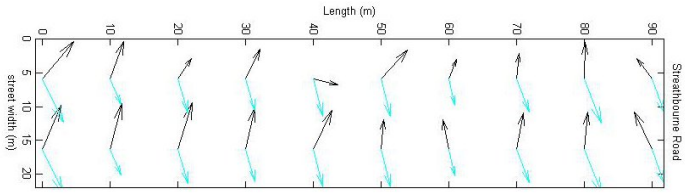

(b) Vector Plot Taken on Streathbourne Road on 5th April

15th June

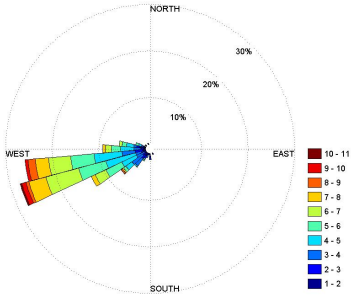

Figure 6: Wind Rose of Weather Station Data Taken on 15th June

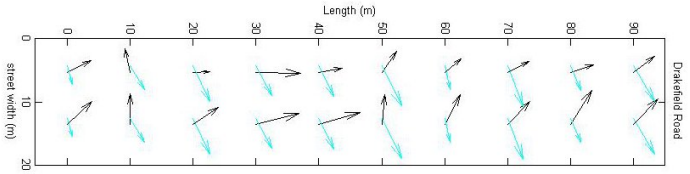

(a) Vector Plot Taken on Drakefield Road on 15th June

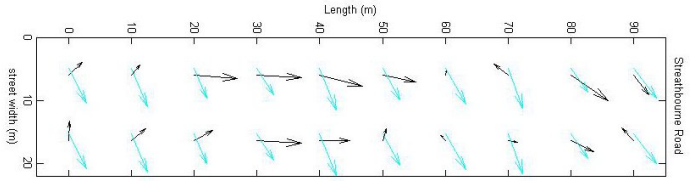

(b) Vector Plot Taken on Streathbourne Road on 15th June

30th June

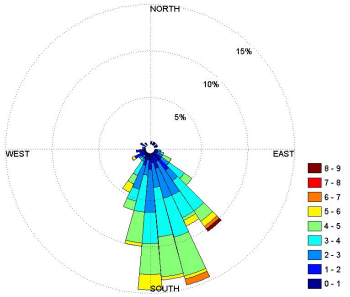

Figure 7: Wind Rose of Weather Station Data Taken on 30th June

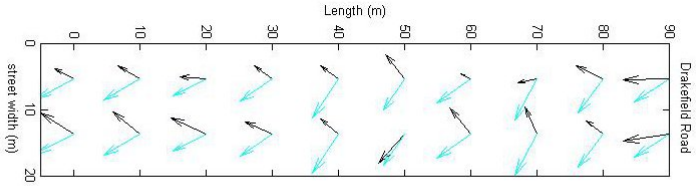

(a) Vector Plot Taken on Drakefield Road on 30th June

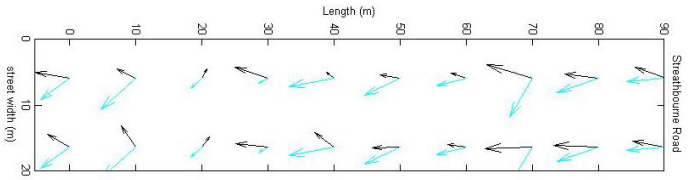

(b) Vector Plot Taken on Streathbourne Road on 30th June

2nd July

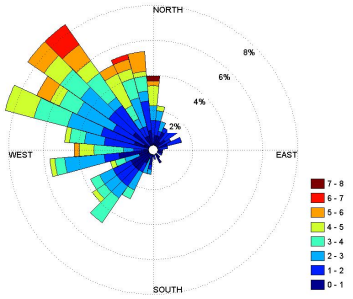

Figure 8: Wind Rose of Weather Station Data Taken on 2nd July

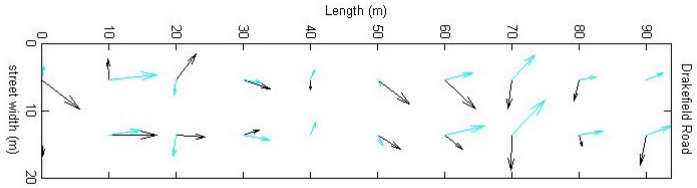

(a) Vector Plot Taken on Drakefield Road on 2nd July

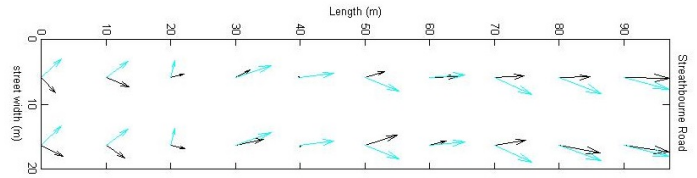

(b) Vector Plot Taken on Streathbourne Road on 2nd July

5th July

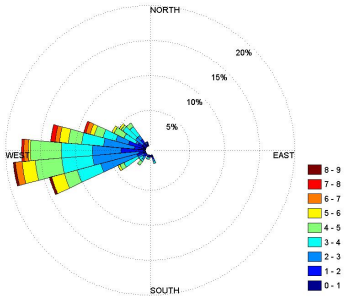

Figure 9: Wind Rose of Weather Station Data Taken on 5th July

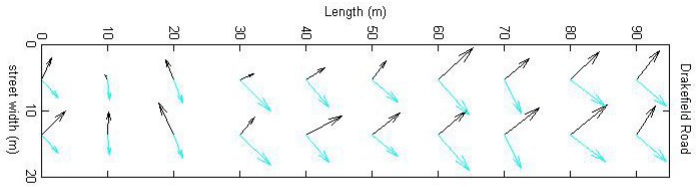

(a) Vector Plot Taken on Drakefield Road on 5th July

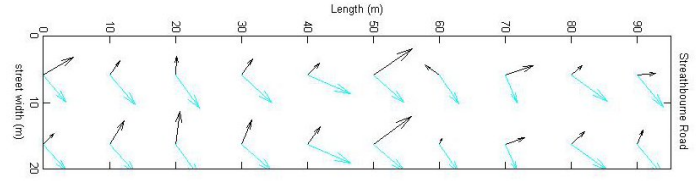

(b) Vector Plot Taken on Streathbourne Road on 5th July

.1.2 Vertical Measurements

6th June

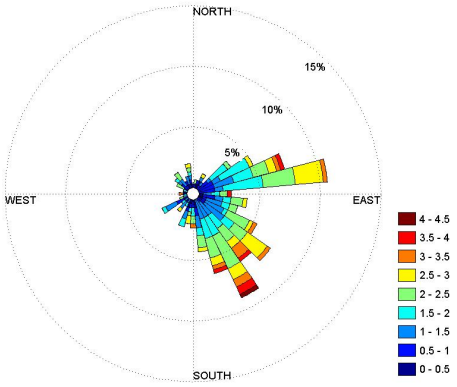

Figure 10: Wind Rose of Weather Station Data Taken on 6th June

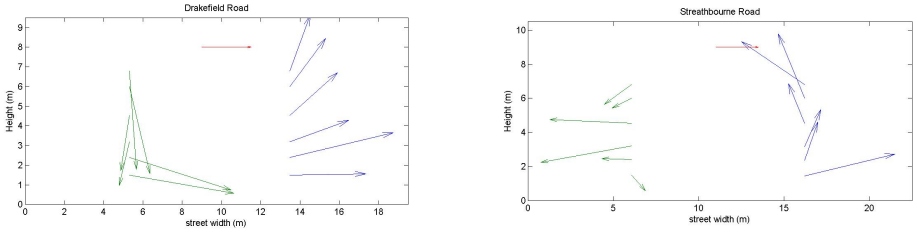

Figure 11: Vector Plot Taken on Drakefield Road (Left) and Streathbourne Road (Right) on 6th June

7th June

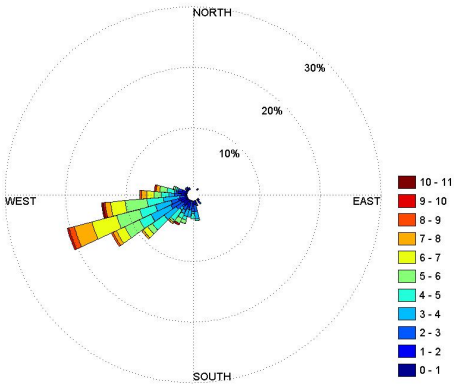

Figure 12: Wind Rose of Weather Station Data Taken on 7th June

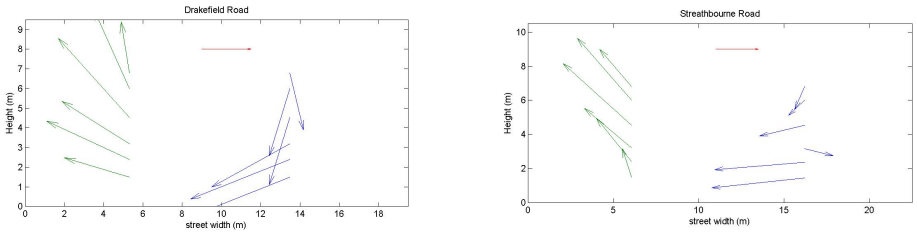

Figure 13: Vector Plot Taken on Drakefield Road (Left) and Streathbourne Road (Right) on 7th June

8th June

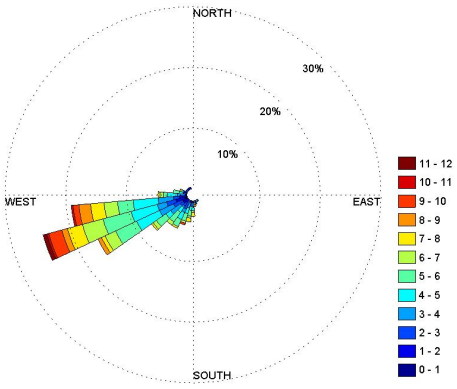

Figure 14: Wind Rose of Weather Station Data Taken on 8th June

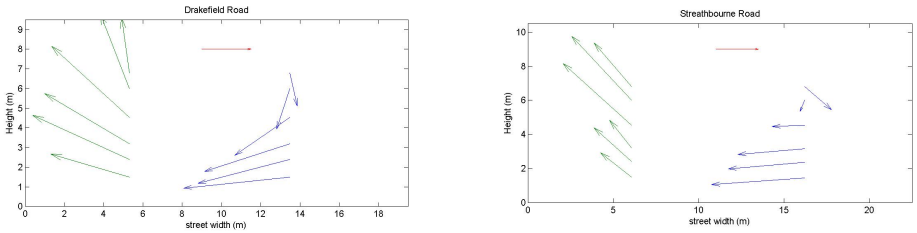

Figure 15: Vector Plot Taken on Drakefield Road (Left) and Streathbourne Road (Right) on 8th June

9th June

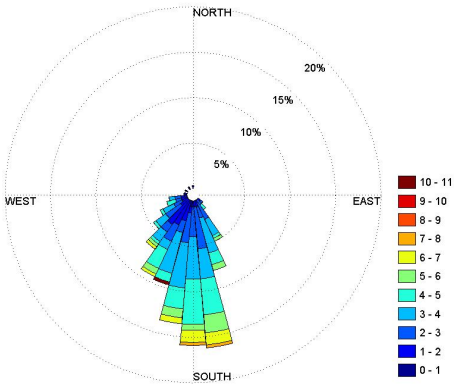

Figure 16: Wind Rose of Weather Station Data Taken on 9th June

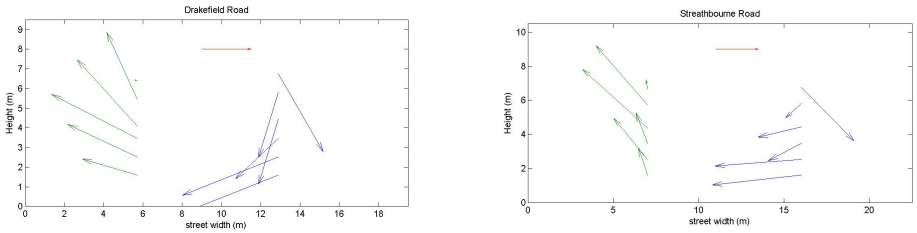

Figure 17: Vector Plot Taken on Drakefield Road (Left) and Streathbourne Road (Right) on 9th June

10th June

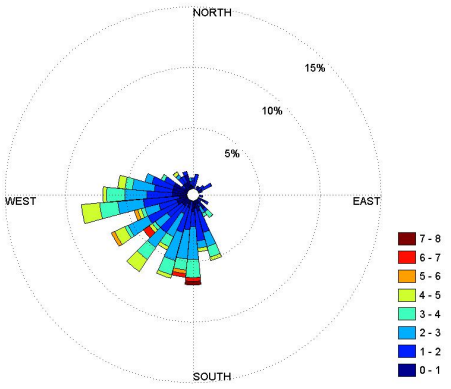

Figure 18: Wind Rose of Weather Station Data Taken on 10th June

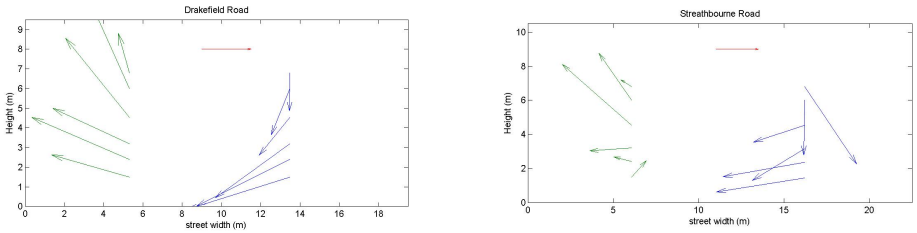

Figure 19: Vector Plot Taken on Drakefield Road (Left) and Streathbourne Road (Right) on 10th June

25th July

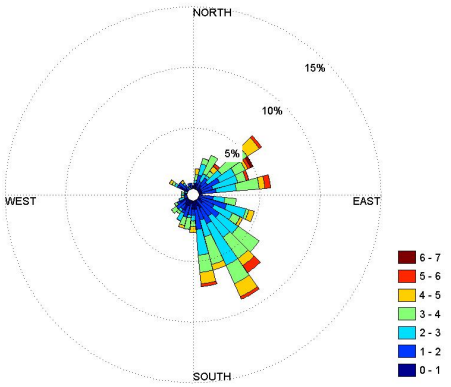

Figure 20: Wind Rose of Weather Station Data Taken on 25th July

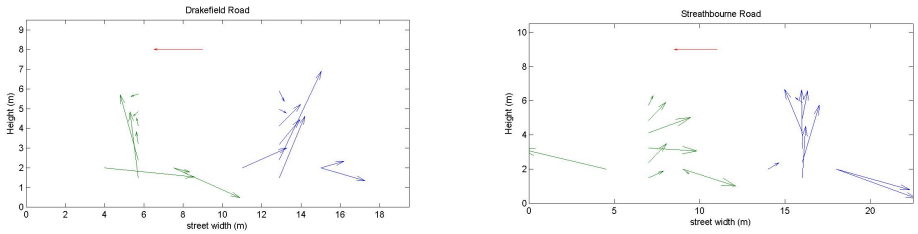

Figure 21: Vector Plot Taken on Drakefield Road (Left) and Streathbourne Road (Right) on 25th July. Red arrow has a scale of 1 m/s for reference and indicates direction of background wind.

26th July

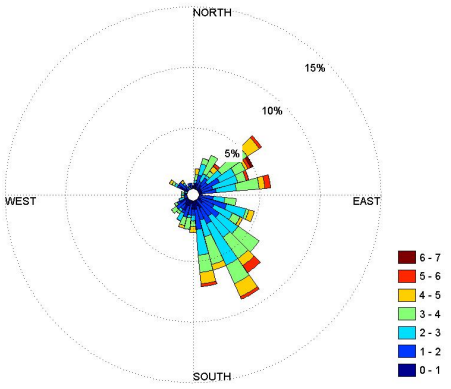

Figure 22: Wind Rose of Weather Station Data Taken on 26th July

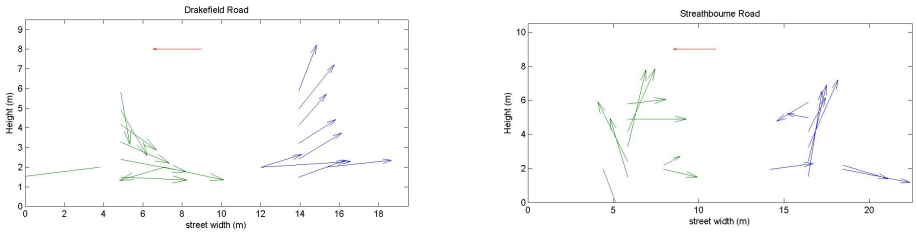

Figure 23: Vector Plot Taken on Drakefield Road (Left) and Streathbourne Road (Right) on 26th July. Red arrow has a scale of 1 m/s for reference and indicates direction of background wind.

27th July

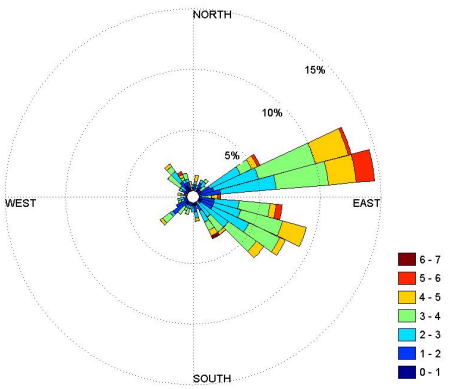

Figure 24: Wind Rose of Weather Station Data Taken on 27th July

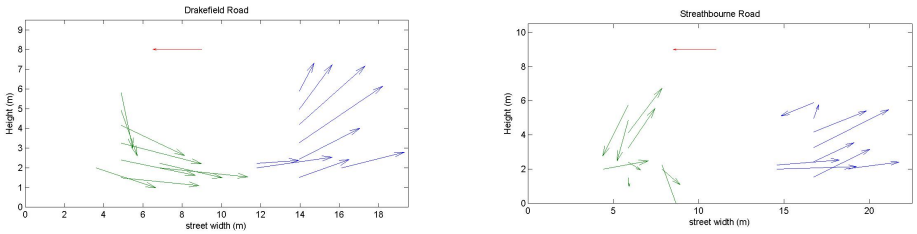

Figure 25: Vector Plot Taken on Drakefield Road (Left) and Streathbourne Road (Right) on 27th July. Red arrow has a scale of 1 m/s for reference and indicates direction of background wind.

28th July

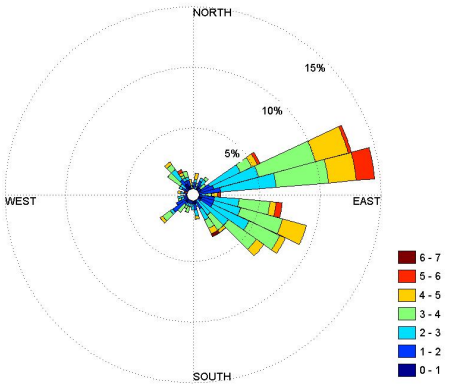

Figure 26: Wind Rose of Weather Station Data Taken on 28th July

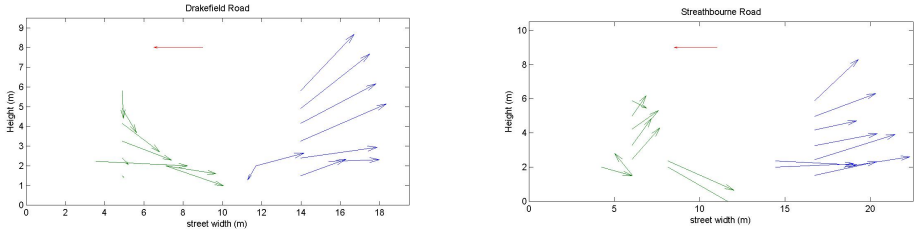

Figure 27: Vector Plot Taken on Drakefield Road (Left) and Streathbourne Road (Right) on 28th July. Red arrow has a scale of 1 m/s for reference and indicates direction of background wind.

29th July

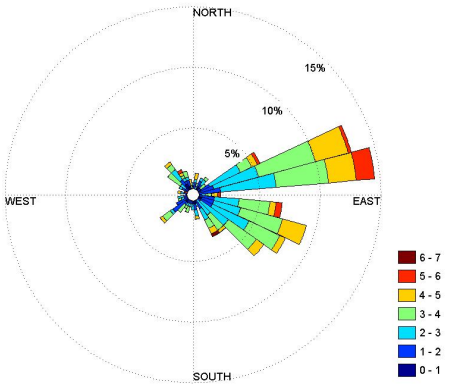

Figure 28: Wind Rose of Weather Station Data Taken on 29th July

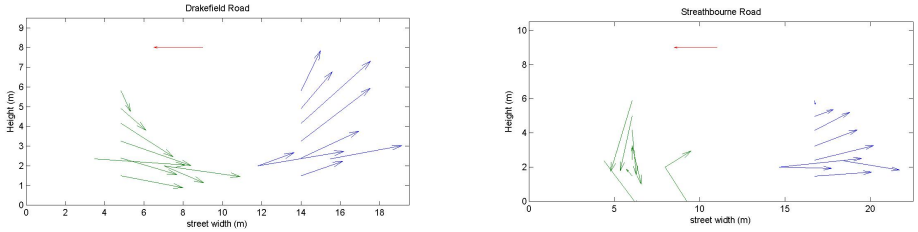

Figure 29: Vector Plot Taken on Drakefield Road (Left) and Streathbourne Road (Right) on 29th July. Red arrow has a scale of 1 m/s for reference and indicates direction of background wind.

2nd September

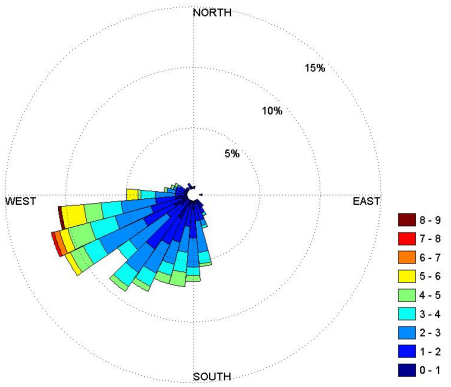

Figure 30: Wind Rose of Weather Station Data Taken on 2nd September

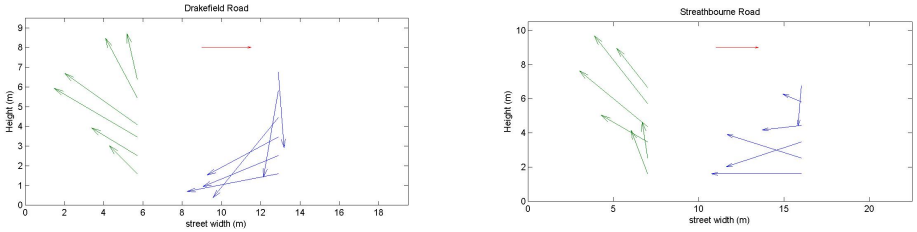

Figure 31: Vector Plot Taken on Drakefield Road (Left) and Streathbourne Road (Right) on 2nd September. Red arrow has a scale of 1 m/s for reference and indicates direction of background wind.

5th September

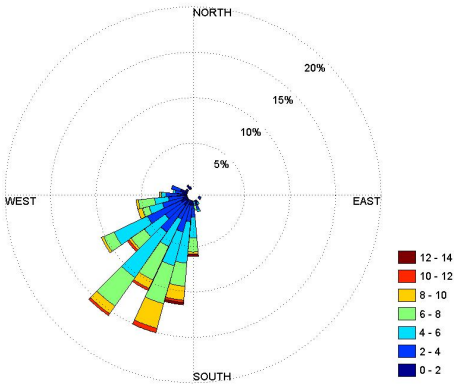

Figure 32: Wind Rose of Weather Station Data Taken on 5th September

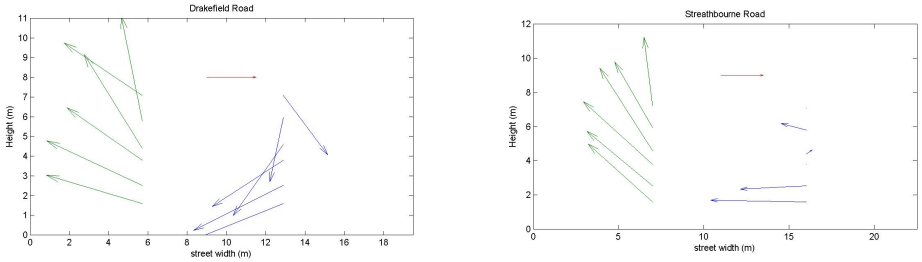

Figure 33: Vector Plot Taken on Drakefield Road (Left) and Streathbourne Road (Right) on 5th September. Red arrow has a scale of 1 m/s for reference and indicates direction of background wind.

6th September

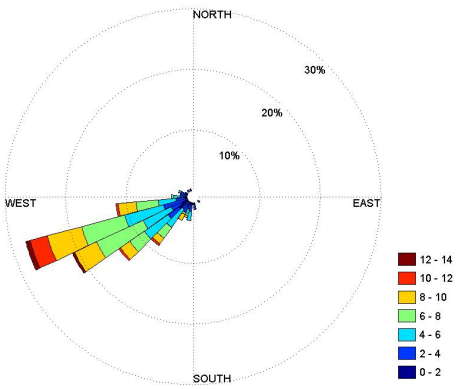

Figure 34: Wind Rose of Weather Station Data Taken on 6th September

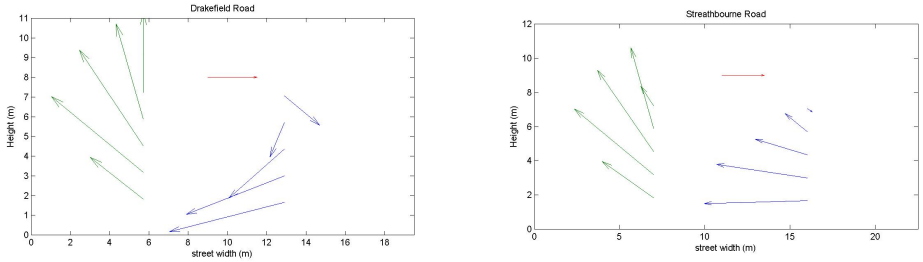

Figure 35: Vector Plot Taken on Drakefield Road (Left) and Streathbourne Road (Right) on 6th September. Red arrow has a scale of 1 m/s for reference and indicates direction of background wind.

7th September

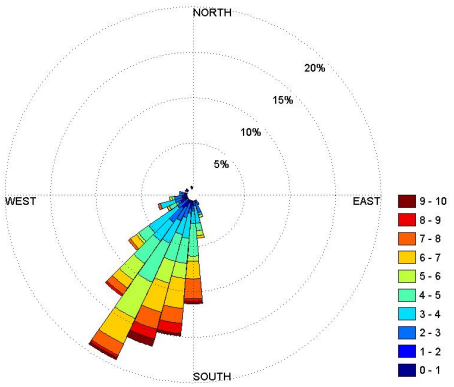

Figure 36: Wind Rose of Weather Station Data Taken on 7th September

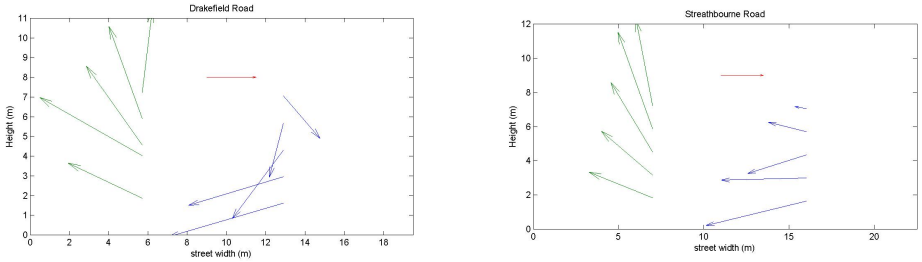

Figure 37: Vector Plot Taken on Drakefield Road (Left) and Streathbourne Road (Right) on 7th September. Red arrow has a scale of 1 m/s for reference and indicates direction of background wind.

8th September

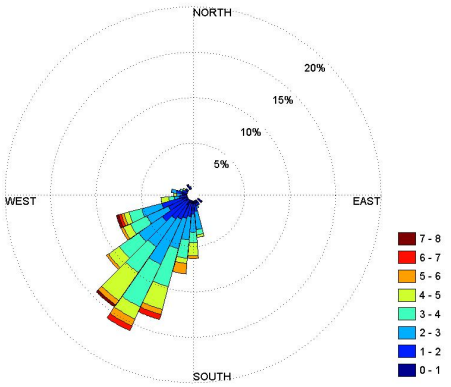

Figure 38: Wind Rose of Weather Station Data Taken on 8th September

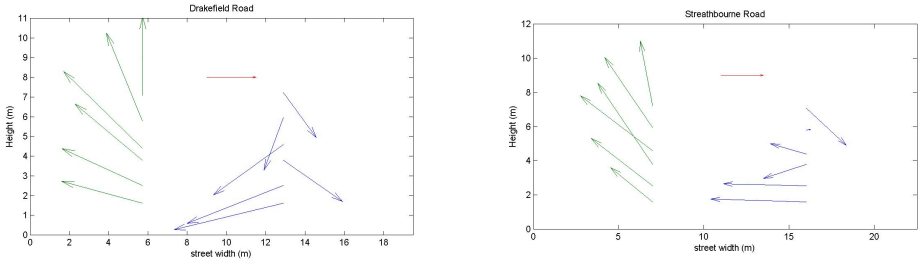

Figure 39: Vector Plot Taken on Drakefield Road (Left) and Streathbourne Road (Right) on 8th September. Red arrow has a scale of 1 m/s for reference and indicates direction of background wind.

Date	Number of anemometers	Heights (m) West side of Street	Heights (m) East side of Street
06/06/2011	4 x 2-D, 1 x 3-D	1.5, 2.5, 3.5, 4.5, 6.0, 7.0	1.5, 2.5, 3.5, 4.5, 6.0, 7.0
07/06/2011	4 x 2-D, 1 x 3-D	1.5, 2.5, 3.5, 4.5, 6.0, 7.0	1.5, 2.5, 3.5, 4.5, 6.0, 7.0
08/06/2011	4 x 2-D, 1 x 3-D	1.5, 2.5, 3.5, 4.5, 6.0, 7.0	1.5, 2.5, 3.5, 4.5, 6.0, 7.0
09/06/2011	4 x 2-D, 1 x 3-D	1.5, 2.5, 3.5, 4.5, 6.0, 7.0	1.5, 2.5, 3.5, 4.5, 6.0, 7.0
10/06/2011	4 x 2-D, 1 x 3-D	1.5, 2.5, 3.5, 4.5, 6.0, 7.0	1.5, 2.5, 3.5, 4.5, 6.0, 7.0
25/07/2011	4 x 2-D, 1 x 3-D	1.5, 2.5, 3.5, 4.5, 6.0, 7.0	1.5, 2.5, 3.5, 4.5, 6.0, 7.0
26/07/2011	4 x 2-D, 1 x 3-D	1.5, 2.5, 3.5, 4.5, 6.0, 7.0	1.5, 2.5, 3.5, 4.5, 6.0, 7.0
27/07/2011	4 x 2-D, 1 x 3-D	1.5, 2.5, 3.5, 4.5, 6.0, 7.0	1.5, 2.5, 3.5, 4.5, 6.0, 7.0
28/07/2011	4 x 2-D, 1 x 3-D	1.5, 2.5, 3.5, 4.5, 6.0, 7.0	1.5, 2.5, 3.5, 4.5, 6.0, 7.0
29/07/2011	4 x 2-D, 1 x 3-D	1.5, 2.5, 3.5, 4.5, 6.0, 7.0	1.5, 2.5, 3.5, 4.5, 6.0, 7.0
02/09/2011	9 x 2-D, 1 x 3-D	1.5, 2.5, 3.5, 4.5, 6.0, 7.0	1.5, 2.5, 3.5, 4.5, 6.0, 7.0
05/09/2011	9 x 2-D, 1 x 3-D	1.5, 2.5, 3.5, 4.5, 6.0, 7.0	1.5, 2.5, 3.5, 4.5, 6.0, 7.0
06/09/2011	9 x 2-D, 1 x 3-D	1.5, 3.5, 4.5, 6.0, 7.0	1.5, 3.5, 4.5, 6.0, 7.0
07/09/2011	9 x 2-D, 1 x 3-D	1.5, 3.5, 4.5, 6.0, 7.0	1.5, 3.5, 4.5, 6.0, 7.0
08/09/2011	9 x 2-D, 1 x 3-D	1.5, 2.5, 3.5, 4.5, 6.0, 7.0	1.5, 2.5, 3.5, 4.5, 6.0, 7.0

Table 1: Table showing heights at which measurements were taken. Heights given in the same colour were taken simultaneously

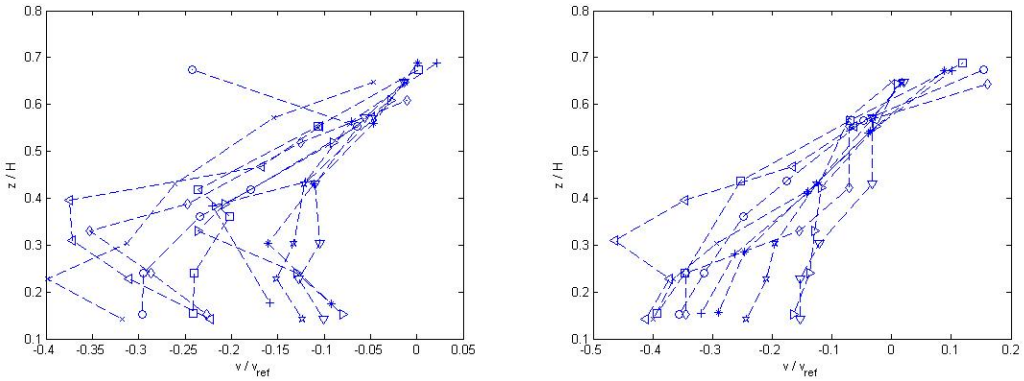

Figure 40: Vertical profiles of v velocity component for Drakefield Road. Given for the upwind side of the street (left) and downwind side of street (right).

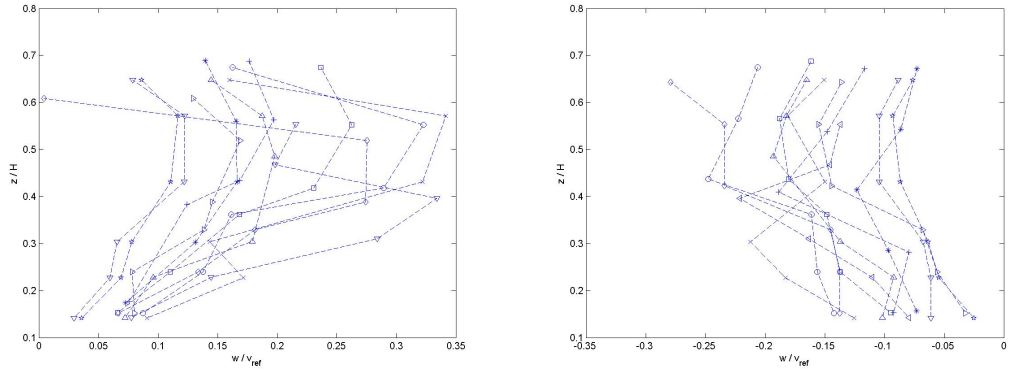

Figure 41: Vertical profiles of w velocity component for Drakefield Road. Given on the upwind side of the street (left) and downwind side of the street (right).

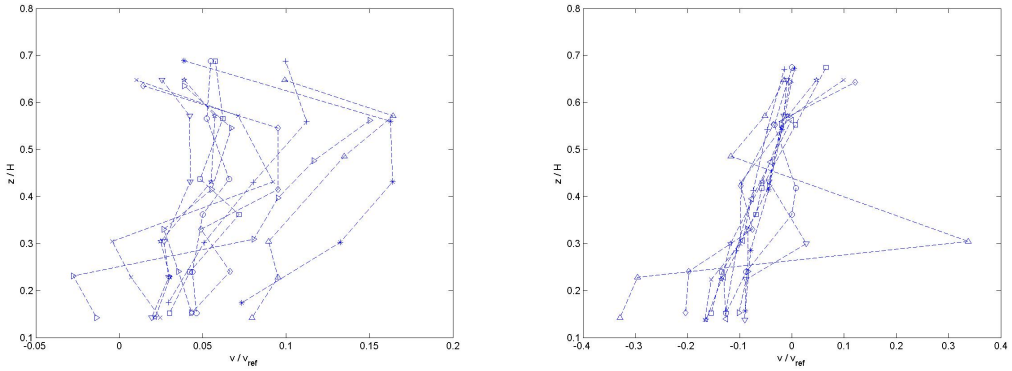

Figure 42: Vertical profiles of v velocity component for Streathbourne Road. Given for the upwind side of the street (left) and downwind side of street (right).

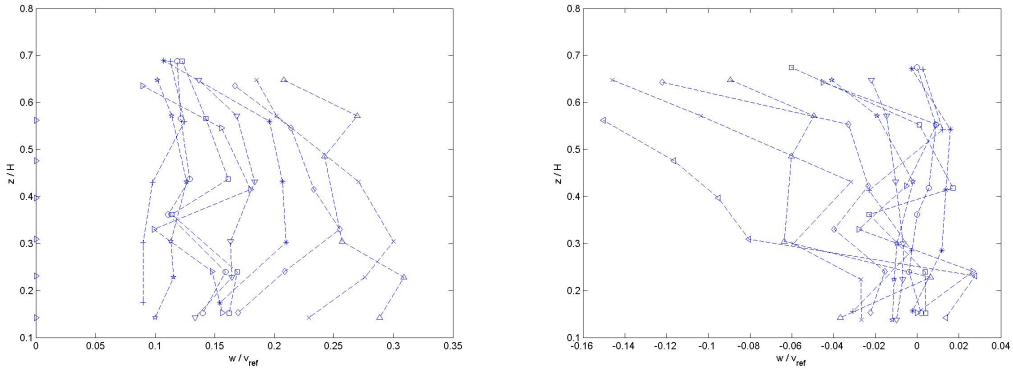

Figure 43: Vertical profiles of w velocity component for Streathbourne Road. Given for the upwind side of the street (left) and downwind side of the street (right).

Appendix 2

.2 CFD Model Set-up

.2.1 Benchmark Study - Boundary Layer Simulation

This section of the appendix provides the settings used in the specification of the CFD model outlined in Chapter 4 Section 4.1.

.2.1.1 Computational Domain and Mesh Specification

The geometry of the empty wind tunnel was replicated in CFX. The dimensions of the empty domain were 2m wide by 1.32m high by 3.24m long.

A total of six hexahedral meshes were tested with varying mesh size closest to the floor of the domain. Details of each mesh size can be found in Table 2. A sand grain roughness was applied to the floor of the domain. The height of the sandgrain roughness must not exceed half the height of the cell next to the wall therefore the sandgrain roughness was adjusted to equal half the smallest cell size for all mesh tested.

Velocity, TKE and Turbulent dissipation profiles for each mesh were plotted at 0.6m down stream of the inlet (see figure 44). This will be the location of the first street canyon therefore these profiles will be the incident profiles for the street canyon model.

Results of the mesh sensitivity test showed that the largest mesh size (mesh 1a) showed a noticible difference in the TKE and dissipation profiles produced whereas the results of all other meshes remained similar. The difference in re-

sults profile between mesh 3a and mesh 2a was less than 1% which is deemed insignificant. Therefore mesh size 3a was chosen for use in this study as it offers the best comprimise between total number of cells within the mesh and error due to discritisation.

.2.1.2 Boundary Settings

Three different boundary layer CFD models were tested. All shared the same settings except for the inlet conditions which varied as follows:

For the first model the experimental data obtained from the wind tunnel data was input directly into the CFD model. The data consisted of velocity and turbulence measurements taken at several heights. This was used to form the velocity and TKE profiles at the inlet, Ansys CFX uses an interpolation function in between the measurement location to form the full profile. The profile is homogeneous across the width of the inlet.

The second model implements the inlet profiles first suggested by Richards and Norris [2011] and are commonly used for atmospheric boundary layer applications. These are

Velocity Inlet Profile:

$$u(z) = \frac{u*}{\kappa} ln\left(\frac{z + z_0}{z_0}\right) \tag{1}$$

the values of u* = 0.56 , z_0 = 0.0008m were taken from the wind tunnel data.

Turbulent Kinetic Energy Inlet Profile:

$$k = \frac{u*^2}{\sqrt{C_\mu}} \tag{2}$$

Turbulent Dissipation Inlet Profile:

$$\varepsilon = \frac{u*^3}{\kappa(z + z_0)} \tag{3}$$

The final model used the inlet boundary conditions specified by Yang et al. [2009]:

$$u = \frac{u*}{k} ln\left(\frac{z + z_0}{z_0}\right) \tag{4}$$

$$k = \frac{u*^2}{\sqrt{C_\mu}} \sqrt{C_1 ln\left(\frac{z + z_0}{z_0}\right) + C_2} \tag{5}$$

The empirical constant C_1 took a value of 0.60 and C_2 had a value of 0.83 respectively. These values were found by fitting a curve to the TKE data, this was done using the Matlab function lsqcurvefit was used which solves non-linear curve fitting problems in the least-squares sense.

$$\varepsilon = \frac{u*^3}{\kappa(z + z_0)} \sqrt{C_1 ln\left(\frac{z + z_0}{z_0}\right) + C_2} \tag{6}$$

For all models the k-ε model parameter where left to their default value with the exception of model three for which the value of σ_ε was set according to equation 4.8.

All other boundary conditions remained the same for the three models. The outlet boundary was set to outflow with static pressure 0 Pa. The top of the domain was set to a wall boundary with an applied shear stress of $\tau = \rho u_*^2$ as suggested by Richards and Hoxey [1993].

A sand grain roughness was used on the floor of the domain to simulate the roughness blocks which were placed on the floor of the wind tunnel. This is necessary in order to maintain a homogeneous boundary flow. The sand grain roughness height was calculated based on half the height of the cell next to the wall this gave a value of 0.006m.

The convergence criteria was set to $1x10^{-5}$ with an imbalance of less than 0.1% as well as velocity and turbulence being monitored at several points to ensure stable conditions were reached. Figures showing convergence of the residuals and plots of the monitoring points can be seen in Figures 45 and 46.

Table 2: Mesh specification for mesh sensitivity test for CFD urban boundary layer model

Mesh	**Minimum cell size**	**Maximum cell size**	**Total number of cells**
Mesh1a	0.048	0.03	74256
Mesh2a	0.024	0.03	340200
Mesh3a	0.012	0.03	1578150
Mesh4a	0.010	0.03	2397600
Mesh5a	0.008	0.03	4455000
Mesh6a	0.006	0.03	7394760

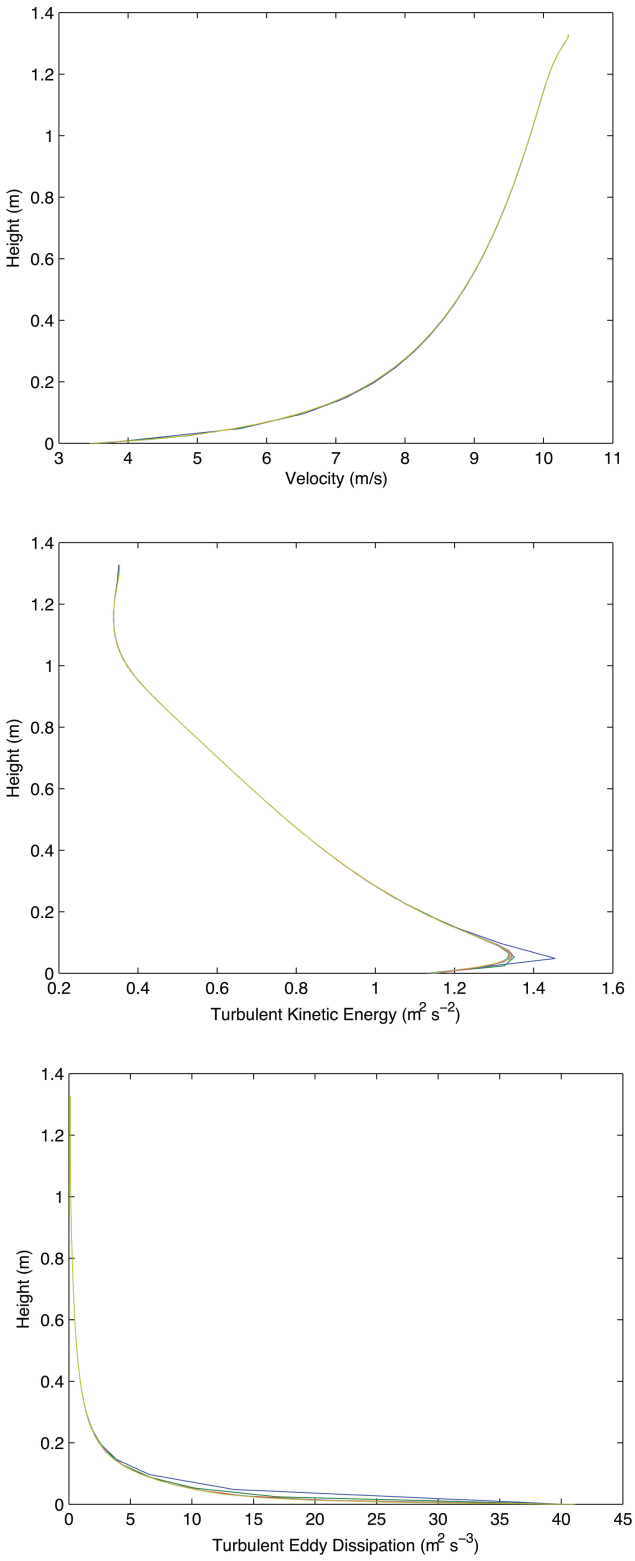

Figure 44: Profiles for 6 different mesh sizes for velocity (top), TKE, (centre) and turbulent dissipation (bottom)

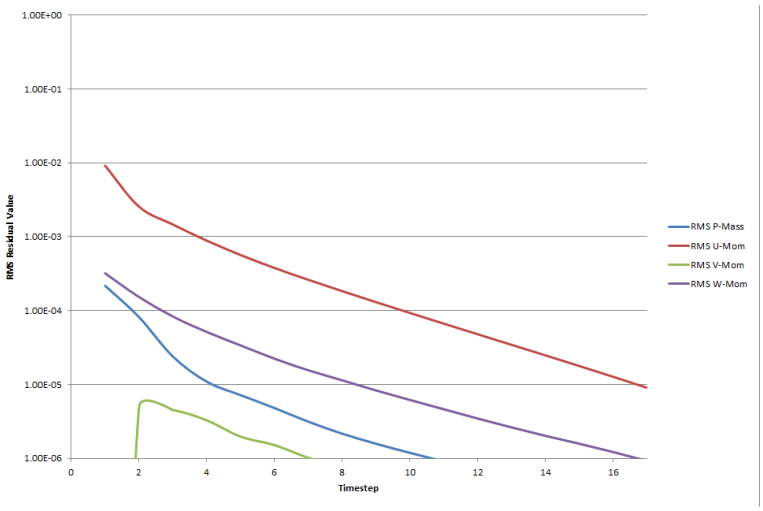

Figure 45: Graph showing RMS values of residuals for boundary layer CFD model

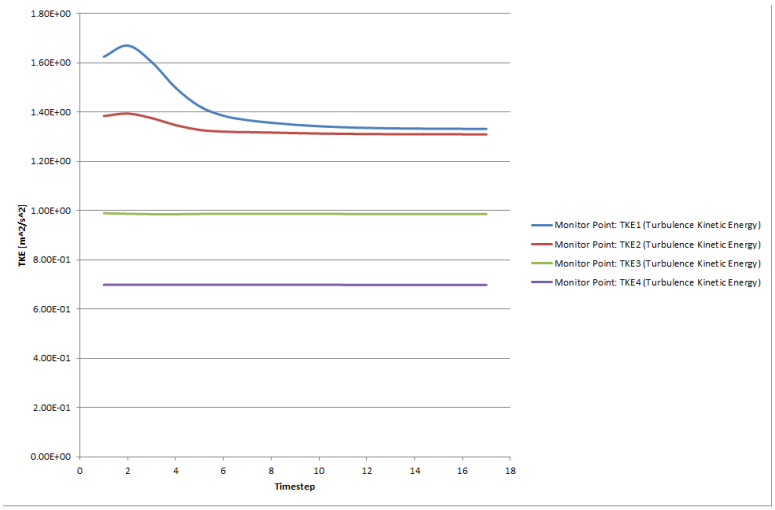

Figure 46: Graph showing TKE values at monitoring points for boundary layer CFD model at various timesteps

.2.2 Benchmark Study - Street Canyon Simulation

This section of the Appendix describes the settings used for the CFD model of the idealised street canyon tested in the wind tunnel. This is discussed in Chapter 4, Section 4.2.

.2.2.1 Computational Domain and Mesh Specification

A fully three-dimensional CFD simulation of the Kastner-Klein wind tunnel experiment [Kastner-Klein et al., 2001] was carried out using ANSYS CFX.The building dimensions used in the CFD model were the same as those for the wind-tunnel, 0.12m x 0.12m x1.8m and consists of two rectangular blocks.

An unstructured hexahedral mesh was used for this study. A mesh sensitivity analysis was carried out in order to limit the error due to numerical approximation and domain descritisation. We know from the previous mesh sensitivity analysis that a mesh size of 0.012m is needed at lower levels in the domain for correct representation of the boundary layer. It has also been recommended that a mesh size of H/10 (where H is the height of the building) should be used if the correct flow features are to be captured surrounding the building. Therefore the maximum cell size close to the ground and within the area of interest was taken to be 0.012m. Five mesh sizes were tested. The different mesh sizes are described in table 3. The minimum mesh size is the mesh size within the area of interest which is the centre portion of the street canyon. The mesh outside this region is increased with and expansion ratio of 1.2 to a maximum size of 0.03m.

Velocity, TKE and dissipation profiles were taken from within the centre of the street canyon for all five meshes and are compared in figure 47. The results show a significant difference in results depending on the mesh size used particularly for TKE. At roof top level reducing the mesh size from 0.012m (H/10) to 0.003m (H/30) results in 70% increase in turbulent kinetic energy. It appears that the mesh within the canyon and immediately above the canyon needs to be fine enough to capture the production of TKE at the leading edge of the upwind building, without this gross underestimate of turbulence levels may occur.

The often quoted guideline of a cell size of H/10 within and immediately above the canyon is reasonable if only a qualitative prediction of flow patterns is needed.

If accurate predictions of turbulence quantities are required, such as simulation of pollution dispersion, then a much finer mesh is recommended.

There was little to no difference in velocity profiles between mesh 4 and 5 and a maximum difference of 5% for the TKE values therefore it was decided mesh 4 could provide a reasonable level of accuracy for this study.

.2.2.2 Boundary Settings

Chapter 4 Section 4.1 investigated the most appropriate boundary conditions to create the correct boundary layer flow of the wind tunnel. Based on these findings the profiles used to specify the velocity, TKE and dissipation at the inlet are given by equations 4, 5 and 6. The outlet boundary was set to outflow with static pressure 0 Pa. The top of the domain was set to a wall boundary with an applied shear stress of $\tau = \rho u_*^2$ as suggested by Richards and Hoxey [1993].

The sand grain roughness was set at a height of 0.006m based on equation the findings of the boundary layer simulation. This roughness parameter was applied to the floor of the domain apart from in the region containing the buildings. No roughness was applied in this area.

The convergence criteria was set to $1\text{x}10^{-5}$ with an imbalance of less than 0.1% as well as velocity and turbulence being monitored at several points to ensure stable conditions were reached. Figures showing convergence of the residuals and plots of the monitoring points can be seen in Figures 48 and 49.

Table 3: Mesh specification for mesh sensitivity test for CFD street canyon model

Mesh	**Minimum cell size**	**Maximum cell size**	**Total number of cells**
Mesh1	0.012	0.03	690400
Mesh2	0.008	0.03	1338300
Mesh3	0.006	0.03	1578812
Mesh4	0.004	0.03	3099600
Mesh5	0.003	0.03	5142980

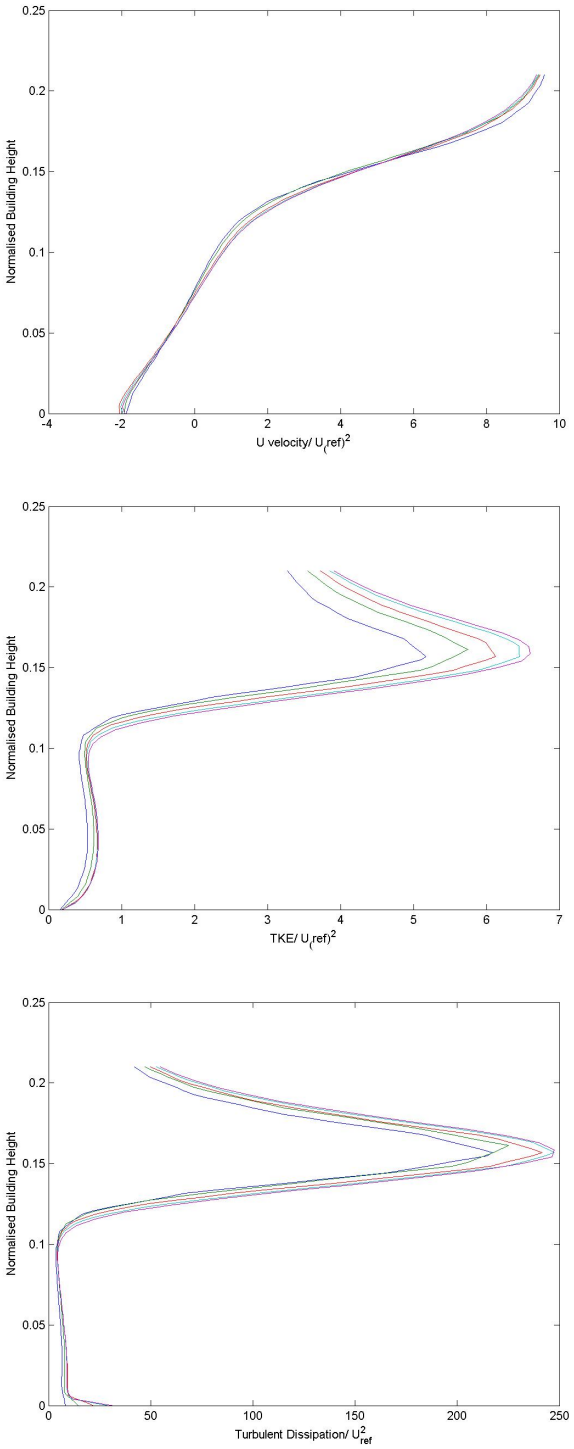

Figure 47: Vertical profiles of streamwise velocity component, u (top), TKE (middle) and dissipation (bottom). Mesh1 - blue, mesh 2 - green, mesh 3 - red, mesh 4 - light blue, mesh 5 - purple

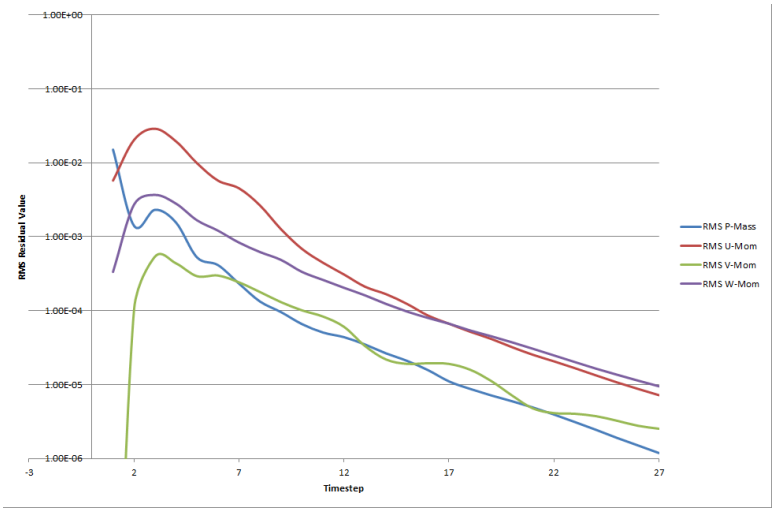

Figure 48: Graph showing RMS values of residuals for street canyon CFD model

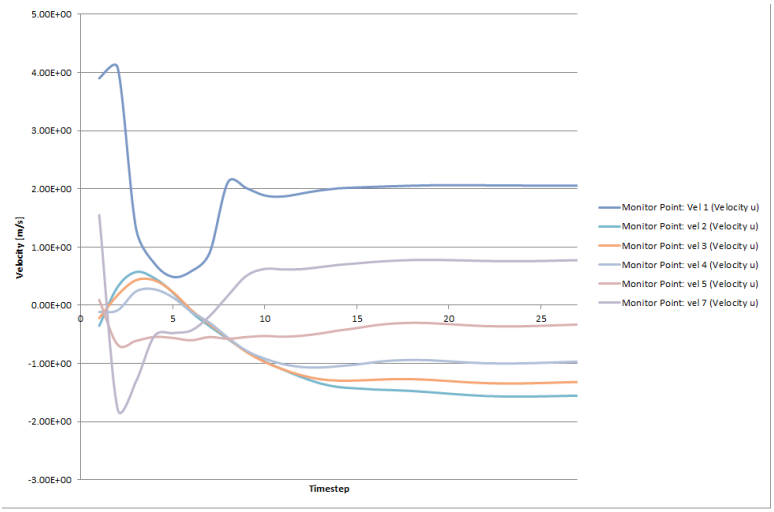

Figure 49: Graph showing velocity values at monitoring points for street canyon CFD model at various timesteps

.2.3 Full Scale Street Canyon Model

This section of the Appendix describes the CFD model setup for the full scale tree-lined and non tree-lined street canyons described in Chapter 6 Sections 6.2 and 6.3

.2.3.1 Computational Domain

Accurately reproducing the 3-dimensional building geometry for use in a CFD simulation requires a large amount of information to create the model as well as a great amount of time and computational cost in running the simulation. It is therefore often necessary to simplify the building geometry when creating a CFD simulation of an urban area without adversely affecting the main features of the flow.

For the case being considered details such as bay windows, narrow gaps between buildings and facade detail was neglected. Such details will have a localised effect on the flow but the significance of such effects is not well known. This is suggested as an area for future work. The buildings were modelled as simple rectangular blocks with two types of roof geometry.

The dimensions of the CFD model with both flat and pitched roof can be seen in figure 52. The length, width and height of the street were taken during the field measurement campaign. The street upwind of Drakefield Road is included as is the garden space in-between the streets. The distance between the inlet and the first street is 75m the distance between the final street and the outlet is 180m and the height of the domain is 120m. This is in line with the COST best practice guidelines [Franke et al., 2011] which states the distance between the inlet and upwind buiding should be at least 5H, the distance between the downwind building and outet should be 15H and the distance to the top of the domain should be at least 5H, where H is the height of the tallest building being modelled.

Street Geometry Two simple roof shapes were tested to see if they could provide a reasonable prediction of the flow patterns within the street. These were a pitched roof and flat roof see figure 50.

Choosing these simple roof shapes allows for easier comparison with previous

research as well as reducing the amount of computational power required due to a smaller mesh size. The pitched roof offers a good approximation to the true roof geometry, however where the dorma windows are located the flat vertical facade of the building extends to the full height of the building. Therefore wind within the street canyon at roof level will be subject to both the sloped section of the roof and the vertical wall of the dorma window which will have an impact on the flow.

Tree Geometry The geometry of the trees was simplified for inclusion in the CFD model with the tree crowns being modelled as ellipsoids and the tree trunks omitted. The effect of the tree trunks on the flow field is suggested for future work. The dimensions and spacing of the trees were determined from on site field measurements. See figure 51 for details of the 3-D model.

.2.3.2 Mesh

An unstructured hexhedral mesh was used for this study. The mesh size was determined based on the mesh sensitivity tests carried out for the previous studies. The mesh was refined at the central portion of each street and increased in size away from this point with an expantion ratio of 1.2 Prisim layers were implemente on the floor of the domain and the buildings within the domain to ensure the flow at the wall was correctly modelled. The total mesh size was 6.5 million cells. This consisted of an unstructured tetrahedral mesh with prism layers on floor of domain. Refinement regions were placed around the streets of interest and trees.

.2.3.3 Boundary Settings

Atmospheric Boundary Layer Specification

A discussion on the appropriate choice of inlet profiles and boundary setting for specification of the atmospheric boundary layer has been made in Section 4.1. It was concluded that the most appropriate choice of inlet profiles for velocity, turbulence kinetic energy and turbulence dissipation were those specified by Yang

Table 4: Values used in specification of atmospheric boundary layer for full scale CFD model

$u*$	C_1	C_2
0.37	0.60	0.83

et al. [2009] as follows:

$$u = \frac{u*}{k} ln \left(\frac{z + z_0}{z_0} \right) \tag{7}$$

$$k = \frac{u*^2}{\sqrt{C_\mu}} \sqrt{C_1 ln \left(\frac{z + z_0}{z_0} \right) + C_2} \tag{8}$$

$$\varepsilon = \frac{u*^3}{\kappa(z + z_0)} \sqrt{C_1 ln \left(\frac{z + z_0}{z_0} \right) + C_2} \tag{9}$$

The implementation of such profiles requires the specification of the frictional velocity, $u*$, the roughness length, z_0 and the empirical constants C_1 and C_2. The value of these constants is often derived from experimental measurements.

In the absence of any measurement data for the atmospheric boundary layer over the site of interest, the ESDU method was implemented in order to determine predicted profiles for the mean wind speed and TKE profiles. The ESDU items [Engineering Sciences Data Unit, 1984] provides a simplified method of estimating the variation of design wind speed with height above the ground and with terrain roughness. Full details regarding the calculation methods can be found in Engineering Sciences Data Unit [1984]. Based on the predicted wind profiles provided by this method along with an assumed roughness length of $z_0 = 0.3$ values can be found for frictional velocity, $u*$ and the the empirical constants, C_1 and C_2. These values are provided in table 4.

Tree Specification

It was decided to test two different models for the inclusion of trees within the CFD model. These are as follows:

- Solid tree crown

- Porous domain with momentum and turbulence source term

Solid Tree Crown Model

The surface of the tree crowns was included in the CFD model as a no slip boundary wall

Porous Tree Crown Model with Momentum and Turbulence Sink

Section **??** discussed the aerodynamic effects of trees. The main effects can be summarised as a reduction in momentum due to the drag produced by the tree, the addition of turbulence kinetic energy due to vortex shedding from leaves and branches and the destruction in turbulence kinetic energy due to the short circuiting of the Kolmogrov scale from the breakdown of large scale turbulence into much smaller scale turbulence which quickly dissipates. In order to incorporate these effects into the CFD model the following terms were added to the transport equations for momentum, turbulence kinetic energy and turbulence dissipation following the formulation of Sanz [2003], Katul et al. [2004]:

$$S_u = -\rho C_d LAD u_i U \tag{10}$$

$$S_k = \rho C_d LAD(\beta_p U^3 - \beta_d U k) \tag{11}$$

$$S_\varepsilon = \rho C_d LAD \frac{\varepsilon}{k}(C_{\varepsilon 4}\beta_p U^3 - C_{\varepsilon 5}\beta_d U k) \tag{12}$$

Where S_u is the term added to the momentum transport equation, S_k is added to the TKE equation and S_ε is the term added to the dissipation equation. ρ is the density of air, C_d is the drag coefficient of the canopy, LAD is the leaf area density, β_p is the fraction of mean kinetic energy that is converted into wake turbulence kinetic energy, β_d the coefficient that accounts for the short-circuiting of the eddy cascade and $C_{\varepsilon 4}$ and $C_{\varepsilon 5}$ are closure constants. The values of these parameters are given in table 5.

The value for the drag coefficient $C_d = 0.8$ was taken from Roodbaraky [1994] who carried out full scale experiments on a London Plane tree to determine a drag coefficient of 0.8 (see section 3.4.0.4).

The value for the leaf area density, LAD = 0.78, was obtained using the formulation of Paula J. Peper [2001] to find the total leaf area. This was calculated for each tree within the area of interest based on the diameter at breast height (dbh) of the trunk. This value was then divided by the estimated crown volume (based on measurements of crown diameter and height) to find the leaf area per unit volume (LAD).

The values for C_4, C_5, β_p and β_d are empirical closure constants and were taken from Katul et al. [2004].

.2.3.4 Other Settings

The wind direction specified in the CFD simulation will be perpendicular to the street axis. This is the most commonly studied wind direction in street canyon literature allowing for easy comparison with other research and the results from our previous section. The reference wind speed at a height of 20m was chosen to be 4m/s as this represents typical conditions measured at the weather station.

The top boundary of the domain was specified as a no slip wall boundary with a specified shear of $\tau = \rho u_*^2$ as suggested by Richards and Hoxey [1993]. The side boundaries of the domain were set to symmetry boundaries. The outlet of the domain was set to pressure outlet. The floor of the domain outside of the streets had a specified sand grain roughness of 0.5m, the floor of the domain within the streets was specified as no slip.

The turbulence model used was the standard k-ε model with the default model constants.

The convergence criteria was set to $1\text{x}10^{-5}$ with an imbalance of less than 0.1% as well as velocity and turbulence being monitored at several points to ensure stable conditions were reached. Figures showing convergence of the residuals and plots of the monitoring points can be seen in Figures 53 and 54.

Table 5: Parameters used in specification of CFD canopy tree model

C_d	LAD	C_4	C_5	β_p	β_d
0.8	0.78	0.9	0.9	1	5.1

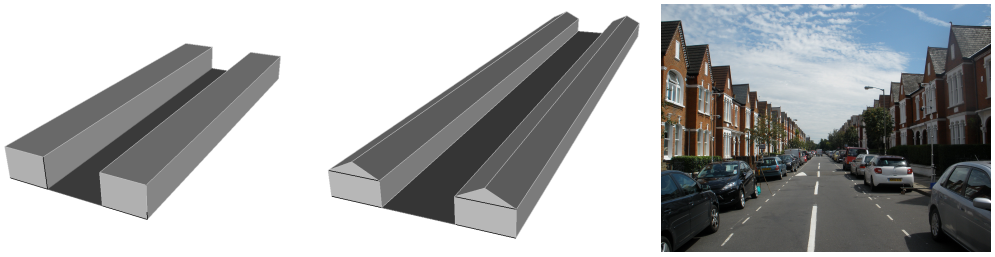

Figure 50: Roof geometry used in CFD models and real life roof geometry

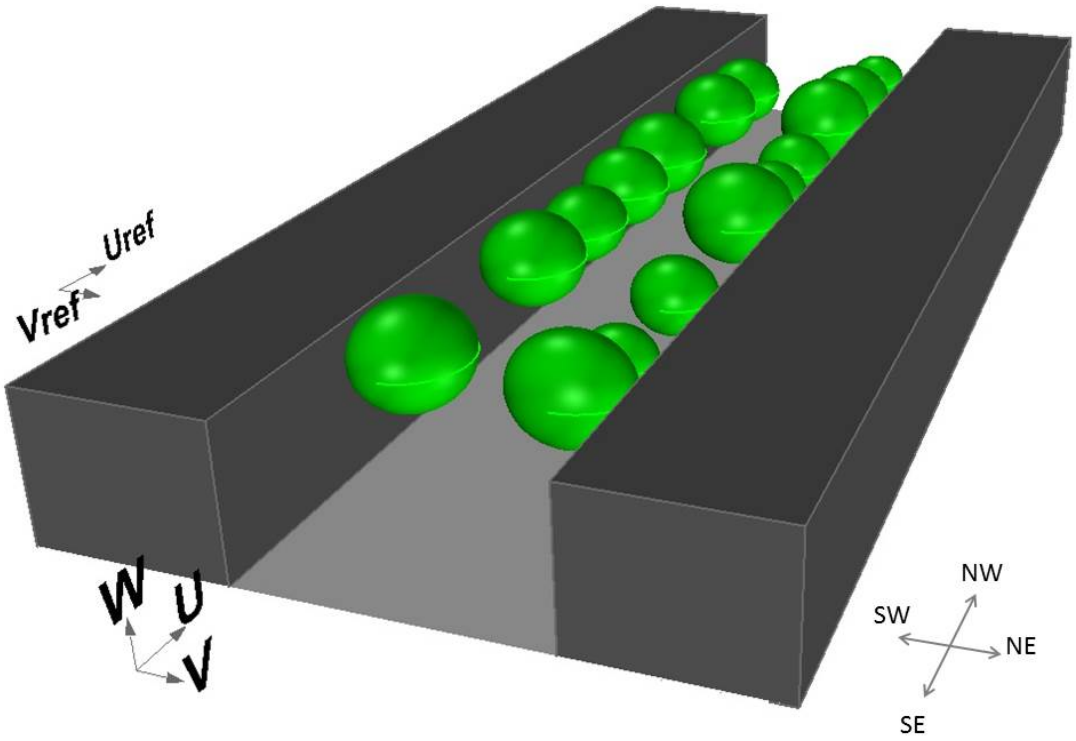

Figure 51: Geometry used in CFD model of tree-lined street

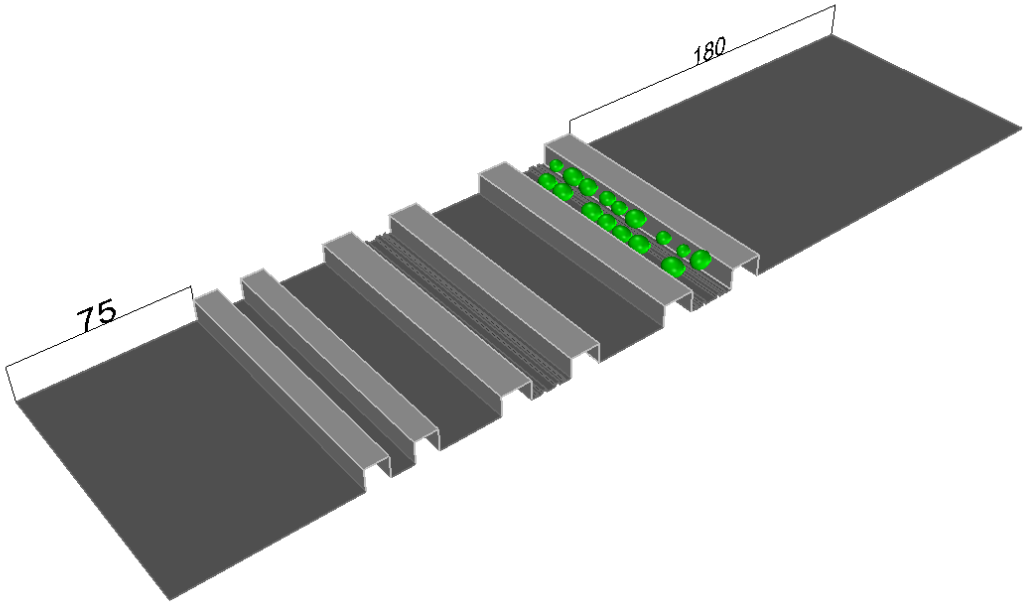

Figure 52: Geometry used for full scale CFD model

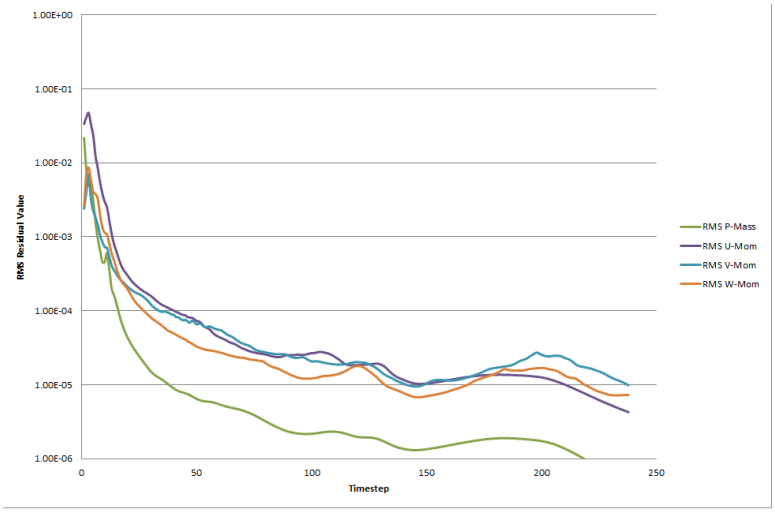

Figure 53: Graph showing RMS values of residuals for full scale CFD model

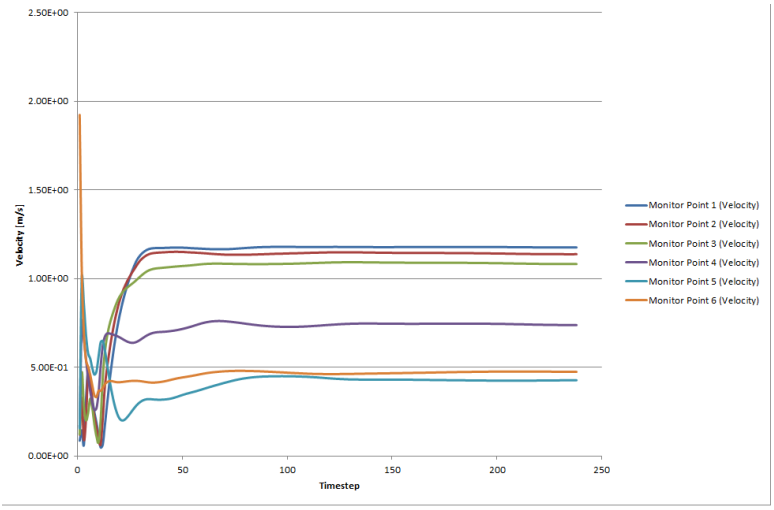

Figure 54: Graph showing velocity values at monitoring points for full scale CFD model at various timesteps

References

S. R. Ahmed, G. Ramm, and G. Faltin. Some salient features of the time-averaged ground vehicle wake. SAE Technical Paper 840300, SAE International, Warrendale, PA, February 1984. 198

J. H. Amorim, V. Rodrigues, R. Tavares, J. Valente, and C. Borrego. CFD modelling of the aerodynamic effect of trees on urban air pollution dispersion. *Science of The Total Environment*, 461462:541–551, September 2013. ISSN 0048-9697. doi: 10.1016/j.scitotenv.2013.05.031. URL `http://www.sciencedirect.com/science/article/pii/S0048969713005743`. 16, 17, 35

Ansys. Ansys CFX Solver Theory Guide, 2009. 24

David Aspley. MACE 42001: Computational hydraulics lecture notes, 2014. 21, 22

K. P. Beckett, P. H. Freer-Smith, and G. Taylor. Urban woodlands: their role in reducing the effects of particulate pollution. *Environmental Pollution*, 99(3): 347–360, 1998. ISSN 0269-7491. doi: 10.1016/S0269-7491(98)00016-5. 13

A. C. M. Beljaars, J. L. Walmsley, and P. A. Taylor. A mixed spectral finite-difference model for neutrally stratified boundary-layer flow over roughness changes and topography. *Bound.-Layer Meteor.*, 38(3):273–303, 1987. ISSN 0006-8314. doi: 10.1007/BF00122448. 51, 52

ACM Beljaars, JL Walmsley, and PA Taylor. A MIXED SPECTRAL FINITE-DIFFERENCE MODEL FOR NEUTRALLY STRATIFIED BOUNDARY-LAYER FLOW OVER ROUGHNESS CHANGES AND TOPOGRAPHY.

BOUNDARY-LAYER METEOROLOGY, 38(3):273–303, FEB 1987. ISSN 0006-8314. 58, 196

Bert Blocken and Jan Carmeliet. Pedestrian wind environment around buildings: Literature review and practical examples. *Journal of Thermal Envelope and Building Science*, 28(2):107–159, October 2004. ISSN 1744-2591, 1744-2583. doi: 10.1177/1097196304044396. 203

Bert Blocken, Ted Stathopoulos, and Jan Carmeliet. CFD simulation of the atmospheric boundary layer: wall function problems. *Atmos. Environ.*, 41(2): 238–252, January 2007. ISSN 1352-2310. doi: 10.1016/j.atmosenv.2006.08.019. 8, 43

Bert Blocken, Ted Stathopoulos, Jan Carmeliet, and Jan L. M. Hensen. Application of computational fluid dynamics in building performance simulation for the outdoor environment: an overview. *J. Building Perform. Simul.*, 4(2): 157–184, 2011. 25

Bert Blocken, Ted Stathopoulos, and Jan Carmeliet. CFD simulation of the atmospheric boundary layer: wall function problems. *Atmos. Environ.*, 41(2): 238–252, JAN 2007. ISSN 1352-2310. doi: {10.1016/j.atmosenv.2006.08.019}. xi, 24, 27, 28, 31, 195

Cheng-Hsin Chang and Robert N. Meroney. Concentration and flow distributions in urban street canyons: wind tunnel and computational data. *Journal of Wind Engineering and Industrial Aerodynamics*, 91(9):1141–1154, September 2003. ISSN 0167-6105. doi: 10.1016/S0167-6105(03)00056-4. 12

Sai Hung Cheung, Todd A. Oliver, Ernesto E. Prudencio, Serge Prudhomme, and Robert D. Moser. Bayesian uncertainty analysis with applications to turbulence modeling. *Reliability Engineering & System Safety*, 96(9):1137–1149, September 2011. ISSN 0951-8320. doi: 10.1016/j.ress.2010.09.013. 50

Ronald M. Cionco. Intensity of turbulence within canopies with simple and complex roughness elements. *Boundary-Layer Meteorology*, 2(4):453–465, June 1972. doi: 10.1007/BF00821548. 15

K. Czder, M. Balcz, and J. Eichhorn. Modelling of flow and dispersion in a street canyon by means of numerical simulation. pages 47–52, Hungary, March 2009. ISBN 978-963-661-866-7. 16

Arthur Da Silva, Carole Sinfort, Cyril Tinet, Daniel Pierrat, and Serge Huberson. A lagrangian model for spray behaviour within vine canopies. *Journal of Aerosol Science*, 37(5):658–674, May 2006. ISSN 0021-8502. doi: 10.1016/j.jaerosci.2005.05.016. 38

F. T. DePaul and C. M. Sheih. Measurements of wind velocities in a street canyon. *Atmospheric Environment (1967)*, 20(3):455–459, 1986. ISSN 0004-6981. doi: 10.1016/0004-6981(86)90085-5. 10

Argiro Dimoudi and Marialena Nikolopoulou. Vegetation in the urban environment: microclimatic analysis and benefits. *Energy and Buildings*, 35(1):69–76, January 2003. ISSN 0378-7788. doi: 10.1016/S0378-7788(02)00081-6. 13

A. Dobre, S.J. Arnold, R.J. Smalley, J.W.D. Boddy, J.F. Barlow, A.S. Tomlin, and S.E. Belcher. Flow field measurements in the proximity of an urban intersection in london, UK. *Atmospheric Environment*, 39(26):4647–4657, August 2005. ISSN 1352-2310. doi: 10.1016/j.atmosenv.2005.04.015. 11, 82, 86

M. C. Dunn, B. Shotorban, and A. Frendi. Uncertainty quantification of turbulence model coefficients via latin hypercube sampling method. *Journal of fluids engineering*, 133(4), 2011. 49

Paul A. Durbin. Separated flow computations with the k-epsilon-v-squared model. *AIAA journal*, 33(4):659664, 1995. 52

I. Eliasson, B. Offerle, C. S. B. Grimmond, and S. Lindqvist. Wind fields and turbulence statistics in an urban street canyon. *Atmospheric environment*, 40 (1):1–16, 2006. 11

A. Melese Endalew, M. Hertog, M.A. Delele, K. Baetens, T. Persoons, M. Baelmans, H. Ramon, B.M. Nicola, and P. Verboven. CFD modelling and wind

tunnel validation of airflow through plant canopies using 3d canopy architecture. *International Journal of Heat and Fluid Flow*, 30(2):356–368, April 2009. ISSN 0142-727X. doi: 10.1016/j.ijheatfluidflow.2008.12.007. 14, 16

Engineering Sciences Data Unit. *Wind speed profiles over terrain with roughness changes for flat or hilly sites.* Engineering Sciences Data Unit, London, 1984. ISBN 0856794732 9780856794735. 195, 253

H. Foudhil, Y. Brunet, and J. P. Caltagirone. A fine-scale k model for atmospheric flow over heterogeneous landscapes. *Environmental Fluid Mechanics*, 5(3):247–265, June 2005. doi: 10.1007/s10652-004-2124-x. 14

Jorg Franke, Antti Hellsten, K. Heinke Schlunzen, and Bertrand Carissimo. The COST 732 Best Practice Guideline for CFD simulation of flows in the urban environment: a summary. *International Journal of Environment and Pollution*, 44(1):419–427, 2011. 251

Yevgeny A. Gayev and Eric Savory. Influence of street obstructions on flow processes within urban canyons. *Journal of Wind Engineering and Industrial Aerodynamics*, 82(1-3):89–103, August 1999. ISSN 0167-6105. doi: 10.1016/S0167-6105(98)00212-8. 12

C. Gorl, J. van Beeck, P. Rambaud, and G. Van Tendeloo. CFD modelling of small particle dispersion: The influence of the turbulence kinetic energy in the atmospheric boundary layer. *Atmospheric Environment*, 43(3):673–681, January 2009. ISSN 1352-2310. doi: 10.1016/j.atmosenv.2008.09.060. 30, 52

P. F. Grant and W. G. Nickling. Direct field measurement of wind drag on vegetation for application to windbreak design and modelling. *Land Degradation & Development*, 9(1):57–66, 1998. doi: 10.1002/(SICI)1099-145X(199801/02)9:1⟨57::AID-LDR288⟩3.0.CO;2-7. 16

S.R. Green, J. Grace, and N.J. Hutchings. Observations of turbulent air flow in three stands of widely spaced sitka spruce. *Agricultural and Forest Meteorology*, 74(34):205–225, May 1995. ISSN 0168-1923. doi: 10.1016/0168-1923(94)02191-L. 34

Christof Gromke, Riccardo Buccolieri, Silvana Di Sabatino, and Bodo Ruck. Dispersion study in a street canyon with tree planting by means of wind tunnel and numerical investigations - evaluation of CFD data with experimental data. *Atmospheric Environment*, 42(37):8640–8650, December 2008. ISSN 1352-2310. doi: 10.1016/j.atmosenv.2008.08.019. 14, 16

G. Gross. A numerical study of the air flow within and around a single tree. *Boundary-Layer Meteorology*, 40(4):311–327, September 1987. ISSN 0006-8314, 1573-1472. doi: 10.1007/BF00116099. xi, 14, 15, 19, 38

Serge Guillas, Nina Glover, and Liora Malki-Epshtein. Bayesian calibration of the constants of the turbulence model for a CFD model of street canyon flow. *Computer Methods in Applied Mechanics and Engineering*, 279:536–553, September 2014. ISSN 0045-7825. doi: 10.1016/j.cma.2014.06.008. 194

David Hamlyn and Rex Britter. A numerical study of the flow field and exchange processes within a canopy of urban-type roughness. *Atmospheric Environment*, 39(18):3243–3254, June 2005. ISSN 1352-2310. doi: 10.1016/j.atmosenv.2005.02.020. 8

K. Hanjalic and B. E. Launder. A reynolds stress model of turbulence and its application to thin shear flows. *Journal of fluid Mechanics*, 52(04):609638, 1972. ISSN 0022-1120. 50

Gordon M. Heisler and David R. Dewalle. 2. Effects of windbreak structure on wind flow. *Agriculture, Ecosystems & Environment*, 2223:41–69, August 1988. ISSN 0167-8809. doi: 10.1016/0167-8809(88)90007-2. 15

J. C. R. Hunt, E. C. Poulton, and J. C. Mumford. The effects of wind on people; new criteria based on wind tunnel experiments. *Building and Environment*, 11 (1):15–28, 1976. ISSN 0360-1323. doi: 10.1016/0360-1323(76)90015-9. 203

W.P Jones and B.E Launder. The prediction of laminarization with a two-equation model of turbulence. *International Journal of Heat and Mass Transfer*, 15(2):301–314, February 1972. ISSN 0017-9310. 25

P. Kastner-Klein and E. J. Plate. Wind-tunnel study of concentration fields in street canyons. *Atmospheric Environment*, 33(24-25):3973–3979, October 1999. ISSN 1352-2310. doi: 10.1016/S1352-2310(99)00139-9. 41

P. Kastner-Klein, E. Fedorovich, and M. W. Rotach. A wind tunnel study of organised and turbulent air motions in urban street canyons. *J. Wind Eng. Ind. Aerodyn.*, 89(9):849–861, July 2001. ISSN 0167-6105. doi: 10.1016/S0167-6105(01)00074-5. 41, 68, 246

P. Kastner-Klein, R. Berkowicz, and R. Britter. The influence of street architecture on flow and dispersion in street canyons. *Meteorology and Atmospheric Physics*, 87(1):121–131, 2004. doi: 10.1007/s00703-003-0065-4. URL `http://dx.doi.org/10.1007/s00703-003-0065-4`. xi, 11, 18, 41, 149

Petra Kastner-Klein. kastner-klein details of experiment set up. xi, 41, 45

Gabriel G. Katul, Larry Mahrt, Davide Poggi, and Christophe Sanz. ONE- and TWO-equation models for canopy turbulence. *Boundary-Layer Meteorology*, 113(1):81–109, October 2004. ISSN 0006-8314, 1573-1472. doi: 10.1023/B:BOUN.0000037333.48760.e5. 34, 254, 255

Marc C. Kennedy and Anthony O'Hagan. Bayesian calibration of computer models. *Journal of the Royal Statistical Society. Series B (Statistical Methodology)*, 63(3):425–464, 2001. ISSN 13697412. 53, 54

Sung-Eun Kim and Ferit Boysan. Application of CFD to environmental flows. *Journal of Wind Engineering and Industrial Aerodynamics*, 81(1-3):145–158, May 1999. ISSN 0167-6105. doi: 10.1016/S0167-6105(99)00013-6. 31

Akio Koizumi, Jun-ichi Motoyama, Kei Sawata, Yoshihisa Sasaki, and Takuro Hirai. Evaluation of drag coefficients of poplar-tree crowns by a field test method. *Journal of Wood Science*, 56(3):189–193, June 2010. ISSN 1435-0211, 1611-4663. doi: 10.1007/s10086-009-1091-8. 38, 39

A. Kovar-Panskus, P. Louka, J.-F. Sini, E. Savory, M. Czech, A. Abdelqari, P. G. Mestayer, and N. Toy. Influence of geometry on the mean flow within urban street canyons a comparison of wind tunnel experiments and numerical

simulations. *Water, Air, & Soil Pollution: Focus*, 2(5):365–380, 2002. doi: 10.1023/A:1021308022939. 12

B. E Launder and D. B Spalding. *Lectures in Mathematical Models of Turbulence*. Academic Press, London, 1972. ISBN 0124380506. 50

B. E. Launder and D. B. Spalding. The numerical computation of turbulent flows. *Comput. Meth. Appl. Mech. Eng.*, 3(2):269–289, March 1974. ISSN 0045-7825. doi: 10.1016/0045-7825(74)90029-2. 26

Olivier P Le Maitre, Omar M Knio, Habib N Najm, and Roger G Ghanem. A stochastic projection method for fluid flow: I. basic formulation. *Journal of Computational Physics*, 173(2):481–511, November 2001. ISSN 0021-9991. doi: 10.1006/jcph.2001.6889. 49

J. K. Leenders, J. H. van Boxel, and G. Sterk. The effect of single vegetation elements on wind speed and sediment transport in the sahelian zone of burkina faso. *Earth Surface Processes and Landforms*, 32(10):1454–1474, 2007. doi: 10.1002/esp.1452. 14

Xian-Xiang Li, Chun-Ho Liu, Dennis Y.C. Leung, and K.M. Lam. Recent progress in CFD modelling of wind field and pollutant transport in street canyons. *Atmospheric Environment*, 40(29):5640–5658, September 2006. ISSN 1352-2310. doi: 10.1016/j.atmosenv.2006.04.055. 12

F. S. Lien, E. Yee, and Y. Cheng. Simulation of mean flow and turbulence over a 2D building array using high-resolution CFD and a distributed drag force approach. *Journal of Wind Engineering and Industrial Aerodynamics*, 92(2): 117–158, February 2004. ISSN 0167-6105. 31, 32

J. Liu, J. M. Chen, T. A. Black, and M. D. Novak. E- modelling of turbulent air flow downwind of a model forest edge. *Boundary-Layer Meteorology*, 77(1): 21–44, January 1996. ISSN 0006-8314, 1573-1472. doi: 10.1007/BF00121857. 34, 35

A. Loeffler, A. Gordon, and T. Gillespie. Optical porosity and windspeed reduction by coniferous windbreaks in southern ontario. *Agroforestry Systems*, 17 (2):119–133, February 1992. doi: 10.1007/BF00053117. 15

P. Louka, S. E. Belcher, and R. G. Harrison. Modified street canyon flow. *Journal of Wind Engineering and Industrial Aerodynamics*, 74-76:485–493, April 1998. ISSN 0167-6105. doi: 10.1016/S0167-6105(98)00044-0. 11

P Louka, S.E Belcher, and R.G Harrison. Coupling between air flow in streets and the well-developed boundary layer aloft. *Atmospheric Environment*, 34 (16):2613–2621, 2000. ISSN 1352-2310. doi: 10.1016/S1352-2310(99)00477-X. 10, 71

A. McNabola, B.M. Broderick, and L.W. Gill. A numerical investigation of the impact of low boundary walls on pedestrian exposure to air pollutants in urban street canyons. *Science of The Total Environment*, 407(2):760–769, January 2009. ISSN 0048-9697. doi: 10.1016/j.scitotenv.2008.09.036. 12

E. G. (ed) McPherson. Energy-conserving site design. January 1984. URL `http://www.osti.gov/scitech/biblio/5628644`. 37

Akashi Mochida, Yuichi Tabata, Tatsuaki Iwata, and Hiroshi Yoshino. Examining tree canopy models for CFD prediction of wind environment at pedestrian level. *Journal of Wind Engineering and Industrial Aerodynamics*, 96(10-11): 1667–1677, 2008. ISSN 0167-6105. doi: 10.1016/j.jweia.2008.02.055. 35

S Murakami. Comparison of various turbulence models applied to a bluff body. *Journal of Wind Engineering and Industrial Aerodynamics*, 4647:21–36, August 1993. ISSN 0167-6105. doi: 10.1016/0167-6105(93)90112-2. 32, 71

Shuzo Murakami and Kiyotaka Deguchi. New criteria for wind effects on pedestrians. *Journal of Wind Engineering and Industrial Aerodynamics*, 7(3):289–309, May 1981. ISSN 0167-6105. doi: 10.1016/0167-6105(81)90055-6. 203

Habib N. Najm. Uncertainty quantification and polynomial chaos techniques in computational fluid dynamics. *Annual Review of Fluid Mechanics*, 41:35–52,

January 2009. ISSN 0066-4189, 1545-4479. doi: 10.1146/annurev.fluid.010908.165248. 49

M. D. Novak. Chicago's urban forest ecosystem results of the chicago urban forest climate project. Technical report. URL `http://www.nrs.fs.fed.us/pubs/gtr/gtr_ne186.pdf`. 14

David J. Nowak. Notes: estimating leaf area and leaf biomass of open-grown deciduous urban trees. *Forest Science*, 42(4):504–507, 1996. 36, 37

T. Oke. Street design and urban canopy layer climate. *Energy and Buildings*, Mar(22):103–113, 1988. xi, 7, 9, 12, 18

Todd A Oliver and Robert D Moser. Bayesian uncertainty quantification applied to RANS turbulence models. *Journal of Physics: Conference Series*, 318(4): 042032, December 2011. ISSN 1742-6596. doi: 10.1088/1742-6596/318/4/042032. 49

Ioannis Panagiotou, Marina K.-A. Neophytou, David Hamlyn, and Rex E. Britter. City breathability as quantified by the exchange velocity and its spatial variation in real inhomogeneous urban geometries: An example from central london urban area. *Science of The Total Environment*, 442:466–477, January 2013. ISSN 0048-9697. doi: 10.1016/j.scitotenv.2012.09.001. 8

H.A. Panofsky and J.A. Dutton. *Atmospheric turbulence: models and methods for engineering aplications*. New York; John Wiley & Sons, 1984. 51

E. Gregory McPherson Paula J. Peper. Equations for predicting diameter, height, crown width and leaf area of san joaquin valley street trees. 2001. 36, 37, 255

Svetlana Poroseva and Gianluca Iaccarino. Simulating separated flows using the k-" model. *Annual Research: Briefs 2001*, 2001. 51, 52

M. R. Raupach and R. H. Shaw. Averaging procedures for flow within vegetation canopies. *Boundary-Layer Meteorology*, 22(1):79–90, January 1982. doi: 10.1007/BF00128057. URL `http://dx.doi.org/10.1007/BF00128057`. 14, 15, 33, 34, 166

PJ Richards and RP Hoxey. APPROPRIATE BOUNDARY-CONDITIONS FOR COMPUTATIONAL WIND ENGINEERING MODELS USING THE KAPPA-EPSILON TURBULENCE MODEL. *JOURNAL OF WIND ENGINEERING AND INDUSTRIAL AERODYNAMICS*, 46-7:145–153, AUG 1993. ISSN 0167-6105. 1ST INTERNATIONAL SYMP ON COMPUTATIONAL WIND ENGINEERING (CWE92), TOKYO, JAPAN, AUG 21-23, 1992. 42, 58, 196

P.J Richards and R.P Hoxey. Appropriate boundary conditions for computational wind engineering models using the k-ε turbulence model. *J. Wind Eng. Ind. Aerodyn.*, 46-47:145–153, August 1993. ISSN 0167-6105. doi: 10.1016/0167-6105(93)90124-7. 28, 29, 51, 242, 247, 255

P.J. Richards and S.E. Norris. Appropriate boundary conditions for computational wind engineering models revisited. *Journal of Wind Engineering and Industrial Aerodynamics*, 99(4):257–266, April 2011. ISSN 0167-6105. doi: 10.1016/j.jweia.2010.12.008. 28, 30, 241

Hilary Jane Roodbaraky. *Dynamics and aerodynamics of deciduous urban trees*. PhD, University of Nottingham, 1994. 38, 39, 254

Christopher J. Roy and William L. Oberkampf. A comprehensive framework for verification, validation, and uncertainty quantification in scientific computing. *Computer Methods in Applied Mechanics and Engineering*, 200(25-28):2131–2144, June 2011. ISSN 0045-7825. doi: 10.1016/j.cma.2011.03.016. 49

Christophe Sanz. A note on k - modelling of vegetation canopy air-flows. *Boundary-Layer Meteorology*, 108(1):191–197, July 2003. ISSN 0006-8314, 1573-1472. doi: 10.1023/A:1023066012766. 35, 254

Efisio Solazzo, Xiaoming Cai, and Sotiris Vardoulakis. Improved parameterisation for the numerical modelling of air pollution within an urban street canyon. *Environ. Modell. Softw.*, 24(3):381–388, 2009. 32

Charles G. Speziale. On nonlinear k-l and k- models of turbulence. *Journal of Fluid Mechanics*, 178:459–475, 1987. doi: 10.1017/S0022112087001319. 32

R.H. Thuillier. The influence of instrumentation, siting, exposure height, and temporal averaging methodology on meteorological measurements from SJVAQS/AUSPEX. *Journal of applied meteorology*, 34(8):1815–1823, 1995. 87

M. H. Tourin and W Shen. Deciduous forest diffusion study. *Final Report to US Army, Dugway Proving grounds, Contract DA42-007-AMC*, 8, 1966. 15

Jiyuan Tu. *Computational Fluid Dynamics: A Practical Approach*. Butterworth-Heinemann, Burlington, MA, 2008. ISBN 9780750685634. 20

V. N. Pilipenko V. A. Ioselevich. Logarithmic velocity profile for flow of a weak polymer solution near a rough surface. *Soviet Physics Doklady*, 1974. 24

H. K Versteeg. *An Introduction to Computational Fluid Dynamics: The Finite Volume Method*. Pearson Education Ltd, Harlow, 2nd ed edition, 2007. ISBN 9780131274983. 20

R.J. Yamartino and G. Wiegand. Development and evaluation of simple models for the flow, turbulence adn pollutant concentration fields within an urban street canyon. *Atmospheric Environment - Part A General Topics*, 20(11): 2137–2156, 1986. ISSN 0004-6981. 10

Yi Yang, Ming Gu, Suqin Chen, and Xinyang Jin. New inflow boundary conditions for modelling the neutral equilibrium atmospheric boundary layer in computational wind engineering. *Journal of Wind Engineering and Industrial Aerodynamics*, 97(2):88–95, February 2009. ISSN 0167-6105. doi: 10.1016/j.jweia.2008.12.001. 29, 43, 52, 195, 242, 252